Factors Affecting Fiber Orientation and Properties in Semi-Flexible Fiber Composites: Including the Addition of Carbon Nanotubes

By

Kevin D. Herrington

Dissertation submitted to the faculty of
Virginia Polytechnic Institute and State University
in partial fulfillment of the requirements for the degree of

DOCTOR OF PHILOSOPHY

In

Chemical Engineering

Donald G. Baird, Chairman

Michael J. Bortner

Scott W. Case

Stephen M. Martin

August 24, 2015

Blacksburg, VA

Keywords: Fiber Reinforced Polymer Composites, Long Glass Fiber, Long Carbon Fiber, Multi-scale Composites, Carbon Nanotube, Fiber Lengths, Orientation Distribution, Injection Molding

Factors Affecting Fiber Orientation and Properties in Semi-Flexible Fiber Composites: Including the Addition of Carbon Nanotubes

Kevin Daniel Herrington

(Abstract)

Fiber reinforced polymer composites formed via injection molding are used in the automotive and aerospace industries because they exhibit increased mechanical properties compared to their unfilled counterparts. However, their mechanical properties are highly dependent on the post-processing fiber orientation due to the reinforcing effect of the fibers. As the fiber lengths in these composites increase the modulus at higher strains, impact toughness, and tensile strength of the composites also increase. Therefore, a thorough understanding of the evolution of fiber orientation and length in injection molding is needed.

Within this research, factors affecting the orientation of injection molded long fiber composites in an end-gated plaque were investigated. Matrix viscosity was found to have a small effect on fiber orientation. The impact matrix viscosity had on orientation was dependent on fiber loading. At lower fiber loadings, the higher viscosity material had a more asymmetric orientation profile throughout the samples and less of a shell-core-shell orientation. At higher fiber loadings, there were few differences in orientation due to matrix viscosity. Fiber concentration was found to have a larger influence on fiber orientation than matrix viscosity. Increased fiber concentration led to a lower degree of flow alignment and a broader core region at all locations examined, following the trend previously reported for short fiber composites.

The orientations of three different fiber length distributions of glass fiber (GF) were compared. The GF composites had length averages in the long fiber regime, number average length (L_n) of 0.99 mm

and weight average length (L_w) of 3.22 mm, short fiber regime, L_n 0.4 mm L_w of 7.4 mm, and in-between the two, L_n of 0.77 and L_w 1.22 mm. The GF orientations were compared to the orientation of long carbon fiber (CF) composites with an L_n of 0.36 mm and L_w of 1.71 mm at equivalent volume loadings. The longer fibers in the fiber length distribution were shown to have a disproportionate effect on orientation, with weight average aspect ratio being better than number average aspect ratio at indicating if the GF and CF samples orientated comparably.

To improve properties transverse to the main flow direction, the super critical carbon dioxide aided deagglomeration of multi-walled carbon nanotubes (CNTs) was used to create injection molded multiscale composites with CNT, CF, and polypropylene. The addition of CNTs greatly improved the tensile and electrical properties of the composites compared to those without CNTs. The degree of improvement from adding CNTs was found to be dependent on CF concentration, indicating that the CNTs were most likely interacting with the CF and not the polymer. A CNT concentration of 1 wt% with a tenfold degree of expansion at 40 wt% CF proved to be optimum. A large improvement in the tensile properties transverse to the flow direction was found implying that the CNTs were not highly flow aligned. Tensile and electrical properties began to fall off at higher CNT loadings and degrees of expansion indicating the importance of obtaining a good dispersion of CNTs in the part.

Original Contributions

The following are considered to be the significant contributions of this research:

- Obtained a thorough set of experimental data on the effect of matrix viscosity on long fiber composite orientation in injection molded end-gated plaques and how fiber concentration influenced this effect.

- Demonstrated that weight average aspect ratio was a better indicator than number average aspect ratio of how different fiber length distributions orient using experimental fiber orientation.

- Created injection molded multiscale composites with improved tensile and electrical properties using carbon nanotubes and long carbon fiber polypropylene composites. The efforts in this work were also the first to use the super critical carbon dioxide aided deagglomeration of CNTs to further improve the properties of injection multiscale composites.

Acknowledgements

I would like to express my thanks and gratitude to my advisor Dr. Donald G. Baird for his guidance and support that resulted in the completion of this work. Additionally I would like to thank my committee members Dr. Michael Bortner, Dr. Scott Case, and Dr. Stephen Martin for their comments and suggestions during the evolution of this work.

I am grateful to my parents whose love, constant support, and advice have been crucial not just for this work but for everything I have accomplished through the years. I would also like to express my gratitude for my brother and extended family whose friendship and guidance have always been important to me.

I would like to acknowledge my current and former lab members who have impacted my life and research: John Quigley, Mark Cieslinski, Kevin Meyer, Chen Qian, Chen Chen, John Hofmann, Hongyu Chen, Matt Hopkins, and Jier Yang

I greatly appreciate the chemical engineering department staff whose help was irreplaceable: Diane Cannaday, Tina Russell, Nora Bentley, Jane Price, Melanie Darden, Riley Chan, Kevin Holshouser, and Michael Vaught.

Finally, I cannot thank my fiancée Sara Horsey enough. Without her love, advice, encouragement, and unending patience this dissertation would not have been possible. I will be forever grateful.

Format of Dissertation

This dissertation is written in manuscript format. Chapters 3-5 are self-contained papers that will be submitted for journal publication. Each paper separately describes the experiment, results, and conclusions relative to each chapter. The data presented in the papers is can be found in the Appendixes

Table of Contents

1 Chapter 1: Introduction 1

1.1 Fiber Reinforced Polymers 2

1.2 Orientation Model Basics 2

1.3 Factors Influencing Orientation 3

1.4 Carbon Fiber 4

1.5 Multiscale Composites 4

1.6 Objectives 5

1.7 References 7

2 Literature Review 10

2.1 Classification of Fiber Composites 11

2.1.1 Production Methods 12

2.1.2 Concentration Regimes 13

2.1.3 Fiber Length 15

2.2 Representing Orientation 16

2.2.1 Distribution Function 17

2.2.2 Orientation Tensor 17

2.3 Experimental Determination of Fiber Orientation 20

2.3.1 Method of Ellipses 21

2.3.2 Optical 24

2.3.3 Scanning Electron Microscopy 30

2.3.4 Confocal Microscopy 30

2.3.5 Scanning Acoustical Microscopy 31

2.3.6 Microcomputer Tomography 32

2.3.7 Other Methods 34

2.4 Modeling Orientation 34

2.4.1 Jeffery's Model 35

2.4.2 Closure Approximations 36

2.4.3 Folgar-Tucker Model 37

2.4.4 Folgar-Tucker Model Modifications 38

2.4.5 Bead-Rod Model 39

2.4.6 Fitting of Model Parameters 40

2.5 Fiber Orientation Studies 41
2.5.1 Test Geometries 41
2.5.2 Short Glass Fiber 43
2.5.3 Processing Conditions 44
2.5.4 Fiber Length 46
2.6 References 49
3 Fiber Concentration and Matrix Viscosity Effects on Long Glass Fiber Orientation 55
3.1 Abstract 56
3.2 Background and Motivation 56
3.3 Materials and Methods 59
3.3.1 Materials 59
3.3.2 Injection molding 59
3.3.3 Sample Preparation 60
3.3.4 Method of Ellipses 61
3.3.5 Fiber Length 62
3.3.6 Rheology 62
3.4 Results and Discussion 62
3.4.1 Rheology 62
3.4.2 Fiber Lengths 63
3.4.3 Orientation Differences 65
3.5 Conclusions 71
3.6 References 73
4 Effect of Fiber Length Distribution on the Orientation of Injection Molded Long Carbon and Long Glass Fiber Polypropylene Composites 75
4.1 Abstract 76
4.2 Background and Motivation 76
4.3 Materials and Methodology 78
4.3.1 Materials 78
4.3.2 Methods 79
4.4 Results and Discussion 82
4.4.1 Rheology 82
4.4.2 Fiber Length 83
4.4.3 Fiber Orientation 86

4.5 Conclusions 91
4.6 References 92
5 Injection Molded Carbon Nanotube/Long Carbon Fiber Multiscale Composites 95
5.1 Abstract 96
5.2 Background and Motivation 96
5.3 Experimental Materials and Methodology 100
5.3.1 Materials 100
5.3.2 Methods 100
5.4 Results and Discussion 103
5.4.1 Effect of CF Concentration 103
5.4.2 CNT Concentration 106
5.4.3 CNT Degree of Expansion 109
5.4.4 Electrical Conductivity 110
5.4.5 Scanning Electron Microscopy 117
5.5 Conclusions 120
5.6 References 122
6 Conclusions and Recommendations for Future Work 125
6.1 Conclusions from this Research 126
6.2 Recommendations for Future Work 127
6.3 References 130
Appendix A: Preliminary Results on the Effect of Initial Pellet Length on the Orientation and Fiber Length of Long Fiber Composites 131
A.1. Introduction 132
A.2. Experimental 132
A.2.1. Materials 132
A.2.2. Injection Molding 132
A.2.3. Fiber Length 133
A.2.4. Orientation Measurements 133
A.3. Results 134
A.3.1. Fiber Length 134
A.3.2. Orientation Results 135
A.4. Conclusions 138
A.5. References 140

Appendix B: Multiscale Tensile and Conductivity Results 141
Appendix C: Rheological Data 148
Appendix D: Fiber Lengths 154
Appendix E: Orientation Measurements 161

List of Figures

Figure 2-1: Concentration regimes as a function of fiber aspect fraction and volume fraction adapted from [23].....14

Figure 2-2: Vector p representing a rigid fiber and its characteristic angles.....17

Figure 2-3: Representation of a fiber using the bead-rod model.....19

Figure 2-4: Illustration of the parameters required for the MOE:(a) View of a fiber in sample (b) 2-D view, adapted from [50].....21

Figure 2-5: Ambiguity in ϕ for MOE adapted from [50].....22

Figure 2-6: Tridimensional marker on a sample 25

Figure 2-7: Effects of plasma etching (a) before (b) after adapted from [50] 26

Figure 2-8: Serial Sectioning Method 28

Figure 2-9: Top down view to determine end-to-end vector in the x-y plane.....29

Figure 2-10: Illustration of SAM image adapted from[67].....31

Figure 2-11: CGD.....42

Figure 2-12: EGP.....42

Figure 2-13: Representative graph of A_{11} component 43

Figure 3-1: Experimental geometry and the selected inspection locations for the end-gated plaque. Grey squares represent the inspection locations. 60

Figure 3-2: Ellipse created by a fiber and characteristic parameters.....61

Figure 3-3: Viscosity comparison low and high viscosity Sabic PP ■ high viscosity ●low viscosity. Filled points are oscillatory and steady shear data. Unfilled points are capillary data.....63

Figure 3-4: Fiber length analysis after injection molding for the 30 wt% GF (top) and 50 wt% GF sample (bottom) comparing breakage in (—) Low Viscosity and (— —) High Viscosity PP. Plotted as normalized frequency as a function of the aspect ratio of the fibers. 64

Figure 3-5: A_{11} component of the orientation tensor as a function of part thickness along the center-plane for 50 wt % GF (■) high viscosity and (●) low viscosity PP samples at (a) 0 %, (b) 10%, (c) 40%, and (d) 90% plaque length.....65

Figure 3-6: 50 wt % glass fiber high viscosity polypropylene at the gate-mold interface.....66

Figure 3-7: A_{11} component of the orientation tensor for 50 wt% GF at 40% plaque length 50% plaque width (top) 90% plaque width (bottom) for (■) high viscosity and (●) low viscosity PP samples. 67

Figure 3-8: A_{11} component of the orientation tensor as a function of part thichness for 50 wt% (●) and 30 wt% (◊) GF PP low viscosity samples along the center plane at (a) 0 %, (b) 10%, (c) 40%, and (d) 90% plaque length. 68

Figure 3-9: A_{11} component of the orientation tensor as a function of part thickness along the center-plane for 30 wt % GF (■) high viscosity and (◊) low viscosity PP samples at (a) 0 %, (b) 10%, (c) 40%, and (d) 90% plaque length. 69

Figure 3-10: A_{11} component of the orientation tensor for 30 wt% GF (▲) high viscosity and (◊) low viscosity PP samples at 40% plaque length at 50% plaque width (top) and 90% plaque width (bottom). 70

Figure 3-11: Optical images of Y-Z plane at 95% of plaque length along the center plane for 50 wt% GF low viscosity (left) and high viscosity (right) PP samples. 71

Figure 4-1: Experimental geometry and the selected inspection locations for the end-gated plaque. Grey squares represent the inspection locations. 81

Figure 4-2: Rheology of Sabic (■) and Plasticomp (●) polypropylene. Filled points are oscillatory and steady shear data. Unfilled points are capillary data. 83

Figure 4-3: Fiber length distributions for (—) CF, (—•) GF 1 bar 200 rpm, (— —) GF 5 bar 200 rpm, and (•) GF 10 bar 200 rpm. 86

Figure 4-4: Diagonal components of the second orientation tensor, **A**, (▲ A_{11}, ■ A_{22}, ● A_{33}.) for 30 vol% GF PP injection molded at 5 bar along the center-plane at 40% of plaque length. 87

Figure 4-5: A_{11} component of the orientation tensor as a function of part thickness for 30 vol% GF and CF PP down the center-plane of an end-gated plaque at (a) 0%, (b) 10%, (c) 40 % and (d) 90% of plaque length for (■) 1 bar GF, (▲) 5 bar GF, (●) 10 bar GF, and (○) CF. 88

Figure 4-6: A_{11} component of the orientation tensor as a function of part thickness for 40% of part length at 50 % (top) and 90 % (bottom) of part width for (■) 1 bar GF, (▲) 5 bar GF, and (○) CF 90

Figure 5-1: Locations in plaque tensile tested in the flow direction (A) and transverse to blow direction (B) the grey boxes represent the strips cut from the plaque. 102

Figure 5-2: Young's modulus of CF/ CNT/ PP composites at varying CF concentrations using (•) 0 wt% CNT, (■) 1 wt% DB CNT, and (▲) 1 wt% 10X CNT in both the flow (—) and transverse to flow (— —) directions. Error bars represent standard deviation. 103

Figure 5-3: Optical image of a 50 wt% CF PP composite showing representative voids. 106

Figure 5-4: Young's modulus (left) and tensile strength (right) dependence on CNT concentration for 30wt% CF for (■) DB and (▲) 10X CNTs in both the flow (—) and transverse to flow (— —) directions. 107

Figure 5-5: Young's modulus (left) and tensile strength (right) dependence on CNT concentration for 40wt% CF for (■) DB and (▲)10X CNTs in both the flow (-) and (- -) transverse to flow directions. 109

Figure 5-6: Young's modulus (top) and tensile strength (bottom) at varying degrees of CNT expansion for 40 wt% CF 1 wt% CNT in the flow (●) and transverse to flow (■) directions. 109

Figure 5-7: Surface (top) and volume (bottom) conductivity at varying CF concentrations with (•) 0 wt%, (■) 1 wt% DB, and (▲) 1 wt% 10X CNT. 111

Figure 5-8: Effect of CNT loading on surface conductivity for 30 wt% (top) and 40 wt% (bottom) CF with for (■) DB and (▲)10X CNTs. 114

Figure 5-9: Effect of the degree of CNT expansion on surface(top) and volume (bottom) conductivity for 40wt% CF 1wt% CNT PP composites. 116

Figure 5-10: SEM images of Frature surface for transvers to flow samples (A) 40wt% CF, (B) 40 wt% CF 1 % DB CNT, (C) 40 wt% CF 1 wt% 10X CNT, (D) 30 wt% CF 1 wt% 10X CNT 118

Figure 5-11: SEM images of fracture surface for flow direction samples A) 40wt% CF, B) 40 wt% CF 1 wt% 10X CNT, C) 30 wt% CF 1 wt% 10X CNT..... 119

Figure A-1: Experimental geometry and the selected inspection locations for the end-gated plaque. Grey squares represent the inspection locations. 133

Figure A-2: Normalized fiber length distributions for (•) 4 mm, (- -) 8 mm, and (–) 13 mm initial pellet lengths. 135

Figure A-3: A_{11} as a function of part thickness along the center-plane for 50 wt % GF at (a) 0 %, (b) 10%, (c) 40%, and (d) 90% plaque length with initial pellet lengths of ■ 4 mm, ▲8 mm, and ●13 mm..... 136

Figure A-4: A_{11} component of the orientation tensor as a function of part thickness at 40 % plaque length and 50%(bottom) and 90 % (top) width for 50 wt % GF PP with an initial pellet lengths of ▪ 4 mm, ▲8 mm, and ●13 mm 137

List of Tables

Table 4.1: Summary of fiber lengths after injection molding 84

Table 5.1: Conditions used for $scCO_2$ treatment of Nanocyl CNT 101

Table A.1: Fiber lengths in an end-gated plaque from 50 wt% GF PP with different initial pellet lengths 134

Table B.1: Tensile test results for CF concentrations for PP multiscale composites with 1 wt% CNT 142

Table B.2: Modulus results from CNT expansion at 40 wt% CF 1 wt% CNT PP 143

Table B.3: Young's modulus results from different CNT loadings at 30 and 40 wt% CF PP 143

Table B.4: Young's modulus error results from different CNT loadings at 30 and 40 wt% CF PP 143

Table B.5: Tensile strength for different CNT concentrations at 30 and 40 wt% CF PP 144

Table B.6: Tensile strength error for different CNT concentrations at 30 and 40 wt% CF PP 144

Table B.7: Elongation at break for different degrees of CNT expansion in 40wt% CF 1 wt% CNT PP 144

Table B.8: Elongation at break for different CNT loadings in 30 and 40 wt% CF PP 145

Table B.9: Elongation at break error for different CNT loadings in 30 and 40 wt% CF PP 145

Table B.10: Surface conductivity at different CF loadings for 1 wt% CNT PP composites 145

Table B.11: Volume conductivity at different CF loadings for 1 wt% CNT PP composites 146

Table B.12: Surface conductivity at different CNT concentrations in 30 wt% CF PP 146

Table B.13: Surface conductivity at different CNT concentrations in 30 wt% CF PP 146

Table B.14: Volume conductivity at different CNT concentrations in 40 wt% CF PP 146

Table B.15: Volume conductivity at different CNT concentrations in 30 wt% CF PP 147

Table B.16: Surface and volume conductivity at different CNT degrees of expansion in 40 wt% CF 1 wt% CNT PP 147

Table C.1: Sabic HV dynamic rheology 149

Table C.2: Plasticomp dynamic PP data 150

Table C.3: Plasticomp PP steady shear data 151

Table C.4: Plasticomp PP capillary data 151

Table C.5: Sabic Low viscosity dynamic rheology data 152

Table C.6: Sabic LV capillary data 153

Table D.1: End-gated plaque fiber lengths at 30 vol% long fiber 155

Table D.2: Fiber length distribution backpressure results 156

Table D.3: Fiber length distribution matrix viscosity and concentration effects 158

Table E.1: Orientation measurements 30 wt% GF low viscosity PP at 0L 0W 162

Table E.2: Orientation measurement error 30 wt% GF low viscosity PP at 0L 0W 162
Table E.3: Orientation measurement 30 wt% GF low viscosity PP at 10L 0W 163
Table E.4: Orientation measurement error 30 wt% GF low viscosity PP at 10L 0W 163
Table E.5: Orientation measurements 30 wt% GF low viscosity PP at 40L 0W 164
Table E.6: Orientation measurement error 30 wt% GF low viscosity PP at 40L 0W 164
Table E.7: Orientation measurements 30 wt % GF low viscosity PP at 90L 0W 165
Table E.8: Orientation measurement error at 30 wt % GF low viscosity PP at 90L 0W 165
Table E.9: Orientation measurements at 30 wt % GF low viscosity PP at 40L 50W 166
Table E.10: Orientation measurement error at 30 wt % GF low viscosity PP at 40L 50W 166
Table E.11: Orientation measurements at 30 wt % GF low viscosity PP at 40L 90W 167
Table E.12: Orientation measurement error at 30 wt % GF low viscosity PP at 40L 90W 167
Table E.13: Orientation measurements at 30 wt % GF high viscosity PP at 0L 0W 168
Table E.14: Orientation measurements at 30 wt % GF high viscosity PP at 10L 0W 168
Table E.15: Orientation measurements at 30 wt % GF high viscosity PP at 40L 0W 169
Table E.16: Orientation measurements at 30 wt % GF high viscosity PP at 90L 0W 169
Table E.17: Orientation measurements at 30 wt % GF high viscosity PP at 40L 50W 170
Table E.18: Orientation measurements at 30 wt % GF high viscosity PP at 40L 90W 170
Table E.19: Orientation measurements for 50 wt% GF low viscosity PP at 0L 0W 171
Table E.20: Standard deviation for orientation measurements at 50 wt% GF low viscosity PP at 0L 0W 171
Table E.21: Orientation measurements for 50 wt% GF low viscosity PP at 10L 0W 172
Table E.22: Standard deviation for orientation measurements at 50 wt% GF low viscosity PP at 10L 0W 172
Table E.23: Orientation measurements for 50 wt% GF low viscosity PP at 40L 0W 173
Table E.24: Standard deviation for orientation measurements at 50 wt% GF low viscosity PP at 40L 0W 173
Table E.25: Orientation measurements for 50 wt% GF low viscosity PP at 90L 0W 174
Table E.26: Standard deviation for orientation measurements at 50 wt% GF low viscosity PP at 90L 0W 174
Table E.27: Orientation measurements for 50 wt% GF low viscosity PP at 40L 50W 175
Table E.28: Standard deviation for orientation measurements at 50 wt% GF low viscosity PP at 40L 50W 175
Table E.29: Orientation measurements for 50 wt% GF low viscosity PP at 40L 90W 176

Table E.30: Standard deviation for orientation measurements at 50 wt% GF low viscosity PP at 40L 50W 176
Table E.31: Orientation measurements for 50 wt% GF high viscosity PP at 0L 0W 177
Table E.32: Standard deviation for orientation measurements at 50 wt% GF high viscosity PP at 0L 0W 177
Table E.33: Orientation measurements for 50 wt% GF high viscosity PP at 10L 0W 178
Table E.34: Standard deviation for orientation measurements at 50 wt% GF high viscosity PP at 10L 0W 178
Table E.35: Orientation measurements for 50 wt% GF high viscosity PP at 40L 0W 179
Table E.36: Standard deviation for orientation measurements at 50 wt% GF high viscosity PP at 40L 0W 179
Table E.37: Orientation measurements for 50 wt% GF high viscosity PP at 90L 0W 180
Table E.38: Standard deviation for orientation measurements at 50 wt% GF high viscosity PP at 90L 0W 180
Table E.39: Orientation measurements for 50 wt% GF high viscosity PP at 40L 50W 181
Table E.40: Standard deviation for orientation measurements at 50 wt% GF high viscosity PP at 40L 50W 181
Table E.41: Orientation measurements for 50 wt% GF high viscosity PP at 40L 90W 182
Table E.42: Standard deviation for orientation measurements at 50 wt% GF high viscosity PP at 40L 90W 182
Table E.43: Orientation measurements for 50 wt% GF low viscosity PP molded at 5 bar 200 rpm at 0L 0W 183
Table E.44: Orientation measurement error for 50 wt% GF low viscosity PP molded at 5 bar at 0L 0W 183
Table E.45: Orientation measurements for 50 wt% GF low viscosity PP molded at 5 bar at 10L 0W 184
Table E.46: Orientation measurement error for 50 wt% GF low viscosity PP molded at 5 bar at 10L 0W 184
Table E.47: Orientation measurements for 50 wt% GF low viscosity PP molded at 5 bar at 40L 0W 185
Table E.48: Orientation measurement error for 50 wt% GF low viscosity PP molded at 5 bar at 40L 0W 185
Table E.49: Orientation measurements for 50 wt% GF low viscosity PP molded at 5 bar at 90L 0W 186
Table E.50: Orientation measurement error for 50 wt% GF low viscosity PP molded at 5 bar at 90L 0W 186
Table E.51: Orientation measurements for 50 wt% GF low viscosity PP molded at 5 bar at 40L 50W ... 187
Table E.52: Orientation measurement error for 50 wt% GF low viscosity PP molded at 5 bar at 40L 50W 187

Table E.53: Orientation measurements for 50 wt% GF low viscosity PP molded at 5 bar at 40L 90W ... 188

Table E.54: Orientation measurement error for 50 wt% GF low viscosity PP molded at 5 bar at 40L 90W ... 188

Table E.55: Orientation measurements for 50 wt% GF low viscosity PP molded at 10 bar at 0L 0W ... 189

Table E.56: Orientation measurement error for 50 wt% GF low viscosity PP molded at 10 bar at 0L 0W ... 189

Table E.57: Orientation measurements for 50 wt% GF low viscosity PP molded at 10 bar at 10L 0W ... 190

Table E.58: Orientation measurement error for 50 wt% GF low viscosity PP molded at 10 bar at 10L 0W ... 190

Table E.59: Orientation measurements for 50 wt% GF low viscosity PP molded at 10 bar at 40L 0W ... 191

Table E.60: Orientation measurement error for 50 wt% GF low viscosity PP molded at 10 bar at 40L 0W ... 191

Table E.61: Orientation measurements for 50 wt% GF low viscosity PP molded at 10 bar at 90L 0W ... 192

Table E.62: Orientation measurement error for 50 wt% GF low viscosity PP molded at 10 bar at 90L 0W ... 192

Table E.63: Orientation measurements for 30 wt% CF PP at 0L 0W ... 193

Table E.64: Standard deviation for orientation measurements for 30 wt% CF PP at 0L 0W ... 193

Table E.65: Orientation measurements for 30 wt% CF PP at 10L 0W ... 194

Table E.66: Standard deviation for orientation measurements for 30 wt% CF PP at 10L 0W ... 194

Table E.67: Orientation measurements for 30 wt% CF PP at 40L 0W ... 195

Table E.68: Standard deviation for orientation measurements for 30 wt% CF PP at 40L 0W ... 195

Table E.69: Orientation measurements for 30 wt% CF PP at 90L 0W ... 196

Table E.70: Standard deviation for orientation measurements for 30 wt% CF PP at 90L 0W ... 196

Table E.71: Orientation measurements for 30 wt% CF PP at 40L 50W ... 197

Table E.72: Standard deviation for orientation measurements for 30 wt% CF PP at 40L 50W ... 197

Table E.73: Orientation measurements for 30 wt% CF PP at 40L 90W ... 198

Table E.74: Standard deviation for orientation measurements for 30 wt% CF PP at 40L 90W ... 198

1 Chapter 1: Introduction

1.1 Fiber Reinforced Polymers

Fiber reinforced polymer composites (FRP) exhibit increased impact toughness, strength, stiffness, strength to weigh ratio, and dimensional stability compared with pure polymers [1]. This has led to FRP's extensive use in the automotive and aerospace industries as light weight alternatives to metallic parts. However, traditional continuous fiber materials are expensive and time consuming to produce [2]. In recent years, long discontinuous FRP have been investigated due to the fact they possess most of the properties of continuous fiber composites, with the added benefit of being melt processable. As a result, commercial processing techniques can be utilized, most commonly injection molding [2]. The mechanical properties of discontinuous FRP are dependent not only on the matrix and fiber choice, but also on fiber length and orientation due to the reinforcing effect of the fibers [3, 4]. Therefore, a thorough understanding of the evolution of fiber orientation and length in injection molding is needed.

1.2 Orientation Model Basics

Fiber aspect ratio and concentration, matrix rheology, melt temperature, injection speed, and mold design all affect the evolution of fiber orientation in an injection molded part [5, 6]. By understanding how these parameters influence orientation, mold design and processing parameters can be tuned to optimize the mechanical properties of the part. Thus, it is desirable to be able to model the development of fiber orientation in flow.

Most fiber orientation models stem from the work of Jeffery [7] on the dynamics of high aspect ratio particles in dilute suspensions. More recent orientation models extended Jeffery's theory to non-dilute suspension by accounting for particle interactions through isotropic rotary diffusion, slowed orientation kinetics, and anisotropic diffusion [8-10]. The resulting models have proven to better match experimental orientation in multiple systems [10-12].

Strautins and Latz [13] developed the bead-rod model, which accounts for semi-flexible fibers in dilute solutions by modeling fibers as three beads connected by two rods. Ortman et al. [14] extended the model to non-dilute systems by adding an isotropic rotary diffusion term and a slip parameter. These account for slowed orientation kinetics and fiber bending due to fiber-fiber interactions. While a few studies have been performed using the bead-rod model [14-16], a better understanding of how processing conditions and system choices (e.g. concentration, fiber length, fiber concentration, and matrix type) affect long fiber orientation is needed to be able to assess if the current models can capture these changes [17].

1.3 Factors Influencing Orientation

Simple injection molded parts made with short glass fiber (GF) composites exhibit a shell-core-shell orientation. Near the walls of the mold, shear flow dominates and fibers align in the direction of the flow [13-17]. In the center of the mold, extensional flow dominates and fibers align transverse to the flow [13-17]. Injection speed, temperature, and fiber concentration are the most widely studied parameters that influence short fiber orientation in injection molded composites. Injection speed and temperature have similar effects on the orientation profile of the composites [13, 14, 18-21]. At high injection speeds and temperatures, fibers align more perpendicular to the flow. At low injection speeds and temperatures, a thicker shell region is formed and there is a higher degree of alignment in the direction of flow. An increase in fiber concentration leads to a decrease in flow alignment for short fibers [18, 19]. An increase in injection speed or fiber content also leads to an increase in fiber breakage in the mold, decreasing the average fiber length in the composite [21]. A few studies have looked at the influence of polymer choice on short fiber orientation but none have linked these results well with the rheology of the polymers [20, 21].

While short GF composites have been thoroughly examined, few studies have been performed that examine the experimental fiber orientation in long GF composites [22-25]. In general, long fiber composites have been shown to possess a shell-core-shell structure with a broader core region and less alignment in the shell than their short fiber counterparts [16, 22, 23]. The studies on long fiber orientation have not examined how injection molding conditions and system properties affect orientation. A fundamental understanding is necessary for mold design and the evaluation of existing orientation models.

1.4 Carbon Fiber

Carbon fiber (CF) offers decreased weight and increased mechanical properties compared to glass fiber (GF) composites [26]. As CF's price has decreased, its use in discontinuous fiber composites has increased, but limited studies have been performed examining how the orientation of CF in the injection molding process differs from GF. CF breaks more during processing than GF yielding shorter fiber lengths in the final part under equivalent conditions [27]. One of the causes of increased fiber breakage is the reduced diameter of the standard commercial CF used compared to the standard GF, 7 μm versus 14 μm. Therefore, the aspect ratio of the fibers needs to be used as the point of comparison for fiber lengths between the two fiber types. An understanding of the differences in fiber orientation between GF and CF injection molded composites and the causes of these differences is needed, to be able to successfully predict the CF parts properties and optimize their injection molding conditions.

1.5 Multiscale Composites

In continuous fiber composites, the unidirectional reinforcement of fibers causes poor compression performance and delamination resistance, which has led to interest in multiscale composites [28]. Multiscale or hybrid composites typically contain GF or CF with carbon nanotubes (CNTs) [28-32]. The small size of the CNTs allows them to penetrate the inter-fiber spacing, enhancing properties in the matrix-dominated directions, without the decreased inplane mechanical properties observed in woven

composite structures [28]. Multiscale composite research has been focused on thermosets [29, 30] created using resin transfer molding (RTM) [31-33]. In studies that have been performed on thermoplastic multiscale composites the composites were created using the compression molding of fiber mats and polymer/CNT master batches [34-36]. In all cases, obtaining a good dispersion of CNTs within the composite has been key to obtaining improved properties.

CNTs also have the potential to improve the properties of injection molded fiber composites, but creating well-dispersed CNTs using melt compounding typically requires large mixing energies [37, 38]. At high mixing energies, CNT lengths can become severely reduced decreasing the composite's properties [38-40]. In multiscale composites, large mixing energies would also cause a significant decrease in the average fiber length further decreasing their performance [41-47].

Previous work in our lab has shown that super critical carbon dioxide can be used to deagglomerate CNTs before melt compounding them into a polymer with a single screw extruder [48-50]. This process improved the dispersion of CNTs in the polymer without the severe breakage of CNTs typical of using a twin screw extruder [38, 49, 51]. Using super critical carbon dioxide treated CNTs mixed with fiber composites in the injection molder may allow improved CNT dispersion, without the decreased fiber and CNT lengths from melt compounding the composite before injection molding.

1.6 Objectives

The primary goal of this research is to investigate how system properties (e.g. matrix choice, concentration, and fiber length) affect fiber orientation and if adding additional filler types to the composite can further improve properties. The specific goals are:

1. Examine if number average fiber length and aspect ratio are adequate ways of representing semi-flexible fiber length distributions by comparing long glass and long carbon fiber orientation in an injection molded end-gated plaque.

2. Assess the effect matrix viscosity has on fiber orientation in long fiber composites and how dependent is that effect on fiber concentration by inspecting the orientation of two different grades of polypropylene long glass fiber composites in an end-gated plaque.

3. Test if properties of injection molded long fiber composites can be improved through the addition of super critical carbon dioxide deagglomerated carbon nanotubes.

1.7 References

1. Truckenmüller, F. and H.G. Fritz, *Injection molding of long fiber-reinforced thermoplastics: A comparison of extruded and pultruded materials with direct addition of roving strands.* Polymer Engineering & Science, 1991. **31**(18): p. 1316-1329.
2. Mallick, P.K., *Composites engineering handbook*. 1997, New York: M. Dekker.
3. Chin, W.-K., H.-T. Liu, and Y.-D. Lee, *Effects of fiber length and orientation distribution on the elastic modulus of short fiber reinforced thermoplastics.* Polymer Composites, 1988. **9**(1): p. 27-35.
4. Avérous, L., et al., *Granulometric Characterization of Short Fiberglass in Reinforced Polypropylene. Relation to Processing Conditions and Mechanical Properties.* International Journal of Polymer Analysis and Characterization, 1995. **1**(4): p. 339-347.
5. Yang, K. and R. Ozisik, *Effects of processing parameters on the preparation of nylon 6 nanocomposites.* Polymer, 2006. **47**(8): p. 2849-2855.
6. SadAbadi, H. and M. Ghasemi, *Effects of Some Injection Molding Process Parameters on Fiber Orientation Tensor of Short Glass Fiber Polystyrene Composites (SGF/PS).* Journal of Reinforced Plastics and Composites, 2007.
7. Jeffery, G.B., *The Motion of Ellipsoidal Particles Immersed in a Viscous Fluid.* Proceedings of the Royal Society of London. Series A, 1922. **102**(715): p. 161-179.
8. Folgar, F. and C.L. Tucker, *Orientation Behavior of Fibers in Concentrated Suspensions.* Journal of Reinforced Plastics and Composites, 1984. **3**(2): p. 98-119.
9. Sepehr, M., G. Ausias, and P.J. Carreau, *Rheological properties of short fiber filled polypropylene in transient shear flow.* Journal of Non-Newtonian Fluid Mechanics, 2004. **123**(1): p. 19-32.
10. Phelps, J.H. and C.L. Tucker Iii, *An anisotropic rotary diffusion model for fiber orientation in short- and long-fiber thermoplastics.* Journal of Non-Newtonian Fluid Mechanics, 2009. **156**(3): p. 165-176.
11. Vélez-García, G.M., et al., *Simulation of Injection Molding Using a Model with Delayed Fiber Orientation.* International Polymer Processing, 2011. **26**(3): p. 331-339.
12. Chung, D.H. and T.H. Kwon, *Fiber orientation in the processing of polymer composites.* Korea-Australia Rheology Journal, 2002. **14**(4): p. 175-188.
13. Strautins, U. and A. Latz, *Flow-driven orientation dynamics of semiflexible fiber systems.* Rheologica Acta, 2007. **46**(8): p. 1057-1064.
14. Ortman, K., et al., *Using startup of steady shear flow in a sliding plate rheometer to determine material parameters for the purpose of predicting long fiber orientation.* Journal of Rheology (1978-present), 2012. **56**(4): p. 955-981.
15. Meyer, K.J., *Improved Prediction of Glass Fiber Orientation in Basic Injection Molding Geometries*, in *Chemical Engineering*. 2013, Virginia Polytechnic Institute and State University.
16. Hofmann, J.T., *Extension of the Method of Ellipses to Determining the Orientation of Long, Semi-flexible Fibers in Model 2- and 3- dimensional Geometries*, in *Macromolecular Science and Engineering*. 2013, Virginia Polytechnic Institute and State University.
17. Meyer, K.J., J.T. Hofmann, and D.G. Baird, *Prediction of Short Glass Fiber Orientation in the Filling of an End-Gated Plaque.* Composites Part A: Applied Science and Manufacturing, 2014.
18. Murty, K.N. and G.F. Modlen, *Experimental characterization of the alignment of short fibers during flow.* Polymer Engineering & Science, 1977. **17**(12): p. 848-853.
19. Kim, E., J. Park, and S. Jo, *A study on fiber orientation during the injection molding of fiber-reinforced polymeric composites:(Comparison between image processing results and numerical simulation).* Journal of Materials Processing Technology, 2001. **111**(1): p. 225-232.

20. Sousa, R.A., et al., *Integrated compounding and injection moulding of short fibre reinforced composites.* Plastics, Rubber & Composites, 2004. **33**(6): p. 249-259.
21. Bay, R.S. and C.L. Tucker, *Fiber orientation in simple injection moldings. Part II: Experimental results.* Polymer Composites, 1992. **13**(4): p. 332-341.
22. Nguyen, B.N., et al., *Fiber Length and Orientation in Long-Fiber Injection-Molded Thermoplastics — Part I: Modeling of Microstructure and Elastic Properties.* Journal of Composite Materials, 2008. **42**(10): p. 1003-1029.
23. Lafranche, E., et al., *Injection moulding of long glass fibre reinforced polyamide 6-6: guidelines to improve flexural properties.* Express Polym Lett, 2007. **1**(7): p. 456-466.
24. Hofmann, J.T., et al., *Application and evaluation of the method of ellipses for measuring the orientation of long, semi-flexible fibers.* Polymer Composites, 2013. **34**(3): p. 390-398.
25. Cieslinski, M.J., P. Wapperom, and D.G. Baird, *Influence of fiber concentration on the startup of shear flow behavior of long fiber suspensions.* Journal of Non-Newtonian Fluid Mechanics, 2015. **222**(0): p. 163-170.
26. Park, S.-J. and SpringerLink, *Carbon Fibers*. Vol. 210. 2015, Dordrecht: Springer Netherlands.
27. Fu, S.Y., et al., *Tensile properties of short-glass-fiber- and short-carbon-fiber-reinforced polypropylene composites.* Composites Part A: Applied Science and Manufacturing, 2000. **31**(10): p. 1117-1125.
28. Díez-Pascual, A.M., et al., *Multiscale fiber-reinforced thermoplastic composites incorporating carbon nanotubes: A review.* Current Opinion in Solid State and Materials Science, 2014. **18**(2): p. 62-80.
29. Thostenson, E.T., et al., *Carbon nanotube/carbon fiber hybrid multiscale composites.* Journal of Applied Physics, 2002. **91**(9): p. 6034.
30. Bekyarova, E., et al., *Multiscale Carbon Nanotube−Carbon Fiber Reinforcement for Advanced Epoxy Composites.* Langmuir, 2007. **23**(7): p. 3970-3974.
31. Jingjing, Q., et al., *Carbon nanotube integrated multifunctional multiscale composites.* Nanotechnology, 2007. **18**(27): p. 275708.
32. Kim, M., *Modeling, manufacturing, and characterization of nanocomposites and multiscale composites.* 2009.
33. Fan, Z., K.-T. Hsiao, and S.G. Advani, *Experimental investigation of dispersion during flow of multi-walled carbon nanotube/polymer suspension in fibrous porous media.* Carbon, 2004. **42**(4): p. 871-876.
34. Ashrafi, B., et al., *Processing and properties of PEEK/glass fiber laminates: Effect of addition of single-walled carbon nanotubes.* Composites Part A: Applied Science and Manufacturing, 2012. **43**(8): p. 1267-1279.
35. Díez-Pascual, A.M., et al., *High performance PEEK/carbon nanotube composites compatibilized with polysulfones-I. Structure and thermal properties.* Carbon, 2010. **48**(12): p. 3485-3499.
36. Shen, Z., et al., *The effects of carbon nanotubes on mechanical and thermal properties of woven glass fibre reinforced polyamide-6 nanocomposites.* Composites Science and Technology, 2009. **69**(2): p. 239-244.
37. Müller, M.T., et al., *Influence of feeding conditions in twin-screw extrusion of PP/MWCNT composites on electrical and mechanical properties.* Composites Science and Technology, 2011. **71**(13): p. 1535-1542.
38. Pötschke, P., T. Villmow, and B. Krause, *Melt mixed PCL/MWCNT composites prepared at different rotation speeds: Characterization of rheological, thermal, and electrical properties, molecular weight, MWCNT macrodispersion, and MWCNT length distribution.* Polymer, 2013. **54**(12): p. 3071-3078.

39. Guo, J., et al., *Aspect ratio effects of multi-walled carbon nanotubes on electrical, mechanical, and thermal properties of polycarbonate/MWCNT composites.* Journal of Polymer Science Part B: Polymer Physics, 2014. **52**(1): p. 73-83.
40. Socher, R., et al., *The influence of matrix viscosity on MWCNT dispersion and electrical properties in different thermoplastic nanocomposites.* Polymer, 2012. **53**(2): p. 495-504.
41. Phelps, J.H., et al., *A model for fiber length attrition in injection-molded long-fiber composites.* Composites Part A: Applied Science and Manufacturing, 2013. **51**(0): p. 11-21.
42. Thomason, J., *The influence of fibre length and concentration on the properties of glass fibre reinforced polypropylene: 5. Injection moulded long and short fibre PP.* Composites Part A: Applied Science and Manufacturing, 2002. **33**(12): p. 1641-1652.
43. Thomason, J.L., *The influence of fibre length, diameter and concentration on the modulus of glass fibre reinforced polyamide 6,6.* Composites Part A: Applied Science and Manufacturing, 2008. **39**(11): p. 1732-1738.
44. Thomason, J.L. and W.M. Groenewoud, *The influence of fibre length and concentration on the properties of glass fibre reinforced polypropylene: 2. Thermal properties.* Composites Part A: Applied Science and Manufacturing, 1996. **27**(7): p. 555-565.
45. Thomason, J.L. and M.A. Vlug, *Influence of fibre length and concentration on the properties of glass fibre-reinforced polypropylene: 1. Tensile and flexural modulus.* Composites Part A: Applied Science and Manufacturing, 1996. **27**(6): p. 477-484.
46. Thomason, J.L. and M.A. Vlug, *Influence of fibre length and concentration on the properties of glass fibre-reinforced polypropylene: 4. Impact properties.* Composites Part A: Applied Science and Manufacturing, 1997. **28**(3): p. 277-288.
47. Thomason, J.L., et al., *Influence of fibre length and concentration on the properties of glass fibre-reinforced polypropylene: Part 3. Strength and strain at failure.* Composites Part A: Applied Science and Manufacturing, 1996. **27**(11): p. 1075-1084.
48. Quigley, J., et al., *Benign reduction of carbon nanotube agglomerates using a supercritical carbon dioxide process.* Applied Physics A, 2014. **117**(3): p. 1003-1017.
49. Quigley, J.P., K. Herrington, and D.G. Baird, *Enhanced electrical properties of polycarbonate/carbon nanotube nanocomposites prepared by a supercritical carbon dioxide aided melt blending method.* Polymer, 2014. **55**(23): p. 6167-6175.
50. Chen, C., et al., *Using supercritical carbon dioxide in preparing carbon nanotube nanocomposite: Improved dispersion and mechanical properties.* Polymer Composites, 2012. **33**(6): p. 1033-1043.
51. Lee, H.S., et al., *Persistence Length of Multiwalled Carbon Nanotubes with Static Bending.* The Journal of Physical Chemistry C, 2007. **111**(51): p. 18882-18887.

2 Literature Review

This section provides the reader with the necessary background to understand the concepts presented throughout this proposal. First, the classification of fiber reinforced polymer composites based on production methods, concentration, and length is presented in § 2.1. The basics of reporting fiber orientation are covered in § 2.2. Different methods for experimentally determining the fiber orientation are presented in section § 2.3 and the basics of modeling fiber orientation for rigid and semi-flexible fibers are covered in § 2.4. Finally, a review of orientation studies is covered in §2.5.

2.1 Classification of Fiber Composites

Fiber reinforced polymer composites (FRP) exhibit an increase in impact toughness, strength, stiffness, and dimensional stability compared to their unfilled counterparts [1]. These properties depend on the polymer matrix and fiber used as well as the length, concentration, and orientation of the fibers [2].

In the broadest terms, FRP can be separated into continuous and discontinuous fiber composites. Continuous fiber composites have fibers that cover the entire dimension of a part without break or interruption [2]. They are most commonly used in mats or plies, where the orientation can be controlled. The major disadvantages of continuous fiber composites are their price and difficulty of production. The layers of the composite need to be manually assembled and combined, often through vacuum assisted resin transfer molding or compression molding [2]. This makes them labor intensive and expensive to produce.

Discontinuous fiber composites, where the fibers are smaller than the part size, offer many of the benefits of continuous composites, with the advantage of being melt processable. This means they can be manufactured using common commercial processes such as injection, compression, or resin transfer molding decreasing production cost and time [2].

The proposed work focuses on the fiber orientation produced from injection molding carbon fiber and glass fiber discontinuous fiber composites. As such, the following sections describe the classifications used for discontinuous fiber composites. The different production methods used to produced FRP are covered in § 2.1.1. The classification of concentration in fiber–filled systems is addressed in § 2.1.2 and the use of fiber length (FL) to classify FRP is discussed in § 2.1.3.

2.1.1 Production Methods

Commercially available discontinuous fiber composites are produced through two main processes, compounding and pultrusion, with pultrusion being the more common method [3-5]. The individual fibers are about 10-14 mm in diameter for glass fiber and around 7 mm for carbon fiber. It is worth noting that before production, the fibers are chemically treated to promote interaction between the polymer matrix and fiber. While sizing on a fiber accounts for a very small part of the composite, it can increase the strength of the composite by 50% [6]. In pultrusion, a continuous bundle of fiber strands is passed through a polymer resin bath and then a die. This process forms a polymer coated strand of fibers that is dried and cut to the desired length in a pelletizer. Typical lengths range from less than 1 mm for short fiber (SF) composites to around 13 mm for long fiber (LF) composites.

The compounding of fibers and polymer can be performed in an extruder, kneader, or kinetic mixer [5]. However, compounding normally yields decreased stiffness and fracture toughness compared to the pultrusion process, because of fiber breakage in the mixing process [5]. In order to overcome this, the integration of compounding and the injection molding of the final part has been tested [3, 7]. In this method, fibers are fed into the second stage of an extruder with an integrated injection molder. This creates increased FL compared to the pultrusion process, combined with injection molding separately [3]. However, integrated compounding and injection molding generates poorer dispersion of fibers and requires specialized equipment that has not been widely adopted [7].

Compression and injection molding are the most common methods used to form composite parts. The studies involving the compression molding of discontinuous FRP have been limited [8-11]. Most studies have focused on injection molding due to the ease of part production, low cost, and high production speed achievable [12-16]. During the injection molding process, fibers are broken leading to a fiber length distribution (FLD) in the final part [3, 4, 17-19]. The majority of fiber breakage occurs in the screw of the injection molder [17]. However, if length is maintained in the screw, significant breakage can be seen in the , gate, and mold of a part [20]. A low-shear screw, low compression ratio, slow injection speed, and small backpressure help maintain fiber length and yield improved mechanical properties in the final part [18]. The decrease in mechanical properties, due to fiber breakage in an injection molder, is in many cases balanced out by the increase in fiber dispersion and flow alignment, when compared to compression molding [5].

2.1.2 Concentration Regimes

Doi and Edwards [21] defined three concentration regimes for FRP; dilute, semi-dilute, and concentrated based on the interactions a fiber has with its neighbors. This interaction is controlled by the volume fraction of fibers defined by equation (2-1.

$$\Phi_v = \frac{\pi n L^3}{4 a_r^2} \tag{2-1}$$

Where n is the number of fibers per unit volume, with each fiber having a length L. The aspect ratio a_r is defined by equation 2-2, where d is the diameter of the fibers.

$$a_r = \frac{L}{d} \tag{2-2}$$

Figure 2-1, estimated from Dinh and Armstrong theory for aligned fibers, shows how the concentration regimes change with the aspect ratio and volume fraction of fibers [22].

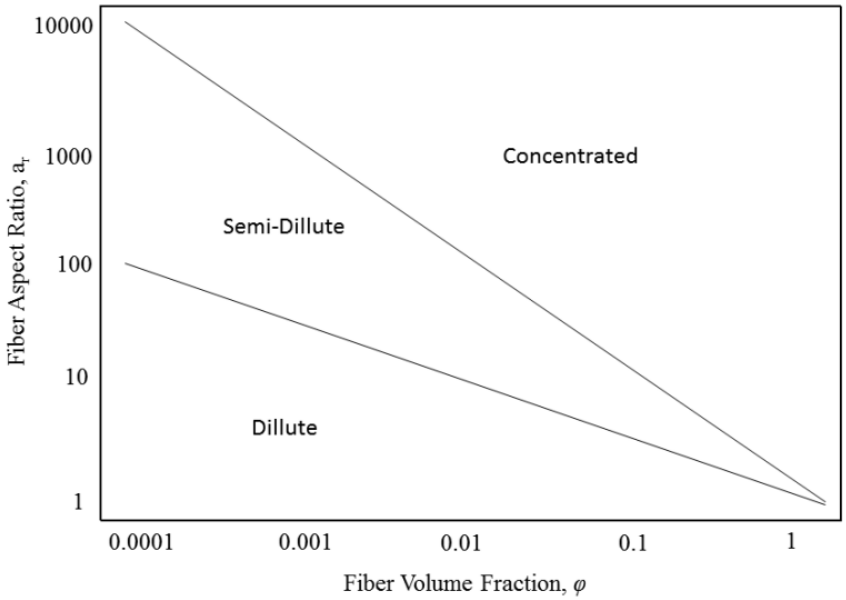

Figure 2-1: Concentration regimes as a function of fiber aspect fraction and volume fraction adapted from [23]

In a dilute suspension, a fiber does not interact with any of the other fibers in the solution [21]. This only occurs when you can rotate the fiber in a full sphere and not encounter any other particles, meaning that average particle distance must be greater than the average length of the fibers in the suspension. Therefore, n needs to be less than $1/L^3$, applying this to equation (2-1 gives the limiting conditions for a dilute suspension, equation 2-3.

$$\Phi_v < \frac{1}{a_r^2} \tag{2-3}$$

In a semi-dilute suspensions there are hydrodynamic interactions but little fiber-fiber interactions [21]. This occurs when n is greater than $1/L^3$ and the distance between fibers is greater than the fiber diameter. This creates both an upper and lower limit on the semi-dilute region. The upper limit is dependent on the fibers' degree of alignment. For systems with a random orientation, the volume fraction range for a semi-dilute suspension is given in equation 2-4. In the case of a perfectly aligned sample the upper limit is $\pi/4$.

$$\frac{1}{a_r^2} << \Phi_v << \frac{1}{a_r} \tag{2-4}$$

Concentrated systems are defined as any system above the semi-dilute region. Fiber-fiber interactions and hydrodynamic interactions are both present in this region. At very high volume fractions fibers can form nematic phases, or clusters of locally preferentially aligned fibers, similar to liquid crystalline polymers [21]. The concentrated regime is understood less than dilute and semi-dilute regimes, due to the complexities induced by fiber interactions.

2.1.3 Fiber Length

Discontinuous fiber composites can be separated into long and short composites based on their flexibility. SF, < 1mm for glass, behave like rigid rods during processing. LF are able to bend during processing [19]. An aspect ratio of around 100 can be used as a rough metric for the division between LF and SF, with higher aspect ratio fibers being long [24-26]. The fiber effective stiffness, S_{eff}, introduced by Switzer and Klingenberg [27] and defined by equation 2-5 gives a way to quantify the flexibility of a fiber.

$$S_{eff} = \frac{E_y \pi}{64 \eta \dot{\gamma} a_r^4} \tag{2-5}$$

E_y is the Young's modulus of the fiber, η is the viscosity of the matrix, and $\dot{\gamma}$ is the deformation rate. As S_{eff} approaches zero, the fiber becomes completely flexible, and as S_{eff} approaches infinity, the fiber becomes completely rigid. Because aspect ratio is raised to the fourth power, a small change in aspect ratio has a large effect on the flexibility and, therefore, the properties of the end part.

Due to breakage in the production process, fiber suspensions do not have a homogenous length but rather a FLD. Typical injection molded parts have a high concentration of SF with a long tail of LF. FLD is represented mathematically as a Weibull or log normal distribution [17, 28-30]. The Weibull distribution

is given by equation 2-6, where $f(l)$ is the probability density that a fiber is between l and $l + dl$. The shape parameters, b and c, are fit to the data.

$$f(l) = \frac{c}{b}\left(\frac{l}{b}\right)^{c-1} e^{-\left(\frac{l}{b}\right)^{c}} \tag{2-6}$$

FLD are typically measured by placing the sample of interest in a high temperature oven, at temperatures greater than 450 °C, for a few hours. The polymer burns off from the sample, leaving behind the fibers [31]. A small section of the fibers left after burn off are injected with epoxy [32]. This epoxy plug is then burnt off a second time, to give fewer fibers but an unbiased representation of the FLD. Fibers are then dispersed and imaged with either an optical microscope or flatbed scanner. The fibers in the resulting image are traced to determine the FLD [32]. Generally, about 1000 fibers are measured per sample, to ensure an accurate FLD [31, 32]. With this method, it is impossible to measure the orientation and FLD of the exact same fibers. Only micro-CT allows for this and that method has its own drawbacks which are covered in depth in §2.3.6. After a FLD has been experimentally measured, the first and second moments of the FLD, number average (L_n) and weight average (L_w) respectively, are calculated using equation 2-7 and 2-8.

$$L_n = \frac{\sum n_i L_i}{\sum n_i} \tag{2-7}$$

$$L_w = \frac{\sum n_i L_i^2}{\sum n_i L_i} \tag{2-8}$$

2.2 Representing Orientation

It is impractical to report the location and orientation of each fiber in a FRP. Therefore, fiber orientation in a FRP is reported as a fiber orientation distribution (FOD). FOD are typically represented as a distribution function (§ 2.2.1) or as orientation tensors (§2.2.2).

2.2.1 *Distribution Function*

Fiber orientation in a FRP was originally expressed as an orientation distribution, equation 2-9 [33].

$$P(\theta_1 \leq \theta \leq \theta_1 + d\theta, \phi_1 \leq \phi \leq \phi_1 + d\phi) = \psi(\theta_1, \phi_1) sin(\theta_1) d\theta d\phi \quad (2\text{-}9)$$

This represents the probability (P), that a fiber will be found between the angles (θ_1, ϕ_1) and the angles $(\theta_1 + d\theta, \phi_1 + d\phi)$. While this is the most general description of orientation, it is very cumbersome for systems with a large number of fibers [34, 35]. Orientation tensors are a much more efficient way of representing the FOD and allow for a large decrease in processing time for modeling applications [33]. Therefore, orientation tensors will be used for all of the following work.

2.2.2 *Orientation Tensor*

A rigid fiber's orientation can be represented as a vector $(\bar{p})$ that runs through the center of the fiber, Figure 2-2. The vector $\bar{p}$ can be constructed through equations 2-10-2-13.

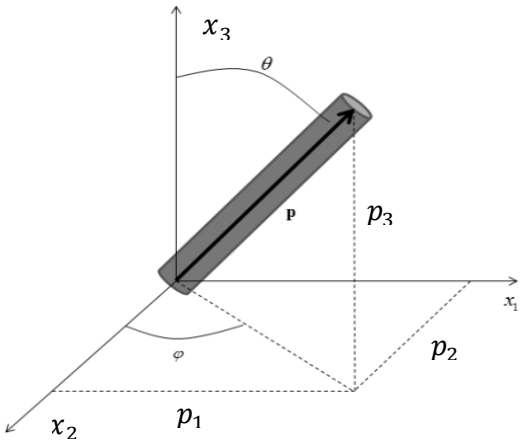

Figure 2-2: Vector p representing a rigid fiber and its characteristic angles

$$\bar{p} = p_1\bar{\delta}_1 + p_2\bar{\delta}_2 + p_3\bar{\delta}_3 \tag{2-10}$$

$$p_1 = sin\theta cos\phi \tag{2-11}$$

$$p_2 = sin\theta sin\phi \tag{2-12}$$

$$p_3 = cos\theta \tag{2-13}$$

By representing fibers as vectors, orientation tensors can be developed that are defined as the second and fourth moment of the orientation distribution function, given in equations 2-14 and 2-15. This was first explored by Hinch and Leal [36] for liquid crystalline polymers and then expanded to FRP by Advani and Tucker [33].

$$\bar{\bar{A}} = \oint \overline{pp}\,\psi(\bar{p},t)dp \tag{2-14}$$

$$\bar{\bar{A}}_4 = \oint \overline{pppp}\,\psi(\bar{p},t)dp \tag{2-15}$$

There are some limitations to representing the FOD as tensors. First, there is a closure problem where the fourth order tensor cannot be directly calculated and needs to be approximated using the second order tensor, in order to obtain a closed set of equations [37]. Second, fiber concentration is assumed spatially uniform, which is not true for many real parts especially those at higher concentrations [38] and LF [39]. Finally in order for this representation to work the fiber needs to be rigid which works for SF but is problematic for LF [33].

For LF composites, orientation tensors have been developed around modeling a semi-flexible fiber using a pair of orientation vectors, $\bar{p}$ and $\bar{q}$, called the "bead-rod" model. Strautins and Latz [40] developed one of the first models to use this method. It is developed from polymer theory where the fiber

is represented as three beads connected by two rigid rods, Figure 2-3, the angle between the rods can change providing flexibility [41, 42].

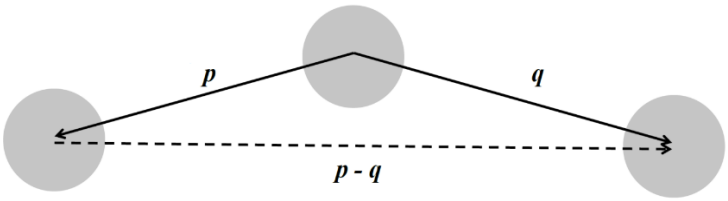

Figure 2-3: Representation of a fiber using the bead-rod model

In order to utilize this model, the following assumptions need to be made. First, the fiber is only semi-flexible with a limited extent of curvature. Bending only occurs at the center, meaning $\bar{p} = -\bar{q}$. The first and second moments of the orientation vectors $\bar{p}$ and $\bar{q}$ are assumed to be equal. Three tensors arise from analysis of the semi-flexible system, equations 2-16-2-18 [40].

$$\bar{\bar{A}} = \iint \bar{p}\,\bar{q}\,\psi(\bar{p},\bar{q},t)d\bar{p}d\bar{q} \tag{2-16}$$

$$\bar{\bar{B}} = \iint \bar{p}\,\bar{q}\,\psi(\bar{p},\bar{q},t)d\bar{p}d\bar{q} \tag{2-17}$$

$$\bar{C} = \iint \bar{p}\,\psi(\bar{p},\bar{q},t)d\bar{p}d\bar{q} \tag{2-18}$$

The second moment of the orientation distribution function of $\bar{p}$ is $\bar{\bar{A}}$ (eq. 2-16) and is similar to rigid rod model tensor in equation 2-14. $\bar{\bar{B}}$ (eq. 2-17) is the mixed second moment of the orientation distribution function. The first moment of the orientation distribution function is $\bar{C}$ (eq. 2-18). When the fiber is straight $\bar{\bar{B}}$ and $\bar{C}$ reduce to zero and the rigid rod case is recovered.

Ortman et al. [43] proposed using an end-to-end vector to describe a semi flexible fibers. This is equivalent to connecting the ends of a semi-flexible fiber with a vector, shown as $(\bar{p} - \bar{q})$ in Figure 2-3. It

is possible to form an orientation tensor $\bar{\bar{r}}$ from the end-to-end vector that can be related back to $\bar{\bar{\mathrm{A}}}$ and $\bar{\bar{B}}$ given in equation 2-19. A normalized dimensionless form of $\bar{\bar{\mathrm{r}}}$, $\bar{\bar{\mathrm{R}}}$, was also developed and is given in equation 2-20. As before, when the fiber is straight $\bar{\bar{\mathrm{R}}}$ reduces to $\bar{\bar{A}}$ and the rigid rod case is recovered.

$$\bar{\bar{r}} = \iint l_b^2(\bar{p}-\bar{q})\,(\bar{p}-\bar{q})\psi(\bar{p},\bar{q},t)d\bar{p}d\bar{q} = 2l_b^2(\bar{\bar{A}}-\bar{\bar{B}}) \tag{2-19}$$

$$\bar{\bar{R}} = \frac{\bar{\bar{r}}}{tr(\bar{\bar{r}})} = \frac{\bar{\bar{A}}-\bar{\bar{B}}}{1-tr(\bar{\bar{B}})} \tag{2-20}$$

2.3 Experimental Determination of Fiber Orientation

An accurate experimental FOD is extremely important for FRP. The ultimate goal is to be able to model fiber orientation and breakage in the injection molding of complex parts. This allows mold design and processing conditions to be optimized, without having through go through physically making several molds. Fiber orientation often varies with the length, width, and thickness of a part therefore, accurate determination of orientation can be difficult. As a result, several different methods for determining fiber orientation have been developed. The different techniques commonly used will be assessed in this section.

The most common method of determining FOD, the method of ellipses (MOE), is covered in §2.3.1. The next several sections discuss experimental ways to image FRP to obtain FOD. Optical microscopy is by far the most common method and is covered in depth in §2.3.2. Other common methods are covered in the following sections including: scanning electron microscopy (§2.3.3), confocal microscopy (§2.3.4), scanning acoustical microscopy (§2.3.5), and microcomputer tomography (§2.3.6). Finally, some less common techniques are covered in §2.3.7.

2.3.1 *Method of Ellipses*

The most commonly used method for determining fiber orientation is the MOE [26, 44-49]. This method allows 3-D reconstruction of the fibers to be made from 2-D images. The projections allow a quasi-3-D measurement of fiber orientation and quantification of the orientation tensor, $\bar{\bar{A}}$ (eq.2-14) [26]. In order to use this method, it must be assumed that the fibers are perfectly rigid and circular. While these assumptions are reasonable for SF, the rigidity requirement means that as fibers become longer the accuracy of this method become questionable. In most cases, a time-consuming sample preparation process and/or specialized equipment is required in order to obtain high quality images.

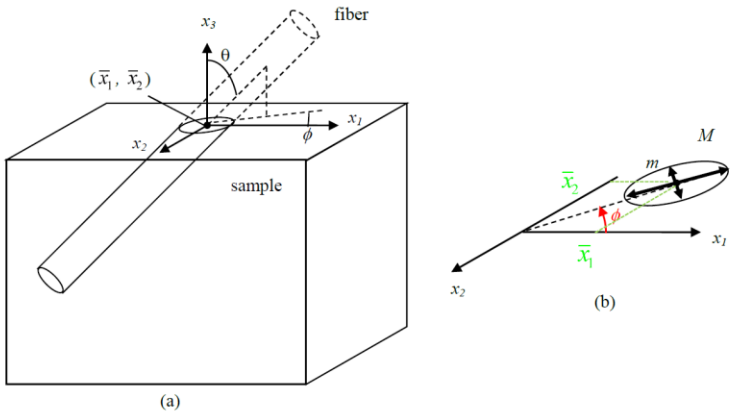

Figure 2-4: Illustration of the parameters required for the MOE:(a) View of a fiber in sample (b) 2-D view, adapted from [50]

When you cut a rigid rod at an angle the resulting rod appears as an ellipse, illustrated in Figure 2-4. Fiber position can be determined from the center of mass $(\overline{x_1},\overline{x_2})$ and the fiber orientation can be detmined by the minor (m) and major (M) axis of the ellipses. The in-plane (azimuth) angle, ϕ, is define as the angle between the major axis and the x_1 axis. The major and minor axis can be used to calculate the out-of-plane (polar) angle, θ, using equation 2-21.

$$\theta = cos^{-1}\left(\frac{m}{M}\right) \tag{2-21}$$

One of the major disadvantages of this method is that it does not give complete 3-D information about the fiber [26]. The in-plane angle has an ambiguity inherent in it. A single ellipse can represent ϕ or $\phi + \pi$, as shown in Figure 2-5. Several methods have been proposed to solve this problem [51, 52], which will be discussed in later sections. From the orientation angles, the components of the second order orientation tensor (A_{ij}) can be calculated using Equations 2-22-2-27 [26].

$$(A_{11})_n = sin^2(\theta)\, cos^2(\phi) \tag{2-22}$$

$$(A_{12})_n = (A_{21})_n = sin^2(\theta)\, cos(\phi)\, sin(\phi) \tag{2-23}$$

$$(A_{13})_n = (A_{31})_n = sin(\theta)\, cos(\theta)\, cos(\phi) \tag{2-24}$$

$$(A_{22})_n = sin^2(\theta)\, sin^2(\phi) \tag{2-25}$$

$$(A_{23})_n = (A_{32})_n = sin(\theta)\, cos(\theta)\, sin(\phi) \tag{2-26}$$

$$(A_{33})_n = cos^2(\theta) \tag{2-27}$$

The ambiguity in ϕ means that the values for A_{13} and A_{23} are uncertain. A_{11}, A_{12}, A_{22}, and A_{33} are identical regardless of ambiguity in ϕ.

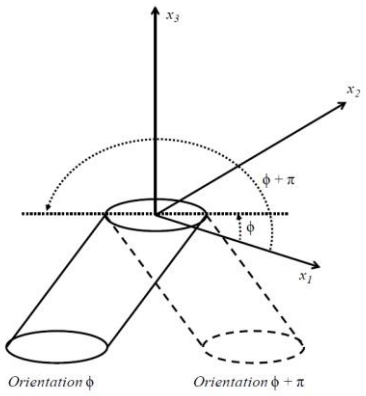

Figure 2-5: Ambiguity in ϕ for MOE adapted from [50]

A correction on the observed orientation is necessary based on stereological principles [26, 53]. The probability of a randomly placed plane intersecting a fiber aligned perpendicular to the plane, is higher than it intersecting a fiber parallel to the plane. Therefore, circular cross sections, i.e. fibers that are transverse to the inspection plane, are more likely to be observed than elongated ellipses. This bias is corrected for using equation 2-28 [26].

$$\bar{A}_{ij} = \frac{\sum (A_{ij})_n L_n F_n}{\sum L_n F_n} \tag{2-28}$$

F_n is the weighting function of the n^{th} fiber, and L_n is the length of the n^{th} fiber. While a few different weighting functions have been developed, the most general weighting function was developed by Konicek [53] and is given in equation 2-29. Here, d_n is the diameter of the n^{th} fiber.

$$F_n = \frac{1}{L_n \cos(\theta_n) + d_n \sin(\theta_n)} \tag{2-29}$$

While the Konicek function can be used with complete and partial ellipses of any size, the Bay weighting function, given in equations 2-30-2-32, is limited to fibers with greater than half an ellipse visible [26].

$$F_n = \frac{1}{L_n \cos(\theta_n)} \qquad For\ \theta_n < \theta_c \tag{2-30}$$

$$F_n = \frac{1}{d_n} \qquad For\ \theta_n > \theta_c \tag{2-31}$$

$$\theta_c = \cos^{-1}\left(\frac{d}{L}\right) \tag{2-32}$$

Here θ_c is the cutoff angle used to prevent the weighting function from going to singularity before θ becomes $\pi/2$, d is the average fiber diameter, and L is the average FL.

2.3.2 Optical

Optical microscopy is the most common method of imaging samples for experimentally determining fiber orientation. Images are obtained via a reflective optical microscope and analyzed using the MOE. It has the advantages of using relatively low cost readily available equipment and ease of automation. However, the sample preparation for this method is labor intensive. Standard sample preparation includes cutting, marking, mounting, grinding, polishing, etching, and sputtering of the samples and is covered in § 2.3.2.1. Image acquisition is covered in § 2.3.2.2. Methods to overcome the ambiguity problem in the MOE using optical microscopy are covered in § 2.3.2.3. Finally, the methods used to obtain orientation from LF using optical microscopy are discussed in § 2.3.2.4.

2.3.2.1 Sample Preparation

The first step is to cut the region of interest out of the original part. Using an aggressive cut causes fractures and surface irregularities. This induces errors into the MOE, where being off by a few pixels for circular objects can have a large effect [52]. A border of 2 mm between the surface being cut and the area to be analyzed is used to provide a buffer [54]. Cuts are performed with a low speed diamond saw to further minimize fiber breakage during the cutting process [55, 56]. Once a sample has been cut, a polymeric tridimensional marker is glued to it at the line of interest, Figure 2-6. The marker serves as a guide for polishing, and imaging [54], marking when the polishing step has reached the correct depth and the location of interest for imaging. When the glue is dried, the sample is hot mounted in acrylic resin using compression molding, with the area of the sample to be polished off facing down. This stabilizes the sample for polishing, ensuring that the sample is perpendicular to the polishing plane.

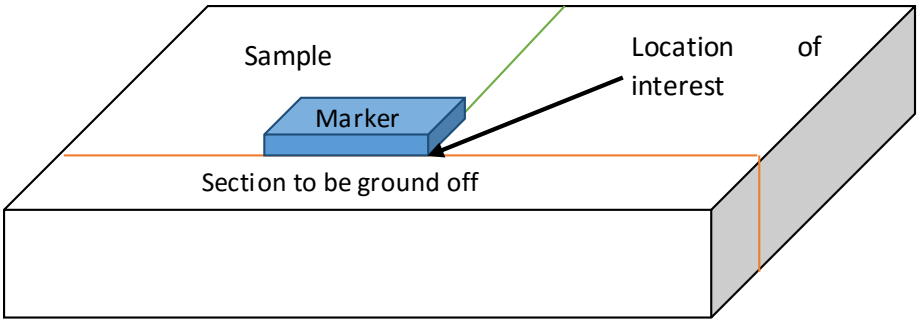

Figure 2-6: Tridimensional marker on a sample

After mounting, a two-step procedure is used to ensure the imaging surface is smooth. First, the sample is ground down and rough polished by hand using sand paper. Then, the sample is fine polished with an automatic polisher. Initially, 180 grit sandpaper is used to grind the sample down until the marker is just exposed. During the grinding process, the sandpaper is kept wet, to avoid fiber breakage, and rotated 90° every 30 seconds to ensure a flat surface. Any surface grooves in the sample are removed using 240, 320, 400, then 600 grit sandpaper for 2 minutes at each grade [54].

An automated polisher is necessary for the degree of control needed to achieve high quality samples during the fine polishing stage. A hole is drilled in the top center of the sample, so it can be mounted on the polishing apparatus. Alumina particles of 5, 3, 1, and 0.3 µm diameter, in an aqueous suspension, are used with a synthetic nap cloth to polish the samples. The sample is polished with each size for 30 minutes using 22.2 N of force at 45 rpm. At the end of each polishing step, the samples are sonicated to ensure the removal of residual polishing solution.

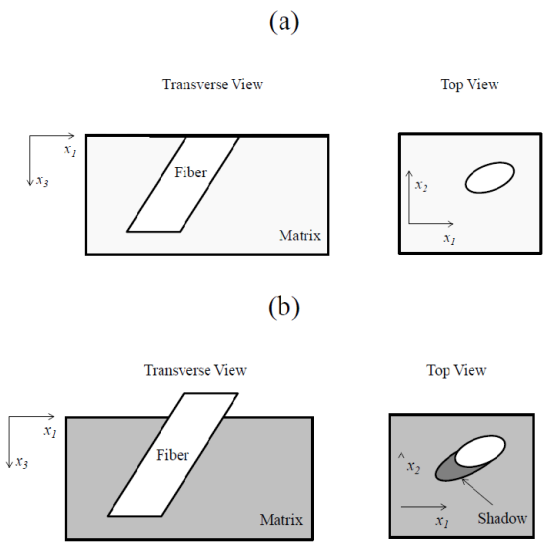

Figure 2-7: Effects of plasma etching (a) before (b) after adapted from [50]

In order to automate the MOE, high contrast between the fiber and matrix is required. For many fiber matrix combinations, polishing the sample does not give enough contrast. Plasma etching in an oxygen-rich environment is frequently utilized to provide extra contrast. Etching uniformly removes a small layer of polymer matrix, leaving the fiber protruding from the sample surface [57, 58]. This causes the matrix to appear darker and causes fibers at an angle to create shadows, Figure 2-7 [52]. The required etching time varies based on the matrix [54] and crystallinity of the sample [59].

If additional contrast is needed after plasma etching, gold sputtering can be used as an additional contrast enhancement method. Samples are often sputtered for 30 seconds to increase the brightness of the fibers [47]. However, it is not necessary for performing optical microscopy on most samples [54]. For more detail on sample preparation, the reader is directed to Vélez-García et al. [54].

2.3.2.2 Image Acquisition

Once sample preparation is finished, a reflective optical microscope is used to collect high resolution images. Uniform illumination and proper magnification must be used in order to reduce

systematic errors. A 20x magnification for glass fiber and a 50x magnification for carbon fiber provides the best balance between resolution and image size [26, 60, 61].

For most samples, a relatively large area needs to be imaged to obtain an accurate fiber orientation. The area of the sample being imaged affects the fiber orientation results and is dependent on the average FL in the sample [54, 62]. For short glass fiber composites, an image the width of the sample, with a length of 0.750 mm is traditionally used [54]. This size strikes a balance between containing enough fibers to be statistically accurate and small enough that large changes in orientation are not visible throughout the image length. For LF, care needs to be taken that fibers are not being cut short by the imaging size. Hofmann et al. [62] suggest using a length 1.4 times the number average FL. A motorized stage and image stitching software is used ease capturing images covering these large areas.

2.3.2.3 Ambiguity

Three main methods have been devolved to deal with the ambiguity inherent in calculate A_{ij} using the MOE and optical microscopy. Unfortunately, all the methods are time consuming. Zak et al. [63] proposed a serial sectioning method to resolve in plane ambiguity. The initial steps are the same as the standard optical microscopy method. After sample prep and imaging, the sample goes through a second polishing to a depth of one-tenth the average FL. The sample is then imaged and analyzed a second time. Finally, matching ellipse pairs from the two sections are identified using the projection from the first image, Figure 2-8. Additional sectioning can be performed to improve accuracy. This allows the ambiguity problem to be solved without expensive equipment.

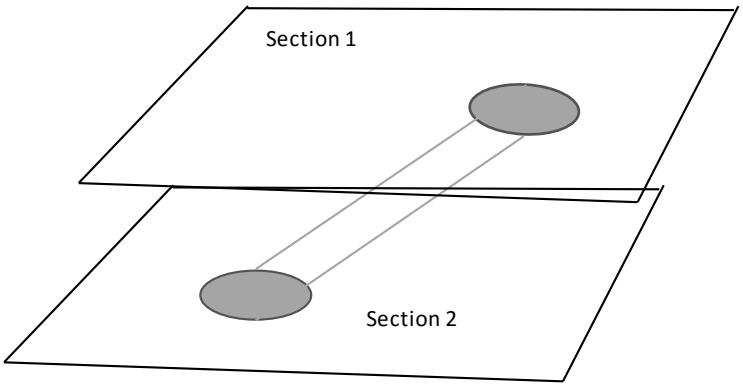

Figure 2-8: Serial Sectioning Method

This method does have several drawbacks. One of the largest is that it requires almost doubling the processing time for each sample, because polishing and image analysis must be performed twice for each sample. Second, the amount of material removed needs to be extremely accurate, less than 1 micron error [63], in order for the analysis to be accurate. This method is not an option for very short fiber lengths, due to a minimum for material that can be removed during repeat polishing. It also has the inherent limitation in the MOE, where the fibers need to behave like rigid rods in order for the projection of the fiber location to be correct.

Vélez-García et al. [52] developed a method using the shadows of ellipses created during plasma etching, shown in Figure 2-7, to calculate unambiguous orientation. Elliptical fibers, when plasma etched, will have a dark shadow that represents a portion of fiber underneath the polished plane. While the shadows are not distinct for circular fibers, the values of ϕ are small and will not have a large effect on the p-components [52]. While this is an elegant solution, it means plasma etching becomes a required step for all fiber matrix combinations and expensive equipment is needed. Automatic recognition of the shadows is difficult, making the image analysis of high fiber concentrations time consuming.

The analysis of multiple planes at the same location has also been attempted [53]. While this will yield unambiguous data, it also means that for data at each location, three samples need to be prepared

and analyzed. The data will be from different samples and slightly different locations in the sample, meaning that different fiber populations are being examined. This will give an estimate of the ambiguous values, but will not give an exact value at the point of interest.

2.3.2.4 Long Fibers

Hofmann et al. [62] extend the MOE using optical microscopy to LF. They compared results taken from the traditional view plane (x-z plane) with the "top down" view (x-y plane). Fiber flexibility is rarely seen in the x-z plane, but is more apparent in the x-y plane. Flexibility was accounted for by taking the end-to-end vector of any curved fiber, $\bar{r}$, show in Figure 2-9. The normalized end-to-end tensor orientation tensor, $\bar{\bar{R}}$, is then calculated using equation 2-20, it is examined in more depth in §2.2.2 . It was shown that by expanding the image analyzed to a length of 5.5 mm, or 1.4 times the number average FL, in the x-z plane, matching results from both inspection planes could be obtained [62].

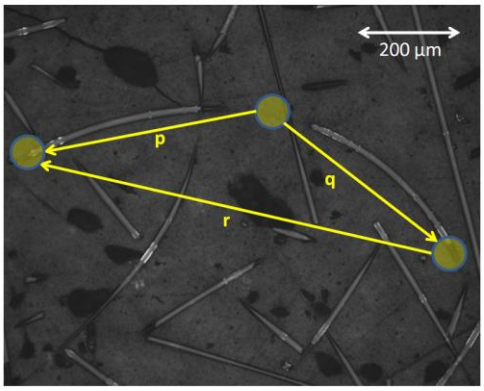

Figure 2-9: Top down view to determine end-to-end vector in the x-y plane

In order to perform analysis on top down images, it must be assumed that both endpoints of the fiber are visible. While thin injection molded parts tend to be planer with respect to z, they are not completely flat [35]. It is likely that many of the fiber ends were not visible and the end-to-end vector was slightly off. In addition, if the area of interest has a rapidly changing orientation, in the gate region

for example, averaging the orientation over such a large area will not produce accurate results for orientation at a specific location.

2.3.3 Scanning Electron Microscopy

Scanning electron microscopy (SEM) is an alternative to optical microscopy for acquiring 2-D images of FRP. The sample preparation is similar to that of optical microscopy, with a sample cut, polished, and imaged at high magnification [31, 64]. The resulting images are also analyzed by the MOE to determine orientation. SEM gives higher contrast between the fiber and polymer matrix when compared to optical microscopy [31]. Thresholding the image at high and low voltage tensions makes the shadows of the fiber visible, without the need for plasma etching [31]. However, SEM equipment is expensive and sample preparation is just as difficult for SEM images as it is for optical images. Because most of the benefits from SEM imaging can be obtained by plasma etching the sample and imaging at a sufficiently high resolution, evaluation of sample via optical microscopy tends to be preferred.

2.3.4 Confocal Microscopy

Confocal laser scanning microscopy (CLSM) offers another method for determining FOD. Using CLSM one can see a small depth into semi-transparent samples. This allows for imaging at multiple depths, removing the ambiguity of the MOE without multiple polishing steps [44, 60]. In CLSM, a reflective mode similar to an optical microscope can be used or a florescence mode can be used. In fluorescence mode, a laser of set wavelength is used to provide illumination for the sample. The wavelength is tuned so that the fibers or matrix will fluoresce, providing contrast with the non-fluorescing phase. It has been found that wavelengths between 514-540 nm work well for glass fiber and carbon fiber composites [44, 65]. This will need to be adjusted based on the matrix and sizing used in the samples. Fluorescence mode allows CLSM to focus deeper into the sample than taking images in reflective mode [44]. Basic sample preparation is similar to optical microscopy and the method can be automated [60].

This technique's usefulness is limited to lower fiber concentrations and semitransparent matrices, the combination of both is not always possible. While Clarke et al. [44] were able to see depths of up to 150 µm in polyoxymethylene 30 wt% glass fiber, they were only able to see to a depth of 10 µm in 50 wt% carbon fiber samples. Eberle et al. [65] were limited to a depth of 8 µm in polybutylene terephthalate 30 wt% glass fiber samples. While images of higher fiber content and nontransparent matrices can be acquired, there will be no advantage over optical microscopy because one cannot see into the sample. Additionally, CLSM equipment is more expensive than optical equipment.

2.3.5 Scanning Acoustical Microscopy

Scanning acoustical microscopy (SAM) offers an interesting alternative to optical microscopy. In SAM, high frequency acoustic waves and their reflections are used to image the fibers. A 2-D image is produced that appears similar to an optical image. "Fringes" associated with the ellipses that are similar to the shadows in optical microscopy are obtained, Figure 2-10. These fringes are caused by echoes reflected by the fibers [66] and allow for unambiguous determination of the FOD. In addition to giving unambiguous orientation, SAM images can be taken on samples without polishing and plasma etching, saving considerable time [51]. SAM can also be used to estimate variations in elastic properties throughout a part [66].

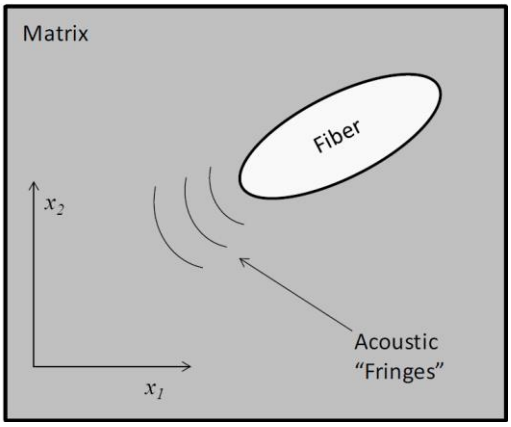

Figure 2-10: Illustration of SAM image adapted from [67]

SAM does have a few drawbacks other than requiring specialized equipment. Fringes are not visible for fibers with out-of-plane angles > 71.92° [51]. Therefore these fibers are ambiguous and SAM is not well suited for samples with a large population of fibers transverse to the inspection plane. Because the calculation of FOD is based off the MOE, it is assumed that the fibers are rigid, which is not true for LF composites.

2.3.6 Microcomputer Tomography

One of the newer techniques devolved for determining orientation in FRP is X-ray microcomputer tomography, or micro-CT. In micro-CT, X-ray images of a sample are taken from multiple angles. The cross sections are then assembled to form a complete 3-D image of the samples [68]. The technique was first applied to FRP in order to look at composite foams and then later expanded to more traditional FRP [29].

Micro-CT offers many benefits over the traditional methods of determining FOD. First, it is completely nondestructive [29, 69]. The only sample prep needed is for the sample to be cut to the desired size. This decreases a large amount of the manual labor and several sources for error [54]. It also allows the technique to be used on more delicate samples that would not have survived the polishing process [29]. One of the other major advantages of micro-CT is that it is possible to obtain FLD and FOD from the same sample using the same technique [70-72]. This eliminates all the steps and errors associated with traditional methods of calculating FLD [32]. Because a full 3-D image is acquired by micro-CT, the full 3-D FOD can be determined unambiguously with an error that is much smaller than that in optical image processing [73]. Due to the fact a full 3-D image is created and not a projection, as in the MOE, there is no need to assume that the fiber is a rigid rod. It is possible to trace a flexible fiber and determine its actual shape [74-76]. In the early development of micro-CT, there was a concern that high concentrations would be an issue, but samples up to 65 vol% fiber have been characterized [74].

There are, however, some key drawbacks to micro-CT. One of the primary issues with micro-CT is its difficulty imaging carbon fiber. The X-ray absorption of carbon fiber and most polymers are similar enough that there is not enough contrast to distinguish carbon fibers from the surrounding matrix [77]. In order to overcome this, a very strong radiation source needs to be used. The only successful micro-CT images of carbon fiber reported have been performed using a synchrotron beam as a radiation source [77, 78]. Because this is not an option for most experiments, micro-CT is limited to samples with large differences in absorption coefficients between the matrix and fibers. It is very expensive to perform micro-CT. Not only is the equipment expensive but it can cost hundreds of dollars per image if a high resolution is desired, limiting its wide spread adoption. The sample size that can be used is on the small size, with a limitation in part thickness of around 2 mm [69].

In the last few years, the focus in papers has been on automating the tracing of fibers in the resulting 3-D image [29, 70-72, 75]. Many of the techniques used to trace fibers in micro-CT were first developed for biological use to follow axonal tracts from diffusion tensor imaging [79]. They involve using the intensity gradient between the center and edges of a fiber to trace individual fibers giving an accurate orientation and length for each fiber [70]. This is very computationally intensive for high fiber content samples and requires a high powered computer to process the images [68]. To decrease computational time, a mean intercept length (MIL) method to calculate FOD has been developed [77, 80, 81]. A grid of parallel lines of known length and orientation is superimposed on the original image. The number of intersections between each line and the fibers is counted and the MIL is evaluated. The grid is then rotated through a variety of angles with the MIL calculated at each angle. While this method is computationally faster, it assumes rigid rods and removes the ability to calculate in situ FL, two of the major advantages of micro-CT [80]. Because most of the recent work has focused on improving the automation process or obtaining FLD, there is not a lot of FOD data that has been produced using this technique [29, 76, 80].

Although it seems one of the more promising techniques for determining the FOD for LF composites, all studies so far have focused on SF or continuous fiber composites.

2.3.7 Other Methods

There are a variety of other methods that have been explored for fiber orientation but are rarely used. The use of tracer fibers has been shown to be an effective nondestructive method for obtaining orientation [82]. In this method, a very small amount of opaque fibers are added to a sample of glass fibers in a transparent matrix. The orientation of the opaque fibers are analyzed and taken as representative of the part. This method limits observations to transparent matrices and fibers, which is not practical in many cases [82].

Watanabe et al. [83] used ferromagnetic fibers in a polymer matrix. By changing the magnetic field around a sample and measuring the torque induced on the sample, it is possible to obtain an average orientation of fibers in the sample. For this technique to work, the fibers need to be ferromagnetic and have uniform length, which is almost impossible in injection molded parts. Thus, there are very limited circumstances where this technique is useful [83].

2.4 Modeling Orientation

The following section outlines the techniques used for continuum-based modeling of fiber orientation evolution in FRP. If fiber orientation can be modeled in injection-molded parts, mold design and injection settings can more easily optimized to control fiber orientation and length providing the desired composite properties.

First in §2.4.1 Jeffery's model, which is the basis of the more complex models, is covered. Next, the closure approximations needed to use orientation tensors in models are covered in §2.4.2. The modification of Jeffery's model for non-dilute systems is discussed in §2.4.3. Further modifications to this model, in order to obtain a closer match with experimental data, are presented in §2.4.4. The extension

of models to semi-flexible systems is reviewed in §2.4.5. Finally, the fitting of model parameters is examined in §2.4.6.

2.4.1 Jeffery's Model

Most fiber orientation models developed from Jeffery's model for dilute high aspect ratio particles [84]. The model is based on a set of assumptions about the particle and the fluid. The particle is assumed rigid, neutrally buoyant, and large enough that Brownian motion is negligible. The matrix is assumed to be Newtonian, viscous enough that particle inertia and buoyancy are negligible, and velocity gradients are constant over the particle length. Under these assumptions the time rate of change of a vector, $\bar{p}$, is given by equation 2-33 [84]. $\bar{\bar{W}}$ is the vorticity tensor, $\bar{\bar{D}}$ is the rate of strain tensor defined in equations 2-34 and 2-35, respectively. λ is a parameter that represents the ellipticity of the particle.

$$\frac{D\bar{p}}{Dt} = \bar{\bar{W}} \cdot \bar{p} + \lambda[\bar{\bar{D}} \cdot \bar{p} - \bar{p}(\bar{p} \cdot \bar{\bar{D}} \cdot \bar{p})] \tag{2-33}$$

$$\bar{\bar{W}} = \frac{1}{2}[\nabla\bar{v} - (\nabla\bar{v})^t] \tag{2-34}$$

$$\bar{\bar{D}} = \frac{1}{2}[\nabla\bar{v} + (\nabla\bar{v})^t] \tag{2-35}$$

Jeffery's model can then be adapted to a continuum form using the orientation tensors $\bar{\bar{A}}$ and $\bar{\bar{A}}_4$, and a function of the particles aspect ratio, ξ, shown in equations 2-36 and 2-37 [33].

$$\frac{D\bar{\bar{A}}}{Dt} = \bar{\bar{W}} \cdot \bar{\bar{A}} - \bar{\bar{A}} \cdot \bar{\bar{W}} + \xi[\bar{\bar{D}} \cdot \bar{\bar{A}} + \bar{\bar{A}} \cdot \bar{\bar{D}} - 2\bar{\bar{D}}\colon \bar{\bar{A}}_4] \tag{2-36}$$

$$\xi = \frac{a_r^2 - 1}{a_r^2 + 1} \tag{2-37}$$

For FRP ξ usually reduces to 1 [33]. The definition of $\overline{\overline{\mathrm{A}}}$ is given by equation 2-14 and it can be calculated experimentally using equations 2-22-2-27. However, for modeling $\bar{\bar{A}}_4$ is normally estimated from a closure approximation coved in the next section [33].

2.4.2 Closure Approximations

The choice of closure approximation for $\bar{\bar{A}}_4$ can have a large effect on the accuracy of the orientation models [33, 85]. The first closure approximation developed was a linear method by Hand [86]. This method, equation 2-38, uses linear combinations of $\overline{\overline{\mathrm{A}}}$ to calculate the 15 independent terms of $\bar{\bar{A}}_4$. The linear closure approximation leads to results that are exact for randomly orientated fibers and maintains the symmetry of $\bar{\bar{A}}_4$.

$$A_{ijkl} \approx -\frac{1}{35}\left(\delta_{ij}\delta_{kl} + \delta_{ik}\delta_{jl} + \delta_{il}\delta_{jk}\right) + \frac{1}{7}(A_{ij}\delta_{kl} + A_{ik}\,\delta_{jl} + A_{il}\delta_{jk} + A_{kl}\delta_{ij} + A_{jl}\delta_{ik} + A_{jk}\delta_{il}) \tag{2-38}$$

The quadratic closure approximation was developed by Doi [87], in which the higher order tensor is the product of the lower order tensors, equation 2-39. This gives results that are exact for completely aligned fibers, but poor results for random fibers and it does not possess the full symmetries of $\bar{\bar{A}}_4$ $(A_{ijkl} \neq A_{ikjl})$ [33].

$$A_{ijkl} \approx A_{ij}A_{kl} \tag{2-39}$$

A hybrid closure approximation was developed by Advani and Tucker [33] that combines linear and quadratic closures. While useful over a larger range of orientations than the linear or quadratic closure approximations, the results are still not very accurate and do not possess the full symmetries of $\bar{\bar{A}}_4$ [37].

Verleye and Dupret [88] proposed a natural closure approximation that is based off neglecting fiber-fiber interactions. It gives accurate results under many situations, but can yield singularities [37]. Cintra and Tucker [89] developed an orthotropic fitted closure approximation using eigenvalues and fitting the unknown parameters to flow data. While results are accurate in most situations, there are nonphysical oscillations for low fiber-fiber interactions [37]. However, modifications were later made that removed the oscillations [85].

Chung and Kwon [37] created the invariant based closure approximation (IBOF). It's fitting parameters are functions of the invariants of the orientation tensor. IBOF shows accurate predictions of orientation over a wide range of flow and fiber conditions [85]. The major advantage it has over orthotropic methods is computational efficacy. IBOF yields results comparable to the improved orthotropic closure method, using 30% of the computation time [85]. IBOF has become the most common closure approximation due to its accuracy and computation speed [23, 85, 90].

2.4.3 Folgar-Tucker Model

Folgar and Tucker [35] extended Jeffery's model to non-dilute systems by adding an isotropic rotary diffusion term to Jeffery's model (eq. 2-36) to account for fiber-fiber interactions, shown in equation 2-49. $\bar{\bar{\mathrm{I}}}$ is the identity tensor and C_I is a system specific rotary diffusion term. C_I can be determined experimentally by fitting model results to known orientation or by using a variety of empirical expressions for C_I that were developed based on different part characteristics including: fiber volume fraction, aspect ratio, average distance between fibers, and simple shear experiments [91-93]. Fitting C_I to experimental data for the system of interest, has proven to be more accurate than the analytical methods. The Folgar-Tucker model has proven accurate for SF composites at low fiber concentrations [40, 91]. As fiber concentration increases, the model over predicts the rate of orientation evolution [50, 94-96].

$$\frac{D\bar{\bar{A}}}{Dt} = \bar{\bar{W}} \cdot \bar{\bar{A}} - \bar{\bar{A}} \cdot \bar{\bar{W}} + \xi\left[\bar{\bar{D}} \cdot \bar{\bar{A}} + \bar{\bar{A}} \cdot \bar{\bar{D}} - 2\bar{\bar{D}} : \bar{\bar{A}}_4\right] + 2C_I\dot{\gamma}(\bar{\bar{I}} - 3\bar{\bar{A}}) \tag{2-40}$$

2.4.4 Folgar-Tucker Model Modifications

In order to address the rate of orientation disagreement between models and experimental results, a variety of modifications to the Folgar-Tucker model have been proposed. Sepher et al. [95] proposed adding a "slip parameter" α, with a value between 0 to 1, to delay the fiber orientation rate and better match the experimental orientation data, equation 2-41. While this modification leads to improved accuracy it also results in a loss of model objectivity [50, 95-98]

$$\frac{D\bar{\bar{A}}}{Dt} = \alpha\left[\bar{\bar{W}} \cdot \bar{\bar{A}} - \bar{\bar{A}} \cdot \bar{\bar{W}} + \xi\left[\bar{\bar{D}} \cdot \bar{\bar{A}} + \bar{\bar{A}} \cdot \bar{\bar{D}} - 2\bar{\bar{D}} : \bar{\bar{A}}_4\right] + 2C_I\dot{\gamma}(\bar{\bar{I}} - 3\bar{\bar{A}})\right] \tag{2-41}$$

To maintain objectivity with slowed orientation kinetics, Wang et al. [98] used a reduced strain closure factor (RSC), k. In order to achieve objectivity, k behaves similar to α but acts only on the eigenvalues of the $\bar{\bar{A}}_4$ and does not modify the eigenvectors. The reference frame for predicting fiber orientation during injection molding does not change. Therefore, the difference in results between the RSC model and slip parameter models are small and may be negligible for most applications [99].

A more recent modification to the Folgar-Tucker model is the anisotropic rotary diffusion model (ARD) developed by Phelps and Tucker [100] given in equations 2-42-2-45. In equation 2-43, $b_1 - b_5$ are empirically fit constants. λ and e in equations 2-44 and 2-45 are the eigenvalues and vectors respectively. This model expanded on previous non-isotropic work to make a fibers rate of diffusivity dependent on both the rate of deformation and the orientation state of the fiber [93, 101, 102]. The ARD model was combined with RSC to give an objective model that improved orientation predictions compared to the Folgar-Tucker and RSC models for SF composites [100]. The model still is not accurate for LF composites, because it fails to address the semi-flexible nature of LF [17].

$$\frac{D\bar{\bar{A}}}{Dt} = \bar{\bar{W}} \cdot \bar{\bar{A}} - \bar{\bar{A}} \cdot \bar{\bar{W}} + \xi\{\bar{\bar{D}} \cdot \bar{\bar{A}} + \bar{\bar{A}} \cdot \bar{\bar{D}} - 2[\bar{\bar{A}}_4 + (1-k)(\bar{\bar{L}}_4 - \bar{\bar{M}}_4 : \bar{\bar{A}}_4) : \bar{\bar{D}}]\}$$
$$+ \dot{\gamma}\{2[\bar{\bar{C}} - (1-k)\bar{\bar{M}}_4 : \bar{\bar{C}}] - 2k\, tr(\bar{\bar{C}})\bar{\bar{A}} - 5(\bar{\bar{C}} \cdot \bar{\bar{A}} + \bar{\bar{A}} \cdot \bar{\bar{C}}) \quad (2\text{-}42)$$
$$+ 10[\bar{\bar{A}}_4 + (1-k)(\bar{\bar{L}}_4 - \bar{\bar{M}}_4 : \bar{\bar{A}}_4)] : \bar{\bar{C}}\}$$

$$\bar{\bar{C}} = b_1\bar{\bar{I}} + b_2\bar{\bar{A}} + b_3\bar{\bar{A}}^2 + \frac{b_4}{\dot{\gamma}}\bar{\bar{D}} + \frac{b_5}{\dot{\gamma}^2}\bar{\bar{D}}^2 \quad (2\text{-}43)$$

$$\bar{\bar{L}}_4 = \sum_{i=1}^{3} \lambda_i \bar{e}_i \bar{e}_i \bar{e}_i \bar{e}_i \quad (2\text{-}44)$$

$$\bar{\bar{M}}_4 = \sum_{i=1}^{3} \bar{e}_i \bar{e}_i \bar{e}_i \bar{e}_i \quad (2\text{-}45)$$

2.4.5 Bead-Rod Model

Strautins and Latz [40] derived orientation functions for a system modeling fibers as three beads connected by two rods, shown in Figure 2-3. This model allows the two end beads to move with respect to center bead accounting for fiber flexibility. However, the model was developed for infinitely dilute fiber suspensions, which makes it inappropriate for typical commercial suspensions that are in the 10-50 wt% range [2, 40]. In addition, the model does not include a way to account for bending due to fiber-fiber interactions [40, 43].

In order to address this, Ortman et al. [43] added an isotropic rotary diffusion term, C_I, and a slip parameter, α, to the bead-rod model. Similar to those used in the Folgar-Tucker model, these parameters expand the model's applicability to non-dilute systems. The non-dilute model is presented in equations 2-46-2-49. $\bar{\bar{A}}$, $\bar{\bar{B}}$, and $\bar{C}$ describe the orientation of a flexible fiber and are defined in equations 2-16-2-18. The k term represents a restorative potential that resists the bending of a fiber. As the value of k approaches infinity, the fiber becomes rigid. As k approaches 0, the fiber becomes infinitely flexible. The

k value can be used as a fitting parameter or calculated from beam theory [40, 43]. The rotary diffusion term accounts for a slowing of orientation and fiber bending due to fiber-fiber interactions. C_I is generally fit from experimental data. The slip parameter, as in the rigid rod case, is between 0 and 1 and slows up the rate of fiber orientation; it is also fit to experimental data.

$$\frac{D\bar{\bar{A}}}{Dt} = \alpha\left[\bar{\bar{W}}\cdot\bar{\bar{A}} - \bar{\bar{A}}\cdot\bar{\bar{W}} + \xi\left[\bar{\bar{D}}\cdot\bar{\bar{A}} + \bar{\bar{A}}\cdot\bar{\bar{D}} - 2\bar{\bar{D}}\colon\bar{\bar{A}}_4\right] + \frac{l_b}{2}\left[\bar{C}\bar{m} + \bar{m}\bar{C} - 2(\bar{m}\cdot\bar{C})\bar{\bar{A}}\right] + 2k\left[\bar{\bar{B}} - \bar{\bar{A}}\,tr\left(\bar{\bar{B}}\right)\right] - 6C_I\dot{\gamma}\left(\bar{\bar{A}} - \frac{1}{3}\bar{\bar{I}}\right)\right] \tag{2-46}$$

$$\frac{D\bar{\bar{B}}}{Dt} = \alpha\left[\bar{\bar{W}}\cdot\bar{\bar{B}} - \bar{\bar{B}}\cdot\bar{\bar{W}} + \xi\left[\bar{\bar{D}}\cdot\bar{\bar{B}} + \bar{\bar{B}}\cdot\bar{\bar{D}} - \left(2\bar{\bar{D}}\colon\bar{\bar{A}}\right)\bar{\bar{B}}\right] + \frac{l_b}{2}\left[\bar{C}\bar{m} + \bar{m}\bar{C} - 2(\bar{m}\cdot\bar{C})\bar{\bar{B}}\right] + 2k\left[\bar{\bar{A}} - \bar{\bar{B}}\,tr\left(\bar{\bar{B}}\right)\right] - 4C_I\dot{\gamma}\bar{\bar{B}}\right] \tag{2-47}$$

$$\frac{D\bar{C}}{Dt} = \alpha\left[\nabla\bar{v}^T\cdot\bar{C} - \left(\bar{\bar{A}}\colon\nabla\bar{v}^T\right)\bar{C} + \frac{l_b}{2}\left[\bar{m} - \bar{C}(\bar{m}\cdot\bar{C})\right] - k\bar{C}\left[1 - tr\left(\bar{\bar{B}}\right)\right] - 2C_I\dot{\gamma}\bar{C}\right] \tag{2-48}$$

$$\bar{m} = \sum_{i=1}^{3}\sum_{j=1}^{3}\sum_{k=1}^{3}\frac{d^2v_i}{dx_j dx_k}A_{jk}\bar{\delta}_i \tag{2-49}$$

2.4.6 Fitting of Model Parameters

In all of the models presented above, there are constants that need to be fit to the system being modeled. Traditionally, model parameters are fit to experimental orientation near the mold-gate interface in the part and then used to model the remainder of the part [35, 50]. Eberle et al. [96] proposed fitting model parameters for SF to transient shear rheology. This proved successful for SF composites in simple shear flow and it gives a faster method of fitting model parameters [96]. Ortman et al. [43] extended this technique to long fiber composites and used it to successfully predict orientation in simple shear. Rheology alone proved insufficient and orientation data from the simple shear test was needed to fit the parameters.

Meyer et al. [103] were able to use this technique to predict long glass fiber orientation, in a simple injection molded part with a 2-D flow field. However, parameters obtained from transient shear were unable to predict the experimental orientation in a more complex part with a fully 3-D flow field [99]. The model parameters had to be fit to the orientation at the gate-mold interface of the part being modeled, to obtain accurate results. An independent method of obtaining model parameters that does not involve injection molding the part to be modeled is needed.

2.5 Fiber Orientation Studies

The following sections summarize the major orientation studies over the last several decades. A description of the typical mold geometries used is covered in §2.5.1. The experimental results of short glass fiber studies are discussed in §2.5.2. A summary of studies addressing how orientation changes with processing parameters is presented in §2.5.3. While FL can be thought of as a processing parameter, it has such a large effect on the performance of parts and models used, it is covered separately in §2.5.4.

2.5.1 Test Geometries

The test geometries used to characterize experimental orientation need to have certain characteristics. Due to limitations in modeling speed the test geometries used need to be simple. This also allows for easier determination of experimental orientation. Geometries with a uniform cross section are preferred because they allow orientation to be visualized as a function of part thickness.

One of the most common test geometries used is a center-gated disk (CGD), shown in Figure 2-11. The CGD is axisymmetric in the θ direction. This means the CGD has a simplified flow field, compared to many parts, that only varies in the thickness, z, and radius, r, directions. Modeling and experimental orientation in a CGD is traditionally performed along a line of constant θ.

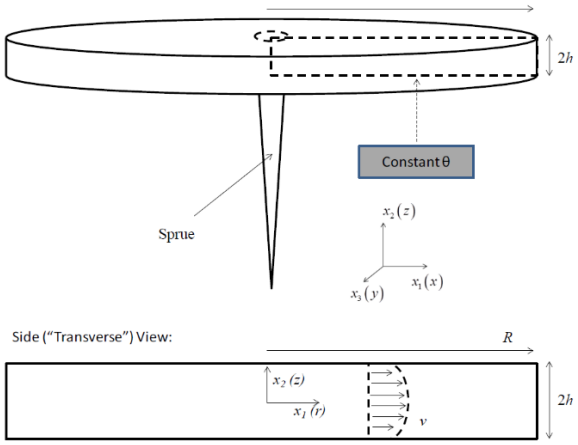

Figure 2-11: CGD

The second common geometry commonly used is the end-gated plaque (EGP), which is sometimes referred to as a film-gated strip [49], Figure 2-12. The EGP is not axisymmetric, giving it a full 3-D velocity field, where orientation varies with the thickness, length, and width of the plaque. In most studies the orientation along the centerline, where flow is similar to that in a CGD, has been examined.

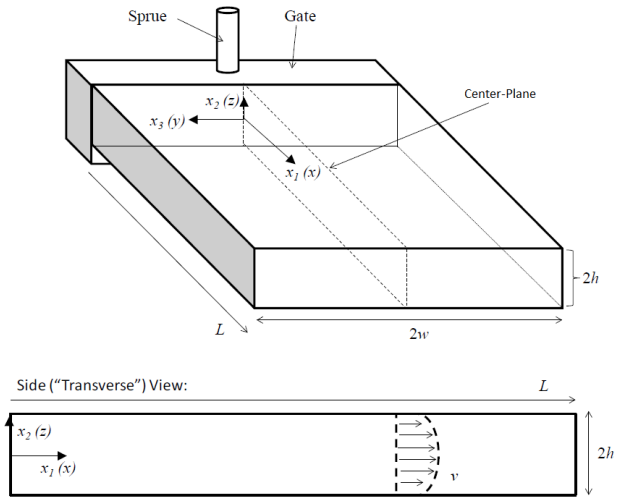

Figure 2-12: EGP

2.5.2 Short Glass Fiber

Initial studies on injection molded FRP FOD were conducted on short glass fiber composites; due to the fact they were one of the first commercially available FRP and have the advantage of fibers that behave like rigid rods. Most of the early studies looked at the FOD in a qualitative manner and found that FRP tend to have a multilayer structure created by different flow regions [104-106]. Near the walls of the mold, shear flow dominates and fibers align in the direction of the flow [53]. In the center of the mold, extensional flow dominates and fibers align transverse to the flow [53]. Bay and Tucker [49] labeled this a shell-core-shell orientation shown in Figure 2-13. Here z/h is the dimensionless thickness of the part with +1 representing the top of the mold (sprue side) and -1 the bottom of the mold. All studies have shown that for these simple geometers the fibers lie relatively flat in the thickness plane.

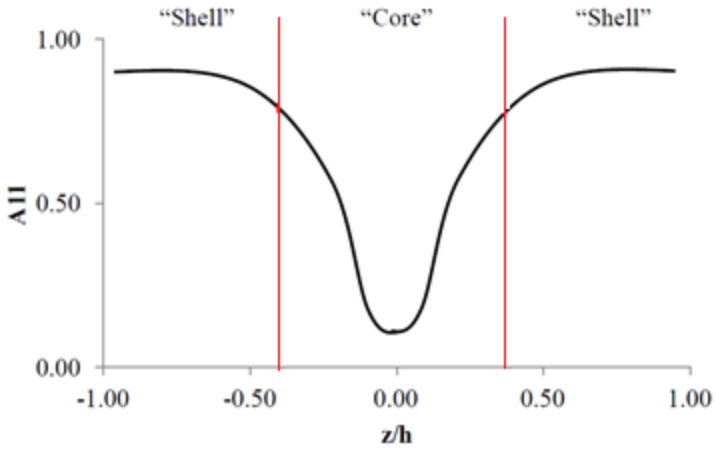

Figure 2-13: Representative graph of A_{11} component

At the advancing front, there is a region of fountain flow that is dominated by extension [107]. In fountain flow, fluid elements move toward the front of the flow, are stretched, and move towards the wall. It creates a much flatter flow profile that has proven difficult to model [85, 90, 91]. Behind the

advancing front, fibers reorient transitioning to a shell-core-shell orientation. This reorientation behind the advancing front is a major contributor to the variability in orientation along the length of sample [90].

Bay and Tucker [49] compared results in a CGD and EGP and found both structures exhibit similar layered structures. The CGD exhibited a core that was distinctly transverse to flow, while the EGP exhibited a core region that was random in plane. They proposed that the greater extensional flow in the CGD caused the higher transverse alignment. Gupta and Wang [108] performed an in-depth study of FOD in the EGP geometry. They found that, along the center plane and entrance of the plaque, fibers align more with the flow than in the CGD. This is due to converging flow from the gate to the mold cavity. Towards the end of the plaque, fibers exhibited a larger transverse alignment, due to diverging flow in the fountain region. At 50% of plaque length and 90% of plaque width, they found that shear effects dominated and fibers were flow aligned. These results demonstrated that the EGP is a fully 3-D geometry with orientation that varies with plaque length, thickness and width.

2.5.3 Processing Conditions

Injection speed has been shown to have a large effect on FOD [32, 53, 104, 109-111]. At high injection speeds, fibers align more perpendicular to the flow. At low injection speeds, a thicker shell region is formed and there is a higher degree of alignment with the flow. An increase in injection speed also leads to an increase in fiber breakage in the mold, decreasing the average FL in the composite [32]. The mold and melt temperature had a smaller effect on the FOD than injection speed [49, 110]. Lower temperatures cause a thicker shell region, due to polymer solidifying on the mold walls. Chang et al. [110] found that under certain conditions a skin layer, caused by solidification of polymer on the wall, could be found in addition to the shell-core region.

Several authors have investigated the effect of fiber concentration on FOD and FLD. As fiber content increases fiber-fiber interactions increase causing more complex orientations. An early

investigation by Murty and Modlen [112] reported that increasing fiber concentration decreased the degree of alignment obtained in FRP. Their findings, however, were qualitative in nature. Kim et al. [113] took a more quantitative look at the effects of fiber concentration on short glass fiber systems. They also found less alignment as fiber content increased. In addition, they modeled 30, 50, and 70 wt% FRP and found that models matched experimental results at 30 wt% but were unable to capture the complexities present at higher fiber content. However, they used the standard Folgar-Tucker model instead of the ARD model, which has been proven to be more accurate for high fiber concentrations [100]. Ranganathan et al. [38] found that as fiber content increases, fibers group together and form clusters in the flow field. The work only examined fiber content up to 10 wt%, therefore a wider range of concentrations needs to be studied to fully understand the phenomenon. Thomason [114] showed that as fiber content increases, fiber breakage increases. Little work has been performed looking into the effect of fiber concentration on LF systems.

Hine et al. [57] showed that matrix type is of secondary importance to mold geometry in controlling fiber orientation. However, other works have shown that matrix choice does affect the FOD. Bay and Tucker [49] tested polypropylene, polycarbonate, and nylon 6,6. They found polypropylene had a wider core region and no skin layer. The polycarbonate and nylon samples had skin layers, with polycarbonate having a narrower core region. The authors explained this by stating that polypropylene was strongly shear thinning and very temperature sensitive compared to the other matrices used, but no quantitative data was shown. Rheology on the different pure matrices would have given a better understanding of the differences in orientation.

Sousa et al. [7] looked at the effect of two grades of high-density polyethylene. They found that the lower molecular weight (MW) matrix gave increased stiffness, strength, impact performance and FL. The higher MW matrix had parabolic flow marks in the core region that were not evident in the low MW samples. The paper only examined orientation qualitatively so the exact difference in orientation between

the samples is not known. No effort was made to separate the effects of increased FL and matrix properties. In addition, only melt flow indexing was performed to characterize the matrices, which will not show any of the viscoelastic responses of the systems used.

2.5.4 Fiber Length

FLD has a large effect on the mechanical properties of FRP. Longer fibers led to an increase in impact toughness, strength, stiffness, and increased thermal stability [3, 115]. Studies on different length SF composites have shown that shorter fibers orient faster and have a higher degree of alignment perpendicular to the flow direction in the core [64].

Rheologically, FL does not cause a large difference in the steady state shear viscosity of FRP [19]. In general, FRP display a shear thinning behavior and at high shear rates FL, long or short, has a very small effect on shear viscosity compared with fiber content and matrix viscosity [116, 117]. However, long fiber composites are slightly more viscoelastic than SF composites and the elongational viscosity of FRP has proven very sensitive to FL [19, 116]. Ortman et al. [43] showed that FL effects the shape and steady state values of stress curves in transient shear. Long glass fiber composites showed more flow regions and initial orientation had a larger effect on the resulting rheology than for SF composites.

Toll and Andersson [39] compared orientation and FLD in long and short FRP for glass fiber nylon 6,6 composites in an EGP. FL, weight, and volume measurements were taken at multiple locations through the thickness, width, and length of the parts. It was found that in SF composites the fiber content was evenly distributed. In LF composites, the fiber content was higher in the core region and increased along the length of the part. They also found that fibers were shorter in the shell than in the core region. The only difference in orientation between the SF and LF samples was a broader core in the LF. However, the average FL in their samples was 1.2 mm and because of the FLD shape, most of the fibers in the samples

were short. In addition, full 3-D orientation was not reported for any of the parts tested and fiber curvature was not addressed.

Hine et al. [47] carried out one of the first efforts to characterize long glass fiber composites using the orientation tensor. They examined the orientation of 28 wt% long glass fiber, nylon 6,6 composite in an EGP. Orientation was obtained at four locations along the center plane in the mold and one in the gate. Two additional locations, near the mold wall and half way between the mold wall and center plane, were examined at 50% of the mold length. They found that the core region broadens and becomes more defined as one moves down the plaque. Moving from the center plane towards the wall, the core region shrinks and a higher degree of flow alignment is found. At the mold wall, no distinct core region is present. No effort was made to address fiber curvature. As a FLD was not given, it is impossible to know how many semi-flexible fibers were in the final part to know if this needed to be addressed.

Nguyen et al. [17] looked at long glass fiber composites in both the CGD and the EGP. They examined orientation along a line of constant theta in the CGD and along the center plane in the EGP. They found a skin-core-shell structure and very wide FLD with fibers breaking from an initial length of 13 mm down to a number average length of 1.6 mm. The orientation results are presented for a region approximately 40% down the length of the plaque from the gate. A broader core region with a less aligned skin region was observed for LF samples. It was determined that SF composite models were not able to accurately predict orientation. In order to account for fiber bending, any fibers that had a visible curvature were broken into a series of linear segments, similar to micromechanical analysis of fibers [118]. This method only addresses curvature that can be seen in the 2-D inspection plane and ignores any fibers that appear elliptical but may have curvature in the 3-D part. Due to the Weibull distribution of the FLD and the short average FL of the samples, most of the fibers in these samples were less than 1 mm and therefore rigid.

Hofmann et al. [67] examined the 3-D orientation of long glass fiber in depth in both the CGD and EGP to verify the MOE using optical microscopy for LF composites. First, the image size used to examine FOD was optimized by minimizing the standard deviation between simple shear samples. An image width approximately 1.4 times the number average FL was found to be optimal [62]. In both the CGD and the EGP, negligible fiber curvature was observed in the r-z and x-z plane, respectively. However, fiber curvature was observable in the θ-r and x-y plane or top down view [67]. In the CGD, FOD obtained from the θ-r plane match closely with FOD from the standard and larger image size in the x-z plane [62]. The EGP had more fiber curvature in the top down view than the CGD did, because of the more complex flow field present in the EGP. As a result, the FOD obtained from the standard image size did not match FOD data obtained from the top down view in the EGP. The FOD obtained from the larger image size in the x-z plane closely matched the top down FOD. While this shows that the MOE can be modified to apply to LF, the top down view method assumes that the full length of every fiber is visible. This is not the case using optical microscopy, so the results from the top down method may be in error . While the extended bin width data in the EGP matched up with the top down view, there is little guarantee this would hold true in more complicated flow fields or more flexible fibers, because the imaging bin width was empirically fit. The orientation data reported by Hofmann et al. [67] is flatter than the FOD reported by most other studies. It is not clear if this is due to the matrix used or the fact the parts have a longer average FL than those previously reported.

2.6 References

1. Silverman, E.M., *Effect of glass fiber length on the creep and impact resistance of reinforced thermoplastics.* Polymer Composites, 1987. **8**(1): p. 8-15.
2. Mallick, P.K., *Composites engineering handbook*. 1997, New York: M. Dekker.
3. Truckenmüller, F. and H.G. Fritz, *Injection molding of long fiber-reinforced thermoplastics: A comparison of extruded and pultruded materials with direct addition of roving strands.* Polymer Engineering & Science, 1991. **31**(18): p. 1316-1329.
4. Hassan, A., et al., *Tensile, Impact and Fiber Length Properties of Injection-Molded Short and Long Glass Fiber-Reinforced Polyamide 6,6 Composites.* Journal of Reinforced Plastics and Composites, 2004. **23**(9): p. 969-986.
5. Barkoula, N.M., S.K. Garkhail, and T. Peijs, *Effect of Compounding and Injection Molding on the Mechanical Properties of Flax Fiber Polypropylene Composites.* Journal of Reinforced Plastics and Composites, 2010. **29**(9): p. 1366-1385.
6. Guo, R., J. Azaiez, and C. Bellehumeur, *Rheology of fiber filled polymer melts: Role of fiber-fiber interactions and polymer-fiber coupling.* Polymer Engineering & Science, 2005. **45**(3): p. 385-399.
7. Sousa, R.A., et al., *Integrated compounding and injection moulding of short fibre reinforced composites.* Plastics, Rubber & Composites, 2004. **33**(6): p. 249-259.
8. Dweib, M.A. and C.M.Ó. Brádaigh, *Compression molding of glass reinforced thermoplastics: Modeling and experiments.* Polymer Composites, 2000. **21**(5): p. 832-845.
9. Dweib, M.A. and C.M. ÓBrádaigh, *Extensional and shearing flow of a glass-mat-reinforced thermoplastics (GMT) material as a non-Newtonian viscous fluid.* Composites Science and Technology, 1999. **59**(9): p. 1399-1410.
10. Gibson, A.G. and S. Toll, *Mechanics of the squeeze flow of planar fibre suspensions.* Journal of Non-Newtonian Fluid Mechanics, 1999. **82**(1): p. 1-24.
11. Servais, C., A. Luciani, and J.-A.E. Månson, *Squeeze flow of concentrated long fibre suspensions: experiments and model.* Journal of Non-Newtonian Fluid Mechanics, 2002. **104**(2–3): p. 165-184.
12. Baird, D.G.C.D.I., *Polymer processing : principles and design*. 1998, New York: Wiley.
13. Bryce, D.M., *Plastic injection molding : manufacturing process fundamentals*. 1996, Dearborn, Mich.: Society of Manufacturing Engineers.
14. Dym, J.B., *Injection molds and molding : a practical manual*. 1987, New York: Van Nostrand Reinhold.
15. Greener, J.W.-F.R., *Precision injection molding : process, materials, and applications*. 2006, Munich; Cincinnati: Hanser ; Hanser Gardner Publications.
16. Olmsted, B.A.D.M.E., *Practical injection molding*. 2001, New York: Marcel Dekker.
17. Nguyen, B.N., et al., *Fiber Length and Orientation in Long-Fiber Injection-Molded Thermoplastics — Part I: Modeling of Microstructure and Elastic Properties.* Journal of Composite Materials, 2008. **42**(10): p. 1003-1029.
18. Tanaka, K., et al., *INJECTION MOLDING OF FLAT GLASS FIBER REINFORCED THERMOPLASTICS.* International Journal of Modern Physics B: Condensed Matter Physics; Statistical Physics; Applied Physics, 2010. **24**(15/16): p. 2555-2560.
19. Thomasset, J., et al., *Rheological properties of long glass fiber filled polypropylene.* Journal of Non-Newtonian Fluid Mechanics, 2005. **125**(1): p. 25-34.
20. Phelps, J.H., et al., *A model for fiber length attrition in injection-molded long-fiber composites.* Composites Part A: Applied Science and Manufacturing, 2013. **51**(0): p. 11-21.

21. Doi, M.E.S.F., *The theory of polymer dynamics*. 1987, Oxford [Oxfordshire]; New York: Clarendon Press ; Oxford University Press.
22. S. M. Dinh, R.C.A., *A Rheological Equation of State for Semiconcentrated Fiber Suspensions.* Journal of Rheology, 1984. **28**: p. 207-227.
23. Meyer, K.J., *Improved Prediction of Glass Fiber Orientation in Basic Injection Molding Geometries*, in *Chemical Engineering*. 2013, Virginia Polytechnic Institute and State University.
24. Goto, S., H. Nagazono, and H. Kato, *The flow behavior of fiber suspensions in Newtonian fluids and polymer solutions.* Rheologica Acta, 1986. **25**(3): p. 246-256.
25. Kitano, T. and T. Kataoka, *The rheology of suspensions of vinylon fibers in polymer liquids. I. Suspensions in silicone oil.* Rheologica Acta, 1981. **20**(4): p. 390-402.
26. Bay, R.S. and C.L. Tucker, *Stereological measurement and error estimates for three-dimensional fiber orientation.* Polymer Engineering & Science, 1992. **32**(4): p. 240-253.
27. Switzer, L.H. and D.J. Klingenberg, *Rheology of sheared flexible fiber suspensions via fiber-level simulations.* Journal of Rheology (1978-present), 2003. **47**(3): p. 759-778.
28. Chin, W.-K., H.-T. Liu, and Y.-D. Lee, *Effects of fiber length and orientation distribution on the elastic modulus of short fiber reinforced thermoplastics.* Polymer Composites, 1988. **9**(1): p. 27-35.
29. Shen, H., S. Nutt, and D. Hull, *Direct observation and measurement of fiber architecture in short fiber-polymer composite foam through micro-CT imaging.* Composites Science and Technology, 2004. **64**(13–14): p. 2113-2120.
30. From Peter, S. and R. Pyrz, *Computer Assisted Stereology Of Short Fibre Composites, I: Determination Of Fibre Length Distribution*, in *Science and Engineering of Composite Materials*. 1999. p. 143.
31. Avérous, L., et al., *Granulometric Characterization of Short Fiberglass in Reinforced Polypropylene. Relation to Processing Conditions and Mechanical Properties.* International Journal of Polymer Analysis and Characterization, 1995. **1**(4): p. 339-347.
32. Kunc, V., et al. *Fiber Length Distribution Measurement for long Glass and Varbon Fiber Reinforced Injection Molded Thermoplastics*. in *SPE Automotive*. 2007. Troy, MI.
33. Advani, S.G. and C.L. Tucker, *The Use of Tensors to Describe and Predict Fiber Orientation in Short Fiber Composites.* Journal of Rheology (1978-present), 1987. **31**(8): p. 751-784.
34. Lee, C.-C., F. Folgar, and C.L. Tucker, *Simulation of Compression Molding for Fiber-Reinforced Thermosetting Polymers.* Journal of Manufacturing Science and Engineering, 1984. **106**(2): p. 114-125.
35. Folgar, F. and C.L. Tucker, *Orientation Behavior of Fibers in Concentrated Suspensions.* Journal of Reinforced Plastics and Composites, 1984. **3**(2): p. 98-119.
36. Hinch, E. and L. Leal, *Constitutive equations in suspension mechanics. Part 2. Approximate forms for a suspension of rigid particles affected by Brownian rotations.* Journal of Fluid Mechanics, 1976. **76**(01): p. 187-208.
37. Chung, D.H. and T.H. Kwon, *Invariant-based optimal fitting closure approximation for the numerical prediction of flow-induced fiber orientation.* Journal of Rheology (1978-present), 2002. **46**(1): p. 169-194.
38. Ranganathan, S. and S.G. Advani, *Characterization of orientation clustering in short-fiber composites.* Journal of Polymer Science Part B: Polymer Physics, 1990. **28**(13): p. 2651-2672.
39. Toll, S. and P.O. Andersson, *Microstructure of long- and short-fiber reinforced injection molded polyamide.* Polymer Composites, 1993. **14**(2): p. 116-125.
40. Strautins, U. and A. Latz, *Flow-driven orientation dynamics of semiflexible fiber systems.* Rheologica Acta, 2007. **46**(8): p. 1057-1064.
41. Yamakawa, H., *Helical wormlike chains in polymer solutions*. 1997, Berlin; New York: Springer.

42. Bird, R.B., R.C. Armstrong, and O. Hassager, *Dynamics of polymer liquids*. 1987, Wiley, New York.
43. Ortman, K., et al., *Using startup of steady shear flow in a sliding plate rheometer to determine material parameters for the purpose of predicting long fiber orientation.* Journal of Rheology (1978-present), 2012. **56**(4): p. 955-981.
44. Clarke, A.R., G. Archenhold, and N.C. Davidson, *A novel technique for determining the 3D spatial distribution of glass fibres in polymer composites.* Composites Science and Technology, 1995. **55**(1): p. 75-91.
45. Clarke, A., N. Davidson, and G. Archenhold, *Measurements of fibre direction in reinforced polymer composites.* Journal of Microscopy, 1993. **171**(1): p. 69-79.
46. Hine, P.J., et al., *Hydrostatically extruded glass-fiber-reinforced polyoxymethylene. I: The development of fiber and matrix orientation.* Polymer Composites, 1996. **17**(5): p. 720-729.
47. Hine, P.J., et al., *Measuring the fibre orientation and modelling the elastic properties of injection-moulded long-glass-fibre-reinforced nylon.* Composites Science and Technology, 1995. **53**(2): p. 125-131.
48. Hine, P.J., et al., *Modelling of the elastic properties of fibre reinforced composites. I: Orientation measurement.* Composites Science and Technology, 1993. **47**(1): p. 65-73.
49. Bay, R.S. and C.L. Tucker, *Fiber orientation in simple injection moldings. Part II: Experimental results.* Polymer Composites, 1992. **13**(4): p. 332-341.
50. Velez-Garcia, G.M., *Experimental Evaluation and Simulations of Fiber Orientation in Injection Molding of Polymers Containing Short Glass Fibers*, in *Macromolecular Science and Engineering*. 2012, Virginia Polytechnic Institute and State University.
51. Kawamura, M., et al., *Unambiguous Determination of 3D Fiber Orientation Distribution in Thermoplastic Composites Using SAM Image of Elliptical Mark and Interference Fringe.* Journal of Composite Materials, 2005. **39**(4): p. 287-299.
52. Vélez-García, G.M., et al., *Unambiguous orientation in short fiber composites over small sampling area in a center-gated disk.* Composites Part A: Applied Science and Manufacturing, 2012. **43**(1): p. 104-113.
53. Konicek, T.S., *A Method to Determine Three Dimensional Fiber Orientation in Fiber Reinforce Polymers*. 1987, University of Illinois at Urbana- Champaign.
54. Vélez-García, G.M., et al., *Sample preparation and image acquisition using optical-reflective microscopy in the measurement of fiber orientation in thermoplastic composites.* Journal of Microscopy, 2012. **248**(1): p. 23-33.
55. Hayes BS, G.L., *Optical Microscopy of Fiber Reinforced Composites*. 2010, Materials Park, OH: ASM International.
56. Sawyer LC, G.D., Meyers GF, *Polymer Microscopy*. 2008, New York: Springer Science+Business Media, LLC.
57. Hine, P.J. and R.A. Duckett, *Fiber orientation structures and mechanical properties of injection molded short glass fiber reinforced ribbed plates.* Polymer Composites, 2004. **25**(3): p. 237-254.
58. Mlekusch, B., *Thermoelastic properties of short-fibre-reinforced thermoplastics.* Composites Science and Technology, 1999. **59**(6): p. 911-923.
59. Junkar, I., et al., *The Role of Crystallinity on Polymer Interaction with Oxygen Plasma.* Plasma Processes and Polymers, 2009. **6**(10): p. 667-675.
60. Eberhardt, C. and A. Clarke, *Fibre-orientation measurements in short-glass-fibre composites. Part I: automated, high-angular-resolution measurement by confocal microscopy.* Composites Science and Technology, 2001. **61**(10): p. 1389-1400.
61. Davidson, N.C., A.R. Clarke, and G. Archenhold, *Large-area, high-resolution image analysis of composite materials.* Journal of Microscopy, 1997. **185**(2): p. 233-242.

62. Hofmann, J.T., et al., *Application and evaluation of the method of ellipses for measuring the orientation of long, semi-flexible fibers.* Polymer Composites, 2013. **34**(3): p. 390-398.
63. Zak, G., C.B. Park, and B. Benhabib, *Estimation of Three-Dimensional Fibre-Orientation Distribution in Short-Fibre Composites by a Two-Section Method.* Journal of Composite Materials, 2001. **35**(4): p. 316-339.
64. Avérous, L., et al., *Evolution of the three-dimensional orientation distribution of glass fibers in injected isotactic polypropylene.* Polymer Engineering & Science, 1997. **37**(2): p. 329-337.
65. Eberle, A.P.R., et al., *Obtaining reliable transient rheological data on concentrated short fiber suspensions using a rotational rheometer.* Journal of Rheology (1978-present), 2009. **53**(5): p. 1049-1068.
66. Lisy, F., et al., *Application of scanning acoustic microscopy to polymeric materials.* Journal of Applied Polymer Science, 1994. **52**(2): p. 329-352.
67. Hofmann, J.T., *Extension of the Method of Ellipses to Determining the Orientation of Long, Semi-flexible Fibers in Model 2- and 3- dimensional Geometries*, in *Macromolecular Science and Engineering*. 2013, Virginia Polytechnic Institute and State University.
68. Stock, S.R., *Microcomputed tomography: methodology and applications*. 2008: CRC press.
69. Stock, S.R., *X-ray microtomography of materials.* International Materials Reviews, 1999. **44**(4): p. 141-164.
70. Teßmann, M., et al., *Automatic Determination of Fiber-Length Distribution in Composite Material Using 3D CT Data.* EURASIP Journal on Advances in Signal Processing, 2010: p. 1-9.
71. Tan, J., J. Elliott, and T. Clyne, *Analysis of tomography images of bonded fibre networks to measure distributions of fibre segment length and fibre orientation.* Advanced Engineering Materials, 2006. **8**(6): p. 495-500.
72. Salaberger, D., et al., *Evaluation of computed tomography data from fibre reinforced polymers to determine fibre length distribution.* International Polymer Processing, 2011. **26**(3): p. 283-291.
73. Desplentere, F., et al., *Micro-CT characterization of variability in 3D textile architecture.* Composites Science and Technology, 2005. **65**(13): p. 1920-1930.
74. Requena, G., et al., *3D-Quantification of the distribution of continuous fibres in unidirectionally reinforced composites.* Composites Part A: Applied Science and Manufacturing, 2009. **40**(2): p. 152-163.
75. Krause, M., et al., *Determination of the fibre orientation in composites using the structure tensor and local X-ray transform.* Journal of Materials Science, 2010. **45**(4): p. 888-896.
76. Young, S.A., *High Resolution X-ray Tomography of Fiber Reinforced Polymeric Composites*, in *Engineering Science*. 2009, University of Tennessee.
77. Cosmi, F., A. Bernasconi, and N. Sodini, *Phase contrast micro-tomography and morphological analysis of a short carbon fibre reinforced polyamide.* Composites Science and Technology, 2011. **71**(1): p. 23-30.
78. Martín-Herrero, J. and C. Germain, *Microstructure reconstruction of fibrous C/C composites from X-ray microtomography.* Carbon, 2007. **45**(6): p. 1242-1253.
79. Mori, S. and P. van Zijl, *Fiber tracking: principles and strategies–a technical review.* NMR in Biomedicine, 2002. **15**(7-8): p. 468-480.
80. Bernasconi, A., F. Cosmi, and P.J. Hine, *Analysis of fibre orientation distribution in short fibre reinforced polymers: A comparison between optical and tomographic methods.* Composites Science and Technology, 2012. **72**(16): p. 2002-2008.
81. Cosmi, F. and A. Bernasconi, *Micro-CT investigation on fatigue damage evolution in short fibre reinforced polymers.* Composites Science and Technology, 2013. **79**(0): p. 70-76.
82. McGrath, J.J. and J.M. Wille, *Determination of 3D fiber orientation distribution in thermoplastic injection molding.* Composites Science and Technology, 1995. **53**(2): p. 133-143.

83. Watanabe, Y., *Evaluation of Fiber Orientation in Ferromagnetic Short-Fiber Reinforced Composites by Magnetic Anisotropy.* Journal of Composite Materials, 2002. **36**(8): p. 915-923.
84. Jeffery, G.B., *The Motion of Ellipsoidal Particles Immersed in a Viscous Fluid.* Proceedings of the Royal Society of London. Series A, 1922. **102**(715): p. 161-179.
85. Chung, D.H. and T.H. Kwon, *Fiber orientation in the processing of polymer composites.* Korea-Australia Rheology Journal, 2002. **14**(4): p. 175-188.
86. Hand, G.L., *A theory of anisotropic fluids.* Journal of Fluid Mechanics, 1962. **13**(01): p. 33-46.
87. Doi, M., *Molecular dynamics and rheological properties of concentrated solutions of rodlike polymers in isotropic and liquid crystalline phases.* Journal of Polymer Science: Polymer Physics Edition, 1981. **19**(2): p. 229-243.
88. Verleye V. , D., F. *Prediction of the fiber orientation in complex injection molded parts*. in *ASME 1993 Winter Anuual Meeting*. 1993.
89. Cintra, J.S. and C.L. Tucker, *Orthotropic closure approximations for flow-induced fiber orientation.* Journal of Rheology (1978-present), 1995. **39**(6): p. 1095-1122.
90. Mazahir, S.M., et al., *Evolution of fibre orientation in radial direction in a center-gated disk: Experiments and simulation.* Composites Part A: Applied Science and Manufacturing, 2013. **51**(0): p. 108-117.
91. Bay, R.S. and C.L. Tucker, *Fiber orientation in simple injection moldings. Part I: Theory and numerical methods.* Polymer Composites, 1992. **13**(4): p. 317-331.
92. Ranganathan, S. and S. Advani, *Fiber–fiber interactions in homogeneous flows of nondilute suspensions.* Journal of Rheology (1978-present), 1991. **35**(8): p. 1499-1522.
93. Phan-Thien, N., et al., *Folgar–Tucker constant for a fibre suspension in a Newtonian fluid.* Journal of Non-Newtonian Fluid Mechanics, 2002. **103**(2): p. 251-260.
94. Sepehr, M., et al., *COMPARISON OF RHEOLOGICAL PROPERTIES OF FIBER SUSPENSIONS WITH MODEL PREDICTIONS*, in *Journal of Polymer Engineering*. 2004. p. 579.
95. Sepehr, M., G. Ausias, and P.J. Carreau, *Rheological properties of short fiber filled polypropylene in transient shear flow.* Journal of Non-Newtonian Fluid Mechanics, 2004. **123**(1): p. 19-32.
96. Eberle, A.P.R., et al., *Using transient shear rheology to determine material parameters in fiber suspension theory.* Journal of Rheology (1978-present), 2009. **53**(3): p. 685-705.
97. Tanner, R.I., *Engineering rheology*. 2000: Oxford University Press.
98. Wang, J., J.F. O'Gara, and C.L. Tucker, *An objective model for slow orientation kinetics in concentrated fiber suspensions: Theory and rheological evidence.* Journal of Rheology (1978-present), 2008. **52**(5): p. 1179-1200.
99. Meyer, K.J., J.T. Hofmann, and D.G. Baird, *Prediction of Short Glass Fiber Orientation in the Filling of an End-Gated Plaque.* Composites Part A: Applied Science and Manufacturing, 2014.
100. Phelps, J.H. and C.L. Tucker Iii, *An anisotropic rotary diffusion model for fiber orientation in short- and long-fiber thermoplastics.* Journal of Non-Newtonian Fluid Mechanics, 2009. **156**(3): p. 165-176.
101. Koch, D.L., *A model for orientational diffusion in fiber suspensions.* Physics of Fluids (1994-present), 1995. **7**(8): p. 2086-2088.
102. Fan, X., N. Phan-Thien, and R. Zheng, *A direct simulation of fibre suspensions.* Journal of Non-Newtonian Fluid Mechanics, 1998. **74**(1): p. 113-135.
103. Meyer, K.J., J.T. Hofmann, and D.G. Baird, *Initial conditions for simulating glass fiber orientation in the filling of center-gated disks.* Composites Part A: Applied Science and Manufacturing, 2013. **49**(0): p. 192-202.
104. Bright, P., R. Crowson, and M. Folkes, *A study of the effect of injection speed on fibre orientation in simple mouldings of short glass fibre-filled polypropylene.* Journal of Materials Science, 1978. **13**(11): p. 2497-2506.

105. Darlington, M.W. and P.L. McGinley, *Fibre orientation distribution in short fibre reinforced plastics.* Journal of Materials Science, 1975. **10**(5): p. 906-910.
106. Malzahn, J.C. and J.M. Schultz, *Transverse core fiber alignment in short-fiber injection-molding.* Composites Science and Technology, 1986. **25**(3): p. 187-192.
107. Rose, W., *Fluid-Fluid Interfaces in Steady Motion.* Nature, 1961. **191**(4785): p. 242-243.
108. Gupta, M. and K. Wang, *Fiber orientation and mechanical properties of short-fiber-reinforced injection-molded composites: Simulated and experimental results.* Polymer Composites, 1993. **14**(5): p. 367-382.
109. Folkes, M.J. and D.A.M. Russell, *Orientation effects during the flow of short-fibre reinforced thermoplastics.* Polymer, 1980. **21**(11): p. 1252-1258.
110. Chang, S.-H., J.-R. Hwang, and J.-L. Doong, *Manufacturing Process Optimization of Short Glass Fiber Reinforced Polycarbonate Composites in Injection Molding.* Journal of Reinforced Plastics and Composites, 2000. **19**(4): p. 301-321.
111. Vincent, M. and J. Agassant, *Experimental study and calculations of short glass fiber orientation in a center gated molded disc.* Polymer composites, 1986. **7**(2): p. 76-83.
112. Murty, K.N. and G.F. Modlen, *Experimental characterization of the alignment of short fibers during flow.* Polymer Engineering & Science, 1977. **17**(12): p. 848-853.
113. Kim, E., J. Park, and S. Jo, *A study on fiber orientation during the injection molding of fiber-reinforced polymeric composites:(Comparison between image processing results and numerical simulation).* Journal of Materials Processing Technology, 2001. **111**(1): p. 225-232.
114. Thomason, J., *The influence of fibre length and concentration on the properties of glass fibre reinforced polypropylene: 5. Injection moulded long and short fibre PP.* Composites Part A: Applied Science and Manufacturing, 2002. **33**(12): p. 1641-1652.
115. Rezaei, F., R. Yunus, and N.A. Ibrahim, *Effect of fiber length on thermomechanical properties of short carbon fiber reinforced polypropylene composites.* Materials & Design, 2009. **30**(2): p. 260-263.
116. McClelland, A.N. and A.G. Gibson, *Rheology and fibre orientation in the injection moulding of long fibre reinforced nylon 66 composites.* Composites Manufacturing, 1990. **1**(1): p. 15-25.
117. Crowson, R.J. and M.J. Folkes, *Rheology of short glass fiber-reinforced thermoplastics and its application to injection molding. II. The effect of material parameters.* Polymer Engineering & Science, 1980. **20**(14): p. 934-940.
118. Bapanapalli, S. and B.N. Nguyen, *Prediction of elastic properties for curved fiber polymer composites.* Polymer Composites, 2008. **29**(5): p. 544-550.

3 Fiber Concentration and Matrix Viscosity Effects on Long Glass Fiber Orientation

3.1 Abstract

The Method of Ellipses (MOE) was applied to long glass fiber (GF) polypropylene composites in order to quantify the fiber orientation distribution within injection molded end-gated plaques. The effects of matrix viscosity and fiber loading on orientation were explored. Orientation was examined along the center plane at the mold gate interface, near the advancing front, and at multiple plaque widths at half of the plaque length. The largest differences in orientation between parts were found in areas of changing flows: the gate-mold interface, 90 % of plaque length, and 50 % of plaque width. At 50 wt% GF, the higher viscosity samples exhibited higher alignment near the mold walls. The 30 wt% GF samples had a more distinct shell-core-shell orientation profile than their equivalent 50 wt% samples. Matrix viscosity had a larger effect on the orientation of the 30 wt% GF samples than the 50 wt% GF samples.

3.2 Background and Motivation

The desire for lightweight alternatives to traditional metal parts has led to the extensive use of fiber reinforced composites in the automotive and aerospace industries. These materials exhibit increased impact toughness, strength, stiffness and dimensional stability compared with pure polymers [1, 2]. In recent years, long discontinuous fiber composites have been investigated due to the fact they possess most of the properties of continuous fiber composites with the added benefit of being melt processable. Thomason et al. [3-7] performed several studies on the impact of fiber length on the properties of discontinuous composites. They found that as fiber length increase: Young's modulus increases until a number average length (L_n) of 0.5mm; modulus at higher strains continued to increase; heat deflection temperature increased; and Charpy impact resistance and tensile strength increased up until an average fiber length of 6mm.

One of the things that distinguishes long fibers from short fibers is their ability to exhibit bending or curvature. The degree of fiber curvature is dependent on the fiber properties, polymer properties, and

flow field in the injection molding process. Switzer and Klingenberg [8] defined an effective stiffness parameter, S^{eff}, to describe the tendency of a fiber to bend. In Eq. 3-1, *E* is the Young's modulus of the fiber, η_m is the viscosity of the matrix, $\dot{\gamma}$ is the shear rate, and a_r is the aspect ratio of the fiber. Experimentally injection molded glass fiber (GF) composites have been observed to exhibit bending at an aspect ratio of 100 [9]. It is important to remember that flexibility is a spectrum and that an aspect ratio of 100 is not a distinct cut off in terms of a flexible fiber.

$$S^{eff} = \frac{E\pi}{64\eta_m \dot{\gamma} a_r^4} \tag{3-1}$$

The increasing fiber length also increases the number of fiber-fiber contacts , N_c. The equation for N_c for a 3D random arrangement of slender fibers is given Eq. 3-2, where ϕ is the volume fraction of fibers in the part [10, 11]. The increased number of fiber-fiber contacts combined with the possibility of bending leads to changes the final GF orientation in the part [12].

$$N_c = \frac{2\Phi a_r}{1 + \frac{\pi}{2}\Phi} \tag{3-2}$$

A primary reason to obtain experimental fiber orientation is for verification of numerical simulation packages. If fiber evolution in flow is well understood, mold design can be optimized for mechanical strength improvement. For injection molded parts, the mold design, processing parameters, and material parameters will influence the evolution of fiber orientation as the mold is filled to generate a part.

Injection molded short fiber composites have been extensively studied and tend to have a shell-core-shell orientation where near the walls of the mold, shear flow dominates and fibers align in the direction of the flow [13-17]. In the center of the mold, extensional flow dominates and fibers align transverse to the flow [13-17]. Injection speed and temperature were found to have similar effects on the orientation profile of the composites [13, 14, 18-21]. At high injection speeds and temperatures, fibers align more perpendicular to the flow. At low injection speeds and temperatures, a thicker shell region is formed and

there is a higher degree of alignment with the flow. An increase in injection speed also leads to an increase in fiber breakage in the mold, decreasing the average FL in the composite [21].

The effects of fiber concentration and polymer viscosity on short fiber composite orientation have been explored in depth in a few studies [3, 17, 22-24]. Murty and Modlen [22] reported that increasing fiber concentration decreased the degree of flow alignment fibers obtained. Kim et al. [23] tested 30, 50, and 70 wt% GF and also found less alignment as fiber content increased. Models matched experimental results at 30 wt% but were unable to capture the orientations present at higher fiber content. Bay and Tucker [17] tested polypropylene, polycarbonate, and nylon 6-6 with short glass fiber. They found polypropylene had a wider core region and no skin layer when compared to the other two polymers. Sousa et al. [24] looked at the effect of two grades of high-density polyethylene. They found that the lower molecular weight (MW) matrix gave increased stiffness, strength, impact performance and fiber length. The higher MW matrix had parabolic flow marks in the core region that were not evident in the low MW samples.

Few studies have been performed that examine the experimental fiber orientation in long fiber composites [12, 25-27]. Nguyen et al. [12] examined orientation in 40 wt% long GF/ polypropylene (PP) along a line of constant theta in a center-gated disk and along the center-plane in an end-gated plaque. They found a shell-core-shell structure and a very wide fiber length distribution with fibers breaking from an initial length of 13 mm down to a number average length of 1.6 mm. A broader core region with a less aligned shell region was observed for long fiber samples versus short fiber samples. Lafranche et al. [25] examined 40 and 50 wt% GF/ polyamide 6-6, but only examined orientation at one location in an end-gated plaque. Hoffman et al. [28] thoroughly examined orientation in an end-gated plaque and center-gated disk for 30 wt% GF / PP and confirmed that the Method of Ellipses (MOE) was applicable to long GF composites but did not examine how any processing or material properties affect orientation. Cieslinski et al. [27] examined concentration effects going from 10 to 40 wt% long GF PP in a sliding plate rheometer.

They found increased stress growth overshoot and shear thinning at higher concentration but little change in how fibers oriented within the rheometer. Due to equipment limitations, only shear rates less than 4 s^{-1} were examined.

The goal of this work is to assess how large of an effect matrix viscosity has on the fiber orientation of commercially available long GF PP composites. In order to test this, 30 and 50 wt% GF composites with high and low viscosity PP were injection molded. Two different fiber loadings were used to ascertain how much of an effect changing the number of fiber contacts would have on the influence of matrix viscosity on fiber orientation.

3.3 Materials and Methods

3.3.1 Materials

Sabic PP Verton long GF PP composite with a high viscosity (HV) matrix and a low viscosity (LV) matrix with an initial pellet length of 13 mm were tested. Two different viscosities of PP from the same manufacturer were used to ensure the same sizing on the fibers and thus interactions between the fibers and matrix. The rheological properties of the base PP was tested to ensure different viscosities. Glass fiber concentrations of 30 and 50 wt% were examined.

3.3.2 Injection molding

The material was injection molded with an Arburg Allrounder 221-55-250; using an 18 mm diameter screw with a screw speed of 200 rpm, backpressure of 1 bar, and fill time of 2 seconds. The melt temperature profile of the injection molding machine was set to 190/210/220/220°C in the feed, compression, metering zones and nozzle respectively, while the mold temperature was held at 80°C . Short shots filling 90% of the mold were used to mitigate packing and frontal wall effects.

End-gated plaques were produced with a sprew length of 65 mm, an initial radius of 1.45 mm, and a final radius of 1.75 mm. The part consisted of a gate and a plaque region. The gate region was 80.68

mm X 6.25 mm X 6.33 mm and the plaque was 75.05 mm X 77.65 mm X 1.55 mm. The first 10 plaques from each run were discarded, to ensure that the machine was operating at equilibrium.

3.3.3 Sample Preparation

The fiber orientation was examined at 0, 10, 40, and 90 % of the part length along the center plane. The center plane of an end-gated plaque experiences a symmetric radial flow similar to a center-gated disk. Away from the center-plane, different flow fields have been observed that create a higher degree of flow alignment [29]. Therefore, at 40 % of part length additional samples were taken at 50% and 90% of plaque width, as shown in Figure 3-1. Samples were marked, cut, polished, and plasma etched in the x-z plane following the procedure developed by Velez-Garcia et al. [30]. Optical microscopy (Nikon Eclipse LV100) was then utilized to image a 2mm x 2mm area with a resolution of 0.25 µm per pixel. The relatively large image area was used because Hofmann et al. [26] found that as fiber length increases the imaged area needs to increase. Due to the fiber clustering, highly elongated ellipses, and curvature, more fibers need to be examined for long fiber composites to obtain accurate orientation averages using the method of ellipses (MOE).

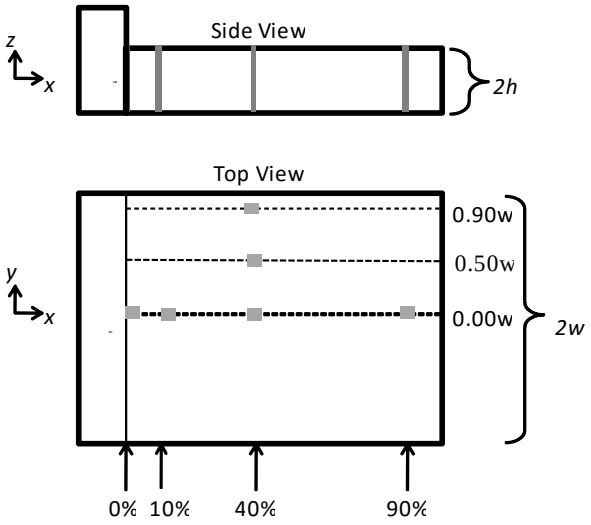

Figure 3-1: Experimental geometry and the selected inspection locations for the end-gated plaque. Grey squares represent the inspection locations.

3.3.4 Method of Ellipses

The optical images were analyzed using the MOE and a custom MatLab program, with the image broken into thirteen bins through the thickness of the sample. The fibers in the polished samples appear as ellipses. From the size of the minor and major axis, denoted as *m* and *M*, respectively , in Figure 3-2, the azimuthal angle, ϕ. The zenith angle, θ, of the fiber can be calculated using the m and M and Eq. 3-3 [9]. From these values the components of the orientation tensor, **A**, can be calculated [9]. The MOE is ambiguous, where a single ellipse can represent ϕ or $\phi + \pi$. In order to overcome this, the shadows of the ellipse created during the plasma etching process were used to indicate which direction the fiber is in [31]. The Bay and Tucker weighting function [9] was used to account for the observational bias involved in cutting and imaging the sample. The error bars shown in Figures 5 and 6-10 are the standard deviation between samples and are representative of what was seen for both samples. Only one set of error bars was shown for ease of reading.

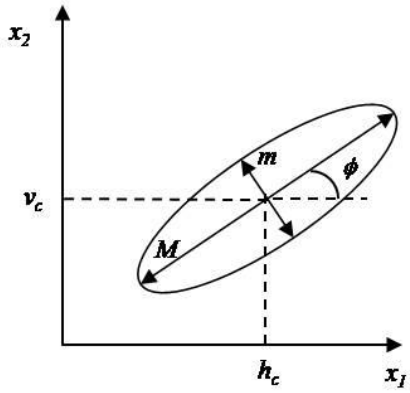

Figure 3-2: Ellipse created by a fiber and characteristic parameters.

$$\theta = \cos^{-1}\left(\frac{m}{M}\right) \tag{3-3}$$

3.3.5 Fiber Length

Fiber length measurements were obtained using an epoxy method developed by Kunc et al. [21]. A 26 mm X 26 mm section from the center of a part was placed in an oven at 450°C, burning off the polymer and leaving behind the fibers. A cylinder of epoxy was injected into the burnt off sample and allowed to dry. This allows a representative section of fibers to be pulled out of the sample minimizing sampling bias. The epoxy plug of fibers was then burnt off a second time. The resulting fibers were imaged with a flatbed scanner (Epson V800) at a resolution of 6000 dpi. A minimum of 2000 fiber lengths from each sample and 2 samples at each condition were manually measured.

3.3.6 Rheology

The neat matrix for each composite type was characterized using a rotational (Rheometrics RMS-800) and capillary rheometer (Gottfert Rheograph 2001). For the rotational samples, 50 mm cone and plate fixtures were used and samples were tested at 180 °C, 220°C, and 240 °C. Steady shear data was taken from a shear rate of 0.01 s^{-1} to 0.5 s^{-1} and oscillatory data at a strain of 2% was taken from 0.1 rad/s to 100 rad/s. Capillary data was taken using 10 mm long with 0.5 mm diameter and 15mm long with 0.5 mm diameter dies at 220 °C. Bagley corrections were applied to account for entry and exit effects. The data was combined to form master curves using the Cox-Merz rule. Time temperature superposition was used to shift all data to 220°C

3.4 Results and Discussion

3.4.1 Rheology

The viscosity curves at 220°C for the two PP matrixes used are given in Figure 3-3. The zero sheer viscosity of the HV and LV material is 720 Pa-S and 153 Pa-S, respectively. The HV material shear thins faster than the LV material with their viscosities becoming similar above a shear rate of 10000 s^{-1}. Under the injection molding conditions used, the shear rate ranges from 10 to 1000 s^{-1} with most of the plaque

in the 10 to 100 s^{-1} range. In that region the two polymers have different viscosities indicating that the tested system should behave slightly differently.

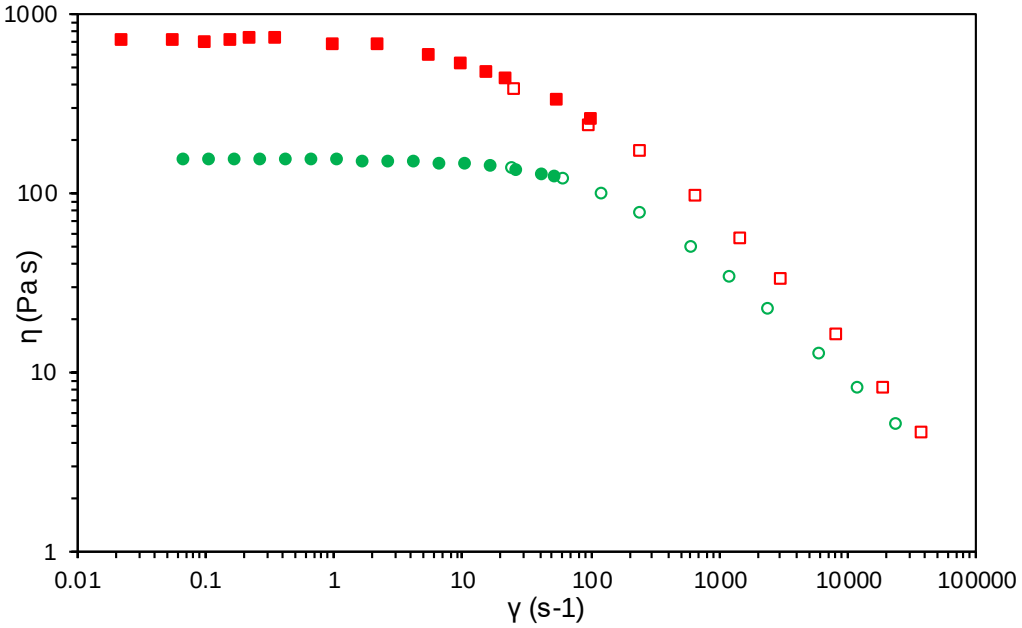

Figure 3-3: Viscosity comparison low and high viscosity Sabic PP ■ high viscosity ● low viscosity. Filled points are oscillatory and steady shear data. Unfilled points are capillary data.

3.4.2 Fiber Lengths

The final fiber lengths in all systems examined were tested as the injection molding process causes a large amount of fiber breakage [32, 33]. If large differences between the HV and LV systems final fiber lengths occurred, it would be impossible to tell if any differences in orientation were due to fiber length or matrix viscosity. The fiber length distributions for all the samples tested are shown in Figure 3-4. For all samples the fiber lengths broke down severely from an initial length of approximately 13 mm to around 1 mm. This breakage is widely reported in the literature and is because of the stresses placed on the fibers during the injection molding process [33]. At 30 wt% GF the LV material has a number average length (L_n) of 0.90 ± 0.01 mm and the HV has a L_n of 0.92 ± 0.03 mm. The expected result would be for the HV material to have a slightly shorter fiber length, but the difference in the results found are negligible.

Because the fibers break down into a distribution of lengths, the weight average lengths (L_w) were also calculated giving 1.73 ±0.06 mm and 1.63 ±0.09 mm for the LV and HV material, respectively. In the 50 wt% GF samples, the HV material has a L_n of 0.77± 0.03 mm and a L_w of 1.50 ± 0.08 mm while the LV samples have a L_n of 0.69 ± 0.02 mm and a L_w of 1.12 ± 0.16 mm. The shorter fiber lengths in the 50 wt% GF samples compared to the 30 wt% GF samples are due to the larger number of fiber-fiber interactions and higher viscosity of the system [10]. The similar fiber lengths in the HV and LV samples indicate that any differences in orientation should be caused by differences in matrix viscosity at the same concentration.

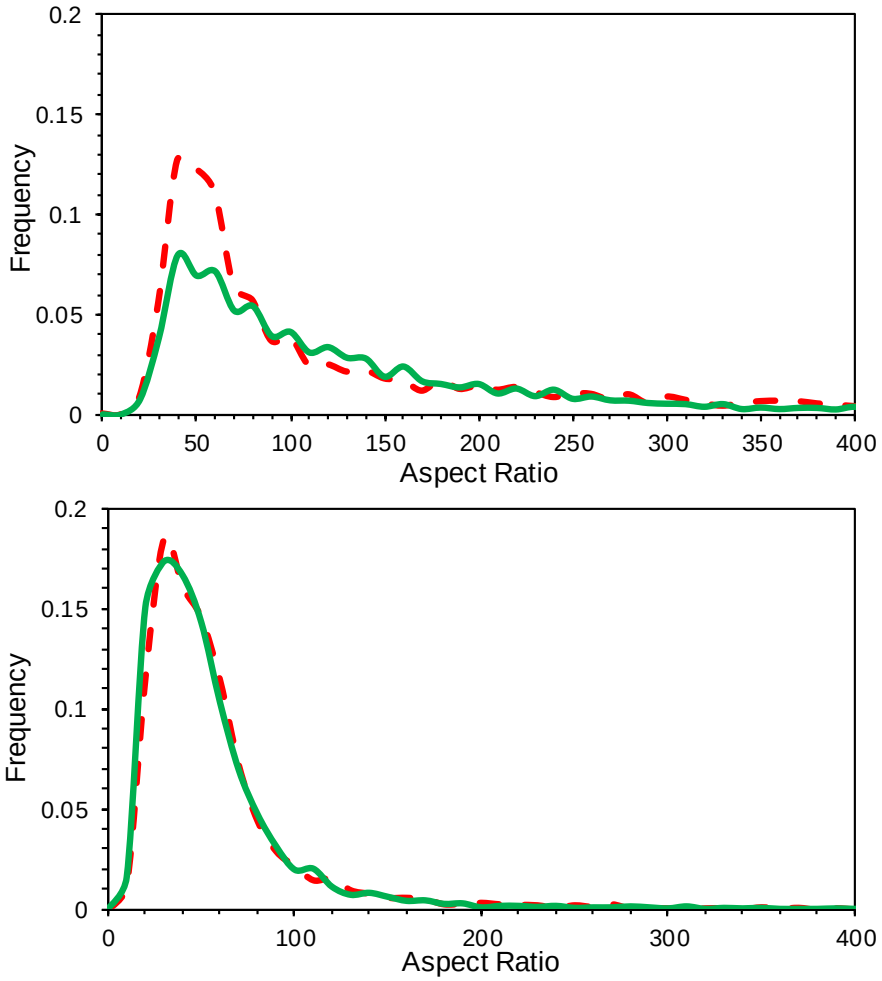

Figure 3-4: Fiber length analysis after injection molding for the 30 wt% GF (top) and 50 wt% GF sample (bottom) comparing breakage in (—) Low Viscosity and (— —) High Viscosity PP. Plotted as normalized frequency as a function of the aspect ratio of the fibers.

3.4.3 *Orientation Differences*

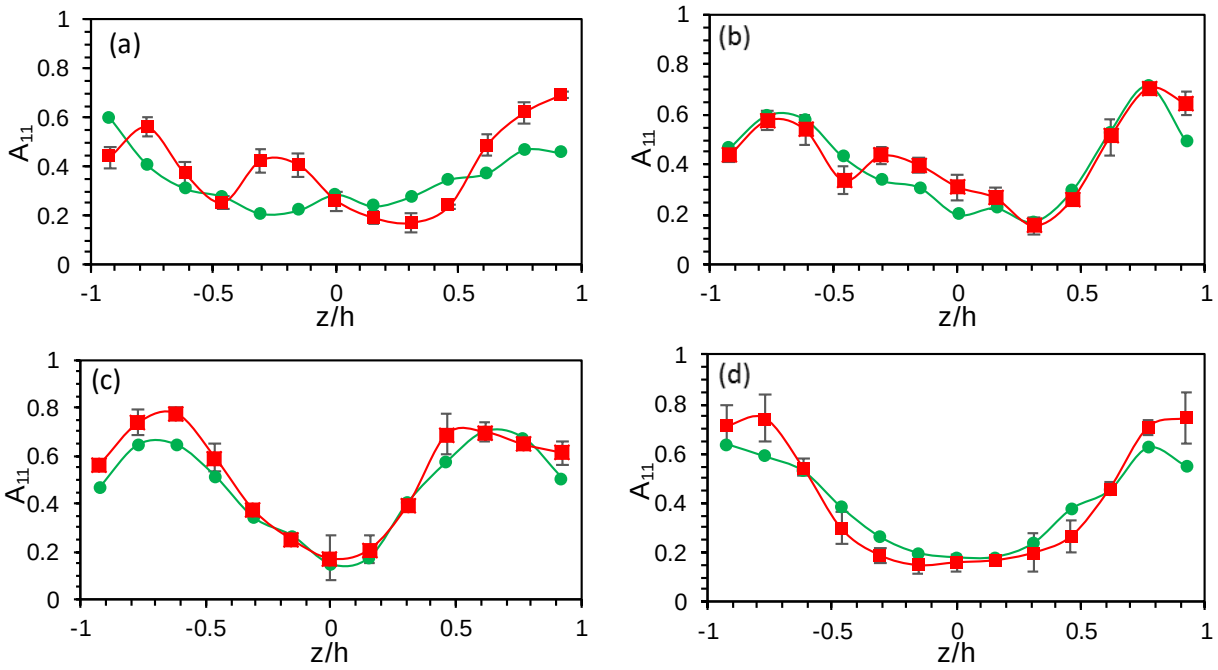

Figure 3-5: A_{11} component of the orientation tensor as a function of part thickness along the center-plane for 50 wt % GF (■) high viscosity and (●) low viscosity PP samples at (a) 0 %, (b) 10%, (c) 40%, and (d) 90% plaque length.

Figure 3-5 shows a comparison between the A_{11} (Flow Direction) component of the orientation tensor through the part thickness for the HV and LV samples at 50 wt% GF along the center plane. The largest difference in the HV and LV samples orientation occurs at the gate-mold interface (0% of plaque length). The LV material has a low degree of orientation in the flow direction throughout the center of the part with a slightly higher degree of alignment near the mold walls. As the fibers move down the part to 10 and 40 % plaque length, the shell-core-shell profile becomes more distinct with a narrower core and a higher degree of alignment towards the mold wall. The lower degree of alignment at a z/h of ± 0.95 is caused by a skin layer that is formed as polymer solidifies along the mold wall [19]. At 90% of plague length the core region of the LV materials orientation profile broadens caused by the advancing front [34].

Figure 3-6: 50 wt % glass fiber high viscosity polypropylene at the gate-mold interface.

Examining the HV material orientation shows that there is a wavy orientation profile at the gate-mold interface, instead of the shell-core-shell profile developed in the LV material, created by clustering in the turn from the gate shown in Figure 3-6. At 10% of the plaque length, the HV samples have a more asymmetric orientation profile than the LV samples. This indicates that the effects from the turn from the gate last further into the part from the HV material because the fibers obtain a more distinct orientation during the turn it affects the orientation further into the part. By 40 % plaque length, the asymmetry caused by the turn from the gate has washed out and a shell-core-shell profile exists. There is a higher degree of flow alignment in the shell region of the part. It is believed that the HV matrix is exerting more force on the fibers causing a higher degree of flow alignment. A similar trend is observed at 90% plaque length where the HV material has a broader core and higher degree of alignment in the shell.

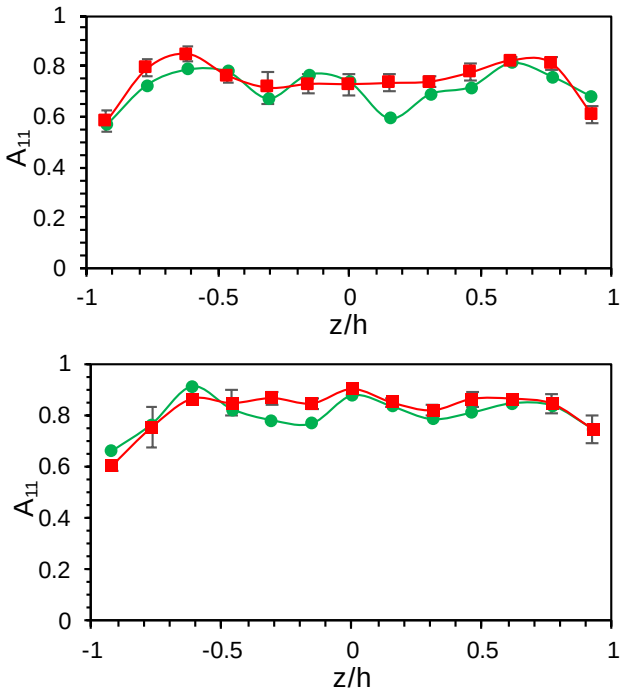

Figure 3-7: A_{11} component of the orientation tensor for 50 wt% GF at 40% plaque length 50% plaque width (top) 90% plaque width (bottom) for (■) high viscosity and (●) low viscosity PP samples.

Away from the center plane the GF in both the LV and HV samples become very flow aligned, displaying the same response to the change in flow field [29]. At 50% of plaque width, both the HV and LV samples are already flow aligned. The HV samples have a slightly higher degree of alignment through the center of the part than the LV samples. At 90% of plaque width, the samples have almost identical orientation distributions with the HV having a slightly higher degree of alignment. In general, the HV samples have a slightly higher degree of flow alignment than the LV samples at 50 wt% GF, but other than at 0% plaque length the differences are small. This indicates that fiber-fiber interaction at 50 wt% is a stronger contributor to the resulting orientation than the difference in matrix viscosity.

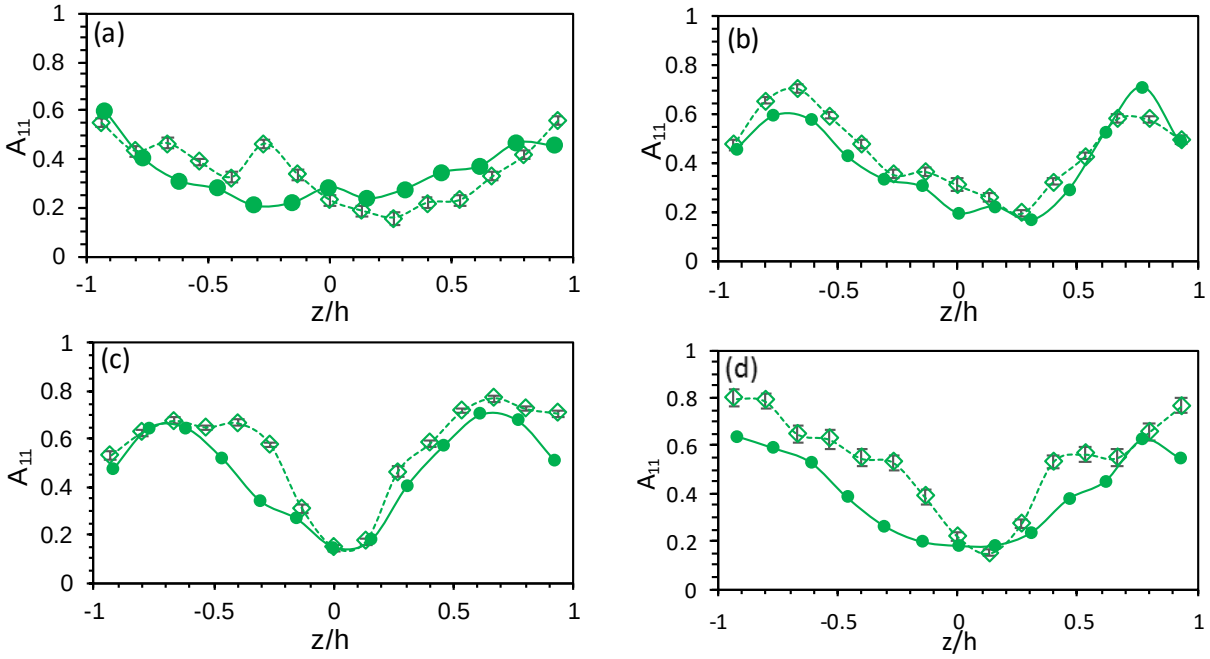

Figure 3-8: A_{11} component of the orientation tensor as a function of part thichness for 50 wt% (●) and 30 wt% (◊) GF PP low viscosity samples along the center plane at (a) 0 %, (b) 10%, (c) 40%, and (d) 90% plaque length.

The effect of concentration on orientation was examined to test if the differences in the HV and LV material would be larger at 30 wt% GF, where there are less fiber- fiber interactions than 50 wt% GF. A comparison between the orientation along the center plane for the 50 wt% GF LV and 30 wt% GF LV is shown in Figure 3-8. Overall, the 30 wt% GF material achieves a higher degree of alignment because of less fiber-fiber interaction. In the gate-mold interface, the 30 wt% GF samples have a more random orientation. At 10 % plaque length, the 30 wt% GF samples have a higher degree of flow alignment. A narrow core with a higher degree of orientation in the shell is achieved in the 30 wt% GF samples at 40% L. At 90% of plaque length, the 30 wt% GF samples have a more distinct shell-core-shell profile. The 50 wt% GF samples have a very broad core indicative of the start of the advancing front. This suggests that the advancing front profile starts earlier in the 50 wt% GF material.

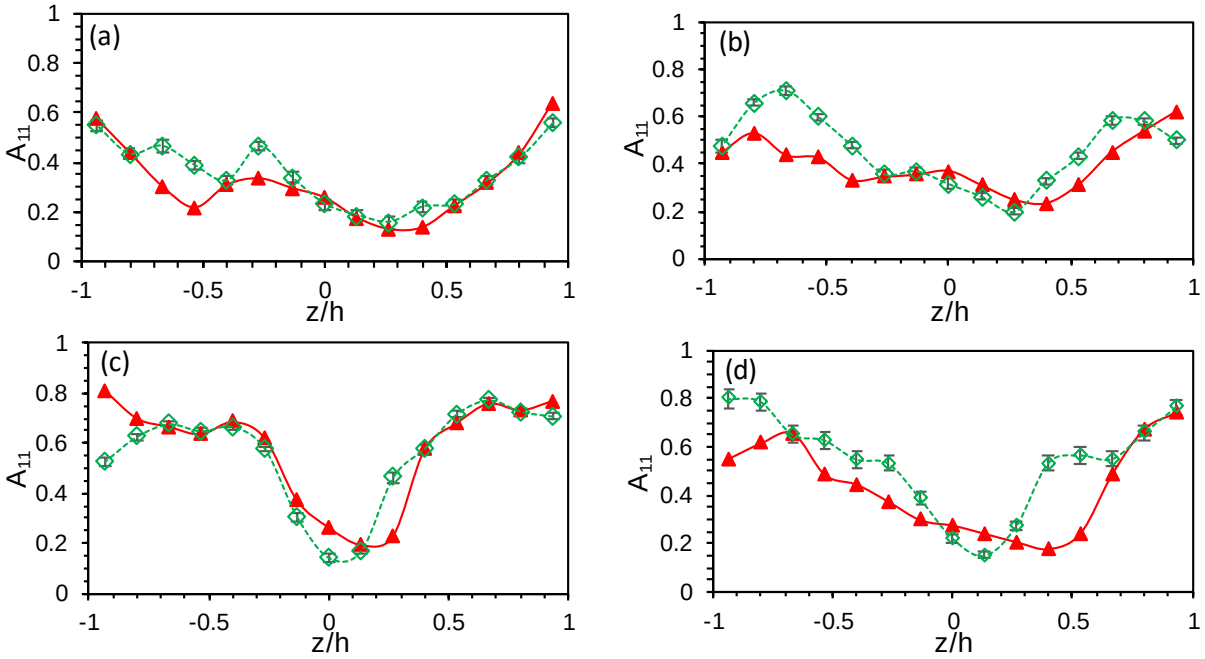

Figure 3-9: A_{11} component of the orientation tensor as a function of part thickness along the center-plane for 30 wt % GF (■) high viscosity and (◊) low viscosity PP samples at (a) 0 %, (b) 10%, (c) 40%, and (d) 90% plaque length.

The HV material has an asymmetric orientation compared to the LV samples at all the locations analyzed in the 30 wt % GF samples, shown in Figure 3-9, with the center of the core region being at a z/h of 0.266 for the HV samples. The asymmetry is likely from the turn from the gate and carries through the part. At 10% plaque length, the LV samples have the start of a shell-core-shell profile while the HV samples have a more random orientation. At 40% plaque length, both samples achieve similar degrees of orientation with the HV orientation being more asymmetric. In addition, there is no skin layer in the HV samples, indicating that high shear at the walls aligned the fibers before the polymer solidified. At 90% plaque length the LV samples still have a distinct shell core profile. The HV samples have a broader core, more of an advancing front orientation profile, indicating that transition areas are larger in the HV material. This can also be observed in the 50 wt% GF material near the front of the plaque, shown in Figure 3-11, where parabolic banding is observable further away from the front of the part than in the LV material. Looking away from the center plane at 40 % plaque length and 50 % plaque width in Figure 3-10 the HV material has more of a shell-core-shell profile demonstrating the larger transition zones in the HV

material. At 40% plaque length 90 % plaque width, the HV and LV samples have the same orientation profile.

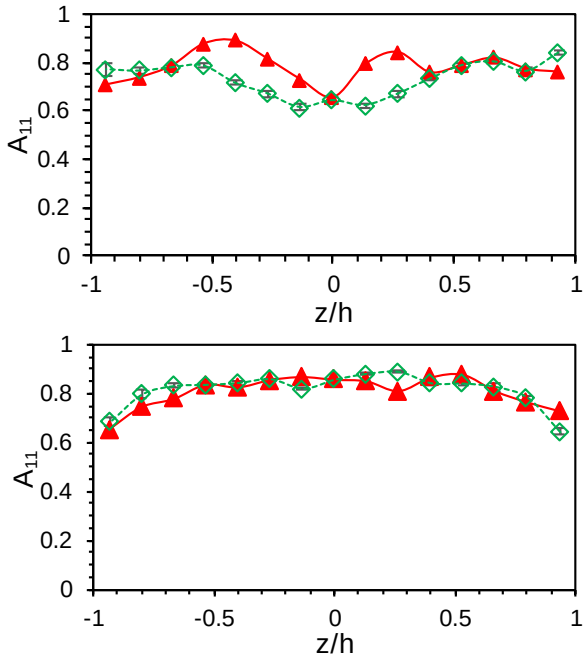

Figure 3-10: A_{11} component of the orientation tensor for 30 wt% GF (▲) high viscosity and (◊) low viscosity PP samples at 40% plaque length at 50% plaque width (top) and 90% plaque width (bottom).

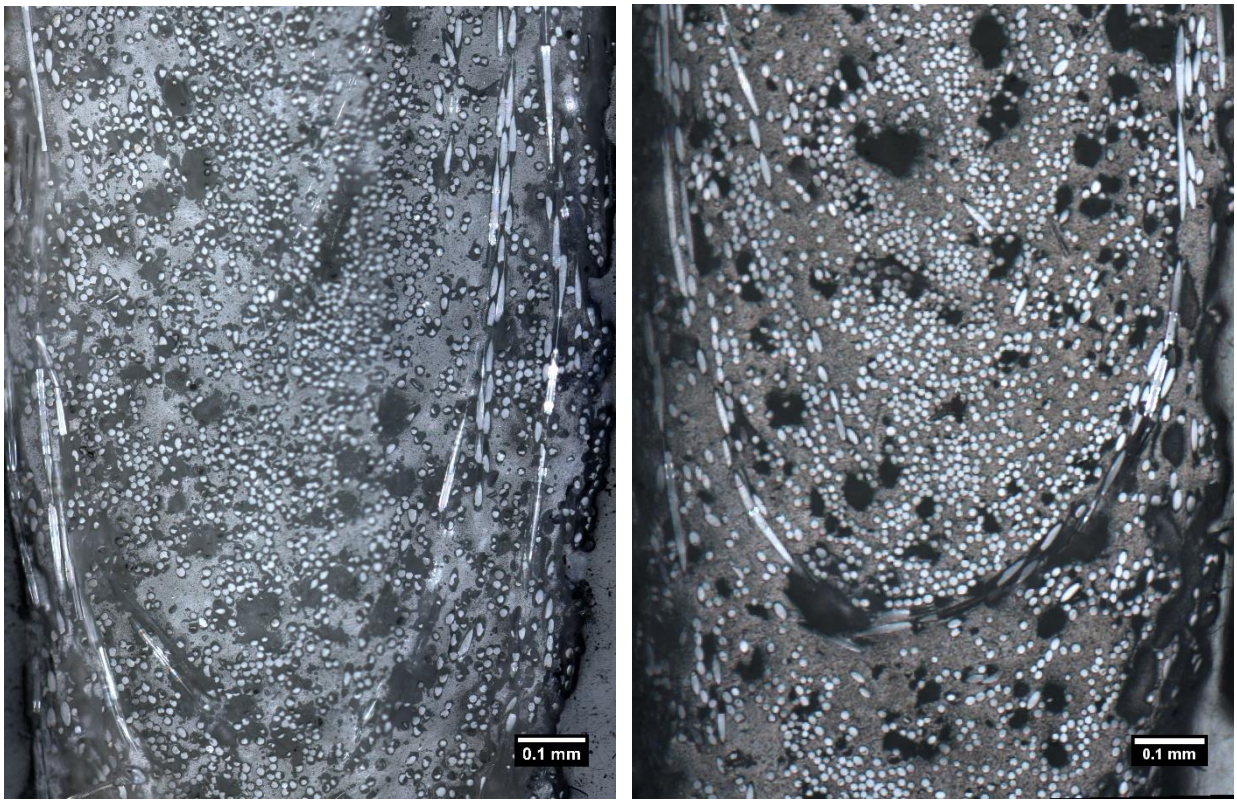

Figure 3-11: Optical images of Y-Z plane at 95% of plaque length along the center plane for 50 wt% GF low viscosity (left) and high viscosity (right) PP samples.

3.5 Conclusions

Matrix viscosity effects on the orientation profile of injection molded long glass fiber PP composites were explored. It was shown that matrix viscosity had a small effect on the orientation of long glass fiber composites at 30 wt% GF. At 30 wt% GF along the center-plane of the end-gated plaque the HV samples had a more asymmetric orientation profile than the LV samples, likely caused by fiber clustering at the gate mold interface. At 90% of plaque length along the center plane, the HV samples orientation exhibit a much broader core region with less flow alignment than the LV samples indicating that changes in flow effect larger areas of the HV samples.

Going from 30 wt% to 50 wt% GF caused a lower degree of flow alignment and a broader core in all the samples tested, matching with what had previously been observed in literature for short fibers [22, 23]. It also decreased the effect of different viscosity matrixes indicating that at high loadings fiber-fiber interactions dominate the orientation kinetics. At 50 wt% GF, the largest differences between the HV and

LV material occurred in the turn from the gate. Here fiber clustering caused a non shell-core-shell orientation profile in the HV samples versus a more traditional profile in the LV samples. This difference signifies that if the mold geometry has any rapid geometry changes, matrix viscosity can have a larger effect at high fiber loadings. In the future, these experimental results will be used to test existing fiber orientation models to assess how well differences in orientation due to matrix viscosity can be captured by current techniques.

3.6 References

1. Truckenmüller, F. and H.G. Fritz, *Injection molding of long fiber-reinforced thermoplastics: A comparison of extruded and pultruded materials with direct addition of roving strands.* Polymer Engineering & Science, 1991. **31**(18): p. 1316-1329.
2. Silverman, E.M., *Effect of glass fiber length on the creep and impact resistance of reinforced thermoplastics.* Journal of Polymer Composites, 1987. **8**(1): p. 8-15.
3. Thomason, J., *The influence of fibre length and concentration on the properties of glass fibre reinforced polypropylene: 5. Injection moulded long and short fibre PP.* Composites Part A: Applied Science and Manufacturing, 2002. **33**(12): p. 1641-1652.
4. Thomason, J.L., et al., *Influence of fibre length and concentration on the properties of glass fibre-reinforced polypropylene: Part 3. Strength and strain at failure.* Composites Part A: Applied Science and Manufacturing, 1996. **27**(11): p. 1075-1084.
5. Thomason, J.L. and W.M. Groenewoud, *The influence of fibre length and concentration on the properties of glass fibre reinforced polypropylene: 2. Thermal properties.* Composites Part A: Applied Science and Manufacturing, 1996. **27**(7): p. 555-565.
6. Thomason, J.L. and M.A. Vlug, *Influence of fibre length and concentration on the properties of glass fibre-reinforced polypropylene: 4. Impact properties.* Composites Part A: Applied Science and Manufacturing, 1997. **28**(3): p. 277-288.
7. Thomason, J.L. and M.A. Vlug, *Influence of fibre length and concentration on the properties of glass fibre-reinforced polypropylene: 1. Tensile and flexural modulus.* Composites Part A: Applied Science and Manufacturing, 1996. **27**(6): p. 477-484.
8. Switzer, L.H. and D.J. Klingenberg, *Rheology of sheared flexible fiber suspensions via fiber-level simulations.* Journal of Rheology (1978-present), 2003. **47**(3): p. 759-778.
9. Bay, R.S. and C.L. Tucker, *Stereological measurement and error estimates for three-dimensional fiber orientation.* Polymer Engineering & Science, 1992. **32**(4): p. 240-253.
10. Toll, S., *Packing mechanics of fiber reinforcements.* Polymer Engineering & Science, 1998. **38**(8): p. 1337-1350.
11. Férec, J., et al., *Modeling fiber interactions in semiconcentrated fiber suspensions.* Journal of Rheology, 2009. **53**(1): p. 49-72.
12. Nguyen, B.N., et al., *Fiber Length and Orientation in Long-Fiber Injection-Molded Thermoplastics — Part I: Modeling of Microstructure and Elastic Properties.* Journal of Composite Materials, 2008. **42**(10): p. 1003-1029.
13. Konicek, T.S., *A Method to Determine Three Dimensional Fiber Orientation in Fiber Reinforce Polymers*. 1987, University of Illinois at Urbana- Champaign.
14. Bright, P., R. Crowson, and M. Folkes, *A study of the effect of injection speed on fibre orientation in simple mouldings of short glass fibre-filled polypropylene.* Journal of Materials Science, 1978. **13**(11): p. 2497-2506.
15. Darlington, M.W. and P.L. McGinley, *Fibre orientation distribution in short fibre reinforced plastics.* Journal of Materials Science, 1975. **10**(5): p. 906-910.
16. Malzahn, J.C. and J.M. Schultz, *Transverse core fiber alignment in short-fiber injection-molding.* Composites Science and Technology, 1986. **25**(3): p. 187-192.
17. Bay, R.S. and C.L. Tucker, *Fiber orientation in simple injection moldings. Part II: Experimental results.* Polymer Composites, 1992. **13**(4): p. 332-341.
18. Folkes, M.J. and D.A.M. Russell, *Orientation effects during the flow of short-fibre reinforced thermoplastics.* Polymer, 1980. **21**(11): p. 1252-1258.

19. Chang, S.-H., J.-R. Hwang, and J.-L. Doong, *Manufacturing Process Optimization of Short Glass Fiber Reinforced Polycarbonate Composites in Injection Molding.* Journal of Reinforced Plastics and Composites, 2000. **19**(4): p. 301-321.
20. Vincent, M. and J. Agassant, *Experimental study and calculations of short glass fiber orientation in a center gated molded disc.* Polymer composites, 1986. **7**(2): p. 76-83.
21. Kunc, V., et al. *Fiber Length Distribution Measurement for long Glass and Varbon Fiber Reinforced Injection Molded Thermoplastics*. in *SPE Automotive*. 2007. Troy, MI.
22. Murty, K.N. and G.F. Modlen, *Experimental characterization of the alignment of short fibers during flow.* Polymer Engineering & Science, 1977. **17**(12): p. 848-853.
23. Kim, E., J. Park, and S. Jo, *A study on fiber orientation during the injection molding of fiber-reinforced polymeric composites:(Comparison between image processing results and numerical simulation).* Journal of Materials Processing Technology, 2001. **111**(1): p. 225-232.
24. Sousa, R.A., et al., *Integrated compounding and injection moulding of short fibre reinforced composites.* Plastics, Rubber & Composites, 2004. **33**(6): p. 249-259.
25. Lafranche, E., et al., *Injection moulding of long glass fibre reinforced polyamide 6-6: guidelines to improve flexural properties.* Express Polym Lett, 2007. **1**(7): p. 456-466.
26. Hofmann, J.T., et al., *Application and evaluation of the method of ellipses for measuring the orientation of long, semi-flexible fibers.* Polymer Composites, 2013. **34**(3): p. 390-398.
27. Cieslinski, M.J., P. Wapperom, and D.G. Baird, *Influence of fiber concentration on the startup of shear flow behavior of long fiber suspensions.* Journal of Non-Newtonian Fluid Mechanics, 2015. **222**(0): p. 163-170.
28. Hofmann, J.T., *Extension of the Method of Ellipses to Determining the Orientation of Long, Semi-flexible Fibers in Model 2- and 3- dimensional Geometries*, in *Macromolecular Science and Engineering*. 2013, Virginia Polytechnic Institute and State University.
29. Meyer, K.J., J.T. Hofmann, and D.G. Baird, *Prediction of Short Glass Fiber Orientation in the Filling of an End-Gated Plaque.* Composites Part A: Applied Science and Manufacturing, 2014.
30. Vélez-García, G.M., et al., *Sample preparation and image acquisition using optical-reflective microscopy in the measurement of fiber orientation in thermoplastic composites.* Journal of Microscopy, 2012. **248**(1): p. 23-33.
31. Vélez-García, G.M., et al., *Unambiguous orientation in short fiber composites over small sampling area in a center-gated disk.* Composites Part A: Applied Science and Manufacturing, 2012. **43**(1): p. 104-113.
32. Gupta, V.B., et al., *Some studies on glass fiber-reinforced polypropylene. Part I: Reduction in fiber length during processing.* Polymer Composites, 1989. **10**(1): p. 8-15.
33. Phelps, J.H., et al., *A model for fiber length attrition in injection-molded long-fiber composites.* Composites Part A: Applied Science and Manufacturing, 2013. **51**(0): p. 11-21.
34. Mazahir, S.M., et al., *Fiber orientation in the frontal region of a center-gated disk: Experiments and simulation.* Journal of Non-Newtonian Fluid Mechanics, 2015. **216**(0): p. 31-44.

4 Effect of Fiber Length Distribution on the Orientation of Injection Molded Long Carbon and Long Glass Fiber Polypropylene Composites

4.1 Abstract

Fiber length and orientation for 30 vol% long glass fiber (GF) and long carbon fiber (CF) polypropylene composites within an injection molded end-gated plaque were measured. The effects of backpressure and screw speed on long glass fiber composites were explored to obtain GF samples with a similar number average aspect ratio to the CF samples. Increasing screw speed and backpressure was found to decrease fiber length. At all conditions tested, lower screw speeds corresponded to a narrower fiber length distribution. The orientation of glass fiber in an end-gated injection molded plaque at 1, 5, and 10 bar backpressure at a screw speed of 200 rpm was compared to the orientation of CF samples molded at a backpressure of 1 bar and screw speed of 200 rpm. The GF and CF samples with comparable number average aspect ratios did not have similar orientations. Samples with comparable weight average aspect ratios were found to have similar orientations, suggesting that the longer fibers in the samples dominate the fiber orientation process, highlighting the need to examine the entire fiber length distribution.

4.2 Background and Motivation

The desire for lightweight alternatives to traditional metal parts has led to fiber reinforced composites being used in the automotive and aerospace industries. Composites exhibit increased impact toughness, strength, stiffness and dimensional stability compared to pure polymers [1, 2]. In recent years, there has been a push to move to discontinuous long fiber composites, which exhibit an increase in tensile strength [3] and impact toughness [1] compared to their short fiber counterparts, yet can still be injection molded.

Discontinuous long fibers are normally defined as containing fibers longer than 1 mm and are produced through a pultrusion process. The additional length grants the fibers the ability to bend during processing. This ability to bend can be estimated from a flexibility parameter, S^{eff}, which is an effective stiffness developed by Switzer and Klingenberg [4] and defined in Eq. 4-1. *E* is the Young's modulus of the fiber, η_m is the viscosity of the matrix, $\dot{\gamma}$ is the shear rate, and a_r is the aspect ratio of the fiber,

traditionally the number average aspect ratio (a_{rn}) for a distribution of fibers is used [5]. Experimentally significant bending has been observed in injection molded parts above an aspect ratio of 100 [6].

$$S^{eff} = \frac{E\pi}{64\eta_m \dot{\gamma} a_r^4} \tag{4-1}$$

Increasing fiber length also increases the number of fiber-fiber contacts in a part [7]. Toll [5] estimated the number of lubricated fiber contacts, N_c, using the volume fraction of the fibers, Φ, number average aspect ratio of the fibers and scalar invariants of the fiber orientation distribution. The result for a 3D random orientation of slender fibers is shown in Eq. 4-2. The ability to bend along with the increased number of fiber interactions changes the way that long fibers orient in the injection molding process and a thorough understanding of these differences would help the optimization of mold design.

$$N_c = \frac{2\Phi a_r}{1 + \frac{\pi}{2}\Phi} \tag{4-2}$$

While most research has previously been focused on short fiber composites [8-29], there have been several studies examining long fiber orientation [30-33]. Most locations within an injection molded composites part exhibit a shell-core-shell orientation profile [8], where fibers have a high degree of flow alignment near the mold walls (shell) and are aligned transverse to the flow in the center of the part (core). Toll and Anderson [30] and Hine [31] compared short and long glass fiber and found that long fiber composites exhibited a broader core region and less orientation at the mold walls.

Carbon Fiber (CF) offers decreased weight and increased mechanical properties performance compared to glass fiber (GF) composites [34]. As CF's price has decreased, its use in thermoplastic composites has increased. Few studies have been performed examining how the orientation of CF in the injection molding process differs from GF. Fu et al. [21] studied fiber length and tensile properties in 8, 16, and 25 wt% short CF and GF polypropylene (PP) composites. They found that the CF parts outperformed the GF parts in terms of tensile strength, elongation at break, and Young's modulus, but

had increased fiber breakage with the weight average length (L_w) for the GF being 650 µm and 270 µm for the CF. They did not examine orientation in the parts. The increase in fiber breakage was attributed to CF being more brittle than GF. One of the major differences between CF and GF used was fiber diameter. Typically commercial GF composites have a 14 µm diameter while CF a has 7 µm diameter. Therefore, an equivalent length CF will be more flexible and have more fiber-fiber interactions. For a true comparison of how the fibers orient equivalent aspect ratio fibers need to be used. Thomason [35] performed a study on the effect of GF diameter and concentration in polyamide 6-6. He found that as fiber diameter decreased so did fiber length, but the modulus of the final parts was not affected by fiber diameter. No clear trend in orientation based on fiber diameter was observed.

The goal of this paper is to determine if L_n and a_{rn} are indicative of how different fiber length distributions (FLD) of semi-flexible composites orient in injection molding. In order to accomplish this, 30 vol% long glass fiber and long carbon fiber PP composites were injection molded into an end-gated plaque. Because of the differences in CF and GF, vol % was chosen as a way of obtaining equivalent amounts of fiber-fiber interactions. Fiber length for the injection molded samples was obtained. The injection molding conditions for the GF samples were adjusted to obtain samples with an equivalent length and samples with an equivalent aspect ratio to the CF. The orientation of the CF samples and GF samples with 3 different fiber lengths was examined to determine if the differences in orientation in the GF and CF were controlled by fiber aspect ratio.

4.3 Materials and Methodology

4.3.1 Materials

Sabic PP Verton long GF PP with a GF loading of 30 vol% (50 wt%) GF was used. The composite was produced using a pultrusion process with an initial pellet length of 13 mm, and a GF diameter of 14 µm. Plasticomp Complete PP CF (1014 NAT) material was used as the CF composite. To form 30 vol% CF

material, 40 and 50 wt% CF pultruded material with an initial pellet length of 13 mm and a CF diameter of 7 µm were mixed in the injection molder to give 44.5 wt% CF in the final material.

4.3.2 Methods

4.3.2.1 Injection molding

Samples were injection molded using an Arburg Allrounder 221-55-250 with an 18 mm screw and fill time of 2 seconds. Screw speed and backpressure were adjusted to change the GF aspect ratio in the resulting parts. These variables were chosen because they do not affect the crystallization, or shear rates experienced in the injection molding process directly in the way injection speed or barrel temperature can. However, they have been shown to affect fiber length [20, 36]. The temperature profile of the injection molding machine was set to 190/210/220/220°C in the feed, compression, metering zones and nozzle, respectively, while the mold temperature was held at 80°C . Short shots filling 90% of the mold were used to mitigate packing and frontal wall effects.

End-gated plaques were produced with a length of 65 mm, an initial radius of 1.45 mm, and a final radius of 1.75 mm. The parts consisted of a gate and a plaque region. The gate region was 80.68 mm X 6.25 mm X 6.33 mm and the plaque section was 75.05 mm X 77.65 mm X 1.55 mm. To ensure that the injection molding machine was operating at equilibrium, the first 10 plaques from each run were discarded.

4.3.2.2 Fiber Length

The epoxy method developed by Kunc et al. [37] was used to obtain fiber length distributions (FLD) from the injection molded parts. A 26 mm X 26 mm section was cut from the center of an injection molded plaque, constrained by aluminum foil, and placed in an oven at 450 °C, burning off the polymer and leaving behind the fibers. Due to the fact that CF degrades around 500 °C care was taken to minimize the time the CF spent at elevated temperature, limiting each burn off to 25 min. A cylinder of epoxy was injected

into the burnt off sample and allowed to dry. Then the epoxy plug was pulled out of the burnt off fibers minimizing sampling bias. The epoxy plug of fibers was then burnt off a second time. After the second burn off the CF can become very brittle, therefore they were placed into a petri dish with a glycol solution that supports the fibers to prevent additional breakage. Next, the fiber solution was sonicated to disperse the fibers. The resulting fibers were imaged with a flatbed scanner (Epson V800) at a resolution of 6000 dpi. A minimum of 2000 fiber lengths from each sample and two samples at each condition were manually measured.

FLD is often represented by an average length value. There are two averages commonly used and care needs to be taken to distinguish between them. L_n was calculated by Eq. 4-3 and the L_w was calculated by Eq. 4-4, where N_i is the number of fibers of length l_i. The L_w is biased towards the longer fibers and is larger than L_n for all cases except when all fibers are the same length. The dispersity index (P) of the fiber lengths, given in Eq. 4-5, is analogous to the polydispersity index for polymer molecular weight and characterizes the breadth of the FLD. Aspect ratio is used to compare different diameter fibers. a_{rn} is the ratio of L_n the diameter of the fiber and weight average aspect ratio (a_{rw}) is the ratio of L_w to the diameter of the fibers.

$$L_n = \frac{\sum N_i l_i}{\sum N_i} \tag{4-3}$$

$$L_w = \frac{\sum N_i l_i^2}{\sum N_i l_i} \tag{4-4}$$

$$P = L_w / L_n \tag{4-5}$$

4.3.2.3 Orientation Measurements

Fiber orientation was examined at 0, 10, 40, and 90 % of the part length along the center-plane as shown in Figure 3-1. Along the center-plane of an end-gated plaque, the flow is symmetric and the resulting orientation closely resembles that of a center-gated disk, but away from the center-plane there

is a different flow field and fibers have been reported to attain a greater degree of flow alignment [31, 38]. To obtain a full picture of how the fibers are orienting additional samples were taken at 40 % of part length at 50 % and 90% of plaque width, shown in Figure 4-1. Samples were marked, cut with a low speed diamond saw, polished using metallographic methods, and plasma etched in the x-z plane following the procedure developed by Velez- Garcia et al. [39]. Hofmann et al. [40] found that due to fiber clustering, highly elongated ellipses and curvature, more fibers need to be examined to obtain accurate orientation averages using the method of ellipses (MOE) for long fibers and therefore a relatively large image area was used. Optical microscopy (Nikon Eclipse LV100) at a resolution of 0.25 µm per pixel was then utilized to image a 2 mm x 2 mm area.

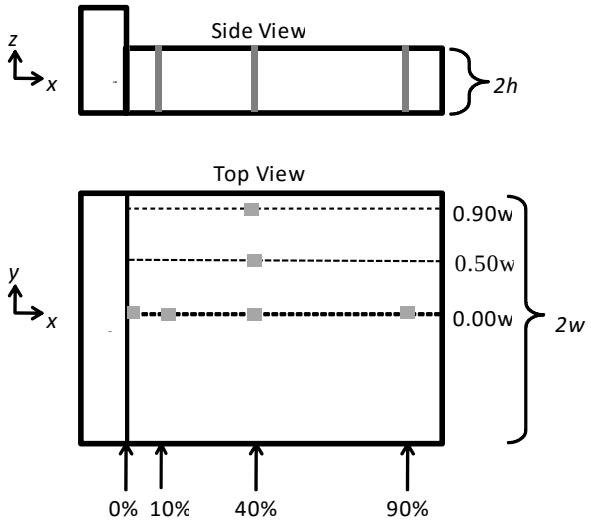

Figure 4-1: Experimental geometry and the selected inspection locations for the end-gated plaque. Grey squares represent the inspection locations.

The resulting images were analyzed using the MOE and a custom Matlab program. The fibers in the polished samples appear as ellipses. The size of the major and minor axis and orientation of the ellipses can be used to calculate the second order orientation tensor, **A** [6]. The MOE can be ambiguous, where a single ellipse can represent two different orientations rotated 180°. In order to overcome this, the

shadows of the ellipse created during the plasma etching process were used to indicate which direction the fiber was pointing [41]. The Bay and Tucker weighting function was used to account for the observational bias involved in cutting and imaging the sample [6]. A minimum of three samples from different plaques were analyzed at each location.

4.3.2.4 Rheology

The pure matrix for each composite type was characterized using a rotational (Rheometrics RMS-800) and a capillary rheometer (Gottfert Rheograph 2001). 50 mm cone and plate fixtures were used in the rotational rheometer, and samples were tested at 180 °C, 220 °C, and 240 °C. Steady shear data was taken from a shear rate of 0.01 s^{-1} to 0.5 s^{-1} and oscillatory data at a strain of 2% was taken from 0.1 rad/s to 100 rad/s. Capillary data was taken using a 10 mm long with a 0.5 mm diameter and a 15mm long with a 0.5 mm diameter dies at 220 °C. Bagley corrections were applied to account for entry and exit effects. Time-temperature superposition was used to shift all data to 220 °C. The data was combined to form master curves.

4.4 Results and Discussion

4.4.1 Rheology

The rheology of the pure matrix used in these samples was tested to ensure that orientation differences in the composites were caused by fiber differences and not in the polymer used. The master curves created from a combination of dynamic, steady shear, and capillary rheology for both the Plasticomp and Sabic PP used, shifted to 220 °C, are shown in Figure 4-2. The results indicate a similar viscous behavior between the two matrixes. The Sabic PP has a zero shear viscosity of 700 Pa s and the Plasticomp PP has a zero shear of 550 Pa s. The Sabic PP shear thins faster than the Plasticomp PP, so that in the shear rate range experienced in the injection molding process of 10-1000 s^{-1} their viscosities are almost identical. This means that any major differences between the CF and GF orientation should not be

affected by the PP rheology. There could be a difference in the sizing and compatibilizers used on the fiber, but that data is not disclosed by the manufacturer.

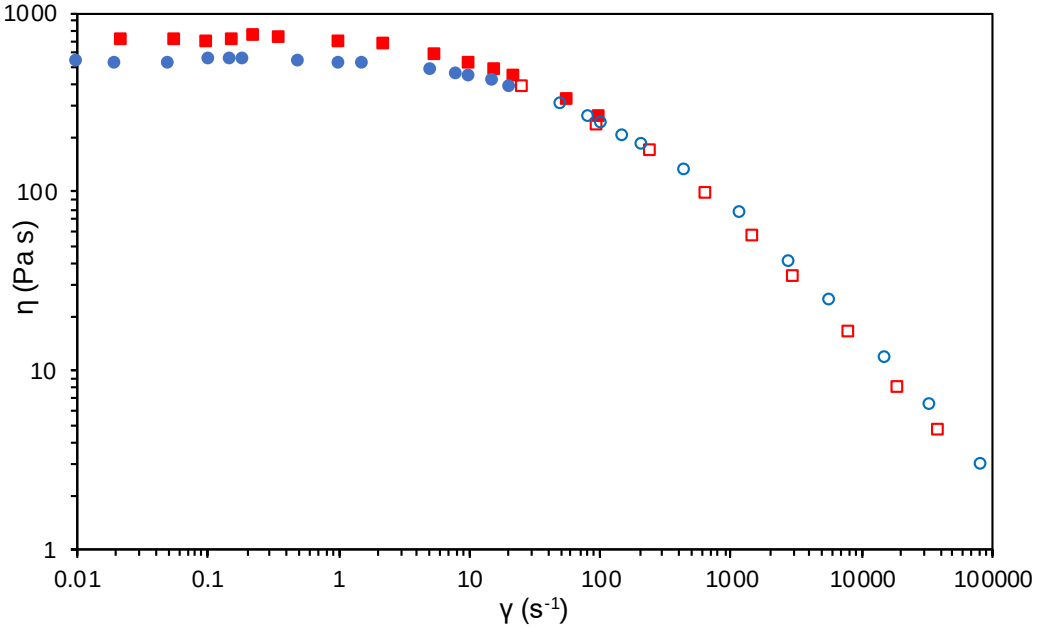

Figure 4-2: Rheology of Sabic (■) and Plasticomp (●) polypropylene. Filled points are oscillatory and steady shear data. Unfilled points are capillary data.

4.4.2 Fiber Length

In order to obtain equivalent fiber aspect ratios between CF and GF, several injection molding conditions for the GF samples were tested. The resulting fiber lengths from the injection molding conditions tried are summarized in Table 4.1. Although orientation was not examined for all conditions, a thorough understanding of how screw speed and backpressure affect long glass fiber length is useful in order to optimize the injection molding process.

Table 4.1: Summary of fiber lengths after injection molding

Fiber Type	Back Pressure (bar)	Screw Speed (RPM)	Number Average Length (mm)	Weight Average Length (mm)	Number Average Aspect Ratio	Weight Average Aspect Ratio	Dispersity Index
CF	1	200	0.36 ± 0.01	1.71 ± 0.05	51.1	244	4.75
GF	1	50	0.81 ± 0.10	1.35 ± 0.22	58.1	96	1.66
GF	1	200	0.99 ± 0.03	3.22 ± 0.08	70.4	230	3.25
GF	5	50	1.03 ± 0.15	1.79 ± 0.17	73.8	128	1.74
GF	5	200	0.77 ± 0.11	1.66 ± 0.31	55.0	119	2.16
GF	10	50	0.74 ± 0.05	1.21 ± 0.02	53.7	86	1.63
GF	10	200	0.40 ± 0.02	0.74 ± 0.04	28.8	53	1.84
GF	12.5	200	0.35 ± 0.01	0.63 ± 0.1	24.9	45	1.81

All samples tested were originally 13 mm pultruded pellets and experienced severe breakage in the screw of the injection molder. The initial conditions used, 1 bar and 200 rpm, were chosen as they match conditions previously used within our lab to make composites, making the resulting orientation comparable to previous results. A backpressure of 1, 5, 10, and 12.5 bar was used with screw speeds of 50 and 200 rpm. The samples generated at 50 rpm and 12.5 bar are not listed because the screw froze in the machine. The CF breaks down to a much larger extent than GF under the same processing conditions, and the GF L_n is approximately three times longer. Part of this breakage is due to the fact CF tested has a 7 µm diameter and the GF 14 µm diameter. However, when examining A_{rn}, the CF breaks down further than the GF, 51 versus 70, agreeing with previous results for short fiber [21].

Increasing screw speed and backpressure increased the amount of fiber breakage that occurred in the GF samples. Backpressure had a large effect on fiber length decreasing L_n from 0.99 mm at 1 bar to 0.4 mm at 12.5 bar. It is interesting to note that decreasing screw rpm decreased the dispersity in the

fiber length for all samples tested. This is likely a factor of screw design as a small diameter standard metering screw was used. The largest dispersity difference was in the samples produced at 1bar with the dispersity going from 3.25 to 1.66 when screw rpm was decreased from 200 to 50. The more pronounced effect at lower backpressures is likely due to longer fibers and a less densely packed screw. It takes more time and rotations of the screw to achieve higher backpressure, increasing the strain applied to the samples before injection. Higher backpressure provides better dispersion of the fibers but causes more breakage [25].

The fiber orientation was examined for four conditions and their FLDs are shown in Figure 4-3. The original injection molding condition for both the CF and glass fiber samples at 1 bar and 200 rpm was examined for a baseline. Because the orientation of fibers in a composite is predicted to be dependent on number average aspect ratio [30, 31], the orientation of the GF samples produced at 5 bar 200 rpm was examined. The 10 bar 50 rpm GF samples have a similar L_n to the 5 bar 200 rpm GF samples, but they have a shorter L_w. Because the CF samples have the highest dispersity of any of the samples tested, the GF samples with a higher dispersity were chosen. The orientation of samples produced at 10 bar 200 rpm were also tested to give an insight into GF samples that have a shorter aspect ratio but same length as the CF samples.

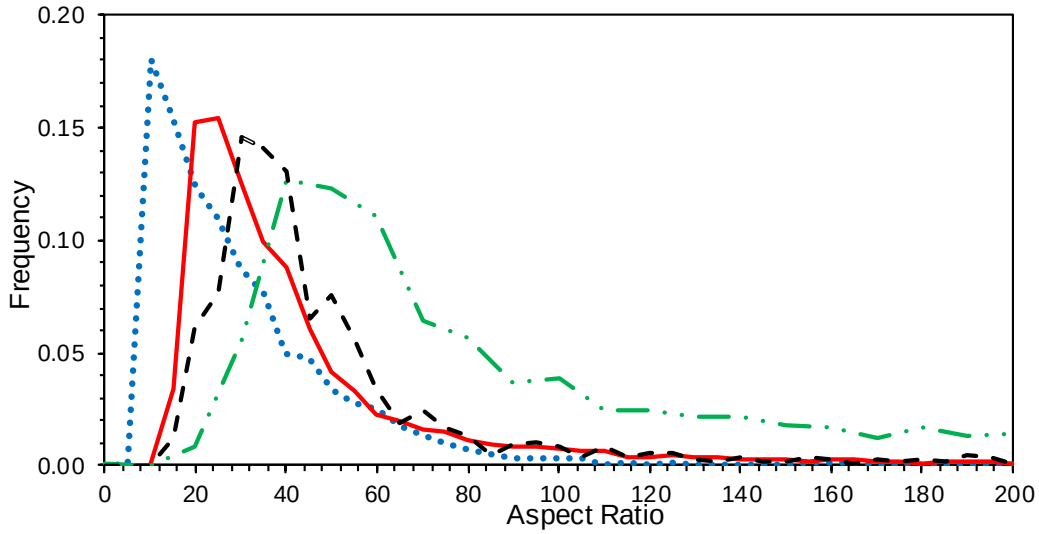

Figure 4-3: Fiber length distributions for (—) CF, (—•) GF 1 bar 200 rpm, (— —) GF 5 bar 200 rpm, and (•) GF 10 bar 200 rpm.

4.4.3 Fiber Orientation

The diagonal components of **A** at the center-plane and 40% of plaque length for the 30 vol% GF PP samples produced at 5 bar and 200 rpm are shown in Figure 4-4. Error bars shown for A_{11} are measurement errors calculated using the method developed by Bay et al. [6] and are representative of the data observed. Error bars are omitted from the comparison data in Figure 4-5 and Figure 4-6 for ease of reading but can be assumed to be equivalent to those shown in Figure 4-4. As is typical of simple injection molded composite parts, the through thickness component of the orientation tensor A_{33} was small, less than 0.1, and the transverse to flow direction component, A_{22}, was an almost mirror image of A_{11}. Therefore, the flow direction component of the orientation tensor, A_{11}, along the center-plane of plaque was used as a point of comparison for the examined samples, is shown in Figure 4-5.

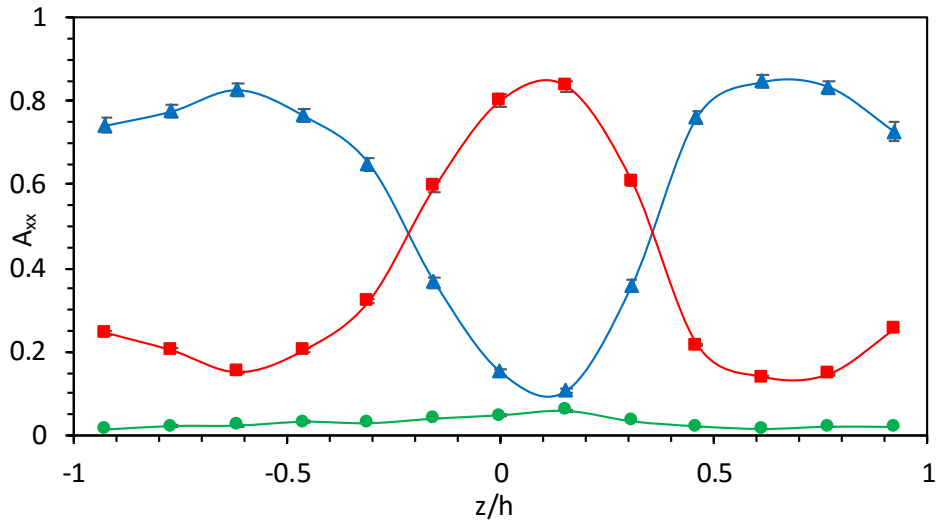

Figure 4-4: Diagonal components of the second orientation tensor, **A**, (▲ A_{11}, ■ A_{22}, ● A_{33}.) for 30 vol% GF PP injection molded at 5 bar along the center-plane at 40% of plaque length.

At most locations along the center-plane, the GF orientation follows the expected trend. The orientation of the 10 bar 200 rpm GF samples at 10, 40, and 90% of plaque length along the center-plane, shown in Figure 4-5, have a distinct shell-core-shell orientation profile, with a core region narrower than the other samples. Even at the gate mold interface, 0% of plaque length, the orientation profile has a shell-core-shell profile just broader and lacking a skin layer. This orientation closely matches what has previously been reported for short fiber composites and is expect from the 10 bar 200 rpm samples L_n of 0.35 mm [36]. At 10% and 40 % of plaque length the orientation of the 5 bar and 10 bar GF samples match closely, with a shell-core shell profile that is asymmetric. At 0% of plaque length the orientation of the GF samples produced at 5 bar is less aligned than the 10 bar GF samples' orientation with an asymmetric shape because of the turn from the gate. At 90% of the part length the shorter fiber length of the 10 bar GF means its orientation still has a shell-core-shell profile whereas the 5 bar samples' orientation has a very broad core that is caused by recirculating flow at the advancing front [42]. The fact that the orientation of the 10 bar samples does not exhibit this profile as distinctly means that the transition regions are not as large in shorter fiber samples likely because of less fiber-fiber interactions.

The GF samples processed at 1 bar and 200 rpm exhibit a long fiber orientation profile [33]. At 0% of plaque length, the orientation profile follows a traditional shell-core-shell profile near the mold walls, but in the center of the part of the plaque there is an increase in flow alignment. This was caused by fiber bundles in the turn from the gate that proved repeatable for multiple samples. At 10% and 40% of plaque width, the 1 bar samples' orientation has a broader core region with a lower degree of orientation throughout the part when compared to the orientation of 5 and 10 bar samples. At 90% of plaque length, the 1 bar samples' orientation falls between the 5 and 10 bar samples. The longer fibers in the 1 bar samples create a broader orientation profile than the 10 bar samples. Even though the L_n of the 5 bar samples falls in the middle the 1 bar and 10 bar samples L_n the 5 bar samples' orientation is a closer match to the 10 bar samples orientation at all locations other than 90% of plaque length. The 5 bar samples' L_w, however, is closer to the 10 bar samples' L_w than the 1 bar samples' L_w. Based on the orientation this indicates that the longer fibers have a larger effect on orientation, and it may be more important to compare samples based on weight average.

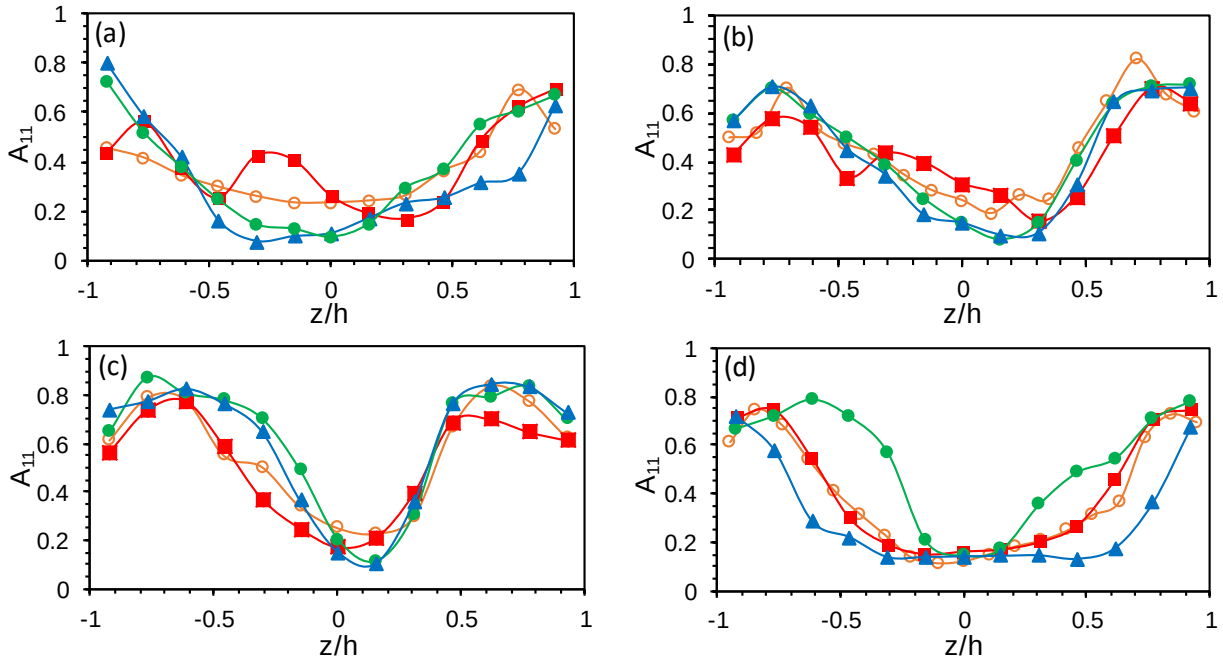

Figure 4-5: A_{11} component of the orientation tensor as a function of part thickness for 30 vol% GF and CF PP down the center-plane of an end-gated plaque at (a) 0%, (b) 10%, (c) 40 % and (d) 90% of plaque length for (■) 1 bar GF, (▲) 5 bar GF, (●) 10 bar GF, and (○) CF.

The CF samples did not follow the expected trend. Based on the a_{rn} the 5 bar GF and CF samples, 55 and 51 respectively, were expected to have similar orientations. However, this was not the case for any of the locations examined. The CF samples orientation did not match up perfectly with any of the samples tested, but behaved similar to the 1 bar samples' orientation especially at 90% of plaque length. The length data suggests that the wrong average was expected to be the point of comparison. The a_{rw} for the CF and 1 bar GF samples, 244 and 230 respectively, are much closer to each other than to the a_{rw} of the 5 bar, 119, or 10 bar, 53, samples. Indicating that for long fiber composites, the longer fibers have a disproportionate effect on orientation. These results suggest that weight average aspect ratio is a better measure of how the fibers will orient for samples with a large dispersity in fiber length. While the samples that had similar orientation also had similar backpressure, the backpressure by itself should have minimal effect on the part orientation. The largest effect on backpressure will be on dispersion and fiber length. These two factors have proven coupled for long fiber composites with fiber length decreasing as dispersion improves in a given system [1]. This means that the fiber length difference can stand as an indicator for the dispersion when all the material variables are held constant and is probably the cause of orientation differences.

At 0, 10, and 40 % of plaque length the CF samples have slightly less orientation in the core of the part and more orientation in the shell than the 1 bar GF samples. Due to the very broad FLD of the CF, this could be expected. Bailey and Kraft [43] and O'Regan and Akay [44] found that fiber lengths varied through the thickness of injection molded parts, with longer fibers in the core of the part and as much as a threefold difference in average length between the skin and core. Because of this difference, it would make sense that the shorter fibers would dominate the orientation in the shell. Therefore, the CF with a a_{rn} shorter than the 1 bar samples a_{rn} could be expected have a higher degree of orientation in the shell.

The slightly higher a_{rw} may be the cause of the degree of orientation in the core for the CF samples than the 1 bar GF samples.

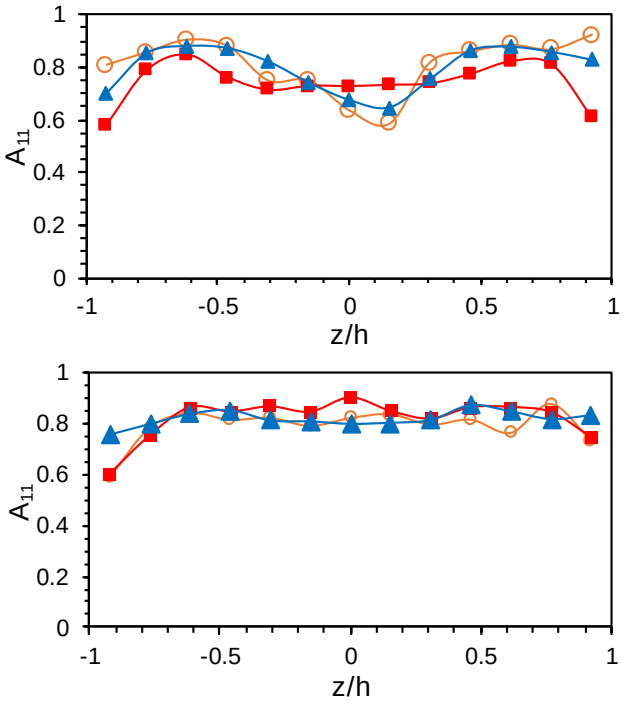

Figure 4-6: A_{11} component of the orientation tensor as a function of part thickness for 40% of part length at 50 % (top) and 90 % (bottom) of part width for (■) 1 bar GF,(▲) 5 bar GF, and (○) CF

The change in orientation across the plaque width at 40 % of plaque length is shown in Figure 4-6. Here the orientation of the 10 bar GF samples closely followed the 5 bar GF samples' orientation so it is not shown on the graphs for ease of reading the other three conditions. At both 50% and 90% of plaque width, the fibers are highly aligned transverse to flow. At 90 % of plaque width, the high shear near the walls creates negligible differences in orientation between the CF samples and the GF samples. At 50 % of plaque width, the orientation of all the samples are similar except in the core where the CF maintains a slight shell-core-shell profile. This is likely because of the longer fibers in the core of the samples orienting slowly creating larger transition zones.

4.5 Conclusions

L_n was a poor indication of how GF composites with different FLDs oriented, under the same injection molding conditions. The GF samples molded at 10 bar and 1 bar backpressure at 200 rpm had orientation profiles similar to what had previously been reported in literature for short and long fibers, respectively. The L_n for the GF samples molded at a 5 bar backpressure and 200 rpm was in the middle of the L_n for samples molded at 10 bar and 1 bar at 200 rpm. However, the samples molded at 5 bar had a fiber orientation that was a closer match to the 10 bar samples. The L_w for the 5 bar and 10 bar samples were closer than the L_w for the samples molded at 1 bar and 5 bar, suggesting that weight average is a better indicator of similarity in how a FLD will behave in injection molding. In order to verify this, future work will need to be performed in a wider variety of injection molding machines and composite systems.

Injection molded CF and GF composite samples with analogous a_{rn} did not have similar fiber orientations, due to the broad FLD of all samples. The GF samples injection molded at5 bar had an a_{rn} of 55 and the CF samples had an a_{rn} of 51, but the GF samples had an orientation with a narrower core and a higher degree of flow alignment near the walls. The GF samples injection molded at 1 bar had a similar orientation profile to the CF samples, indicating that a_{rw}, 230 versus 244 respectively, was a better point of comparison between different FLDs than a_{rn} .These results suggest that the longer fibers in a FLD dominate the orientation behavior, highlighting the importance of examining the entire FLD and not just using number averages.

4.6 References

1. Truckenmüller, F. and H.G. Fritz, *Injection molding of long fiber-reinforced thermoplastics: A comparison of extruded and pultruded materials with direct addition of roving strands.* Polymer Engineering & Science, 1991. **31**(18): p. 1316-1329.
2. Silverman, E.M., *Effect of glass fiber length on the creep and impact resistance of reinforced thermoplastics.* Journal of Polymer Composites, 1987. **8**(1): p. 8-15.
3. Thomason, J.L., et al., *Influence of fibre length and concentration on the properties of glass fibre-reinforced polypropylene: Part 3. Strength and strain at failure.* Composites Part A: Applied Science and Manufacturing, 1996. **27**(11): p. 1075-1084.
4. Switzer, L.H. and D.J. Klingenberg, *Rheology of sheared flexible fiber suspensions via fiber-level simulations.* Journal of Rheology (1978-present), 2003. **47**(3): p. 759-778.
5. Toll, S., *Packing mechanics of fiber reinforcements.* Polymer Engineering & Science, 1998. **38**(8): p. 1337-1350.
6. Bay, R.S. and C.L. Tucker, *Stereological measurement and error estimates for three-dimensional fiber orientation.* Polymer Engineering & Science, 1992. **32**(4): p. 240-253.
7. Férec, J., et al., *Modeling fiber interactions in semiconcentrated fiber suspensions.* Journal of Rheology, 2009. **53**(1): p. 49-72.
8. Darlington, M. and P. McGinley, *Fibre orientation distribution in short fibre reinforced plastics.* Journal of Materials Science, 1975. **10**(5): p. 906-910.
9. Murty, K.N. and G.F. Modlen, *Experimental characterization of the alignment of short fibers during flow.* Polymer Engineering & Science, 1977. **17**(12): p. 848-853.
10. Folgar, F. and C.L. Tucker, *Orientation Behavior of Fibers in Concentrated Suspensions.* Journal of Reinforced Plastics and Composites, 1984. **3**(2): p. 98-119.
11. Vincent, M. and J. Agassant, *Experimental study and calculations of short glass fiber orientation in a center gated molded disc.* Polymer composites, 1986. **7**(2): p. 76-83.
12. Malzahn, J.C. and J.M. Schultz, *Transverse core fiber alignment in short-fiber injection-molding.* Composites Science and Technology, 1986. **25**(3): p. 187-192.
13. Advani, S.G. and C.L. Tucker, *The Use of Tensors to Describe and Predict Fiber Orientation in Short Fiber Composites.* Journal of Rheology (1978-present), 1987. **31**(8): p. 751-784.
14. Fischer, G.E., P, *Measuring Spatial Orientation of Short Fiber Reinforced Thermoplastics by Image Analysis.* Polymer Composites, 1988. **9**(4): p. 297-304.
15. Ranganathan, S. and S.G. Advani, *Characterization of orientation clustering in short-fiber composites.* Journal of Polymer Science Part B: Polymer Physics, 1990. **28**(13): p. 2651-2672.
16. Gupta, M. and K. Wang, *Fiber orientation and mechanical properties of short-fiber-reinforced injection-molded composites: Simulated and experimental results.* Polymer Composites, 1993. **14**(5): p. 367-382.
17. Avérous, L., et al., *Granulometric Characterization of Short Fiberglass in Reinforced Polypropylene. Relation to Processing Conditions and Mechanical Properties.* International Journal of Polymer Analysis and Characterization, 1995. **1**(4): p. 339-347.
18. Chen, C.-H. and C.-H. Cheng, *Effective elastic moduli of misoriented short-fiber composites.* International Journal of Solids and Structures, 1996. **33**(17): p. 2519-2539.
19. Mlekusch, B., *Thermoelastic properties of short-fibre-reinforced thermoplastics.* Composites Science and Technology, 1999. **59**(6): p. 911-923.
20. Chang, S.-H., J.-R. Hwang, and J.-L. Doong, *Manufacturing Process Optimization of Short Glass Fiber Reinforced Polycarbonate Composites in Injection Molding.* Journal of Reinforced Plastics and Composites, 2000. **19**(4): p. 301-321.

21. Fu, S.Y., et al., *Tensile properties of short-glass-fiber- and short-carbon-fiber-reinforced polypropylene composites.* Composites Part A: Applied Science and Manufacturing, 2000. **31**(10): p. 1117-1125.
22. Eberhardt, C. and A. Clarke, *Fibre-orientation measurements in short-glass-fibre composites. Part I: automated, high-angular-resolution measurement by confocal microscopy.* Composites Science and Technology, 2001. **61**(10): p. 1389-1400.
23. Sepehr, M., G. Ausias, and P.J. Carreau, *Rheological properties of short fiber filled polypropylene in transient shear flow.* Journal of Non-Newtonian Fluid Mechanics, 2004. **123**(1): p. 19-32.
24. Hine, P.J. and R.A. Duckett, *Fiber orientation structures and mechanical properties of injection molded short glass fiber reinforced ribbed plates.* Polymer Composites, 2004. **25**(3): p. 237-254.
25. SadAbadi, H. and M. Ghasemi, *Effects of Some Injection Molding Process Parameters on Fiber Orientation Tensor of Short Glass Fiber Polystyrene Composites (SGF/PS).* Journal of Reinforced Plastics and Composites, 2007.
26. Eberle, A.P.R., et al., *Obtaining reliable transient rheological data on concentrated short fiber suspensions using a rotational rheometer.* Journal of Rheology (1978-present), 2009. **53**(5): p. 1049-1068.
27. Eberle, A.P.R., et al., *Fiber orientation kinetics of a concentrated short glass fiber suspension in startup of simple shear flow.* Journal of Non-Newtonian Fluid Mechanics, 2010. **165**(3–4): p. 110-119.
28. Velez-Garcia, G.M., *Experimental Evaluation and Simulations of Fiber Orientation in Injection Molding of Polymers Containing Short Glass Fibers*, in *Macromolecular Science and Engineering*. 2012, Virginia Polytechnic Institute and State University.
29. Meyer, K.J., J.T. Hofmann, and D.G. Baird, *Prediction of Short Glass Fiber Orientation in the Filling of an End-Gated Plaque.* Composites Part A: Applied Science and Manufacturing, 2014.
30. Toll, S. and P.O. Andersson, *Microstructure of long- and short-fiber reinforced injection molded polyamide.* Polymer Composites, 1993. **14**(2): p. 116-125.
31. Hine, P.J., et al., *Measuring the fibre orientation and modelling the elastic properties of injection-moulded long-glass-fibre-reinforced nylon.* Composites Science and Technology, 1995. **53**(2): p. 125-131.
32. Nguyen, B.N., et al., *Fiber Length and Orientation in Long-Fiber Injection-Molded Thermoplastics — Part I: Modeling of Microstructure and Elastic Properties.* Journal of Composite Materials, 2008. **42**(10): p. 1003-1029.
33. Nghiep Nguyen, B., et al., *Prediction of the Elastic—Plastic Stress/Strain Response for Injection-Molded Long-Fiber Thermoplastics.* Journal of Composite Materials, 2009. **43**(3): p. 217-246.
34. Park, S.-J. and SpringerLink, *Carbon Fibers*. Vol. 210. 2015, Dordrecht: Springer Netherlands.
35. Thomason, J.L., *The influence of fibre length, diameter and concentration on the modulus of glass fibre reinforced polyamide 6,6.* Composites Part A: Applied Science and Manufacturing, 2008. **39**(11): p. 1732-1738.
36. Bay, R.S. and C.L. Tucker, *Fiber orientation in simple injection moldings. Part II: Experimental results.* Polymer Composites, 1992. **13**(4): p. 332-341.
37. Kunc, V., et al. *Fiber Length Distribution Measurement for long Glass and Varbon Fiber Reinforced Injection Molded Thermoplastics*. in *SPE Automotive*. 2007. Troy, MI.
38. Hofmann, J.T., *Extension of the Method of Ellipses to Determining the Orientation of Long, Semi-flexible Fibers in Model 2- and 3- dimensional Geometries*, in *Macromolecular Science and Engineering*. 2013, Virginia Polytechnic Institute and State University.
39. Vélez-García, G.M., et al., *Sample preparation and image acquisition using optical-reflective microscopy in the measurement of fiber orientation in thermoplastic composites.* Journal of Microscopy, 2012. **248**(1): p. 23-33.

40. Hofmann, J.T., et al., *Application and evaluation of the method of ellipses for measuring the orientation of long, semi-flexible fibers.* Polymer Composites, 2013. **34**(3): p. 390-398.
41. Vélez-García, G.M., et al., *Unambiguous orientation in short fiber composites over small sampling area in a center-gated disk.* Composites Part A: Applied Science and Manufacturing, 2012. **43**(1): p. 104-113.
42. Mazahir, S.M., et al., *Fiber orientation in the frontal region of a center-gated disk: Experiments and simulation.* Journal of Non-Newtonian Fluid Mechanics, 2015. **216**(0): p. 31-44.
43. Bailey, R. and H. Kraft, *A Study of Fibre Attrition in the Processing of Long Fibre Reinforced Thermoplastics.* Int.Polym.Process, 1987. **2**(2): p. 94-101.
44. O'Regan, D. and M. Akay, *The distribution of fibre lengths in injection moulded polyamide composite components.* Journal of Materials Processing Tech, 1996. **56**(1): p. 282-291.

5 Injection Molded Carbon Nanotube/Long Carbon Fiber Multiscale Composites

5.1 Abstract

Polypropylene (PP)/ long carbon fiber (CF)/ carbon nanotube (CNT) multiscale composites using supercritical carbon dioxide ($scCO_2$) deaglomerated CNTs were processed via injection molding, yielding nanocomposites with enhanced Young's modulus and electrical properties compared to fiber composites. The effects of CF concentration, CNT concentration, and CNT bulk density were explored. Nanocyl NC7000 CNTs were benignly deagglomerated with $scCO_2$ resulting in 4.3 fold (4.3X), 10X, 30X, and 50X decrease in bulk density compared to the as-received CNTs. The treated CNTs were melt blended with pultruded long CF PP and injection molded to form end-gated plaques. The largest improvement in tensile properties due to the addition of CNTs was found to be for the 40 wt% CF with 1 wt% 10 fold expanded CNT samples. The resulting composites yielded a 56 % (5.2 GPa) improvement in Young's modulus in the transverse to the flow direction and a 17 % (3.2 GPa) improvement in Young's modulus in the flow direction, compared to samples without CNTs. The largest improvement in surface conductivity due to the addition of CNT was found to be 30 wt% CF 1 wt% 10X CNT going from $3.04\ x\ 10^{-5}\ S$ to $2.07\ x\ 10^{-4} S$. These results are comparable to improvements reported in literature, for epoxy-based composites using functionalized multi-walled CNT, highlighting the importance of CNT dispersion and maintaining CNT and CF length.

5.2 Background and Motivation

Fiber reinforced polymer composites (FRP) have been used in the automotive and aerospace industries because they exhibit increased impact toughness, strength, stiffness, strength to weight ratio and dimensional stability compared to their unfilled counterparts [1]. The high production costs for continuous fiber reinforced materials have created an interest in long discontinuous FRP. Discontinuous composites possess many of the properties of continuous reinforced material with the benefit of being melt processable commonly by injection molding [2]. However, the mechanical properties of discontinuous fiber composites are highly dependent on the fiber length and orientation within the part

[3, 4]. The flow alignment of fibers in the injection molding process causes anisotropic properties in the resulting part [5].

In continuous fiber composites, poor delamination resistance and a lack of reinforcement transverse to the main fiber direction have led to interest in multiscale composites [6]. Multiscale or hybrid composites contain two or more types of filler in order to add reinforcement on two different size scales. Frequently glass fiber or carbon fiber (CF) with carbon nanotubes (CNTs) have been used [6-10]. The small size of the CNTs allows them to penetrate the inter-fiber spacing in multiscale composites enhancing properties in the matrix-dominated directions, without the decreased inplane mechanical properties observed with woven composite structures [6]. Carbon nanotube (CNT) polymer composites have been heavily researched as a replacement for traditional composite materials in various applications because of their exceptional mechanical [11], electrical[12], and thermal properties[13]. These nanocomposites have become industrially relevant, especially in the areas of electrostatic dissipation [14] and electromagnetic inference shielding [15], but have yet to reach their full potential for mechanical reinforcement[16].

Multiscale composite research has been focused on thermosets [7, 8] created using resin transfer molding (RTM) [9, 10, 17]. Jingjing et al. [9] found that 1wt% functionalized multiwalled CNT (MWCNT) yielded a 14 % improvement in tensile strength and 20 % improvement in Young's modulus in an epoxy carbon fiber composite. However, the fiber layups in RTM can act as a filter to the CNTs in the epoxy. Large bundles of CNTs become caught between the fibers of a tow, resulting in an inconsistent CNT concentration throughout the part, a lack of CNT within the fiber tows, and above approximately 1 wt% CNT incomplete part fill [10].

The studies that have been performed on thermoplastic multiscale composites typically involve engineering thermoplastics [18-20].The composites are formed by melt compounding CNTs and polymer.

Then the polymer CNT master batch is formed into sheets. Layers of CNT/polymer are stacked alternating with layers of fiber reinforcement and the stacks are compression molded [18, 19, 21, 22]. Diez-Pascual et al. [19] combined functionalized single walled CNTs with CF PEEK composites resulting in a 16% improvement in Young's modulus compared to samples without CNT. Work performed in PP has involved CNTs grown on short CF or glass fiber. Here 5 wt% of functionalized CNT treated fibers yielded a 57% improvement in modulus [23]. The major downsides of compression molding are production time and costs compared to injection molding and poor dispersion of the CNTs into the fiber tows [19].

To the best knowledge of the authors, there are no studies on long fiber discontinuous composites injection molded with CNTs. Chen [24] performed some preliminary work combing $scCO_2$ treated CNTs with poly(ether-ether-ketone) CF composites. She melt compound the material in a single screw extruder, then compression molded the resulting polymer strands. While this gave a 23% improvement in Young's modulus, there were large variations in the samples and this improvement was within the reported stand deviation. The difficulty in attaining a good dispersion of the CF and CNTs within a multiscale system is likely the reason for few studies. The addition of CNTs to a system greatly increases its viscosity [25], making it difficult to distribute the CNTs within the polymer. Commercially available MWCNT are typically produced using chemical vapor deposition synthesis [26] which yields large agglomerates on the order of hundreds of microns in diameter [27]. These agglomerates are held together by a combination of physical entanglement and van der Waals forces. In order to fully utilize CNTs in polymer composites, a mixing method that can separate the agglomerates and uniformly distribute the CNTs within the polymer must be used [28]. The most commonly used methods of accomplishing this are melt blending, solution blending, and in situ polymerization [16]. Solution blending and *in situ* polymerization typically yield better dispersion, but melt compounding has the advantages of scalability and a lack of processing solvents.

There has been a large focus in the literature recently in determining how melt processing conditions affect agglomerate size, CNT lengths, CNT dispersion, and composite properties [29-31]. In melt

compounding mixing energy is used as a measure of the amount of external stresses applied to the CNT agglomerates. Generally as mixing energy is increased, the dispersion of CNTs improves, but the CNT can be damaged in the process. Guo et al. [30] melt compounded polycarbonate MWCNT composites in a twin screw microcompounder and observed the effect mixing time had on CNT length and dispersion. They found that at long mixing times the CNTs were reduced by up to 89% of their initial length, leading to a decrease in electrical properties when compared to samples generated using shorter mixing times. Socher et al. [29] and Potschke et al. [31] observed similar trends with regard to matrix viscosity and mixing speed, respectively, where an intermediate value of matrix viscosity and mixing speed yielded improved properties because of high mixing energies causing a decrease in CNT length. The breakage effect will only be exacerbated in multiscale composites where the fibers involved can also experience breakage during processing. In the injection molding process, 13 mm initial fiber lengths commonly break down to an average length around 1 mm [32-34]. Therefore, anything that can be done to decrease the mixing energy need to debundle the CNTs should improve the composite properties.

The rapid expansion of $scCO_2$ to debundle CNT agglomerates was first patented by Gulari et al. [35] and further developed by Chen et al. [36] for use in single screw melt compounding. By debundling the CNTs before melt blending, lower mixing energies can be used in dispersing the CNT into the polymer. Analysis by Quigley et al. [37] showed that the $scCO_2$ process could yield a fifty fold and seventy-five fold decrease in average agglomerate size, for Baytube C150P and Nanocyl NC7000 respectively, without damaging the CNTs. Quigley et al. [38] also tested the electrical conductivity of $scCO_2$ treated Baytube C150P, melt compounded into polycarbonate in a single screw extruder. CNT lengths were maintained throughout the process, an improvement in CNT dispersion was observed, and electrical percolation decreased from 1.53 wt% CNT to 0.83 wt% CNT with the treated CNT.

The goal of this work is to improve the mechanical and electrical properties of injection molded long CF/ PP composites through the addition of $scCO_2$ treated CNTs. In order to gain an understanding of

how the CNT and CF interact, the effect of CF concentration, CNT expansion, and CNT concentration on electrical conductivity and tensile properties are examined. Initially, the CF concentration in the composite is optimized followed by the concentration of CNT and finally the degree of expansion of the CNT.

5.3 Experimental Materials and Methodology

5.3.1 Materials

Nanocyl NC7000 MWCNTs, generated through fixed-bed chemical vapor deposition, were used without functionalization. These CNTs were chosen because their morphology and properties have been well studied [27]. As received these CNTs are in a "combed yarn" structure with a bulk density of approximately 60 kg/m^3 [28, 39] and an average agglomerate size of 674 µm [27]. The weight percentage of CNTs in the composite was calculated based on the weight of the total composite, polymer, CF, and CNT.

Plasticomp Complete Polypropylene (PP) CF (1014 NAT) material was used as the initial polymer/CF composite. The pure PP matrix and 20, 30, 40, and 50 wt% CF/PP samples were tested. The material was created from a pultrusion process using a 35 MI PP with an initial pellet length of 13 mm.

5.3.2 Methods

5.3.2.1 Super Critical CO_2 Processing

MWCNTs were loaded into a 300 ml pressure vessel (Parr Instrument Company) with a maximum operating pressure of 4000 psi. ScCO_2 was pumped into the vessel using a Trexel MuCell super critical fluid system and heated to the appropriate processing conditions. The temperature and pressure were held at these conditions, while the CNTs were mixed with a magnetic stir bar for 30 min to allow the scCO_2 to penetrate the CNT agglomerates. The MWCNT/ scCO_2 mixture was then rapidly released into a 19 L secondary pressure vessel. Finally, the processed CNTs were collected.

The bulk density of the CNTs after $scCO_2$ expansion has been found to correlate to the extent of deagglomertaion [37]. The degree of expansion refers to the factor of CNT bulk density reduction after processing. A ten fold (10X) degree of expansion would be a reduction in bulk density from 60 kg/m^3 to 6 kg/m^3. The quantity of CNTs, temperature, and pressure of the soak period were adjusted to obtain the desired degree of expansion. The conditions used are listed in Table 5.1. Any samples listed as direct blend (DB) are samples that were processed without $scCO_2$ treatment (as-received CNTs). For further information on the $scCO_2$ process readers are directed to Quigley et al. [37].

Table 5.1: Conditions used for $scCO_2$ treatment of Nanocyl CNT

Degree of Expansion	CNT (g)	Temperature (°C)	Pressure (Mpa)	Bulk Density (kg/m^3)
DB	NA	NA	NA	60.0
4.3X	6.5	60	17.2	13.0
10X	5	60	18.6	5.9
30X	2.5	60	18.6	2.0
50X	1	60	18.6	1.2

5.3.2.2 Injection Molding

The CNTs and polymer/CF pellets were mixed together using a stand mixer and dried overnight in a vacuum oven at 80 °C. Then the CNT/CF/polymer mixture was loaded into the hopper of an Arburg Allrounder 221-55-250 injection molder. Parts were injection molded using an 18 mm screw with a screw speed of 60 rpm, backpressure of 3 bar, and fill time of 2 seconds. The melt temperature profile of the injection molding machine was set to 190/ 210/ 220/ 220°C in the feed, compression, metering zones and nozzle, respectively, while the mold temperature was held at 80°C .

End-gated plaques were produced in the injection molder. The plaques had a sprew length of 65 mm with an initial radius of 1.45 mm and a final radius of 1.75 mm. The parts consisted of a gate and plaque region. The gate region was 80.68 mm X 6.25 mm X 6.33 mm, and the plaque was 75.05 mm X

77.65 mm X 1.55 mm. The first 10 plaques from each run were discarded to ensure that the injection molding machine was operating at equilibrium.

5.3.2.3 Tensile Testing

Strips, 12.7 mm (0.5 in) wide and the length and thickness of a plaque, were cut from the center of the injection molded plaques. To help fully assess the impact of CNTs, samples were cut both in the flow direction(x_1) and transverse to flow direction (x_2), shown in Figure 5-1. Tensile tests were performed at room temperature and humidity with an Instron model 4204 testing machine. An extensometer was used to measure strain and calculate Young's modulus accurately. A 5 kN load cell with a cross head speed of 1 mm/min was used for all tensile tests. The mean and standard deviations were calculated for the Young's modulus and tensile strength from at least eight samples. Any data points outside of the average by more than two standard deviations from the mean were omitted.

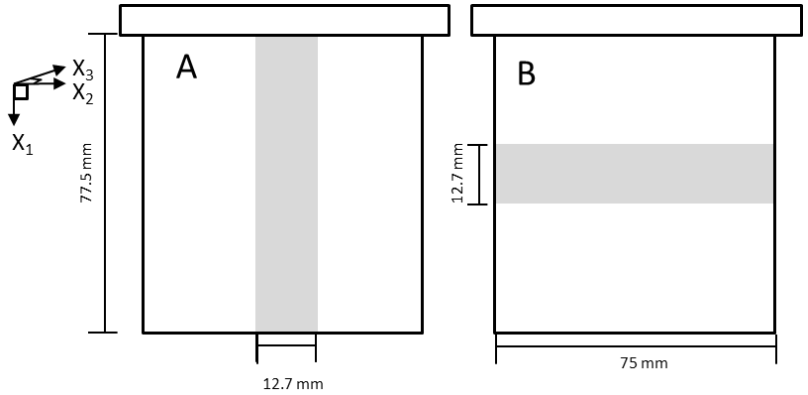

Figure 5-1: Locations in plaque tensile tested in the flow direction (A) and transverse to blow direction (B) the grey boxes represent the strips cut from the plaque.

5.3.2.4 Surface Conductivity

The surface conductivity of the injection molded samples were measured using a Prostat PRF-911 Concentric Ring Set and Keithley 2000 multimeter with a sensitivity of $1\ x\ 10^{-10}\ S$, following ASTM D-257. Due to the surface area required for the concentric ring electrode, the conductivity measurements were performed on full plaques. The reported values are the mean of at least five plaques.

5.4 Results and Discussion

5.4.1 Effect of CF Concentration

CF/PP, CF/ 1 wt% DB CNT/PP and CF/1 wt% 10X CNT/ PP were created using 0/20/30/40 and 50 wt% CF as described above. The resulting surface conductivity and mechanical properties were tested. The effect of the scCO2 aided melt blending method on the Young's modulus of the CF/CNT/PP multiscale composites is illustrated in Figure 5-2.

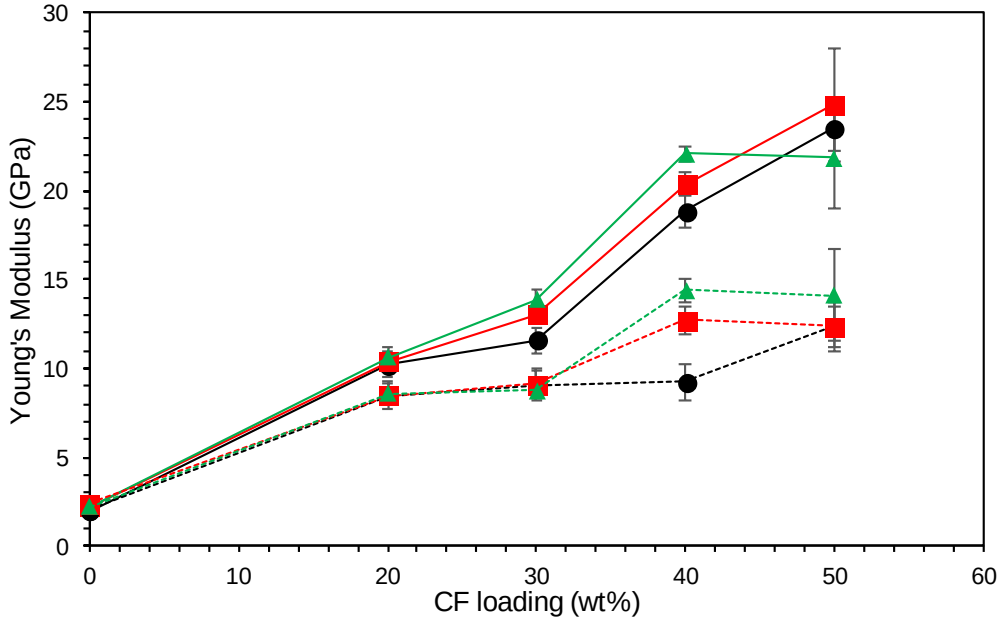

Figure 5-2: Young's modulus of CF/ CNT/ PP composites at varying CF concentrations using (•) 0 wt% CNT, (■) 1 wt% DB CNT, and (▲) 1 wt% 10X CNT in both the flow (—) and transverse to flow (— —) directions. Error bars represent standard deviation.

With no CF in the composite, the addition of 1 wt% CNT led to a 10% improvement in the Young's modulus of about 0.3 GPa in both the flow and transverse to flow direction, for both the DB and 10X CNTs. This small improvement indicates that there is little interaction occurring between the PP and CNT. As un-functionalized CNTs and PP are inert materials a minimal effect on tensile properties was expected. As the alignment of CNTs leads to anisotropic reinforcement, the isotropic reinforcement of CNTs signifies that there is little flow alignment [40]. Previous results using $scCO_2$ treated CNTs have shown improved dispersion of CNTs in pure polymer [38]. The lack of a noticeable difference in the performance of the

$scCO_2$ treated and untreated CNT on Young's modulus, supports that there is little interaction occurring between the CNTs and PP.

At a CF concentration of 20 wt%, there is little difference in the Young's modulus of the composites with and without CNTs. The large improvement in modulus in these samples, compared to those without CF, can be attributed solely to the CF. The difference that appears between the transverse to flow (E_1) and flow direction Young's modulus (E_2) is due to the orientation of the CF that occurs during the injection molding process[41]. Even though the addition of 1 wt% 10X CNTs caused a slight improvement E_1 and E_2 when compared to the DB CNT samples and those without CNTs, the improvements were within the standard deviation of the samples without CNTs, with E_1 going from 10.23 ± 0.68 GPa to 10.64 ± 0.54 GPa and E_2 going from 8.48 ± 0.5 GPa to 8.58 ± 0.58 GPa.

At 30 wt% CF, the addition of CNTs improves E_1 but has little effect on E_2. The 1 wt% DB CNT samples yielded a 12% improvement in E_1 and the addition 1 wt% 10X CNT yielded a 20% improvement in E_1 (11.6 ± 0.70 GPa to 13.9 ± 0.52 GPa), when compared to samples without CNTs. The improvement in modulus in the 10X samples compared to the DB samples is indicative of improved dispersion of the CNTs in the 10X samples.

The 40 wt% CF samples with CNTs show a marked improvement in both E_1 and E_2. In the flow direction, the addition of 1 wt% DB CNT and 1 wt% 10X CNT produced an 8% and a 17% increase in modulus when compared to composites without CNTs. The fact that the CNTs property enhancement is dependent on CF concentration suggests that the CNTs are primarily interacting with the CF and may be creating an interconnected network with the CFs [42]. Going from 30 to 40 wt% CF improves the amount of reinforcement the CNTs provide. In the 40 wt% CF samples the addition of 1 wt% CNT yields a 3.24 GPa improvement in E_1 over the samples without CNTs versus a 2.29 GPa improvement at 30 wt% CF. If the reinforcement was due primarily to interactions with the matrix, the loading of CF would not have a large impact on the amount of reinforcement due to CNTs.

At 40 wt% CF the addition of CNTs produce a 37% and a 56% improvement in E_2 going from 9.25 ± 0.98 GPa to 12.72 ± 0.82 GPa and 14.45 ± 0.66 GPa for the 1 wt% DB CNT and 1 wt% 10X CNT respectively. This change is larger than the increase in E_2 from going from 20 wt% to 40 wt% CF which is only 0.78 GPa. The large increase in transverse modulus from the CNT indicates that unlike the CF, the CNTs are not attaining a high degree of flow alignment through the center of the part in the 40 and 50 wt% CF samples.

At 50 wt% CF all samples tested had a large variability signified by the larger standard deviation, ±1.5-3 GPa, relative to the other concentrations, ± 0.1-0.7 GPa. At 50 wt% CF, the viscosity of the composite is very high, increasing the void content in the CF/ PP samples, an example image of voids typically observed for a 50 wt% CF fiber system is shown in Figure 5-3 [43]. In addition the high CF concentration makes it more difficult to achieve uniform dispersion of CNTs in the system [29]. Additionally, at high fiber loading there are large amounts of fiber bundles that can be found in the parts [1]. With the pultrusion process, the majority of fibers in the composite pellet are in a tow in the center of the pellet. When making discontinuous composites, there is a tradeoff between the end length of the fibers and an even distribution of the fibers in the part. The more shear a pellet is exposed to the more uniform the dispersion of fibers in the samples, but more fiber breakage occurs [34]. The large number of fibers at 50 wt% CF, constrains individual fiber movement preventing the fibers from achieving the same degree of flow alignment and dispersion that they do in the lower concentration samples. The change in orientation is indicated by the increase in the transverse to flow modulus that is observed for the 50 wt% CF sample without CNTs but not the 30 and 40 wt% CF samples.

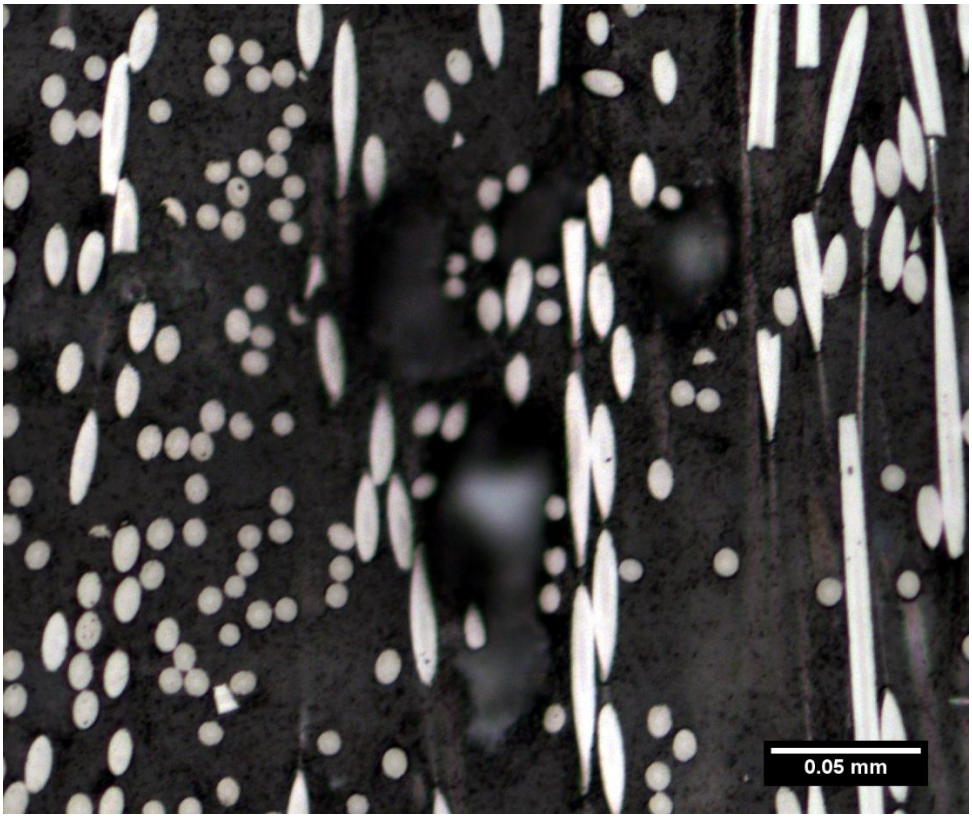

Figure 5-3: Optical image of a 50 wt% CF PP composite showing representative voids.

A difference CF orientation and length compared to the DB samples and samples without CNT is likely what leads to the decrease in E_1 for the 1 wt% 10X CNT samples at 50 wt% CF. The addition of CNTs, particularly the $scCO_2$ treated CNTs, greatly increase the viscosity of the system[38], increasing fiber breakage and impeding fiber orientation[44, 45]. The 14% increase in E_2 compared to the DB and samples without CNT indicate that the CF orientation is likely slightly more in the transverse to flow direction than in the other samples. It is difficult to tell how much of the modulus change in the 50 wt% CF 1 wt% 10X CNT samples is due to CNT reinforcement versus a change in the CF orientation.

5.4.2 CNT Concentration

The large improvement in Young's modulus due to the addition of 1 wt% CNTs at 40 wt% CF suggests an optimum concentration of CF for the tested multiscale system. Therefore, 0.5 wt% CNT at 40 wt% CF and 2 wt% CNT at 30 and 40 wt% CF were tested to try and find an optimum ratio of CNTs to CF and better illustrate the cause of the large transverse to flow modulus increase.

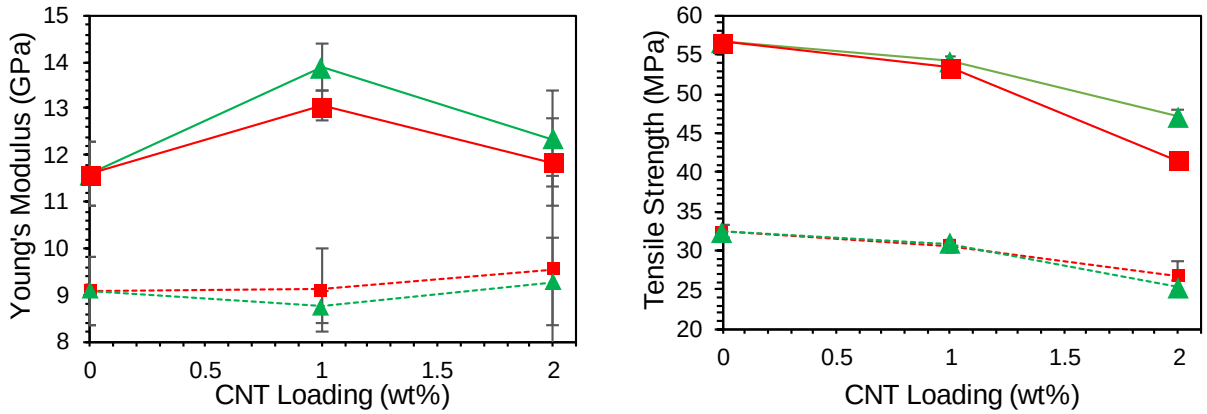

Figure 5-4: Young's modulus (left) and tensile strength (right) dependence on CNT concentration for 30wt% CF for (■) DB and (▲) 10X CNTs in both the flow (—) and transverse to flow (— —) directions.

At 30 wt% CF only 1 and 2 wt% CNT were tested and the results are shown in Figure 5-4. The goal was to examine if by increasing CNT loading similar results could be achieved as with the 1 wt% CNT 40 wt% CF samples. As in the 40 wt% system going from 1 to 2 wt % CNT caused a decrease in tensile strength and Young's modulus. The exception is E_2. However, this slight increase is accompanied by a larger decrease in E_1, indicating that the additional CNTs are likely increasing the viscosity of the system enough that the CF is not orienting to the same degree that it is in the samples without CNTs and with 1 wt% CNTs. The large standard deviation of the 2 wt% CNT samples is an indication of poor uniformity in the dispersion of CNTs in the sample and high void content.

Figure 5-5 shows the tensile testing results for the 40 wt% CF CNT concentration experiments. Going from 1 to 2 wt% CNT loading caused a decrease in E_1 and E_2 for all samples, suggesting that increasing the CNT loading is not providing additional connectivity. At 40 wt% CF the larger change in tensile strength in the flow direction than transverse to flow direction caused by increasing the CNT loading from 1 wt% to 2wt% 10X CNT may signify that the system is overfilled and a different orientation of the CF in the system occurred in the 2 wt% 10X CNT samples. The relatively change in tensile strength for both the 30 and 40wt% GF samples from samples without CNTs to those with 1 wt% CNT indicates that the CNTs are likely not interacting with the PP matrix.

The drop in tensile strength and Young's modulus from increasing CNT concentration to 2 wt% is less pronounced in the DB CNT than in the 10X CNT 40 wt% CF system. The DB CNTs have less of a bulk density mismatch between the CNTs and polymer pellets making for a more uniform feed mixture at higher concentrations of CNT, discussed in depth later in the paper. The 10X CNT samples likely have regions that are CNT rich and poor due to the difficulty of mixing CNTs into the pultruded pellets, and variation in feed concentration.

The 0.5 wt% CNT 40 wt% CF samples display the expected trend with the tensile strength and Young's modulus values falling between the samples without CNT and the 1 wt% CNT samples. The samples with 10X CNTs showed an improvement over the DB samples for both Young's modulus and tensile strength at 0.5 wt% CNT 40 wt% CF. The larger variation between samples at 0.5 wt% CNTs are due to the difficulty in achieving an uniform dispersion of such a small wt% of CNT. For the cases examined 1 wt% 10X CNT appears to be an optimum CNT loading for mechanical properties. Little additional benefit was attained by increasing the CNT concentration from 1 wt% to 2 wt% or decreasing it to 0.5 wt%.

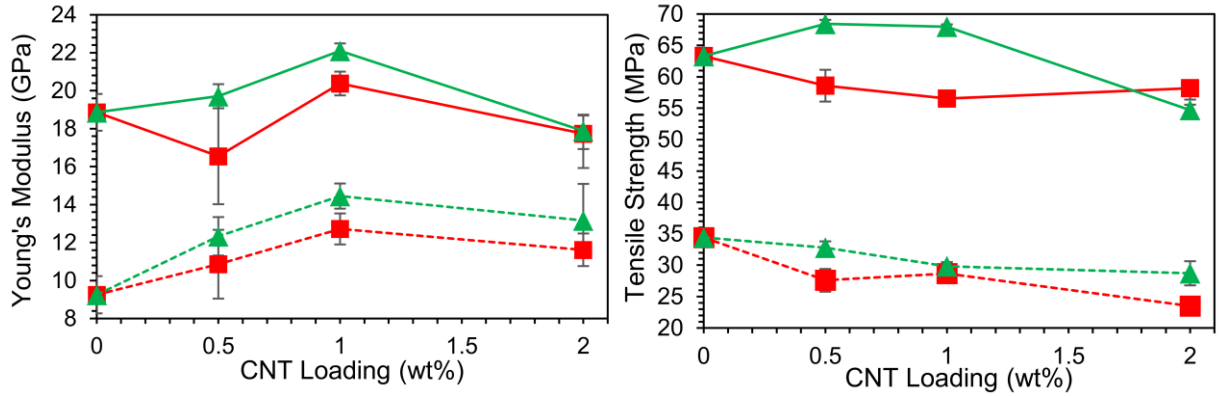

Figure 5-5: Young's modulus (left) and tensile strength (right) dependence on CNT concentration for 40wt% CF for (■) DB and (▲)10X CNTs in both the flow (-) and (- -) transverse to flow directions.

5.4.3 *CNT Degree of Expansion*

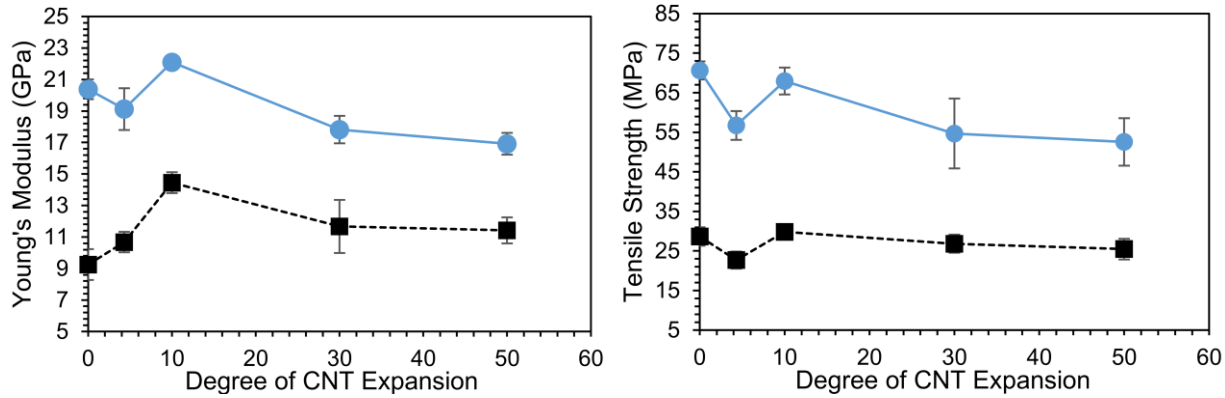

Figure 5-6: Young's modulus (top) and tensile strength (bottom) at varying degrees of CNT expansion for 40 wt% CF 1 wt% CNT in the flow (●) and transverse to flow (■) directions.

Samples with 40 wt% CF and 1 wt% CNT composites were tensile tested with CNTs that had been expanded to 4.3x, 10X, 30x, and 50x to optimize the $scCO_2$ treatment of the CNTs. The tensile test results, shown in Figure 5-6, have a peak in both E_1 and E_2 for the 10X expanded CNTs. The tensile strength of the samples at 10X is about the same as samples without CNTs and falls off at higher degrees of expansion. The decrease in tensile properties at 30X and 50X CNT is likely due to the large density difference between the CNTs and polymer pellets at these conditions. A similar trend was observed by Quigley et al. [38] for

Baytube C150P CNTs in polycarbonate when examining electrical conductivity. At low concentrations, the highly expanded CNTs performed the best, but as the concentration of CNT in the composite increased, there was a performance drop in the highly expanded CNTs. The bulk density difference created a large variation in the CNT loading in the feed and led to decreased performance. In the Nanocyl CF composite, the density mismatch becomes an issue at lower CNT concentrations and degrees of expansion than was reported for the Baytube. The starting bulk density of the Nanocyl CNTs are lower so a 10X degree of expansion corresponds to a bulk density of 6 kg/m^3 for the Nanocyl CNTs, which is a 25X expansion for the Baytubes. Additionally the multiscale system is already highly loaded, making the generation of a uniform distribution of the CNTs more difficult.

5.4.4 Electrical Conductivity

The highly filled nature of the system makes examining the average agglomerate size and distribution of the CNTs by microscopy difficult. Electrical conductivity has been shown to be a good representation of the degree of dispersion and interconnectivity found in a composite system [46], as a conductive path is needed within the composite to improve these properties. Therefore, the surface and volume conductivity of the injection molded multiscale parts were examined.

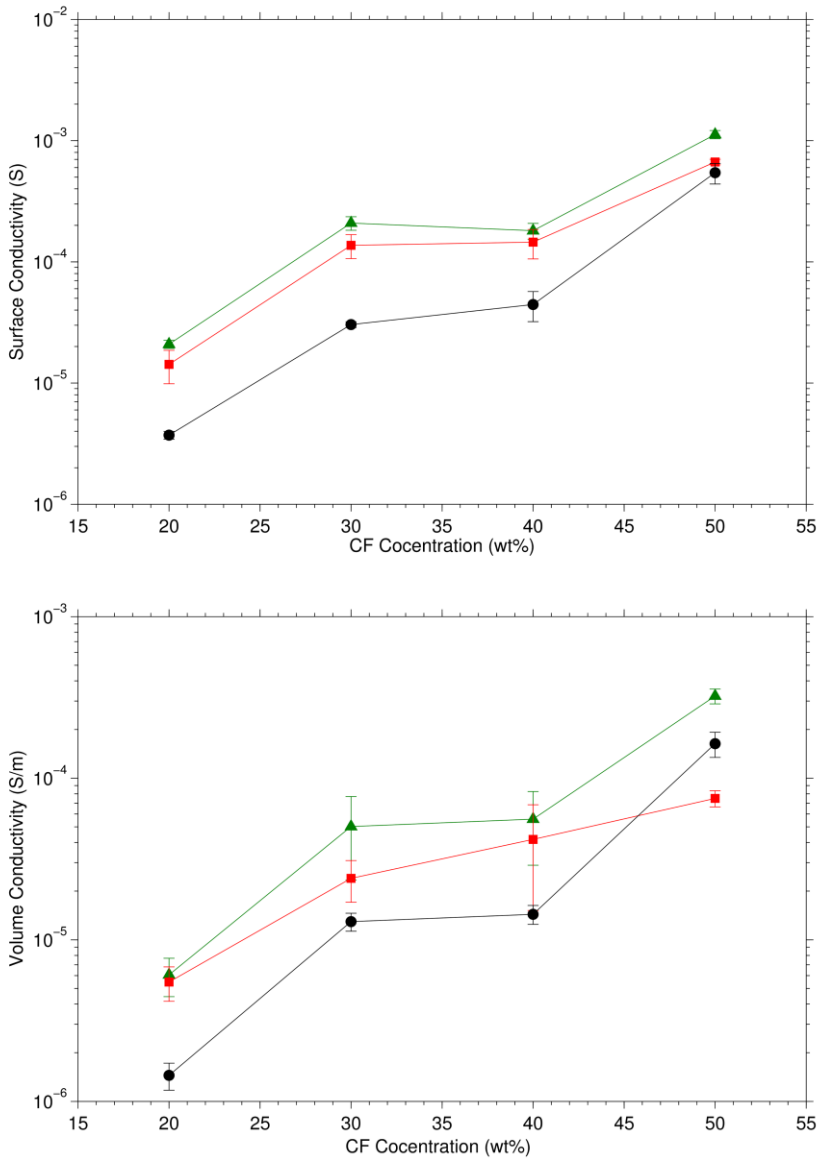

Figure 5-7: Surface (top) and volume (bottom) conductivity at varying CF concentrations with (•) 0 wt%, (■) 1 wt% DB, and (▲) 1 wt% 10X CNT.

The electrical conductivity for samples without CF are not reported because the resulting conductivity was below the sensitivity of the testing system ($1\ x\ 10^{-10}\ S$). The low conductivity of these samples is a product of the injection molding process and conditions used. Often a skin layer can form in injection molded CNT parts that hinders their electrical conductivity [47]. This skin layer along with the fact that annealing CNT parts causes secondary "loose agglomerates" increasing conductivity, is why compression molding is normally used to attain maximum electrical conductivity for CNT composites [48].

For the highly filled systems with CF the effect of the skin layer is less pronounced owing to the conductive path provided by the CF and different flow profile of the composite.

At 20 wt% CF adding 1 wt% CNT yields a large increase in surface conductivity, going form $3.72\,x\,10^{-6} \pm 2.76\,x\,10^{-7}$ siemens (S) to $1.45\,x\,10^{-5} \pm 4.38\,x\,10^{-6}\,S$ and $2.09\,x\,10^{-5} \pm 1.61\,x\,10^{-6}\,S$ for the DB and 10X samples respectively. The increase in conductivity achieved with the $scCO_2$ treated CNT means that the expansion process is allowing the CNTs to achieve better dispersion within the composite relative to the DB CNTs.

Adding 1 wt% of CNTs to the 30 wt% CF samples yielded an additional order of magnitude improvement over what adding 1 wt% CNT to the 20 wt% gave, meaning the higher fiber loading allowed the same amount of CNTs to form more connections within the composite. Surface conductivity increased from $3.04\,x\,10^{-5} \pm 1.64\,x\,10^{-6}\,S$ to $1.37\,x\,10^{-4} \pm 3.07\,x\,10^{-5}S$ and $2.07\,x\,10^{-4} \pm 2.68\,x\,10^{-5}S$ for the DB and 10X samples, respectively, corresponding to a 350 % and 588 % improvement in conductivity for the 30 wt% CF samples. At 40 wt% CF adding 1 wt% CNTs yielded almost the same increase in conductivity as it did at 30wt% going from $4.45\,x\,10^{-5} \pm 1.24x\,10^{-5}S$ to $1.45\,x\,10^{-4} \pm 3.97\,x\,10^{-5}\,S$ and $1.8\,x\,10^{-4} \pm 2.69\,x\,10^{-5}S$ for the DB and 10X samples. This implies that the system has likely reached a percolation point in terms of the number of connections adding 1 wt% CNT will produce.

At 50 wt% CF the addition of 1 wt% DB CNT caused the surface conductivity to increase from $5.43\,x10^{-4} \pm 1.05\,x\,10^{-4}S$ to $6.67x10^{-4} \pm 3.50\,x\,10^{-5}\,S$ giving almost the same increase as in the 30 and 40 wt% CF samples, supporting the idea that a percolation point was reached. The 10X CNTs yielded a larger surface conductivity improvement than for the 30 and 40 wt% CF samples going to $1.12x10^{-3} \pm 8.80\,x\,10^{-5}S$. Based on the tensile testing results, it is likely that the additional improvement is due to a different CF orientation in the 50 wt% CF 1 wt% 10X CNT samples compared to the other samples tested.

Because CF is conductive, it is difficult to know how much of the improvement in surface conductivity is due to the change in orientation and how much is due to the CNTs.

The volume conductivity of the samples follows the same general trend as observed in the surface conductivity with the 10X CNT samples performing the best followed by the DB samples then the samples without CNTs. The addition of 1 wt% 10X CNT yielded about a 3X improvement in conductivity at 20, 30, and 40 wt% CF ($6.06x10^{-6} \pm 1.61\ x\ 10^{-6} S/m$, $5.02x10^{-5} \pm 2.68\ x\ 10^{-5} S/m$, $5.58x10^{-5} \pm 2.69\ x\ 10^{-5} S/m$) compared to samples without CNTs, signifying a similar state of CNT dispersion was achieved in all three samples.

The untreated CNT yielded a more inconsistent result in a volume conductivity improvement of 2.8X, 0.85X, and 1.91X for 20, 30, and 40 wt% CF compared to samples without CF, indicating that the dispersion of the DB CNTs in the 20 wt% CF is almost as good as it is for the 10X samples. At higher loadings of CF, the DB CNT samples lower volume conductivity is likely caused by worse CNT dispersion. This is also demonstrated in the 50 wt% CF 1 wt% DB CNT sample, which has a lower volume conductivity ($7.49x10^{-5} \pm 8.59\ x\ 10^{-6}\ S/m$) than the 50 wt% CF samples without CNT ($1.63X10^{-4} \pm 2.90\ x\ 10^{-5}\ S/m$) and 1 wt% 10X samples ($3.22x10^{-4} \pm 3.40\ x\ 10^{-5}\ S/m$).

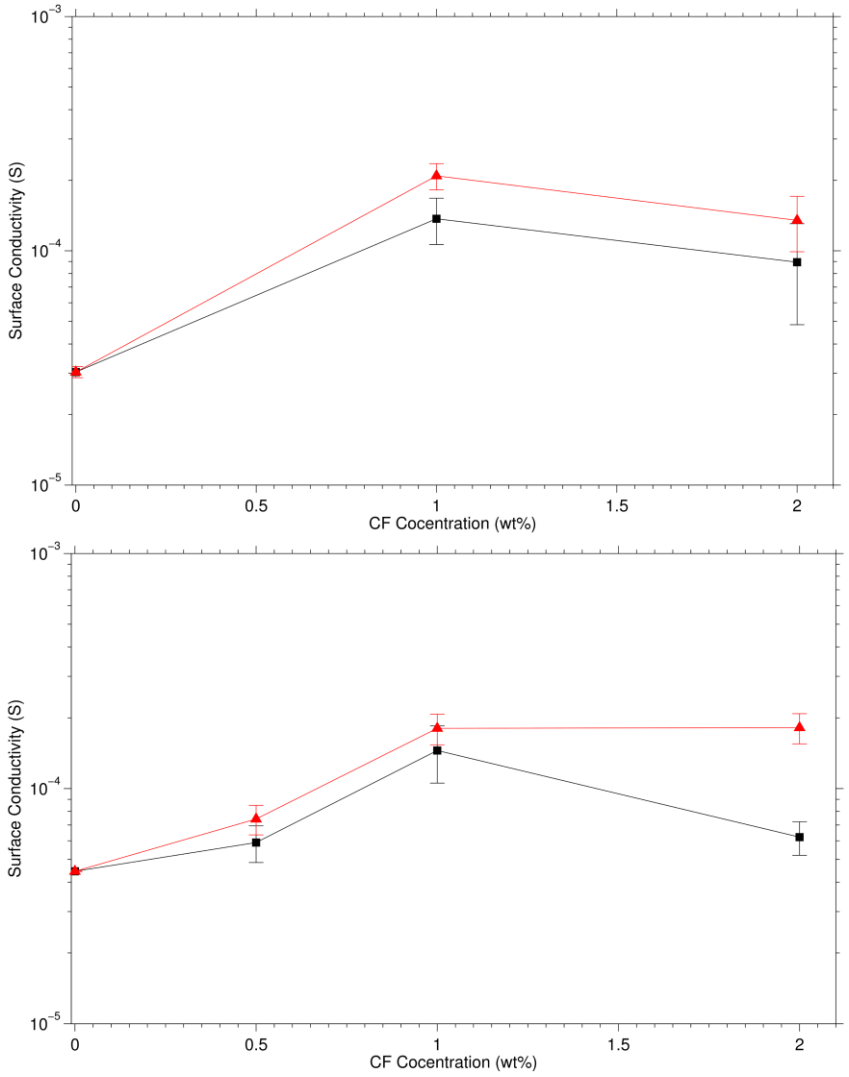

Figure 5-8: Effect of CNT loading on surface conductivity for 30 wt% (top) and 40 wt% (bottom) CF with for (■) DB and (▲)10X CNTs.

The effect of CNT concentration on electrical conductivity is shown in Figure 5-8. At 30 wt% CF, 1 wt% CNT appears to be an optimum for surface conductivity. Increasing the CNT loading from 1 to 2 wt% CNT is decreases the surface conductivity of the samples from $1.37x10^{-4} \pm 3.07\,x\,10^{-5} S$ to $8.94\,x\,10^{-5} \pm 4.11\,x\,10^{-5} S$ and from $2.09\,X\,10^{-4} \pm 2.68\,x\,10^{-5} S$ to $1.35\,X\,10^{-4} \pm 3.58\,x\,10^{-5} S$, for the DB and 10X samples, respectively, signifying that although the CNT content is increasing, the resulting composite is less interconnected. The high CF loading makes dispersing more than 1 wt% CNT by melt

blending difficult. These results match with the tensile testing results where properties either decrease or there is no significant difference from going to 2 wt% CNT.

At 40 wt% CF a similar trend to the 30 wt% is observed. The 0.5 wt% CNT samples fall between the samples with no CNT and the 1 wt% samples, while going from 1 to 2 wt% DB CNT causes a decrease in surface conductivity from $1.45x10^{-4} \pm 3.97\ x\ 10^{-5}$S to $6.22x10^{-5} \pm 1.01\ x\ 10^{-5} S$. The conductivity for the 10X samples can be considered constant between 1 to 2 wt% CNT, going from $1.80x10^{-4} S \pm 2.69\ x\ 10^{-5}$ to $1.82\ x10^{-4} \pm 2.67\ x\ 10^{-5}\ S$, suggesting that the $scCO_2$ treated CNTs are able to disperse better than the DB CNTs.

The tensile test and surface conductivity results suggest that a 1 wt% CNT loading is ideal for the tested system. The difficulty in achieving uniform dispersion at higher loadings of CNTs is likely the cause of the decrease performance of the 2 wt% CNT samples. Muller et al. [49] found that a side feed helped achieve a more even dispersion of CNT, and it may help improve performance of this system at higher CNT loadings.

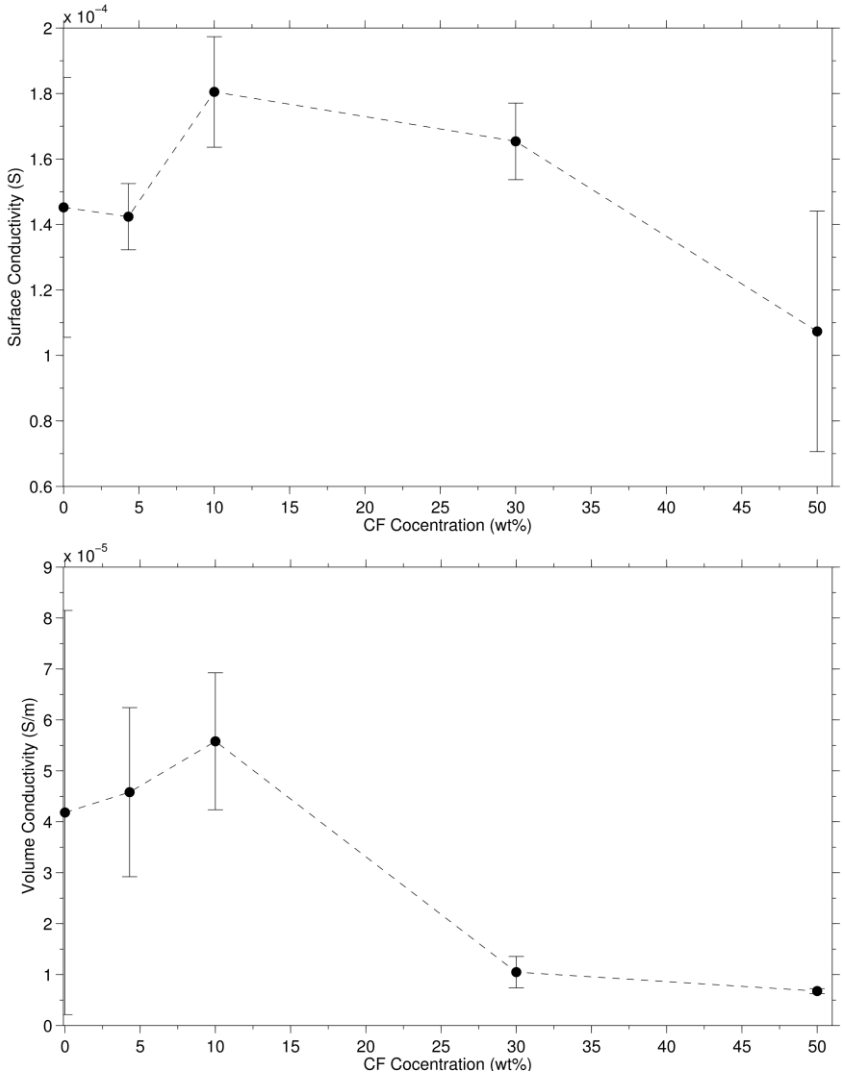

Figure 5-9: Effect of the degree of CNT expansion on surface(top) and volume (bottom) conductivity for 40wt% CF 1wt% CNT PP composites.

In Figure 5-9 is shown the effect of the degree of CNT expansion on the surface and volume electrical conductivity for the 40 wt% CF 1% CNT samples. There is a smaller impact on the surface conductivity due to the degree of CNT expansion than CNT and CF concentration, as only the initial state of the CNTs is changed and not the quantity of conductive material. The largest difference between samples being $1.80x10^{-4} \pm 1.69\ x\ 10^{-5} S$ to $1.07x10^{-4} \pm 3.68\ x\ 10^{-5} S$ for the 10X and 50X samples, respectively.

At 4.3X there is little change in surface conductivity compared to the DB samples. Again 10X appears to be an optimum condition for the surface conductivity, giving a 24% improvement compared to the DB samples at $1.45x10^{-4} \pm 3.97\ x\ 10^{-5} S$. The 30X samples showed a very slight decrease in surface conductivity and the 50X samples showed a larger drop in surface conductivity and increased variability, following the trend observed for Young's modulus and tensile strength.

The degree of CNT expansion had a larger effect on volume conductivity than surface conductivity. This indicates there may be a skin layer of CNTs and a CNT concentration gradient through the thickness of the part [47]. The DB, 4.3X, and 10X CNTs have similar volume conductivities with the trend being a slight decrease as CNT expansion increases going from $4.18\,x10^{-5} \pm 3.97\ x\ 10^{-6} S/m$ to $4.58\,x10^{-5} \pm 1.66\ x\ 10^{-5} S/m$ and $5.58\,X10^{-5} \pm 1.34\,x\ 10^{-5} S/m$, respectively. The 30X and 50X show a steep drop in volume conductivity, going to $1.05\ x10^{-5} \pm 3.07\ x\ 10^{-6} S/m$ and $6.76\ x10^{-6} \pm 4.99\ x\ 10^{-7} S/m$, suggesting that at higher degrees of expansion the CNTs are not as evenly dispersed as at lower degree of expansion.

5.4.5 Scanning Electron Microscopy

Scanning electron microscopy (SEM) images were used to qualitatively examine the fracture surface of the samples tested. Due to the large improvement E_2 at 40 wt% CF 1 wt% CNT an understanding of the morphology of these samples versus the 30 wt% CF 1 wt% CNT is of particular interest.

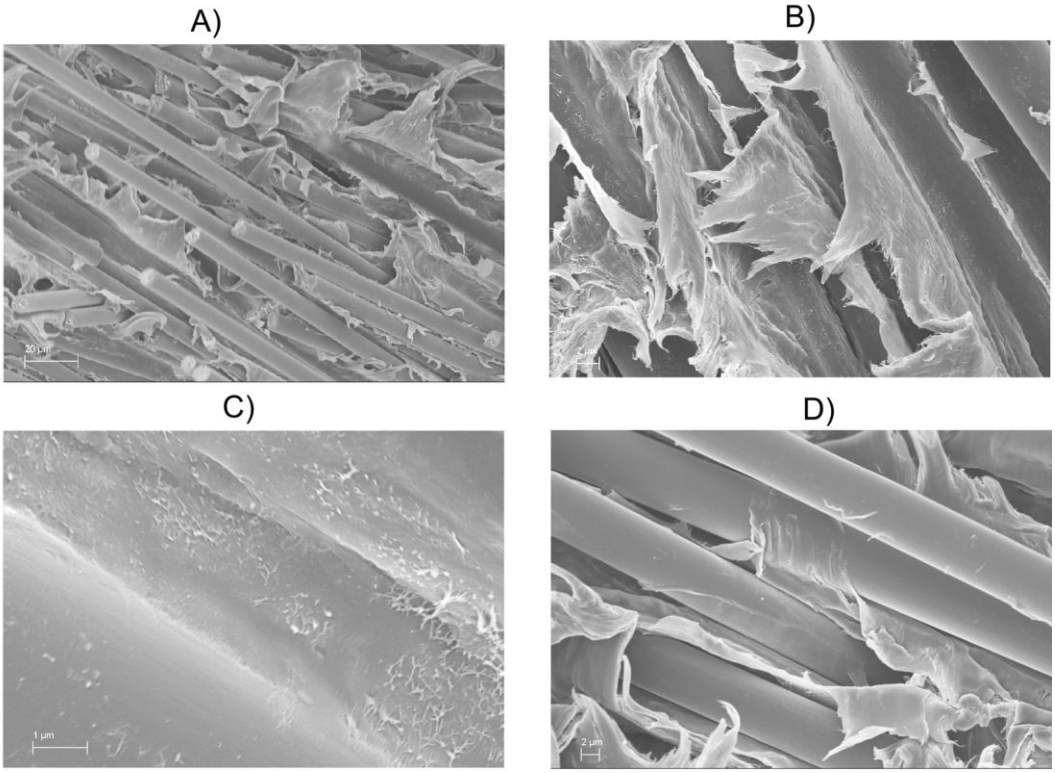

Figure 5-10: SEM images of Frature surface for transvers to flow samples (A) 40wt% CF, (B) 40 wt% CF 1 % DB CNT, (C) 40 wt% CF 1 wt% 10X CNT, (D) 30 wt% CF 1 wt% 10X CNT

SEM images of flow direction samples, Figure 5-10 , and transverse to flow, Figure 5-11, were taken at the fracture surface. The fracture surface of the transverse to flow orientation indicates that poor bonding between the CF and PP is the primary cause of failure for all the samples examined. There is a large amount of plastic deformation in the polymer rich area but little evidence of damage to the CF. Where the CF pulled out of the polymer, there is little evidence of deformation suggesting poor bonding between the PP and the CF [50]. In both the 1 wt% DB and 1 wt% 10X CNT 40 wt% CF samples, there is a concentration of CNTs visible both in the polymer near where the CF pulled out and on the CF itself (Figure 5-10: C and D). The concentration of CNTs near the CF supports the tensile test data which shows that the CNTs are interacting primarily with the CF.

Figure 5-10 D is of the area with the highest visible concentration of CNTs in the 30 wt% CF 1 wt% 10X CNT. Fewer CNTs are visible on the fracture surface implying that the fracture location was an area

that had few CNTs, creating a week point in the part, which led to failure. The difficulty of mixing the CNTs into the PP/ CF samples and larger percentage of PP in the 30 wt% versus 40 wt% samples may be causing more gradients in the CNT distribution in the 30 wt% CF samples.

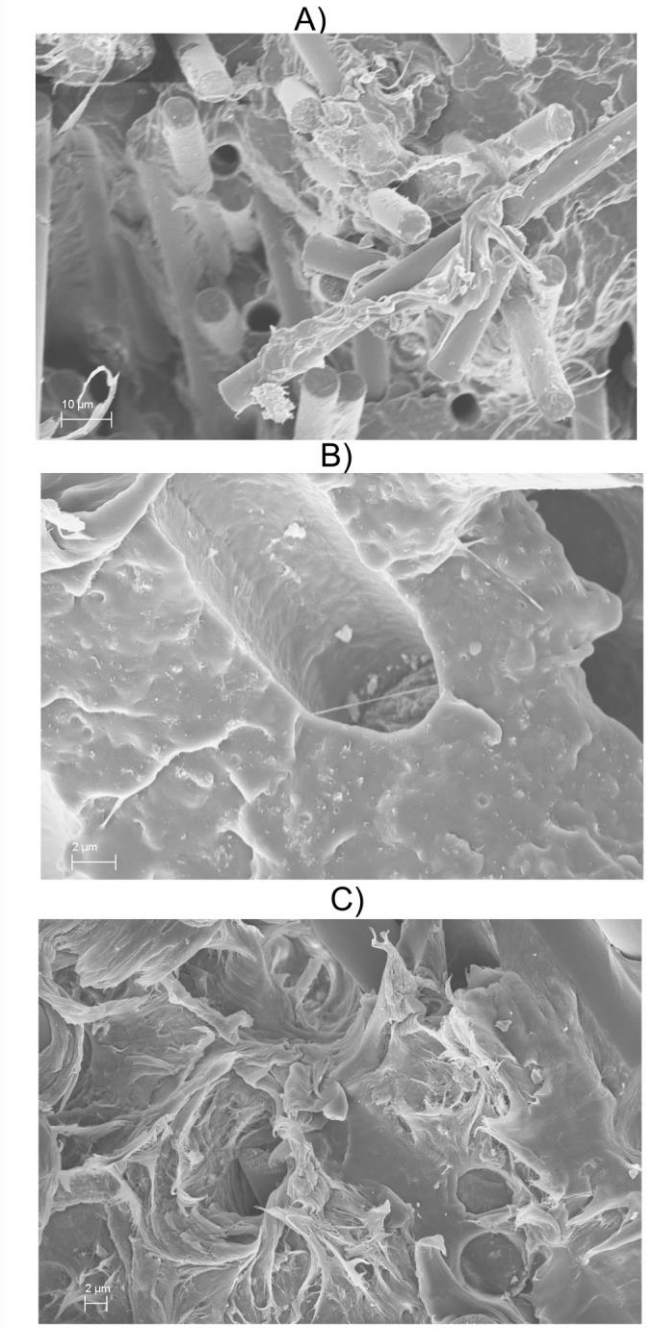

Figure 5-11: SEM images of fracture surface for flow direction samples A) 40wt% CF, B) 40 wt% CF 1 wt% 10X CNT, C) 30 wt% CF 1 wt% 10X CNT

SEM images of the fracture surface for the flow direction samples, shown in Figure 5-11, also indicate that there is poor bonding between the CF and PP. The CF appears to have pulled out of the PP in the 40 wt% CF samples leaving almost perfect holes where the CF was previously. If there had been good adhesion between the polymer and fiber there would be a large amount of deformation around where the CF had been located.

In the 40 wt CF 1 wt% CNT (Figure 5-11: B), a large amount of CNTs can be observed sticking out of the fracture surface, showing good dispersion of the CNTs and possibly a degree of flow alignment. As seen in Figure 5-11 C the 30 wt% 1 wt% 10X CNT transverse to flow samples have few CNTs visible on the flow direction fracture surface signifying that failure is likely to happen in CNT poor regions. This demonstrates that the CNTs are providing some degree of mechanical reinforcement and the distribution of CNTs in the 30 wt% CF 1 wt% CNT samples is likely not as even as in the 40 wt% samples.

5.5 Conclusions

Long CF/ carbon nanotube (CNT) / PP composites produced by injection molding exhibited significantly improved tensile and electrical properties compared to equivalent samples without CNTs. The un-functionalized CNTs interacted primarily with the CF and not the PP. This is demonstrated by the fact that the addition of 1 wt% CNTs 10x gave a 0.3 GPa improvement in transverse modulus, E_2, in samples without CF and a 5.2 GPa improvement in samples with 40 wt% CF. The largest improvement in properties was achieved at 40 wt% CF and 1 wt% 10 fold expanded, 10x, CNTs. Under these conditions, the addition of CNTs to the CF/ PP composite yielded an E_2 of 14.45 GPa and a modulus parallel to the flow, E_1, of 22.1 GPa corresponding to a 56% and 17% improvement compared to samples without CNTs and a 14% and 8% improvement compared to samples with untreated CNTs. The surface conductivity improved to $1.80\ X\ 10^{-4}\ S$ approximately a threefold increase compared to samples without CNTs and a 33% improvement compared to the untreated CNT samples. The volume conductivity was $5.58\ X\ 10^{-5}\ S/m$

approximately a threefold improvement compared to samples without CNT and a 25% improvement compared to the untreated CNT samples.

At 50 wt% CF it is likely that the addition of CNTs is causing a change in the orientation of the CF because of the high viscosity of the system. A low CNT loading of 1 wt% was found to be optimum, indicating the difficulty in dispersion of the CNTs into the multiscale composite using this method of composite fabrication. Side feeding the CNTs into the injection molder or mixing the CNTs into the polymer and then going through the pultrusion process would be likely to yield improvements at higher loading of CNTs. The fact that similar results to those reported in the literature were achieved without functionalization of the CNTs indicates that improved dispersion of the CNTs is achieved using the $scCO_2$ pretreatment and that further improvement in properties may be attainable with the addition of functionalization to the CNTs.

5.6 References

1. Truckenmüller, F. and H.G. Fritz, *Injection molding of long fiber-reinforced thermoplastics: A comparison of extruded and pultruded materials with direct addition of roving strands.* Polymer Engineering & Science, 1991. **31**(18): p. 1316-1329.
2. Mallick, P.K., *Composites engineering handbook*. 1997, New York: M. Dekker.
3. Avérous, L., et al., *Granulometric Characterization of Short Fiberglass in Reinforced Polypropylene. Relation to Processing Conditions and Mechanical Properties.* International Journal of Polymer Analysis and Characterization, 1995. **1**(4): p. 339-347.
4. Chin, W.-K., H.-T. Liu, and Y.-D. Lee, *Effects of fiber length and orientation distribution on the elastic modulus of short fiber reinforced thermoplastics.* Polymer Composites, 1988. **9**(1): p. 27-35.
5. Malzahn, J.C. and J.M. Schultz, *Transverse core fiber alignment in short-fiber injection-molding.* Composites Science and Technology, 1986. **25**(3): p. 187-192.
6. Díez-Pascual, A.M., et al., *Multiscale fiber-reinforced thermoplastic composites incorporating carbon nanotubes: A review.* Current Opinion in Solid State and Materials Science, 2014. **18**(2): p. 62-80.
7. Thostenson, E.T., et al., *Carbon nanotube/carbon fiber hybrid multiscale composites.* Journal of Applied Physics, 2002. **91**(9): p. 6034.
8. Bekyarova, E., et al., *Multiscale Carbon Nanotube−Carbon Fiber Reinforcement for Advanced Epoxy Composites.* Langmuir, 2007. **23**(7): p. 3970-3974.
9. Jingjing, Q., et al., *Carbon nanotube integrated multifunctional multiscale composites.* Nanotechnology, 2007. **18**(27): p. 275708.
10. Kim, M., *Modeling, manufacturing, and characterization of nanocomposites and multiscale composites.* 2009.
11. Salvetat, J.-P., *Elastic Modulus of Ordered and Disordered Multiwalled Carbon Nanotubes.* Advanced materials (Weinheim). **11**(2): p. 161-165.
12. Ebbesen, T.W., et al., *Electrical conductivity of individual carbon nanotubes.* Nature, 1996. **382**(6586): p. 54-56.
13. Berber, S., Y.-K. Kwon, and D. Tománek, *Unusually High Thermal Conductivity of Carbon Nanotubes.* Physical Review Letters, 2000. **84**(20): p. 4613-4616.
14. Smith Jr, J.G., et al., *Carbon nanotube-conductive additive-space durable polymer nanocomposite films for electrostatic charge dissipation.* Polymer, 2004. **45**(18): p. 6133-6142.
15. Yang, Y., et al., *Novel Carbon Nanotube−Polystyrene Foam Composites for Electromagnetic Interference Shielding.* Nano Letters, 2005. **5**(11): p. 2131-2134.
16. Paul, D.R. and L.M. Robeson, *Polymer nanotechnology: Nanocomposites.* Polymer, 2008. **49**(15): p. 3187-3204.
17. Fan, Z., K.-T. Hsiao, and S.G. Advani, *Experimental investigation of dispersion during flow of multi-walled carbon nanotube/polymer suspension in fibrous porous media.* Carbon, 2004. **42**(4): p. 871-876.
18. Ashrafi, B., et al., *Processing and properties of PEEK/glass fiber laminates: Effect of addition of single-walled carbon nanotubes.* Composites Part A: Applied Science and Manufacturing, 2012. **43**(8): p. 1267-1279.
19. Díez-Pascual, A.M., et al., *High performance PEEK/carbon nanotube composites compatibilized with polysulfones-I. Structure and thermal properties.* Carbon, 2010. **48**(12): p. 3485-3499.
20. Shen, Z., et al., *The effects of carbon nanotubes on mechanical and thermal properties of woven glass fibre reinforced polyamide-6 nanocomposites.* Composites Science and Technology, 2009. **69**(2): p. 239-244.

21. Vlasveld, D.P.N., H.E.N. Bersee, and S.J. Picken, *Nanocomposite matrix for increased fibre composite strength.* Polymer, 2005. **46**(23): p. 10269-10278.
22. Díez-Pascual, A.M., et al., *Development and characterization of PEEK/carbon nanotube composites.* Carbon, 2009. **47**(13): p. 3079-3090.
23. Rahmanian, S., et al., *Carbon and glass hierarchical fibers: Influence of carbon nanotubes on tensile, flexural and impact properties of short fiber reinforced composites.* Materials & Design, 2013. **43**(0): p. 10-16.
24. Chen, C., *The Manufacture of Polymer Nanocomposite Materials Using Supercritical Carbon Dioxide*, in *Chemical Engineering*. 2011, Virginia Tech.
25. McNally, T. and P. Pötschke, *Polymer-carbon nanotube composites: preparation, properties and applications*. 2011, Cambridge, UK; Philadelphia, PA: Woodhead Publishing.
26. Kong, J., A.M. Cassell, and H. Dai, *Chemical vapor deposition of methane for single-walled carbon nanotubes.* Chemical Physics Letters, 1998. **292**(4–6): p. 567-574.
27. Krause, B., et al., *Dispersability and particle size distribution of CNTs in an aqueous surfactant dispersion as a function of ultrasonic treatment time.* Carbon, 2010. **48**(10): p. 2746-2754.
28. Alig, I., et al., *Establishment, morphology and properties of carbon nanotube networks in polymer melts.* Polymer, 2012. **53**(1): p. 4-28.
29. Socher, R., et al., *The influence of matrix viscosity on MWCNT dispersion and electrical properties in different thermoplastic nanocomposites.* Polymer, 2012. **53**(2): p. 495-504.
30. Guo, J., et al., *Aspect ratio effects of multi-walled carbon nanotubes on electrical, mechanical, and thermal properties of polycarbonate/MWCNT composites.* Journal of Polymer Science Part B: Polymer Physics, 2014. **52**(1): p. 73-83.
31. Pötschke, P., T. Villmow, and B. Krause, *Melt mixed PCL/MWCNT composites prepared at different rotation speeds: Characterization of rheological, thermal, and electrical properties, molecular weight, MWCNT macrodispersion, and MWCNT length distribution.* Polymer, 2013. **54**(12): p. 3071-3078.
32. Phelps, J.H., et al., *A model for fiber length attrition in injection-molded long-fiber composites.* Composites Part A: Applied Science and Manufacturing, 2013. **51**(0): p. 11-21.
33. Nguyen, B.N., et al., *Fiber Length and Orientation in Long-Fiber Injection-Molded Thermoplastics — Part I: Modeling of Microstructure and Elastic Properties.* Journal of Composite Materials, 2008. **42**(10): p. 1003-1029.
34. Wang, J., et al., *Shear induced fiber orientation, fiber breakage and matrix molecular orientation in long glass fiber reinforced polypropylene composites.* Materials Science and Engineering: A, 2011. **528**(7–8): p. 3169-3176.
35. Gulari, E., G.K. Serhatkulu, and K. Rangaramanujam, *Method of delaminating aggregated particles with a coating agent in a substantially supercritical fluid*. 2008, Google Patents.
36. Chen, C., et al., *Using supercritical carbon dioxide in preparing carbon nanotube nanocomposite: Improved dispersion and mechanical properties.* Polymer Composites, 2012. **33**(6): p. 1033-1043.
37. Quigley, J., et al., *Benign reduction of carbon nanotube agglomerates using a supercritical carbon dioxide process.* Applied Physics A, 2014. **117**(3): p. 1003-1017.
38. Quigley, J.P., K. Herrington, and D.G. Baird, *Enhanced electrical properties of polycarbonate/carbon nanotube nanocomposites prepared by a supercritical carbon dioxide aided melt blending method.* Polymer, 2014. **55**(23): p. 6167-6175.
39. *Product Datasheet Nanocyl NC 7000 series*, S.A. Nanocyl, Editor. 2007: Sambreville, Belgium.
40. Moniruzzaman, M. and K.I. Winey, *Polymer Nanocomposites Containing Carbon Nanotubes.* Macromolecules, 2006. **39**(16): p. 5194-5205.
41. Park, S.-J. and SpringerLink, *Carbon Fibers*. Vol. 210. 2015, Dordrecht: Springer Netherlands.

42. Zhang, J.G., *The effect of carbon fibers and carbon nanotubes on the mechanical properties of polyimide composites.* Mechanics of Composite Materials, 2011. **47**(4): p. 447-450.
43. Lee, B.-H., H.-J. Kim, and W.-R. Yu, *Fabrication of long and discontinuous natural fiber reinforced polypropylene biocomposites and their mechanical properties.* Fibers and Polymers, 2009. **10**(1): p. 83-90.
44. Sousa, R.A., et al., *Integrated compounding and injection moulding of short fibre reinforced composites.* Plastics, Rubber & Composites, 2004. **33**(6): p. 249-259.
45. Bay, R.S. and C.L. Tucker, *Fiber orientation in simple injection moldings. Part II: Experimental results.* Polymer Composites, 1992. **13**(4): p. 332-341.
46. Pötschke, P., et al., *Rheological and dielectrical characterization of melt mixed polycarbonate-multiwalled carbon nanotube composites.* Polymer, 2004. **45**(26): p. 8863-8870.
47. Tiusanen, J., D. Vlasveld, and J. Vuorinen, *Review on the effects of injection moulding parameters on the electrical resistivity of carbon nanotube filled polymer parts.* Composites Science and Technology, 2012. **72**(14): p. 1741-1752.
48. Zhang, C., et al., *Temperature and time dependence of conductive network formation: Dynamic percolation and percolation time.* Polymer, 2006. **47**(1): p. 466-473.
49. Müller, M.T., et al., *Influence of feeding conditions in twin-screw extrusion of PP/MWCNT composites on electrical and mechanical properties.* Composites Science and Technology, 2011. **71**(13): p. 1535-1542.
50. Greenhalgh, E.S., *Failure analysis and fractography of polymer composites*. 2009, Cambridge, UK; Boca Raton, FL: Woodhead Publishing.

6 Conclusions and Recommendations for Future Work

6.1 Conclusions from this Research

1. Matrix viscosity had a small effect on long fiber orientation, and that effect was dependent on fiber concentration. At 30 wt% glass fiber (GF) the higher viscosity polypropylene (PP) had a more asymmetric orientation profile throughout the plaque and less of a shell-core-shell orientation at 90% of plaque length along the center-plane than the low viscosity PP. At 50 wt% GF the differences between the high and low viscosity samples' orientations were minimal. The HV material attained slightly higher orientation in the shell region at 40% and 90% of plaque length. Going from 30 wt% to 50 wt% caused a lower degree of flow alignment and a broader core in all the tested samples. The larger difference because of fiber concentration shows that the number of fiber-fiber interactions are a much stronger factor in orientation than viscosity.
2. Number average fiber length (L_n) and aspect ratio (a_{rn}) was a poor indication of whether two different fiber length distributions (FLDs) orientate in the same way. The orientation of CF and GF samples with similar a_{rn} were very dissimilar. However, analogous weight average length (L_w) and aspect ratio (a_{rw}) were better metrics to determine if the GF and CF samples orientated comparably. This indicates that the longer fibers in a FLD have a disproportionate impact on orientation compared to short fibers in samples with broad FLD.
3. Long CF/ carbon nanotube (CNT) / PP composites produced by injection molding exhibited significantly improved tensile and electrical properties compared to equivalent samples without CNTs. The un-functionalized CNTs interacted primarily with the CF and not the PP. This was demonstrated by the fact that the improvement obtained from adding CNTs to the composite was dependent on CF concentration. The largest improvement in properties was achieved at 40 wt% CF and 1 wt% 10 fold expanded CNTs. Under these

conditions, the addition of CNTs to the CF/ PP composite yielded a transverse to flow Young's modulus, E_2, of 14.45 GPa and a modulus parallel to the flow, E_1, of 22.1 GPa, corresponding to a 56 % and 17 % improvement compared to samples without CNT and a 14 % and 8% improvement compared to samples with untreated CNT. The larger improvement transverse to flow means that the CNTs are not aligning highly with the flow. The surface and volume conductivity both improved to $1.80\ X\ 10^{-4}\ S$ and $5.58\ X\ 10^{-5}\ S/m$, respectively, or about a threefold increase compared to samples without CNTs and a 33% and 25% improvement in conductivity compared to the untreated CNT samples. The improvement of the treated versus untreated CNTs indicated that the deagglomeration process allowed for better dispersion of the CNTs with in the composite. These improvements are comparable to those in literature for CF mat based composites using functionalized CNTs [1-5] [6-8], highlighting the importance of maintaining CNT length and obtaining a good distribution of CNTs within the composite.

6.2 Recommendations for Future Work

1. One of the things missing from literature is a good understanding of void content in long fiber composites. It is known that void content increases at higher fiber loadings and for a higher viscosity material, but a quantitative study of the voids found in these composite and the sample variability of the voids has not been performed. This type of study should be possible with micro-CT or ultrasonic imaging due to the contrast voids will provide versus the polymers. A way of predicting void content in fiber composites would yield improved predictions of mechanical properties.
2. All the samples we run orientation measurements on are 90% short shots to avoid frontal wall and packing effects. These packing effects have not been examined in depth and it would be beneficial for the modeling done with these composites to have experimental data

for how the fiber orientation evolves. Therefore, it is suggested that plaques of different fill percentages be produced and the orientation evolution examined. This would give a dynamic picture of what is happening experimentally in the injection molding process and a comparison between 90 and 100% plaque fills would allow a study of the impact of packing effects on orientation.

3. The orientation data from different viscosity matrixes and fiber concentrations should be used to test existing fiber orientation models to see if they are able to capture the changes in orientation experimentally observed.
4. While there have been comparisons of Micro-CT and MOE data, a good quantification of fiber bending has not been performed [9]. Using micro-CT it should be possible to trace fibers and their degree of bending. This would allow for the verification of Tr(**B**) in the Bead-Rod model for fiber orientation.
5. Properties were greatly improved by the addition of $scCO_2$ treated carbon nanotubes (CNT) to CF composites, but the optimum CNT loading and degree of expansion for the system was lower than expected. This may be caused by the difficulty of dispersing the CNT into the CF/PP in the injection molder. To improve CNT dispersion in the multiscale composite two different methods should be attempted. Adding the CNTs via a side feed on the injection molder could alleviate the solids flow problem in the feed that causes gradients in CNTs concentration for highly expanded CNT. Mixing the CNTs into the polymer using an extruder then pultruding the CF through the polymer CNT mixture would allow a more even dispersion of the CNTs. However, care would need to be taken to maintain CNT lengths as the CNTs would be subjected to more strain and, therefore, a larger possibility of breakage.

6. The tensile tests on multi-scale samples indicated little interaction occurred between the CNTs used and the PP. To be able to achieve larger improvements in the strength of multiscale composites, the bonding between the CNTs and polymer matrix needs to be improved. The $scCO_2$ process should be further explored to see if it can provide similar benefits with functionalized CNTs.
7. Initial results on decreasing initial pellet length used in injection molding long fiber composites indicated that narrow fiber length distributions and possibly longer fibers in the final part are achievable. In order to verify these results running this experiment at a lower fiber loading where fiber lengths tend to be longer and differences in the composite cause larger differences in fiber orientation would be useful. It would be beneficial to test if these results are applicable to different screw sizes. Initial fiber lengths should be taken on air shots to mitigate any breakage that may occur in the mold if longer fiber lengths are attained. The dispersion of the fibers in the final part should be examined to gain an additional understanding of the changes in microstructure occurring.

6.3 References

1. Bekyarova, E., et al., *Multiscale Carbon Nanotube−Carbon Fiber Reinforcement for Advanced Epoxy Composites.* Langmuir, 2007. **23**(7): p. 3970-3974.
2. Thostenson, E.T., et al., *Carbon nanotube/carbon fiber hybrid multiscale composites.* Journal of Applied Physics, 2002. **91**(9): p. 6034.
3. Jingjing, Q., et al., *Carbon nanotube integrated multifunctional multiscale composites.* Nanotechnology, 2007. **18**(27): p. 275708.
4. Kim, M., *Modeling, manufacturing, and characterization of nanocomposites and multiscale composites.* 2009.
5. Fan, Z., K.-T. Hsiao, and S.G. Advani, *Experimental investigation of dispersion during flow of multi-walled carbon nanotube/polymer suspension in fibrous porous media.* Carbon, 2004. **42**(4): p. 871-876.
6. Ashrafi, B., et al., *Processing and properties of PEEK/glass fiber laminates: Effect of addition of single-walled carbon nanotubes.* Composites Part A: Applied Science and Manufacturing, 2012. **43**(8): p. 1267-1279.
7. Díez-Pascual, A.M., et al., *High performance PEEK/carbon nanotube composites compatibilized with polysulfones-I. Structure and thermal properties.* Carbon, 2010. **48**(12): p. 3485-3499.
8. Shen, Z., et al., *The effects of carbon nanotubes on mechanical and thermal properties of woven glass fibre reinforced polyamide-6 nanocomposites.* Composites Science and Technology, 2009. **69**(2): p. 239-244.
9. Gandhi, U., et al., *Method to measure orientation of discontinuous fiber embedded in the polymer matrix from computerized tomography scan data.* Journal of Thermoplastic Composite Materials, 2015.

Appendix A: Preliminary Results on the Effect of Initial Pellet Length on the Orientation and Fiber Length of Long Fiber Composites

A.1. Introduction

In the injection molding process, long fiber composites have shown significant fiber breakage creating broad fiber length distributions (FLDs) in the resulting parts [1-5]. Work on long fiber breakage in a small single screw extruder has shown that a large portion of this breakage can occur in the feed section of the machine, where the 13 mm pellets become pinched by the flights of the screw before the polymer melts [6]. Reducing the initial pellet length should decrease the amount of mechanical breakage that occurs. The goal of this research was to test if decreasing the initial pellet size down to the fiber lengths typically observed in the final part would result in longer fibers and narrower FLDs.

A.2. Experimental

A.2.1. Materials

Sabic 50 wt% long glass fiber (GF) low viscosity polypropylene was used with 13 mm, 8 mm, and 4 mm initial pellet lengths. The 13 mm and 8 mm were pultruded pellets purchased from Sabic. The 4 mm pellets were created by manually cutting the 8 mm pellets in half.

A.2.2. Injection Molding

The material was injection molded using an Arburg Allrounder 221-55-250 with an 18 mm screw, a screw speed of 200 rpm, backpressure of 1 bar, and fill time of 2 seconds. The melt temperature profile of the injection molding machine was set to 190/210/220/220°C in the feed, compression, metering zones and nozzle respectively, while the mold temperature was held at 80°C. Short shots filling 90% of the mold were used to mitigate packing and frontal wall effects.

End-gated plaques were produced with a sprew length of 65 mm, an initial radius of 1.45 mm, and a final radius of 1.75 mm. The part consisted of a gate and a plaque region. The gate region was 80.68 mm X 6.25 mm X 6.33 mm and the plaque was 75.05 mm X 77.65 mm X 1.55 mm. The first 10 plaques from each run were discarded to ensure that the machine was operating at equilibrium.

A.2.3. Fiber Length

Representative samples of fibers were pulled out of the center of injection molded parts using the epoxy method developed by Kunc et al. [4]. After burn off fibers were imaged using a desktop scanner (Epson V800 photo) at 6000 dpi. Fiber lengths were manually measured for at least two samples and 2000 fibers per sample were measured at each condition.

A.2.4. Orientation Measurements

Samples for orientation analysis were marked, cut, polished, and plasma etched following the technique developed by Velez-Garcia et al. [7]. Fiber orientation was examined at 0, 10, 40, and 90 % of the part length along the center plane. Additionally, fiber orientation at 40% of the part length and 50 and 90 % of plaque width was examined. The areas of the plaque examined are shown in Figure A-1. A 2 mm x 2 mm area was imaged with an optical microscope (Nikon Eclipse LV100) at a resolution of 0.25 µm per pixel. Fiber orientation was analyzed using the method of ellipses and a custom Matlab program [8, 9].

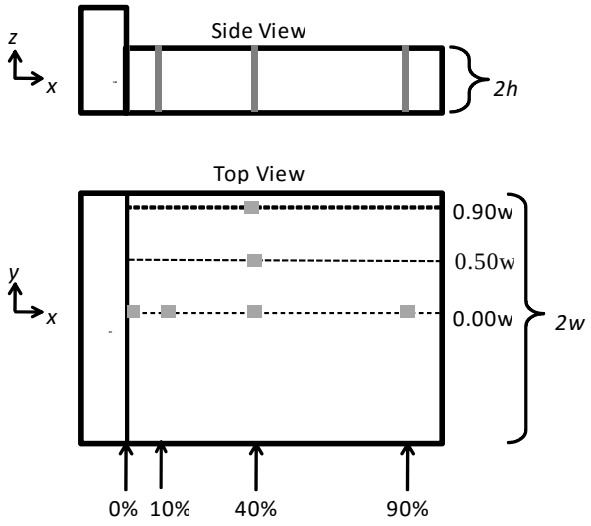

Figure A-1: Experimental geometry and the selected inspection locations for the end-gated plaque. Grey squares represent the inspection locations.

A.3. Results

A.3.1. Fiber Length

Table A.1: Fiber lengths in an end-gated plaque from 50 wt% GF PP with different initial pellet lengths

Length After Processing	Initial Pellet Length		
	13 mm	8 mm	4 mm
Number Average Length (mm)	0.99 ± 0.03	1.76 ± 0.05	0.75 ± 0.04
Weight Average Length (mm)	3.22 ± 0.08	4.05 ± 0.20	1.18 ± 0.02
Dispersity	3.2	2.3	1.57

The FLD was narrower and number average fiber length (L_n) and weight average fiber length (L_w) increased when initial pellet length was decreased from a 13 mm to 8 mm, given in Table A.1. Based on the full FLDs for samples, shown in Figure A-2, more fibers in the 8 mm initial pellet length samples (IPLS) made it through the injection molding process without breaking than in the other samples tested. The lack of fibers between an aspect ratio of 200 and 560 is an indication that most of the fibers that made it through intact were in bundles. In pultruded pellets, the fibers are in a tow in the center of the pellet. At high concentrations, the fibers in the tow have difficulty dispersing well leaving fiber bundles in the final part. Even though bundles decrease fiber breakage they create inconsistent properties in the final part[10].

As the L_w for the 8 mm IPLS was close to 4 mm it was thought that the 4 mm IPLS might yield minimal fiber breakage and a narrow fiber length distribution. The 4 mm IPLS had a narrower FLD, but L_n and L_w was shorter than for the other samples tested. It is possible that the fibers in the 4 mm IPLS dispersed better in the composite and the lack of reinforcement from neighboring fibers led to increased breakage.

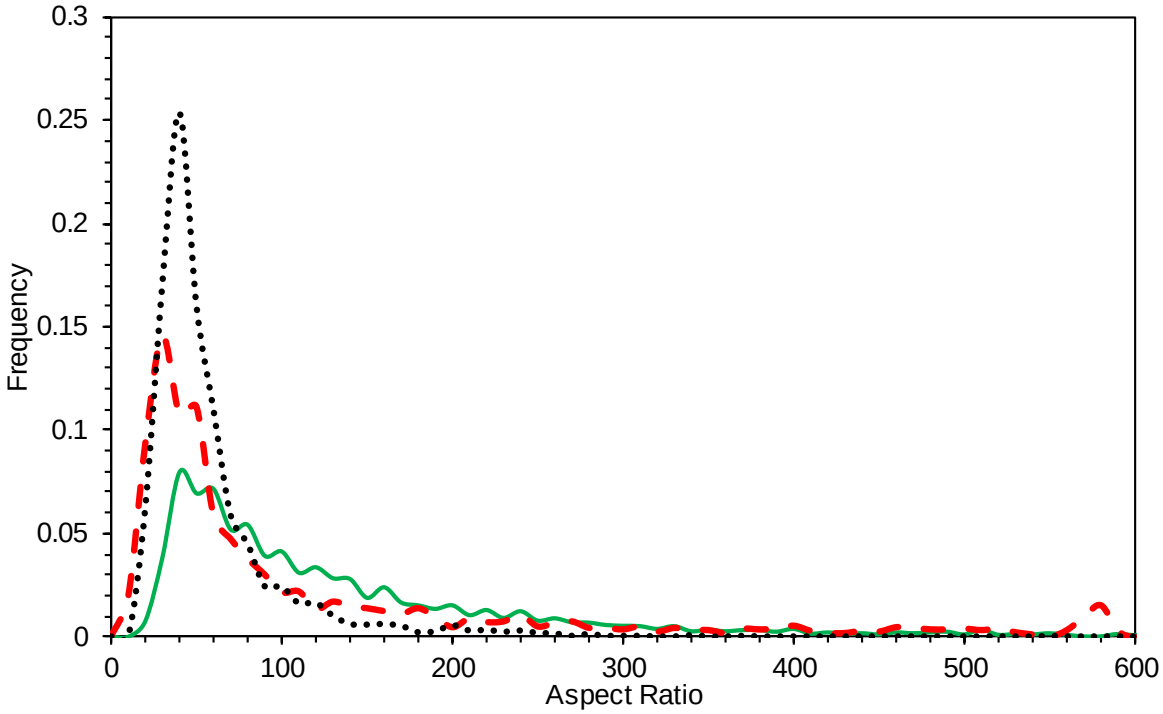

Figure A-2: Normalized fiber length distributions for (•) 4 mm, (- -) 8 mm, and (—) 13 mm initial pellet lengths.

A.3.2. Orientation Results

All the composites tested gave a shell-core-shell orientation profile with a high degree of flow alignment near the mold wall and alignment transverse to flow in the center of the part [11]. The transverse to flow component of the orientation tensor, A_{22}, was a mirror image of primary flow direction component, A_{11}, and the through thickness direction component, A_{33} ,was small. Therefore, A_{11} was chosen as the point of comparison for effect of initial pellet length on orientation.

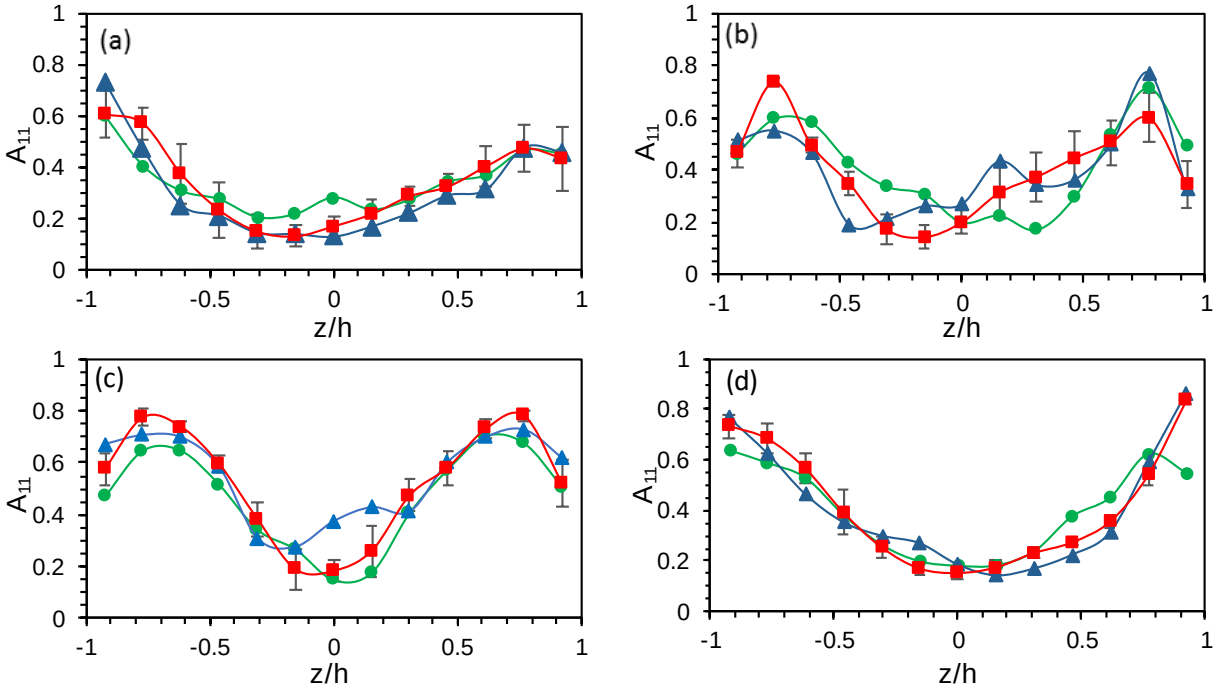

Figure A-3: A_{11} as a function of part thickness along the center-plane for 50 wt % GF at (a) 0 %, (b) 10%, (c) 40%, and (d) 90% plaque length with initial pellet lengths of ■ 4 mm, ▲ 8 mm, and ● 13 mm

There was little variance in orientation between the different IPLS along the center plane, shown in Figure A-3. Representative error bars are only shown for the 4 mm IPLS for ease of reading and are the standard deviation of five samples. It is interesting to note that these three samples were almost identical at 0 % and 90 % of plaque length, along the center plane. These locations have proven to be where the largest differences in orientation occurred for previously tested samples. The 13 mm samples had a slightly lower degree of orientation through the center of the part at 0 % plaque length and near the mold wall at 90 % of plaque length, but these differences were small. At 10 % and 40 % of plaque length along the center plane, the 8 mm IPLS had a different orientation than the 13 mm or 4 mm IPLS in the core of the part and a similar orientation in the shell. Part of the difference in orientation may have been caused by fibers in the core of a plaque being longer than those in the shell [1] [12]. Longer fibers have a lower degree of fiber orientation and the 8 mm IPLS have the largest L_w of any of the samples tested [13]. But, the differences in L_w between samples was expected to have caused a larger difference in orientation throughout the part. These results suggest that the fiber length between the three samples was closer

than the measured FLD indicated. All fiber length measurements were taken in the center of the plaque, as previous work with 13 mm IPLS showed that FLDs did not change throughout the plaque. This may not have been the case for these 8 mm IPLS. If the 8 mm IPLS had more fiber bundles in the center of plaque than at other locations, they could have generated non-representative length measurements.

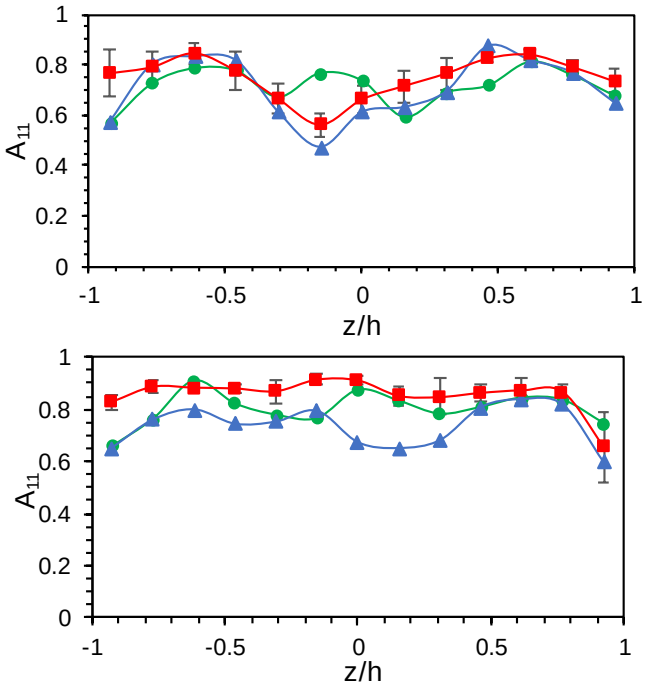

Figure A-4: A_{11} component of the orientation tensor as a function of part thickness at 40 % plaque length and 50%(bottom) and 90 % (top) width for 50 wt % GF PP with an initial pellet lengths of ■ 4 mm, ▲ 8 mm, and ● 13 mm

At 40% of plaque length and 50% of plaque width (half way between the center plane and mold wall), there was no discernable trend in the fiber orientation of the composites, shown in Figure A-4. All samples were more flow aligned than along the center plane, but the variance between the different IPLS' orientations were minimal and inconsistent. At 40% of plaque length and 90% of plaque width, all samples possessed the expected highly flow aligned fiber orientation. The 4 mm IPLS, which had the shortest fiber lengths, attained the highest degree of fiber alignment and the 8 mm IPLS had the lowest degree of flow alignment.

A.4. Conclusions

Decreasing the initial pellet length of long fiber pultruded composites used in small injection molding machines can increase the number average fiber length, L_n, weight average fiber length, L_w, and result in a narrower fiber length distribution in the final part. Decreasing the initial pellet lengths from 13 mm to 8 mm lead to a L_w of 4.02 mm and a L_n of 1.76 mm corresponding to a 78 % and 24 % improvement over the 13 mm IPLS. Further decreasing the initial pellet length to 4 mm narrowed the FLD, but caused a severe decrease in L_w and L_n to 0.75 and 1.18 mm, respectively. Based on the full FLD it is likely that the long L_w in the 8 mm IPLS was created by fiber bundles. The shorter fibers in the 4 mm IPLS was likely because of increase fiber dispersion. However, analysis of the volume fraction of fibers in each bin of the images analyzed, and distance between each fiber and its nearest neighbor is needed to test this theory. The fact that the 8 mm IPLS had the longest final FLD suggests that for a given set of processing conditions there may be an optimum initial pellet size to maintain longer fibers.

There was little change in final fiber orientation caused by the different initial pellet lengths tested. At 10% and 40 % of plaque length along the center plane, the 8 mm IPLS had less alignment in the core but nearly identical alignment in the shell regions to the other samples. Part of this lack of difference could be the high concentration of fibers in the samples. As shown in Chapter 4, at high fiber loadings fiber-fiber interaction can dominate the orientation kinetics and reduce differences that may appear at lower fiber concentrations. It is also possible that the 8 mm IPLS had a larger concentration of fiber bundles in the center of the plaque, which is where the FLD measurements were taken. If this was the case, the samples could be closer in FLDs at other locations in the plaque and the small differences in orientation observed would be expected. In order to test this, FLD at multiple locations in the 8 mm IPLS should to be taken to ensure that the FLD is not changing throughout the plaque.

Running this experiment at a lower fiber loading where fiber lengths tend to be longer and differences in the composite cause larger differences in fiber orientation would be useful. It would also

be beneficial to test if final fiber lengths can be improved through changing initial pellet lengths in different screw sizes. Initial fiber lengths should be taken on air shots to mitigate any breakage that may occur in the mold if longer fiber lengths are attained.

A.5. References

1. Bailey, R. and H. Kraft, *A Study of Fibre Attrition in the Processing of Long Fibre Reinforced Thermoplastics.* Int.Polym.Process, 1987. **2**(2): p. 94-101.
2. Barkoula, N.M., S.K. Garkhail, and T. Peijs, *Effect of Compounding and Injection Molding on the Mechanical Properties of Flax Fiber Polypropylene Composites.* Journal of Reinforced Plastics and Composites, 2010. **29**(9): p. 1366-1385.
3. Hassan, A., et al., *Tensile, Impact and Fiber Length Properties of Injection-Molded Short and Long Glass Fiber-Reinforced Polyamide 6,6 Composites.* Journal of Reinforced Plastics and Composites, 2004. **23**(9): p. 969-986.
4. Kunc, V., et al. *Fiber Length Distribution Measurement for long Glass and Varbon Fiber Reinforced Injection Molded Thermoplastics*. in *SPE Automotive*. 2007. Troy, MI.
5. Nguyen, B.N., et al., *Fiber Length and Orientation in Long-Fiber Injection-Molded Thermoplastics — Part I: Modeling of Microstructure and Elastic Properties.* Journal of Composite Materials, 2008. **42**(10): p. 1003-1029.
6. Chen, H., M. Cieslinski, and D.G. Baird. *Progress in modeling long glass and carbon fiber breakage during injection molding*. in *PROCEEDINGS OF PPS-30: The 30th International Conference of the Polymer Processing Society–Conference Papers*. 2015. AIP Publishing.
7. Vélez-García, G.M., et al., *Sample preparation and image acquisition using optical-reflective microscopy in the measurement of fiber orientation in thermoplastic composites.* Journal of Microscopy, 2012. **248**(1): p. 23-33.
8. Bay, R.S. and C.L. Tucker, *Stereological measurement and error estimates for three-dimensional fiber orientation.* Polymer Engineering & Science, 1992. **32**(4): p. 240-253.
9. Vélez-García, G.M., et al., *Unambiguous orientation in short fiber composites over small sampling area in a center-gated disk.* Composites Part A: Applied Science and Manufacturing, 2012. **43**(1): p. 104-113.
10. Vu-Khanh, T., et al., *The effects of injection molding on the mechanical behavior of long-fiber reinforced PBT/PET blends.* Composites Science and Technology, 1991. **40**(4): p. 423-435.
11. Darlington, M. and P. McGinley, *Fibre orientation distribution in short fibre reinforced plastics.* Journal of Materials Science, 1975. **10**(5): p. 906-910.
12. O'Regan, D. and M. Akay, *The distribution of fibre lengths in injection moulded polyamide composite components.* Journal of Materials Processing Tech, 1996. **56**(1): p. 282-291.
13. Toll, S. and P.O. Andersson, *Microstructure of long- and short-fiber reinforced injection molded polyamide.* Polymer Composites, 1993. **14**(2): p. 116-125.

Appendix B: Multiscale Tensile and Conductivity Results

Table B.1: Tensile test results for CF concentrations for PP multiscale composites with 1 wt% CNT

Carbon Fiber wt %	CNT Content	Flow Direction			Transverse to flow direction		
		Young's Modulus (Gpa)	Strength (mPa)	% elongation at break	Young's Modulus (Gpa)	Tensile Strength (mPa)	% elongation at break
0	0	1.98 ± 0.19	29.87±0.44	28.98 ± 0.67	2.08±0.08	30.57±0.75	12.64 ± 3.88
0	1 wt% DB	2.26±0.09	30.79±1.27	4.80 ± 0.77	2.39±0.17	30.20±0.85	2.51 ± 0.22
0	1 wt% 10x	2.23±0.18	31.58±1.11	3.31 ± 0.42	2.25±0.11	31.03±1.67	2.45± 0.07
20	0	10.23±0.68	54.25±4.95	0.39 ± 0.05	8.48±0.50	30.99±2.55	0.21 ± 0.02
20	1 wt% DB	10.43±0.56	67.54±4.31	0.39 ± 0.03	8.51±0.81	39.46±3.04	0.21 ± 0.02
20	1 wt% 10x	10.64±0.54	66.63±0.66	0.36 ± 0.001	8.58±0.58	37.85±1.30	0.22 ± 0.01
30	0	11.60±0.70	56.54±1.79	0.26 ± 0.03	9.10±0.73	32.43±2.55	0.18 ± 0.01
30	1 wt% DB	13.06±0.33	53.4±4.80	0.20 ± 0.03	9.11±0.88	30.62±0.96	0.17± 0.01
30	1 wt% 10x	13.89±0.52	54.13±2.04	0.20 ± 0.03	8.76±0.34	30.89±1.26	0.18 ± 0.01
40	0	18.86±0.97	63.29±5.80	0.27 ± 0.03	9.25±0.98	34.41±1.38	0.16 ± 0.02
40	1 wt% DB	20.38±0.63	70.64±2.28	0.22 ± 0.02	12.72±0.82	28.66±2.33	0.13±0.04
40	1 wt% 10x	22.10±0.39	67.96±3.40	0.17 ± 0.03	14.45±0.66	29.83±1.26	0.13±0.02
50	0	23.53±1.33	44.69±3.58	0.12 ± 0.02	12.39±1.39	18.58±0.59	0.07±0.01
50	1 wt% DB	24.85±3.16	33.61±4.29	0.09 ± 0.02	12.37±1.15	15.82±0.63	0.07±0.01
50	1 wt% 10x	21.86±2.83	34.12±1.03	0.11 ± 0.02	14.15±2.53	16.82±2.00	0.08±0.01

Table B.2: Modulus results from CNT expansion at 40 wt% CF 1 wt% CNT PP

40 wt% CF PP 1% CNT				
Degree of expansion	Modulus Vertical(MPa)	error	Modulus Horizontal (MPa)	error
0	20.38	0.626	9.251	0.98
4.3	19.12	1.327	10.68	0.65
10	22.1	0.392	14.45	0.663
30	17.82	0.871	11.67	1.686
50	16.92	0.691	11.42	0.827

Table B.3: Young's modulus results from different CNT loadings at 30 and 40 wt% CF PP

CNT Concentration/ modulus (GPa)								
CNT Concentration	40% DB		40% 10X		30% DB		30% 10X	
	V	H	V	H	V	H	V	H
0	18.86	9.251	18.86	9.251	11.6	9.10	11.6	9.10
0.5	16.55	10.86	19.71	12.33				
1	20.38	12.72	22.10	14.45	13.06	9.11	13.89	8.76
2	17.74	11.62	17.88	13.17	11.85	9.56	12.35	9.29

Table B.4: Young's modulus error results from different CNT loadings at 30 and 40 wt% CF PP

CNT Concentration/ Modulus error (GPa)								
CNT Concentration	40% DB		40% 10X		30% DB		30% 10X	
	V	H	V	H	V	H	V	H
0	0.968	0.98	0.97	0.98	0.71	0.73	0.71	0.73
0.5	2.53	1.81	0.64	1.01				
1	0.63	0.82	0.39	0.66	0.33	0.88	0.52	0.34
2	1.81	2.73	0.95	1.92	0.93	1.98	1.04	0.94

Table B.5: Tensile strength for different CNT concentrations at 30 and 40 wt% CF PP

	CNT Concentration / Strength (MPa)							
CNT Concentration	40% DB		40% 10X		30% DB		30% 10X	
	V	H	V	H	V	H	V	H
0	63.29	34.41	63.29	34.41	56.54	32.43	56.54	32.43
0.5	58.59	27.59	68.44	32.78				
1	56.54	28.66	67.96	29.83	53.4	30.62	54.13	30.89
2	58.19	23.49	54.7	28.71	41.48	26.79	47.06	25.33

Table B.6: Tensile strength error for different CNT concentrations at 30 and 40 wt% CF PP

	CNT Concentration/ strength error (MPa)							
CNT Concentration	40% DB		40% 10X		30% DB		30% 10X	
	V	H	V	H	V	H	V	H
0	6.9	1.38	6.9	1.38	1.79	2.55	1.79	2.55
0.5	5.72	2.16	6.83	2.844				
1	2.28	2.33	3.4	1.26	4.8	0.96	2.04	0.48
2	2.69	2.73	4.43	2.67	2.98	1.98	2.02	1.72

Table B.7: Elongation at break for different degrees of CNT expansion in 40wt% CF 1 wt% CNT PP

40wt% CF PP 1wt% CNT Displacement (mm)				
Degree of expansion	Vertical	error	Horizontal	error
0	0.056	0.0052	0.0326	0.0042
4.3	0.0497	0.0068	0.0249	0.0048
10	0.0435	0.0078	0.0326	0.006
30	0.0425	0.0107	0.0281	0.0009
50	0.0482	0.0073	0.0326	0.0118

Table B.8: Elongation at break for different CNT loadings in 30 and 40 wt% CF PP

CNT Concentration / displacement (mm)								
CNT Concentration	40% DB		40% 10X		30% DB		30% 10X	
	V	H	V	H	V	H	V	H
0	0.069	0.0416	0.069	0.0416	0.066	0.0443	0.066	0.0443
0.5	0.0513	0.0339	0.0476	0.032				
1	0.056	0.0326	0.0435	0.0326	0.0519	0.0423	0.0517	0.0455
2	0.0468	0.0239	0.0441	0.0289	0.0443	0.0371	0.0516	0.0362

Table B.9: Elongation at break error for different CNT loadings in 30 and 40 wt% CF PP

CNT Concentration / displacement error (mm)								
CNT Concentration	*40% DB*		*40% 10X*		*30% DB*		*30% 10X*	
	V	H	V	H	V	H	V	H
0	0.0073	0.0061	0.0073	0.0061	0.0067	0.0021	0.0067	0.0021
0.5	0.0027	0.0049	0.0084	0.0053				
1	0.0052	0.0042	0.0078	0.006	0.0066	0.0019	0.007	0.0022
2	0.0037	0.0036	0.004	0.0037	0.0057	0.0035	0.0043	0.0018

Table B.10: Surface conductivity at different CF loadings for 1 wt% CNT PP composites

Surface Conductivity (S)						
Fiber Concentration	0% CNT	0 % error	1 wt % DB CNT	DB error	1 wt% 10X CNT	10X error
20	3.72E-06	2.76E-07	1.42E-05	4.38E-06	2.09E-05	1.61E-06
30	3.04E-05	1.64E-06	1.37E-04	3.07E-05	2.09E-04	2.68E-05
40	4.45E-05	1.24E-05	1.45E-04	3.97E-05	1.80E-04	2.69E-05
50	5.43E-04	1.05E-04	6.67E-04	3.50E-05	1.12E-03	8.8 E-5

Table B.11: Volume conductivity at different CF loadings for 1 wt% CNT PP composites

Volume Conductivity (S/m)						
Fiber Concentration	0% CNT	0% error	1 wt% DB CNT	DB error	1 wt% 10X CNT	10x error
20	1.45E-06	2.76E-07	5.48E-06	1.32E-06	6.06E-06	1.61E-06
30	1.29E-05	1.64E-06	2.40E-05	6.92E-06	5.02E-05	2.68E-05
40	1.44E-05	1.92E-06	4.18E-05	2.66E-05	5.58E-05	2.69E-05
50	1.63E-04	2.90E-05	7.49E-05	8.59E-06	3.22E-04	3.40E-05

Table B.12: Surface conductivity at different CNT concentrations in 30 wt% CF PP

Surface Conductivity 30 wt% CF (S)				
CNT Concentration	DB	DB error	10X	10X error
0	3.04E-05	1.64E-06	3.04E-05	1.64E-06
1	1.37E-04	3.07E-05	2.09E-04	2.68E-05
2	8.94E-05	4.11E-05	1.35E-04	3.58E-05

Table B.13: Surface conductivity at different CNT concentrations in 30 wt% CF PP

Surface Conductivity 40 wt% CF (S)				
CNT Concentration	DB	DB error	10X	10x error
0	4.45E-05	2.76E-07	4.45E-05	2.76E-07
0.5	5.89E-05	1.05E-05	7.43E-05	1.07E-05
1	1.45E-04	3.97E-05	1.80E-04	2.69E-05
2	6.22E-05	1.01E-05	1.82E-04	2.67E-05

Table B.14: Volume conductivity at different CNT concentrations in 40 wt% CF PP

Volume Conductivity 40 wt% CF				
CNT Concentration	DB	DB error	10X	10x error
0	1.44E-05	1.24E-05	1.44E-05	1.24E-05
0.5	1.23E-05	3.37E-06	8.07E-06	2.38E-06
1	4.18E-05	3.97E-05	5.58E-05	2.69E-05
2	5.59E-05	1.86E-05	5.86E-05	5.82E-06

Table B.15: Volume conductivity at different CNT concentrations in 30 wt% CF PP

Volume Conductivity 30 wt% CF				
CNT Concentration	DB	DB error	10X	10 x error
0	1.29E-05	1.64E-06	1.29E-05	1.64E-06
1	2.40E-05	6.92E-06	5.02E-05	3.60E-06
2	3.40E-05	3.40E-06	4.36E-05	3.65E-06

Table B.16: Surface and volume conductivity at different CNT degrees of expansion in 40 wt% CF 1 wt% CNT PP

40 wt% CF 1% CNT Conductivity				
CNT Expansion	Surface (S)	error	Volume (S/m)	error
0	1.45E-04	3.97E-05	4.18E-05	3.97E-06
4.3	1.42E-04	1.01E-05	4.58E-05	1.66E-05
10	1.80E-04	1.69E-05	5.58E-05	1.34E-05
30	1.65E-04	1.17E-05	1.05E-05	3.07E-06
50	1.07E-04	3.68E-05	6.76E-06	4.99E-07

Appendix C: Rheological Data

Table C.1: Sabic HV dynamic rheology

Sabic HV Dynamic Data at 220/493					Sabic HV Dynamic at 180C/453K			
W (rad/s)	G'	G''	tan(d)	η*	G'	G''	tan(d)	h*
rad/s	Pa	Pa		Pa-s	Pa	Pa		Pa-s
0.10	1.8	69.3	38.1	693.5	5.3	166.2	31.5	1663.1
0.16					14.2	256.4	18.0	1620.2
0.25	7.8	182.2	23.3	726.0	26.5	402.0	15.2	1603.9
0.40	17.6	281.1	16.0	707.4	61.7	622.1	10.1	1570.2
0.63	31.7	437.8	13.8	695.7	124.6	958.6	7.7	1532.0
1.00	67.1	683.1	10.2	686.3	245.3	1459.5	5.9	1479.9
1.58	141.2	1047.6	7.4	666.9	462.2	2186.1	4.7	1409.8
2.51	278.0	1583.3	5.7	639.9	844.5	3216.3	3.8	1323.7
3.98	521.7	2370.2	4.5	609.6	1489.5	4633.5	3.1	1222.5
6.31	955.5	3481.9	3.6	572.2	2547.0	6533.2	2.6	1111.3
10.00	1670.1	4995.0	3.0	526.6	4154.7	8993.0	2.2	990.6
15.85	2825.0	7019.3	2.5	477.4	6537.5	12051.8	1.8	865.0
25.12	4574.9	9614.0	2.1	423.8	9919.7	15744.8	1.6	740.8
39.81	7152.2	12815.6	1.8	368.6	14517.2	20018.3	1.4	621.1
63.10	10758.4	16628.2	1.5	313.9	20514.3	24804.9	1.2	510.1
100.00	15597.9	20954.5	1.3	261.2	28047.5	29861.4	1.1	409.7

Table C.2: Plasticomp dynamic PP data

Plasticomp Dynamic Data 180C / 453K				Plasticomp PP 200C/ 473.15K			Platicomp 220 C		
W	G'	G"	h*	G'	G"	h*	G'	G"	h*
rad/s	Pa	Pa	Pa-s	Pa	Pa	Pa-s	Pa	Pa	Pa-s
0.10	1.1	83.9	839.0	0.8	56.6	566.1	0.5	55.3	553.1
0.13	1.5	105.5	838.1	0.9	70.7	561.3	0.7	69.6	552.7
0.16	2.3	132.6	836.9	0.9	88.2	556.8	1.1	87.6	552.6
0.20	4.3	166.6	835.1	2.2	110.0	551.6	1.8	110.2	552.3
0.25	6.0	208.9	831.8	3.1	137.9	549.3	2.8	138.4	551.2
0.32	8.9	261.9	828.8	4.2	173.8	549.7	4.4	174.2	551.0
0.40	13.8	328.5	825.8	5.9	217.8	547.4	6.7	218.7	549.6
0.50	21.1	411.2	821.6	9.6	272.9	544.8	10.1	274.8	548.8
0.63	31.1	515.0	817.7	14.6	343.0	544.2	15.4	344.4	546.4
0.79	47.2	643.3	812.1	21.2	429.2	541.1	23.3	431.5	544.0
1.00	68.9	801.4	804.4	32.3	537.7	538.8	34.6	540.0	541.2
1.26	101.3	997.4	796.4	48.0	671.9	535.1	51.3	674.7	537.5
1.58	145.9	1237.8	786.5	70.9	837.1	530.1	75.1	840.7	532.6
2.00	209.8	1531.8	775.0	104.4	1041.6	524.7	108.7	1045.9	527.1
2.51	295.6	1887.9	760.8	158.6	1297.5	520.5	157.1	1296.5	520.0
3.16	417.6	2327.7	748.0	220.3	1600.0	510.8	224.5	1603.2	512.0
3.98	579.4	2835.8	727.1	304.7	1972.6	501.5	316.6	1974.7	502.4
5.01	806.8	3450.0	707.1	431.0	2426.1	491.7	443.5	2423.7	491.7
6.31	1081.8	4180.1	684.5	596.4	2968.8	480.0	612.5	2963.6	479.7
7.94	1464.6	5037.4	660.6	831.7	3616.9	467.3	837.8	3608.6	466.5
10.00	1948.5	6031.8	634.0	1134.6	4375.6	452.1	1136.1	4364.5	451.1
12.59	2578.1	7182.8	606.3	1537.8	5273.8	436.5	1524.0	5258.2	435.0
15.85	3350.4	8484.4	575.7	2032.6	6312.3	418.5	2019.0	6299.7	417.5
19.95	4310.7	9960.5	544.1	2674.2	7509.7	399.6	2649.9	7494.0	398.5
25.11	5508.3	11604.6	511.5	3499.9	8874.0	379.9	3439.4	8869.5	378.8
31.61	6958.7	13444.7	478.9	4507.4	10421.8	359.2			
39.80	8682.3	15450.8	445.3	5755.0	12135.1	337.5			
50.10	10734.8	17615.6	411.7	7259.2	14052.0	315.7			
63.08	13132.9	19937.1	378.5	9057.1	16140.8	293.4			
79.41	15897.9	22396.1	345.9	11185.9	18383.5	271.0			
100.00	19075.3	24939.2	314.0	13679.8	20771.2	248.7			

Table C.3: Plasticomp PP steady shear data

Plasticomp 220 C Steady Shear	
Rate	h
s-1	Pa-s
0.010	536.7
0.013	528.0
0.016	522.3
0.020	525.7
0.025	526.6
0.032	528.2
0.040	530.3
0.050	531.1
0.063	532.8
0.079	534.1
0.100	535.5
0.126	536.7
0.158	536.1
0.199	535.9
0.251	536.2
0.316	538.2
0.398	539.1
0.501	537.0
0.631	538.0
0.794	535.6
1.000	533.7

Table C.4: Plasticomp PP capillary data

Plasticomp Capillary 220 c	
Shear Rate	Viscosity
1/s	Pa S
67.65	365.14
161.51	243.79
338.38	174.95
917.14	99.96
2150.61	53.82
4426.18	32.59
11957.76	15.51
25626.91	8.57
63168.62	3.92

Table C.5: Sabic Low viscosity dynamic rheology data

	180 °C	190 °C	200 °C	220 °C
W	h*	h*	h*	h*
rad/s	Pa-s	Pa-s	Pa-s	Pa-s
0.10	371.6	293.0	228.0	153.9
0.13	371.5	292.6	226.3	153.7
0.16	371.1	292.8	225.6	153.5
0.20	371.1	292.7	225.2	153.3
0.25	370.7	292.2	224.8	153.1
0.32	370.7	292.3	224.8	153.0
0.40	369.9	292.2	224.5	154.4
0.50	369.3	292.0	224.3	154.2
0.63	368.9	291.8	224.3	154.1
0.79	368.1	291.4	223.1	153.9
1.00	367.4	292.0	223.0	152.8
1.26	365.8	291.4	222.3	152.7
1.58	364.0	290.4	221.9	152.5
2.00	362.1	289.1	221.3	152.2
2.51	359.6	287.7	220.4	151.7
3.16	356.6	285.6	219.4	151.3
3.98	352.8	283.1	218.0	150.7
5.01	348.1	280.0	216.1	149.9
6.31	342.6	276.3	213.9	148.8
7.94	336.2	272.0	211.3	147.6
10.00	328.5	266.8	208.0	146.0
12.59	320.1	262.1	203.9	142.9
15.85	310.4	255.1	199.5	140.7
19.95	299.6	247.2	194.3	137.9
25.11	287.9	238.5	188.6	134.8
31.61	275.2	229.1	182.2	131.2
39.80	261.7	218.8	175.1	127.1
50.10	247.6	208.0	167.5	122.5
63.08	232.8	196.5	159.3	117.5
79.41	217.5	184.6	150.6	112.1
100.00	202.0	172.3	141.5	106.3

Table C.6: Sabic LV capillary data

180°C		220°C	
gamma_dot	eta	gamma_dot	eta
(1/s)	Pa-s	(1/s)	Pa-s
18.49	343.9	18.1	201.7
36.98	225.5	36.2	143.3
92.44	201.3	90.5	117.3
184.89	154.7	181.0	91.4
369.78	102.3	362.0	63.6
924.44	70.3	905.0	40.0
1848.88	48.8	1810.1	26.7
3697.76	29.2	3620.1	19.1
9244.40	13.9	9050.3	10.5
18488.80	8.2	18100.6	6.3
36977.60	4.8	36201.2	3.8

Appendix D: Fiber Lengths

Table D.1: End-gated plaque fiber lengths at 30 vol% long fiber

Fiber Type	Back Pressure (bar)	Screw Speed (RPM)	Number Average Length (mm)	Weight Average Length (mm)	Number Average Aspect Ratio	Weight Average Aspect Ratio	Dispersity Index
CF	1	200	0.36 ± 0.01	1.71 ± 0.05	51.1	244	4.75
GF	1	50	0.81 ± 0.10	1.35 ± 0.22	58.1	96	1.66
GF	1	200	0.99 ± 0.03	3.22 ± 0.08	70.4	230	3.25
GF	5	50	1.03 ± 0.15	1.79 ± 0.17	73.8	128	1.74
GF	5	200	0.77 ± 0.11	1.66 ± 0.31	55.0	119	2.16
GF	10	50	0.74 ± 0.05	1.21 ± 0.02	53.7	86	1.63
GF	10	200	0.40 ± 0.02	0.74 ± 0.04	28.8	53	1.84
GF	12.5	200	0.35 ± 0.01	0.63 ± 0.1	24.9	45	1.81

Table D.2: Fiber length distribution backpressure results

	Number of Fibers			
aspect ratio	GF 1 bar 200 rpm	GF 5 bar 200 rpm	GF 10 bar 200 rpm	44 wt% CF
0	2	0	0	0
5	0	0	0	0
10	39	0	499	1946
15	246	37	429	3200
20	558	187	342	2157
25	540	231	306	1176
30	487	442	243	639
35	282	426	211	409
40	251	395	138	304
45	162	198	133	202
50	171	229	94	173
55	108	170	78	156
60	110	104	70	88
65	94	56	47	89
70	97	74	37	75
75	79	51	27	70
80	75	39	19	55
85	52	15	15	54
90	75	27	9	36
95	56	31	8	47
100	63	25	10	35
105	54	11	9	31
110	60	26	2	25
115	49	10	5	12
120	38	18	0	22
125	46	17	3	18
130	45	8	2	16
135	33	6	2	17
140	44	10	0	19
145	25	5	2	22
150	39	5	0	10
155	32	10	5	8
160	24	9	4	12
165	19	4	3	8
170	25	7	0	6
175	29	5	1	16

180	30	7	1	8
185	29	5	0	3
190	24	14	0	2
195	21	10	1	13
200	18	4	0	9
205	15	3	0	9
210	21	4	0	6
215	11	6	0	5
220	7	2	1	3
225	14	1	0	6
230	14	3	1	4
235	8	1	0	1
240	17	0	1	8
245	13	5	1	5
250	7	2	0	4
255	2	4	0	4
260	4	6	1	4
265	5	5	1	2
270	1	0	1	4
275	1	3	1	0
280	5	1	0	1
285	3	2	0	2
290	1	1	0	2
295	1	4	1	1
300	0	4	0	3
305	3	2	0	2
310	1	3	0	1
315	2	2	0	1
320	3	0	0	2
325	2	3	0	1
330	1	0	0	0
335	1	2	0	1
340	0	0	0	3
345	1	2	0	0
350	0	2	0	2
355	0	2	0	2
360	0	0	0	3
365	0	3	1	1
370	0	1	0	2
375	0	1	0	1
380	0	2	0	0

385	1	0	0	0
390	1	0	0	0
395	0	0	0	1
400	0	2	0	0
Longer	2	16	0	3

Table D.3: Fiber length distribution matrix viscosity and concentration effects

	Number of Fibers			
Aspect Ratio	50 wt% GF LV	50 wt % GF HV	30% GF HV	30 % GF LV
0	0	2	2	0
10	0	0	0	0
20	40	39	39	40
30	202	246	246	202
40	419	558	558	419
50	365	540	540	365
60	376	487	487	376
70	273	282	282	273
80	285	251	251	285
90	206	162	162	206
100	217	171	171	217
110	163	108	108	163
120	177	110	110	177
130	149	94	94	149
140	147	97	97	147
150	99	79	79	99
160	126	75	75	126
170	87	52	52	87
180	80	75	75	80
190	71	56	56	71
200	80	63	63	80
210	55	54	54	55
220	68	60	60	68
230	48	49	49	48
240	65	38	38	65
250	41	46	46	41
260	47	45	45	47
270	37	33	33	37
280	36	44	44	36
290	30	25	25	30
300	28	39	39	28

310	27	32	32	27
320	20	24	24	20
330	27	19	19	27
340	14	25	25	14
350	18	29	29	18
360	14	30	30	14
370	17	29	29	17
380	17	24	24	17
390	13	21	21	13
400	20	18	18	20
410	8	15	15	8
420	11	21	21	11
430	7	11	11	7
440	9	7	7	9
450	6	14	14	6
460	11	14	14	11
470	9	8	8	9
480	11	17	17	11
490	13	13	13	13
500	6	7	7	6
510	18	2	2	18
520	5	4	4	5
530	7	5	5	7
540	6	1	1	6
550	9	1	1	9
560	5	5	5	5
570	1	3	3	1
580	1	1	1	1
590	7	1	1	7
600	4	0	0	4
610	5	3	3	5
620	1	1	1	1
630	1	2	2	1
640	2	3	3	2
650	1	2	2	1
660	3	1	1	3
670	4	1	1	4
680	2	0	0	2
690	1	1	1	1
700	0	0	0	0
710	0	0	0	0

720	1	0	0	1
730	1	0	0	1
740	0	0	0	0
750	0	0	0	0
760	0	0	0	0
770	0	1	1	0
780	1	1	1	1
790	2	0	0	2
800	0	0	0	0
810	1	0	0	1
820	1	1	1	1
830	0	1	1	0
840	0	0	0	0
850	1	0	0	1
860	0	0	0	0
870	0	0	0	0
880	2	0	0	2
890	0	0	0	0
900	2	0	0	2
910	1	0	0	1
920	2	0	0	2
930	4	0	0	4
940	1	0	0	1
950	0	0	0	0
960	0	0	0	0
970	0	0	0	0
980	0	0	0	0
990	0	0	0	0
1000	0	0	0	0
More	1	0	0	1

Appendix E: Orientation Measurements

Unless otherwise stated samples had an initial pellet length of 13 mm and were injection molded at 1 bar and 200 rpm. A_{ijkl} terms are available upon request from Professor Baird.

Table E.1: Orientation measurements 30 wt% GF low viscosity PP at 0L 0W

Z/H	A11	A12	A13	A22	A23	A33
0.933	0.560	-0.077	0.012	0.428	-0.027	0.013
0.800	0.419	-0.082	0.008	0.562	-0.010	0.019
0.667	0.329	-0.001	0.014	0.639	-0.010	0.031
0.533	0.231	0.034	0.013	0.712	-0.053	0.056
0.400	0.220	-0.096	-0.005	0.714	0.005	0.066
0.267	0.158	-0.056	-0.019	0.799	0.026	0.043
0.133	0.185	-0.029	-0.048	0.754	0.034	0.060
0.000	0.230	-0.019	-0.047	0.713	0.011	0.056
-0.133	0.338	-0.061	-0.066	0.614	0.030	0.047
-0.267	0.464	-0.068	-0.067	0.491	0.026	0.046
-0.400	0.326	-0.015	-0.051	0.621	0.019	0.053
-0.533	0.389	-0.015	-0.027	0.559	0.043	0.053
-0.667	0.466	-0.099	-0.026	0.488	0.026	0.045
-0.800	0.435	-0.048	-0.029	0.524	0.046	0.041
-0.933	0.550	0.097	-0.016	0.428	0.020	0.022

Table E.2: Orientation measurement error 30 wt% GF low viscosity PP at 0L 0W

Z/H	A11	A12	A13	A22	A23	A33
0.933	0.024	0.005	0.017	0.020	0.019	0.001
0.800	0.020	0.006	0.022	0.025	0.020	0.001
0.667	0.018	0.006	0.020	0.029	0.023	0.001
0.533	0.016	0.006	0.021	0.033	0.025	0.002
0.400	0.014	0.007	0.022	0.036	0.024	0.003
0.267	0.012	0.006	0.026	0.030	0.028	0.001
0.133	0.012	0.007	0.024	0.029	0.023	0.002
0.000	0.014	0.007	0.022	0.031	0.026	0.002
-0.133	0.014	0.006	0.021	0.035	0.019	0.002
-0.267	0.016	0.006	0.016	0.033	0.019	0.003
-0.400	0.016	0.006	0.019	0.029	0.022	0.002
-0.533	0.017	0.006	0.015	0.026	0.020	0.003
-0.667	0.019	0.007	0.023	0.023	0.021	0.003
-0.800	0.020	0.007	0.023	0.024	0.020	0.002
-0.933	0.026	0.008	0.019	0.025	0.021	0.001

Table E.3: Orientation measurement 30 wt% GF low viscosity PP at 10L 0W

Z/H	A11	A12	A13	A22	A23	A33
0.933	0.501	-0.135	-0.003	0.463	0.017	0.036
0.800	0.581	-0.033	0.000	0.380	0.023	0.038
0.667	0.585	-0.036	0.007	0.372	0.015	0.043
0.533	0.433	-0.091	0.023	0.509	-0.014	0.058
0.400	0.328	-0.046	0.007	0.598	-0.040	0.074
0.267	0.199	-0.050	-0.008	0.696	-0.019	0.105
0.133	0.263	-0.016	-0.037	0.641	-0.008	0.096
0.000	0.316	-0.027	-0.047	0.604	-0.025	0.080
-0.133	0.370	-0.029	-0.047	0.558	0.000	0.072
-0.267	0.359	0.012	-0.028	0.575	0.020	0.066
-0.400	0.480	-0.021	-0.014	0.476	-0.010	0.044
-0.533	0.598	0.021	-0.024	0.356	-0.007	0.046
-0.667	0.709	-0.140	-0.026	0.258	0.008	0.032
-0.800	0.658	-0.042	-0.009	0.301	0.002	0.041
-0.933	0.477	-0.054	0.000	0.472	0.000	0.051

Table E.4: Orientation measurement error 30 wt% GF low viscosity PP at 10L 0W

Z/H	A11	A12	A13	A22	A23	A33
0.933	0.032	0.009	0.015	0.022	0.019	0.002
0.800	0.034	0.008	0.014	0.019	0.019	0.002
0.667	0.039	0.009	0.015	0.023	0.018	0.003
0.533	0.035	0.011	0.014	0.032	0.019	0.003
0.400	0.027	0.009	0.016	0.034	0.017	0.004
0.267	0.019	0.009	0.015	0.041	0.023	0.005
0.133	0.027	0.008	0.016	0.041	0.026	0.005
0.000	0.034	0.010	0.023	0.047	0.022	0.005
-0.133	0.039	0.011	0.018	0.041	0.019	0.005
-0.267	0.032	0.010	0.019	0.034	0.021	0.004
-0.400	0.034	0.009	0.015	0.026	0.014	0.002
-0.533	0.094	0.007	0.015	0.047	0.016	0.006
-0.667	0.114	0.017	0.016	0.037	0.016	0.004
-0.800	0.043	0.009	0.012	0.019	0.010	0.003
-0.933	0.035	0.010	0.024	0.027	0.018	0.003

Table E.5: Orientation measurements 30 wt% GF low viscosity PP at 40L 0W

Z/H	A11	A12	A13	A22	A23	A33
0.933	0.707	-0.068	0.006	0.275	-0.009	0.018
0.800	0.726	-0.023	0.107	0.207	0.002	0.067
0.667	0.772	-0.011	0.008	0.214	0.011	0.015
0.533	0.716	-0.008	0.019	0.259	-0.007	0.024
0.400	0.581	-0.020	0.004	0.378	0.004	0.041
0.267	0.465	0.006	0.005	0.484	-0.004	0.051
0.133	0.172	-0.024	-0.008	0.753	0.016	0.075
0.000	0.145	-0.012	-0.011	0.762	0.045	0.092
-0.133	0.307	-0.035	-0.013	0.618	0.042	0.074
-0.267	0.577	-0.058	-0.019	0.385	0.009	0.037
-0.400	0.666	0.014	0.002	0.313	0.012	0.021
-0.533	0.648	0.003	0.008	0.322	0.005	0.029
-0.667	0.676	0.005	0.014	0.297	0.025	0.027
-0.800	0.627	0.039	-0.011	0.341	0.012	0.032
-0.933	0.528	0.026	-0.003	0.431	0.037	0.041

Table E.6: Orientation measurement error 30 wt% GF low viscosity PP at 40L 0W

Z/H	A11	A12	A13	A22	A23	A33
0.933	0.077	0.009	0.012	0.026	0.008	0.002
0.800	0.094	0.029	0.010	0.032	0.008	0.043
0.667	0.059	0.005	0.013	0.016	0.014	0.001
0.533	0.056	0.005	0.011	0.020	0.012	0.002
0.400	0.038	0.006	0.017	0.023	0.016	0.003
0.267	0.029	0.006	0.020	0.025	0.027	0.003
0.133	0.015	0.006	0.016	0.032	0.018	0.003
0.000	0.016	0.006	0.016	0.046	0.020	0.005
-0.133	0.024	0.007	0.017	0.037	0.017	0.004
-0.267	0.035	0.007	0.010	0.022	0.012	0.002
-0.400	0.044	0.005	0.013	0.019	0.008	0.001
-0.533	0.038	0.006	0.012	0.017	0.010	0.002
-0.667	0.036	0.006	0.013	0.016	0.019	0.001
-0.800	0.034	0.007	0.012	0.018	0.013	0.002
-0.933	0.037	0.007	0.018	0.027	0.017	0.002

Table E.7: Orientation measurements 30 wt % GF low viscosity PP at 90L 0W

Z/H	A11	A12	A13	A22	A23	A33
0.933	0.764	0.040	-0.001	0.218	-0.013	0.018
0.800	0.657	0.012	0.001	0.308	-0.007	0.035
0.667	0.550	0.001	-0.002	0.400	-0.008	0.050
0.533	0.564	-0.010	-0.017	0.374	-0.019	0.062
0.400	0.532	0.002	-0.002	0.425	0.001	0.043
0.267	0.272	-0.094	-0.001	0.654	-0.025	0.074
0.133	0.151	-0.079	-0.005	0.738	-0.050	0.111
0.000	0.223	0.017	-0.035	0.670	-0.010	0.107
-0.133	0.386	-0.012	-0.033	0.542	-0.032	0.072
-0.267	0.531	0.043	-0.026	0.419	-0.021	0.050
-0.400	0.548	-0.037	-0.014	0.403	0.007	0.049
-0.533	0.627	-0.023	0.006	0.338	-0.002	0.035
-0.667	0.650	-0.048	0.012	0.310	0.012	0.040
-0.800	0.787	0.006	0.008	0.191	-0.004	0.022
-0.933	0.797	0.018	0.009	0.187	0.007	0.016

Table E.8: Orientation measurement error at 30 wt % GF low viscosity PP at 90L 0W

Z/H	A11	A12	A13	A22	A23	A33
0.933	0.031	0.005	0.006	0.009	0.009	0.001
0.800	0.033	0.006	0.013	0.016	0.075	0.002
0.667	0.034	0.007	0.015	0.023	0.018	0.003
0.533	0.032	0.007	0.015	0.021	0.016	0.003
0.400	0.030	0.006	0.013	0.021	0.012	0.002
0.267	0.019	0.008	0.016	0.028	0.021	0.003
0.133	0.014	0.008	0.015	0.037	0.012	0.005
0.000	0.017	0.007	0.015	0.031	0.018	0.004
-0.133	0.029	0.007	0.015	0.033	0.017	0.004
-0.267	0.031	0.007	0.014	0.021	0.013	0.002
-0.400	0.034	0.007	0.011	0.023	0.014	0.003
-0.533	0.038	0.006	0.012	0.019	0.011	0.002
-0.667	0.034	0.006	0.012	0.017	0.015	0.002
-0.800	0.035	0.005	0.008	0.009	0.010	0.001
-0.933	0.036	0.004	0.006	0.008	0.007	0.001

Table E.9: Orientation measurements at 30 wt % GF low viscosity PP at 40L 50W

Z/H	A11	A12	A13	A22	A23	A33
0.933	0.841	-0.018	0.024	0.152	0.002	0.007
0.800	0.765	0.042	0.016	0.219	-0.002	0.016
0.667	0.804	0.011	0.020	0.182	-0.003	0.014
0.533	0.788	-0.078	0.011	0.188	-0.013	0.023
0.400	0.731	-0.088	-0.008	0.225	-0.011	0.043
0.267	0.669	-0.004	0.010	0.302	-0.014	0.029
0.133	0.623	0.085	-0.019	0.349	-0.011	0.027
0.000	0.644	0.086	-0.006	0.334	-0.010	0.023
-0.133	0.615	0.146	0.010	0.353	-0.002	0.032
-0.267	0.671	0.068	-0.011	0.310	-0.009	0.019
-0.400	0.715	-0.077	-0.009	0.263	-0.027	0.022
-0.533	0.787	-0.112	0.013	0.195	-0.006	0.018
-0.667	0.779	-0.062	-0.001	0.203	0.007	0.018
-0.800	0.766	0.005	-0.011	0.214	0.001	0.020
-0.933	0.772	-0.023	0.005	0.210	0.015	0.019

Table E.10: Orientation measurement error at 30 wt % GF low viscosity PP at 40L 50W

Z/H	A11	A12	A13	A22	A23	A33
0.933	0.039	0.005	0.009	0.005	0.006	0.000
0.800	0.035	0.006	0.010	0.011	0.012	0.001
0.667	0.039	0.006	0.008	0.010	0.012	0.001
0.533	0.038	0.007	0.008	0.011	0.010	0.002
0.400	0.031	0.008	0.006	0.010	0.008	0.003
0.267	0.031	0.007	0.013	0.013	0.012	0.001
0.133	0.032	0.008	0.009	0.016	0.012	0.001
0.000	0.031	0.007	0.011	0.012	0.012	0.001
-0.133	0.029	0.008	0.012	0.013	0.011	0.002
-0.267	0.035	0.007	0.013	0.014	0.014	0.001
-0.400	0.036	0.007	0.008	0.012	0.009	0.002
-0.533	0.034	0.007	0.007	0.010	0.010	0.001
-0.667	0.049	0.007	0.009	0.012	0.009	0.001
-0.800	0.048	0.006	0.010	0.012	0.007	0.002
-0.933	0.100	0.007	0.026	0.024	0.010	0.002

Table E.11: Orientation measurements at 30 wt % GF low viscosity PP at 40L 90W

Z/H	A11	A12	A13	A22	A23	A33
0.933	0.644	0.029	0.022	0.321	-0.022	0.036
0.800	0.781	0.021	0.023	0.194	0.008	0.025
0.667	0.826	0.054	0.009	0.152	-0.004	0.022
0.533	0.839	0.042	0.008	0.138	-0.002	0.023
0.400	0.840	0.026	-0.007	0.141	-0.007	0.018
0.267	0.886	0.066	0.005	0.100	0.000	0.014
0.133	0.879	0.106	0.012	0.110	0.004	0.012
0.000	0.855	0.057	0.021	0.126	-0.007	0.019
-0.133	0.819	0.007	0.012	0.147	0.013	0.034
-0.267	0.857	0.001	-0.016	0.121	0.010	0.022
-0.400	0.842	-0.017	-0.041	0.125	0.008	0.032
-0.533	0.834	0.030	-0.005	0.140	0.015	0.026
-0.667	0.830	0.053	-0.002	0.152	0.019	0.019
-0.800	0.796	0.037	-0.027	0.183	-0.003	0.021
-0.933	0.684	0.061	-0.007	0.296	0.010	0.020

Table E.12: Orientation measurement error at 30 wt % GF low viscosity PP at 40L 90W

Z/H	A11	A12	A13	A22	A23	A33
0.933	0.038	0.007	0.013	0.018	0.006	0.002
0.800	0.037	0.006	0.008	0.011	0.012	0.002
0.667	0.034	0.006	0.018	0.008	0.012	0.001
0.533	0.035	0.006	0.008	0.008	0.010	0.001
0.400	0.035	0.005	0.007	0.007	0.008	0.001
0.267	0.034	0.005	0.005	0.004	0.012	0.001
0.133	0.030	0.005	0.004	0.004	0.012	0.000
0.000	0.037	0.005	0.008	0.006	0.012	0.001
-0.133	0.058	0.005	0.006	0.012	0.011	0.003
-0.267	0.072	0.006	0.006	0.010	0.014	0.002
-0.400	0.084	0.007	0.006	0.013	0.009	0.003
-0.533	0.044	0.005	0.004	0.010	0.010	0.002
-0.667	0.067	0.007	0.009	0.013	0.009	0.002
-0.800	0.079	0.007	0.018	0.015	0.007	0.003
-0.933	0.042	0.007	0.014	0.017	0.010	0.001

Table E.13: Orientation measurements at 30 wt % GF high viscosity PP at 0L 0W

Z/H	A11	A12	A22	A33	A13	A23
0.933	0.641	-0.009	0.348	0.011	0.007	0.005
0.800	0.437	-0.013	0.539	0.025	0.005	-0.008
0.667	0.316	-0.003	0.656	0.028	0.016	-0.018
0.533	0.226	-0.024	0.728	0.046	0.008	-0.030
0.400	0.138	-0.024	0.803	0.059	-0.003	-0.036
0.267	0.130	-0.053	0.802	0.068	-0.023	-0.019
0.133	0.177	-0.042	0.754	0.069	-0.046	-0.008
0.000	0.259	-0.052	0.676	0.065	-0.066	-0.021
-0.133	0.296	-0.039	0.648	0.056	-0.059	-0.026
-0.267	0.336	-0.042	0.626	0.038	-0.056	-0.004
-0.400	0.310	0.012	0.648	0.042	-0.051	-0.027
-0.533	0.218	-0.021	0.741	0.041	-0.035	-0.028
-0.667	0.304	-0.060	0.661	0.035	-0.030	0.005
-0.800	0.439	-0.063	0.537	0.024	-0.030	-0.011
-0.933	0.575	0.004	0.400	0.025	-0.035	-0.008

Table E.14: Orientation measurements at 30 wt % GF high viscosity PP at 10L 0W

Z/H	A11	A12	A22	A33	A13	A23
0.933	0.623	0.036	0.362	0.015	0.007	0.015
0.800	0.540	-0.065	0.435	0.027	0.020	0.025
0.667	0.450	0.038	0.490	0.052	0.041	0.006
0.533	0.315	0.007	0.650	0.043	0.008	0.036
0.400	0.235	-0.028	0.729	0.038	-0.004	0.036
0.267	0.250	-0.100	0.710	0.035	-0.017	0.040
0.133	0.311	-0.030	0.649	0.042	-0.030	0.040
0.000	0.371	-0.103	0.590	0.042	-0.019	0.039
-0.133	0.355	-0.058	0.612	0.033	-0.027	0.033
-0.267	0.346	-0.026	0.616	0.042	-0.030	0.038
-0.400	0.333	0.006	0.635	0.033	-0.019	0.032
-0.533	0.427	-0.002	0.547	0.027	-0.022	0.026
-0.667	0.437	-0.010	0.533	0.035	-0.033	0.030
-0.800	0.531	-0.015	0.437	0.038	-0.019	0.032
-0.933	0.448	-0.017	0.531	0.022	-0.015	0.021

Table E.15: Orientation measurements at 30 wt % GF high viscosity PP at 40L 0W

Z/H	A11	A12	A22	A33	A13	A23
0.933	0.769	0.028	0.218	0.013	0.002	-0.017
0.800	0.732	-0.032	0.252	0.016	0.002	-0.012
0.667	0.759	0.011	0.213	0.028	0.005	-0.005
0.533	0.680	-0.003	0.287	0.033	0.022	-0.015
0.400	0.576	-0.007	0.392	0.032	0.009	-0.035
0.267	0.226	-0.047	0.728	0.046	-0.003	-0.032
0.133	0.194	-0.104	0.763	0.043	-0.018	-0.007
0.000	0.263	-0.093	0.692	0.045	-0.019	-0.022
-0.133	0.373	-0.096	0.594	0.033	-0.017	-0.013
-0.267	0.620	0.018	0.362	0.018	-0.009	-0.020
-0.400	0.685	0.020	0.299	0.016	-0.015	-0.010
-0.533	0.636	-0.009	0.339	0.024	-0.012	0.000
-0.667	0.666	0.002	0.306	0.029	-0.004	-0.017
-0.800	0.700	0.020	0.281	0.019	-0.021	-0.006
-0.933	0.810	0.061	0.176	0.014	-0.018	-0.003

Table E.16: Orientation measurements at 30 wt % GF high viscosity PP at 90L 0W

Z/H	A11	A12	A22	A33	A13	A23
0.933	0.739	0.045	0.248	0.013	-0.003	-0.006
0.800	0.673	0.052	0.301	0.026	0.012	-0.006
0.667	0.488	-0.032	0.476	0.036	0.004	-0.025
0.533	0.242	-0.096	0.694	0.064	-0.004	-0.035
0.400	0.177	-0.068	0.747	0.077	-0.025	-0.015
0.267	0.205	-0.039	0.714	0.081	-0.042	-0.002
0.133	0.240	-0.062	0.679	0.081	-0.057	-0.028
0.000	0.274	-0.074	0.651	0.075	-0.039	-0.045
-0.133	0.295	-0.089	0.646	0.059	-0.032	-0.052
-0.267	0.371	-0.045	0.582	0.047	-0.022	-0.040
-0.400	0.443	-0.048	0.515	0.042	-0.011	-0.009
-0.533	0.483	-0.095	0.481	0.036	0.001	-0.014
-0.667	0.654	-0.048	0.319	0.027	-0.002	-0.014
-0.800	0.613	-0.032	0.359	0.027	-0.002	-0.020
-0.933	0.550	-0.020	0.422	0.028	0.007	-0.021

Table E.17: Orientation measurements at 30 wt % GF high viscosity PP at 40L 50W

Z/H	A11	A12	A22	A33	A13	A23
0.933	0.762	0.018	0.200	A33	0.069	-0.006
0.800	0.774	-0.012	0.185	0.052	0.073	-0.010
0.667	0.820	0.017	0.150	0.015	0.045	-0.008
0.533	0.790	0.010	0.192	0.021	0.007	-0.014
0.400	0.760	-0.058	0.222	0.027	0.002	-0.003
0.267	0.844	-0.195	0.147	0.017	0.015	-0.004
0.133	0.794	-0.199	0.183	0.024	0.013	-0.020
0.000	0.657	-0.105	0.307	0.049	-0.005	-0.045
-0.133	0.730	-0.043	0.240	0.025	-0.032	-0.026
-0.267	0.813	-0.043	0.172	0.025	-0.032	-0.003
-0.400	0.890	0.018	0.101	0.011	-0.013	0.001
-0.533	0.878	0.022	0.109	0.014	-0.010	-0.004
-0.667	0.787	-0.005	0.190	0.026	-0.019	0.001
-0.800	0.739	-0.007	0.240	0.026	-0.020	-0.007
-0.933	0.710	-0.027	0.276	0.023	-0.021	-0.005

Table E.18: Orientation measurements at 30 wt % GF high viscosity PP at 40L 90W

Z/H	A11	A12	A22	A33	A13	A23
0.933	0.728	0.085	0.255	0.017	0.001	-0.011
0.800	0.764	0.104	0.220	0.016	-0.001	-0.013
0.667	0.809	0.028	0.156	0.035	-0.026	-0.009
0.533	0.876	0.042	0.104	0.020	-0.032	-0.004
0.400	0.864	0.072	0.118	0.017	0.026	0.010
0.267	0.809	0.004	0.163	0.028	0.008	0.014
0.133	0.849	-0.060	0.123	0.028	-0.016	0.023
0.000	0.856	-0.047	0.106	0.038	-0.017	0.005
-0.133	0.867	-0.030	0.096	0.038	-0.020	-0.005
-0.267	0.854	0.036	0.118	0.028	-0.021	-0.007
-0.400	0.824	0.067	0.146	0.030	-0.006	0.000
-0.533	0.835	0.033	0.144	0.021	0.009	0.010
-0.667	0.777	0.039	0.199	0.024	-0.005	-0.011
-0.800	0.744	0.030	0.234	0.022	-0.018	-0.018
-0.933	0.654	-0.007	0.324	0.022	0.000	-0.016

Table E.19: Orientation measurements for 50 wt% GF low viscosity PP at 0L 0W

z/h	A11	A12	A22	A33	A13	A23
-0.923	0.602	-0.009	0.027	0.371	-0.003	0.069
-0.769	0.408	0.004	0.034	0.559	0.034	0.100
-0.615	0.310	0.006	0.051	0.638	0.009	0.134
-0.462	0.278	-0.001	0.067	0.655	0.015	0.163
-0.308	0.208	-0.011	0.075	0.717	-0.015	0.190
-0.154	0.221	-0.025	0.103	0.676	-0.024	0.208
0.000	0.285	-0.034	0.083	0.632	-0.031	0.177
0.154	0.238	-0.006	0.080	0.682	-0.017	0.186
0.308	0.277	-0.025	0.068	0.655	-0.057	0.162
0.462	0.347	-0.024	0.058	0.596	-0.069	0.143
0.615	0.372	-0.016	0.044	0.584	-0.061	0.128
0.769	0.468	-0.026	0.040	0.491	-0.098	0.103
0.923	0.455	-0.034	0.041	0.504	-0.087	0.108

Table E.20: Standard deviation for orientation measurements at 50 wt% GF low viscosity PP at 0L 0W

z/h	A11	A12	A22	A33	A13	A23
-0.923	0.088	0.032	0.017	0.079	0.066	0.027
-0.769	0.035	0.019	0.011	0.044	0.054	0.015
-0.615	0.020	0.021	0.002	0.050	0.075	0.013
-0.462	0.095	0.030	0.014	0.082	0.084	0.032
-0.308	0.018	0.033	0.017	0.009	0.100	0.025
-0.154	0.029	0.055	0.017	0.025	0.119	0.025
0.000	0.041	0.055	0.025	0.050	0.120	0.032
0.154	0.042	0.033	0.015	0.026	0.090	0.029
0.308	0.057	0.017	0.018	0.050	0.052	0.028
0.462	0.059	0.011	0.011	0.049	0.018	0.023
0.615	0.106	0.009	0.009	0.067	0.021	0.027
0.769	0.072	0.010	0.006	0.040	0.047	0.010
0.923	0.114	0.017	0.008	0.106	0.053	0.027

Table E.21: Orientation measurements for 50 wt% GF low viscosity PP at 10L 0W

z/h	A11	A12	A22	A33	A13	A23
-0.923	0.492	0.000	0.048	0.461	0.033	0.103
-0.769	0.715	-0.002	0.021	0.265	0.012	0.050
-0.615	0.530	0.001	0.041	0.428	0.037	0.085
-0.462	0.293	0.030	0.080	0.627	0.037	0.165
-0.308	0.171	0.000	0.094	0.735	0.002	0.210
-0.154	0.226	-0.020	0.089	0.685	-0.067	0.188
0.000	0.200	-0.027	0.172	0.628	-0.061	0.180
0.154	0.308	-0.021	0.088	0.604	-0.026	0.181
0.308	0.337	-0.023	0.071	0.592	-0.039	0.157
0.462	0.430	0.003	0.075	0.495	0.009	0.148
0.615	0.581	-0.011	0.047	0.373	-0.031	0.097
0.769	0.596	-0.019	0.037	0.367	-0.017	0.081
0.923	0.463	0.005	0.050	0.488	0.036	0.105

Table E.22: Standard deviation for orientation measurements at 50 wt% GF low viscosity PP at 10L 0W

z/h	A11	A12	A22	A33	A13	A23
-0.92308	0.080	0.017	0.025	0.089	0.100	0.034
-0.76923	0.087	0.024	0.012	0.094	0.070	0.010
-0.61538	0.082	0.052	0.016	0.074	0.108	0.031
-0.46154	0.131	0.029	0.033	0.153	0.092	0.023
-0.30769	0.080	0.016	0.034	0.086	0.044	0.041
-0.15385	0.075	0.017	0.036	0.081	0.058	0.051
0	0.057	0.016	0.158	0.136	0.040	0.069
0.153846	0.104	0.023	0.022	0.115	0.041	0.028
0.307692	0.155	0.027	0.021	0.168	0.034	0.032
0.461538	0.071	0.020	0.039	0.065	0.068	0.042
0.615385	0.066	0.025	0.022	0.070	0.075	0.028
0.769231	0.054	0.025	0.008	0.058	0.069	0.007
0.923077	0.118	0.025	0.016	0.130	0.109	0.013

Table E.23: Orientation measurements for 50 wt% GF low viscosity PP at 40L 0W

z/h	A11	A12	A22	A33	A13	A23
-0.923	0.508	-0.008	0.030	0.462	-0.055	0.077
-0.769	0.675	0.030	0.033	0.292	0.052	0.063
-0.615	0.702	0.025	0.036	0.261	0.045	0.064
-0.462	0.574	0.014	0.049	0.377	0.023	0.092
-0.308	0.407	0.036	0.056	0.537	0.132	0.126
-0.154	0.176	0.011	0.087	0.736	0.037	0.186
0.000	0.148	-0.003	0.179	0.673	-0.003	0.173
0.154	0.266	-0.017	0.073	0.661	-0.049	0.159
0.308	0.342	-0.006	0.064	0.594	-0.023	0.143
0.462	0.515	0.014	0.068	0.417	0.004	0.095
0.615	0.646	-0.001	0.033	0.321	-0.033	0.070
0.769	0.647	0.006	0.028	0.325	0.026	0.068
0.923	0.470	0.005	0.036	0.494	0.028	0.080

Table E.24: Standard deviation for orientation measurements at 50 wt% GF low viscosity PP at 40L 0W

z/h	A11	A12	A22	A33	A13	A23
-0.923	0.079	0.015	0.008	0.082	0.060	0.016
-0.769	0.096	0.014	0.025	0.071	0.031	0.037
-0.615	0.105	0.012	0.027	0.078	0.017	0.044
-0.462	0.166	0.014	0.035	0.135	0.049	0.057
-0.308	0.068	0.013	0.021	0.058	0.042	0.028
-0.154	0.074	0.019	0.036	0.050	0.077	0.035
0.000	0.058	0.003	0.168	0.129	0.011	0.080
0.154	0.019	0.016	0.037	0.035	0.072	0.039
0.308	0.059	0.029	0.034	0.042	0.077	0.046
0.462	0.054	0.041	0.024	0.070	0.079	0.030
0.615	0.123	0.016	0.019	0.105	0.048	0.034
0.769	0.134	0.008	0.025	0.113	0.014	0.045
0.923	0.168	0.018	0.022	0.164	0.048	0.039

Table E.25: Orientation measurements for 50 wt% GF low viscosity PP at 90L 0W

z/h	A11	A12	A22	A33	A13	A23
-0.923	0.639	0.022	0.020	0.341	0.082	0.062
-0.769	0.589	0.050	0.036	0.374	0.173	0.089
-0.615	0.530	0.048	0.058	0.412	0.135	0.114
-0.462	0.383	0.052	0.088	0.529	0.119	0.162
-0.308	0.264	0.041	0.110	0.626	0.115	0.205
-0.154	0.199	0.031	0.106	0.695	0.075	0.217
0.000	0.181	0.018	0.103	0.716	0.020	0.211
0.154	0.182	-0.006	0.104	0.714	-0.026	0.214
0.308	0.237	-0.009	0.087	0.676	-0.038	0.194
0.462	0.376	-0.006	0.064	0.560	-0.023	0.149
0.615	0.451	0.006	0.055	0.494	0.037	0.126
0.769	0.624	-0.004	0.030	0.346	-0.007	0.078
0.923	0.550	0.011	0.036	0.414	0.026	0.089

Table E.26: Standard deviation for orientation measurements at 50 wt% GF low viscosity PP at 90L 0W

z/h	A11	A12	A22	A33	A13	A23
-0.923	0.063	0.025	0.010	0.065	0.094	0.018
-0.769	0.087	0.008	0.024	0.075	0.063	0.034
-0.615	0.159	0.034	0.044	0.119	0.072	0.062
-0.462	0.126	0.056	0.048	0.085	0.138	0.062
-0.308	0.068	0.064	0.050	0.039	0.127	0.052
-0.154	0.039	0.051	0.039	0.019	0.096	0.050
0.000	0.035	0.017	0.048	0.051	0.043	0.052
0.154	0.039	0.012	0.046	0.075	0.045	0.044
0.308	0.044	0.024	0.022	0.066	0.076	0.013
0.462	0.110	0.050	0.025	0.096	0.159	0.043
0.615	0.077	0.051	0.026	0.070	0.156	0.021
0.769	0.135	0.033	0.015	0.122	0.104	0.030
0.923	0.155	0.025	0.014	0.148	0.058	0.031

Table E.27: Orientation measurements for 50 wt% GF low viscosity PP at 40L 50W

z/h	A11	A12	A22	A33	A13	A23
-0.923	0.567	0.007	0.077	0.356	0.032	0.112
-0.769	0.726	-0.001	0.037	0.237	-0.006	0.065
-0.615	0.786	-0.009	0.032	0.182	-0.009	0.053
-0.462	0.777	-0.001	0.041	0.181	0.013	0.061
-0.308	0.672	-0.028	0.066	0.261	-0.041	0.099
-0.154	0.767	-0.027	0.049	0.183	-0.044	0.075
0.000	0.737	-0.009	0.050	0.213	-0.008	0.073
0.154	0.593	-0.001	0.059	0.348	0.013	0.104
0.308	0.690	-0.015	0.039	0.271	-0.035	0.070
0.462	0.718	0.021	0.041	0.241	0.038	0.065
0.615	0.812	-0.005	0.031	0.157	0.017	0.051
0.769	0.760	0.007	0.032	0.208	0.007	0.060
0.923	0.678	0.022	0.035	0.287	0.068	0.067

Table E.28: Standard deviation for orientation measurements at 50 wt% GF low viscosity PP at 40L 50W

z/h	A11	A12	A22	A33	A13	A23
-0.923	0.122	0.009	0.062	0.063	0.020	0.064
-0.769	0.103	0.018	0.028	0.076	0.034	0.033
-0.615	0.053	0.024	0.018	0.039	0.051	0.021
-0.462	0.060	0.042	0.020	0.044	0.078	0.022
-0.308	0.054	0.021	0.011	0.047	0.047	0.013
-0.154	0.066	0.045	0.020	0.047	0.091	0.027
0.000	0.083	0.057	0.012	0.072	0.125	0.021
0.154	0.212	0.013	0.054	0.180	0.020	0.067
0.308	0.063	0.012	0.013	0.075	0.061	0.006
0.462	0.118	0.011	0.027	0.103	0.006	0.032
0.615	0.044	0.021	0.014	0.035	0.032	0.019
0.769	0.081	0.008	0.021	0.060	0.017	0.031
0.923	0.032	0.013	0.015	0.026	0.042	0.016

Table E.29: Orientation measurements for 50 wt% GF low viscosity PP at 40L 90W

z/h	A11	A12	A22	A33	A13	A23
-0.923	0.660	0.002	0.055	0.285	0.015	0.097
-0.769	0.765	0.009	0.048	0.187	-0.011	0.074
-0.615	0.911	0.022	0.019	0.070	0.040	0.029
-0.462	0.823	0.003	0.044	0.133	0.023	0.058
-0.308	0.780	0.002	0.060	0.160	0.009	0.076
-0.154	0.767	-0.043	0.093	0.140	-0.029	0.073
0.000	0.876	-0.055	0.031	0.093	-0.099	0.042
0.154	0.834	-0.026	0.050	0.116	-0.036	0.058
0.308	0.784	0.002	0.049	0.167	0.030	0.065
0.462	0.810	0.010	0.040	0.150	0.021	0.058
0.615	0.846	-0.010	0.034	0.120	-0.025	0.048
0.769	0.837	0.004	0.030	0.133	0.009	0.048
0.923	0.747	0.011	0.029	0.224	0.033	0.060

Table E.30: Standard deviation for orientation measurements at 50 wt% GF low viscosity PP at 40L 50W

z/h	A11	A12	A22	A33	A13	A23
-0.923	0.033	0.063	0.004	0.029	0.175	0.010
-0.769	0.042	0.047	0.010	0.053	0.090	0.002
-0.615	0.008	0.031	0.007	0.001	0.041	0.008
-0.462	0.011	0.052	0.007	0.005	0.075	0.011
-0.308	0.010	0.048	0.022	0.032	0.096	0.004
-0.154	0.002	0.017	0.026	0.027	0.035	0.006
0.000	0.044	0.008	0.008	0.036	0.015	0.011
0.154	0.074	0.012	0.024	0.050	0.037	0.031
0.308	0.070	0.026	0.007	0.077	0.023	0.009
0.462	0.033	0.042	0.012	0.022	0.077	0.012
0.615	0.067	0.032	0.014	0.053	0.046	0.020
0.769	0.005	0.022	0.001	0.006	0.014	0.004
0.923	0.081	0.010	0.014	0.067	0.076	0.029

Table E.31: Orientation measurements for 50 wt% GF high viscosity PP at 0L 0W

z/h	A11	A12	A22	A33	A13	A23
-0.923	0.439	0.010	0.036	0.525	0.033	0.100
-0.769	0.561	0.026	0.034	0.405	0.058	0.082
-0.615	0.372	0.021	0.059	0.569	0.060	0.142
-0.462	0.254	0.019	0.074	0.672	0.051	0.169
-0.308	0.425	0.053	0.063	0.512	0.094	0.124
-0.154	0.409	0.056	0.062	0.529	0.136	0.136
0.000	0.263	0.047	0.075	0.662	0.126	0.165
0.154	0.191	0.011	0.088	0.720	0.027	0.193
0.308	0.171	0.003	0.069	0.760	0.003	0.156
0.462	0.239	-0.012	0.054	0.707	-0.073	0.141
0.615	0.487	-0.016	0.036	0.476	-0.077	0.096
0.769	0.622	-0.024	0.027	0.351	-0.056	0.068
0.923	0.696	-0.006	0.018	0.287	-0.012	0.049

Table E.32: Standard deviation for orientation measurements at 50 wt% GF high viscosity PP at 0L 0W

z/h	A11	A12	A22	A33	A13	A23
-0.923	0.045	0.008	0.008	0.166	0.032	0.029
-0.769	0.039	0.027	0.009	0.078	0.086	0.016
-0.615	0.048	0.016	0.021	0.076	0.058	0.049
-0.462	0.024	0.005	0.036	0.050	0.014	0.064
-0.308	0.047	0.020	0.032	0.089	0.025	0.034
-0.154	0.049	0.004	0.006	0.096	0.037	0.022
0.000	0.039	0.008	0.017	0.067	0.037	0.042
0.154	0.024	0.013	0.024	0.028	0.028	0.038
0.308	0.036	0.021	0.020	0.077	0.041	0.026
0.462	0.009	0.011	0.013	0.023	0.040	0.019
0.615	0.042	0.015	0.008	0.075	0.009	0.021
0.769	0.043	0.007	0.006	0.080	0.026	0.017
0.923	0.016	0.014	0.005	0.028	0.007	0.010

Table E.33: Orientation measurements for 50 wt% GF high viscosity PP at 10L 0W

z/h	A11	A12	A22	A33	A13	A23
-0.923	0.433	0.001	0.038	0.529	-0.022	0.099
-0.769	0.576	0.022	0.034	0.391	0.030	0.079
-0.615	0.540	0.010	0.028	0.432	0.033	0.084
-0.462	0.337	0.026	0.049	0.614	0.066	0.127
-0.308	0.435	0.036	0.043	0.522	0.085	0.110
-0.154	0.398	0.034	0.047	0.555	0.072	0.124
0.000	0.311	0.051	0.061	0.628	0.116	0.147
0.154	0.267	0.034	0.059	0.675	0.076	0.157
0.308	0.156	-0.001	0.067	0.777	-0.008	0.176
0.462	0.259	-0.013	0.047	0.694	-0.064	0.138
0.615	0.509	-0.003	0.033	0.458	-0.034	0.089
0.769	0.705	-0.016	0.021	0.274	-0.035	0.050
0.923	0.644	-0.004	0.014	0.343	-0.025	0.044

Table E.34: Standard deviation for orientation measurements at 50 wt% GF high viscosity PP at 10L 0W

z/h	A11	A12	A22	A33	A13	A23
-0.923	0.025	0.017	0.013	0.027	0.065	0.009
-0.769	0.037	0.031	0.009	0.045	0.117	0.001
-0.615	0.057	0.017	0.006	0.051	0.069	0.019
-0.462	0.057	0.017	0.021	0.073	0.051	0.022
-0.308	0.031	0.013	0.001	0.111	0.056	0.008
-0.154	0.031	0.032	0.015	0.103	0.087	0.034
0.000	0.053	0.033	0.009	0.100	0.053	0.032
0.154	0.039	0.022	0.013	0.031	0.026	0.026
0.308	0.035	0.005	0.017	0.056	0.024	0.042
0.462	0.019	0.006	0.006	0.025	0.031	0.010
0.615	0.075	0.025	0.006	0.120	0.015	0.024
0.769	0.019	0.001	0.003	0.002	0.027	0.004
0.923	0.048	0.013	0.001	0.078	0.038	0.001

Table E.35: Orientation measurements for 50 wt% GF high viscosity PP at 40L 0W

z/h	A11	A12	A22	A33	A13	A23
-0.923	0.564	0.005	0.040	0.396	0.003	0.081
-0.769	0.738	0.007	0.023	0.238	0.009	0.051
-0.615	0.775	-0.001	0.021	0.203	-0.027	0.047
-0.462	0.591	0.019	0.035	0.374	0.069	0.069
-0.308	0.372	0.005	0.037	0.590	0.035	0.100
-0.154	0.250	0.012	0.066	0.685	0.034	0.158
0.000	0.171	0.012	0.080	0.749	0.015	0.192
0.154	0.209	-0.005	0.065	0.726	-0.038	0.162
0.308	0.396	-0.003	0.044	0.560	-0.020	0.105
0.462	0.689	0.004	0.031	0.280	0.022	0.057
0.615	0.699	-0.016	0.025	0.276	-0.011	0.057
0.769	0.647	-0.013	0.024	0.329	-0.038	0.060
0.923	0.612	-0.003	0.024	0.364	-0.001	0.068

Table E.36: Standard deviation for orientation measurements at 50 wt% GF high viscosity PP at 40L 0W

z/h	A11	A12	A22	A33	A13	A23
-0.923	0.016	0.008	0.010	0.147	0.046	0.010
-0.769	0.055	0.028	0.005	0.050	0.079	0.007
-0.615	0.030	0.019	0.007	0.025	0.049	0.012
-0.462	0.059	0.022	0.005	0.078	0.039	0.011
-0.308	0.011	0.009	0.028	0.115	0.038	0.039
-0.154	0.009	0.007	0.012	0.017	0.049	0.029
0.000	0.094	0.026	0.032	0.075	0.068	0.059
0.154	0.059	0.035	0.039	0.045	0.135	0.065
0.308	0.020	0.038	0.027	0.198	0.113	0.048
0.462	0.087	0.023	0.013	0.035	0.033	0.014
0.615	0.041	0.024	0.007	0.105	0.028	0.020
0.769	0.014	0.019	0.005	0.143	0.032	0.016
0.923	0.049	0.019	0.008	0.049	0.065	0.014

Table E.37: Orientation measurements for 50 wt% GF high viscosity PP at 90L 0W

z/h	A11	A12	A22	A33	A13	A23
-0.923	0.712	0.029	0.022	0.266	0.077	0.059
-0.769	0.744	0.013	0.031	0.226	0.020	0.062
-0.615	0.544	0.008	0.048	0.408	-0.039	0.108
-0.462	0.297	0.005	0.083	0.620	-0.027	0.168
-0.308	0.190	0.003	0.109	0.702	-0.023	0.216
-0.154	0.149	-0.010	0.107	0.744	-0.037	0.225
0.000	0.161	-0.002	0.114	0.725	-0.053	0.221
0.154	0.169	-0.021	0.108	0.723	-0.069	0.219
0.308	0.199	-0.019	0.096	0.705	-0.068	0.206
0.462	0.267	-0.018	0.105	0.628	-0.061	0.194
0.615	0.458	-0.021	0.062	0.480	-0.029	0.132
0.769	0.707	-0.002	0.024	0.269	0.022	0.061
0.923	0.745	0.013	0.022	0.233	0.016	0.052

Table E.38: Standard deviation for orientation measurements at 50 wt% GF high viscosity PP at 90L 0W

z/h	A11	A12	A22	A33	A13	A23
-0.923	0.080	0.021	0.005	0.078	0.067	0.017
-0.769	0.095	0.031	0.010	0.086	0.036	0.023
-0.615	0.033	0.049	0.003	0.033	0.069	0.007
-0.462	0.065	0.058	0.003	0.062	0.102	0.010
-0.308	0.031	0.040	0.013	0.026	0.087	0.008
-0.154	0.039	0.057	0.008	0.040	0.122	0.008
0.000	0.034	0.049	0.005	0.031	0.120	0.030
0.154	0.010	0.052	0.018	0.013	0.095	0.032
0.308	0.079	0.041	0.004	0.076	0.074	0.015
0.462	0.062	0.029	0.010	0.052	0.064	0.014
0.615	0.024	0.055	0.008	0.027	0.108	0.011
0.769	0.027	0.047	0.007	0.022	0.100	0.013
0.923	0.104	0.022	0.011	0.094	0.005	0.030

Table E.39: Orientation measurements for 50 wt% GF high viscosity PP at 40L 50W

z/h	A11	A12	A22	A33	A13	A23
-0.923	0.582	0.000	0.034	0.384	-0.010	0.086
-0.769	0.791	-0.002	0.020	0.190	-0.043	0.043
-0.615	0.848	-0.007	0.020	0.131	-0.012	0.038
-0.462	0.762	-0.011	0.025	0.213	-0.038	0.054
-0.308	0.715	-0.026	0.032	0.253	-0.068	0.063
-0.154	0.730	-0.022	0.028	0.242	-0.040	0.058
0.000	0.729	-0.002	0.024	0.247	-0.002	0.055
0.154	0.734	0.000	0.024	0.243	-0.005	0.055
0.308	0.739	-0.025	0.032	0.229	-0.062	0.054
0.462	0.775	-0.014	0.027	0.198	-0.042	0.050
0.615	0.823	0.005	0.023	0.154	0.001	0.040
0.769	0.812	-0.006	0.015	0.173	-0.014	0.037
0.923	0.609	0.003	0.030	0.361	0.003	0.080

Table E.40: Standard deviation for orientation measurements at 50 wt% GF high viscosity PP at 40L 50W

z/h	A11	A12	A22	A33	A13	A23
-0.923	0.044	0.031	0.010	0.078	0.085	0.023
-0.769	0.034	0.038	0.005	0.063	0.075	0.013
-0.615	0.026	0.007	0.005	0.049	0.026	0.013
-0.462	0.024	0.017	0.002	0.051	0.062	0.007
-0.308	0.063	0.040	0.015	0.112	0.092	0.027
-0.154	0.040	0.038	0.007	0.080	0.043	0.016
0.000	0.043	0.015	0.006	0.084	0.041	0.018
0.154	0.036	0.027	0.003	0.071	0.085	0.012
0.308	0.025	0.035	0.021	0.055	0.060	0.010
0.462	0.032	0.012	0.005	0.063	0.070	0.013
0.615	0.013	0.019	0.005	0.026	0.018	0.004
0.769	0.024	0.010	0.003	0.049	0.038	0.003
0.923	0.034	0.012	0.011	0.071	0.078	0.017

Table E.41: Orientation measurements for 50 wt% GF high viscosity PP at 40L 90W

z/h	A11	A12	A22	A33	A13	A23
-0.923	0.602	-0.028	0.037	0.360	-0.145	0.089
-0.769	0.753	-0.003	0.020	0.228	-0.032	0.049
-0.615	0.863	0.007	0.026	0.111	0.008	0.034
-0.462	0.846	0.010	0.023	0.131	0.034	0.041
-0.308	0.866	0.008	0.035	0.100	0.015	0.038
-0.154	0.845	0.015	0.043	0.112	0.029	0.044
0.000	0.901	0.012	0.025	0.074	0.008	0.029
0.154	0.848	-0.014	0.040	0.111	-0.022	0.045
0.308	0.818	-0.013	0.048	0.134	-0.035	0.055
0.462	0.863	-0.009	0.018	0.119	-0.027	0.034
0.615	0.863	-0.003	0.018	0.119	-0.029	0.030
0.769	0.844	-0.028	0.017	0.139	-0.064	0.031
0.923	0.747	-0.023	0.016	0.237	-0.072	0.043

Table E.42: Standard deviation for orientation measurements at 50 wt% GF high viscosity PP at 40L 90W

z/h	A11	A12	A22	A33	A13	A23
-0.923	0.024	0.030	0.029	0.031	0.082	0.028
-0.769	0.077	0.005	0.008	0.077	0.025	0.016
-0.615	0.005	0.011	0.021	0.018	0.035	0.014
-0.462	0.052	0.004	0.014	0.051	0.024	0.014
-0.308	0.024	0.038	0.015	0.018	0.054	0.010
-0.154	0.020	0.017	0.020	0.032	0.012	0.012
0.000	0.023	0.023	0.014	0.016	0.039	0.007
0.154	0.020	0.023	0.017	0.027	0.067	0.007
0.308	0.018	0.038	0.014	0.021	0.029	0.008
0.462	0.030	0.018	0.004	0.030	0.034	0.005
0.615	0.012	0.028	0.007	0.007	0.073	0.004
0.769	0.035	0.043	0.003	0.034	0.050	0.007
0.923	0.055	0.014	0.007	0.048	0.065	0.010

Table E.43: Orientation measurements for 50 wt% GF low viscosity PP molded at 5 bar 200 rpm at 0L 0W

Z/H	A11	A12	A13	A22	A23	A33
0.923	0.802	0.003	0.010	0.188	0.005	0.010
0.769	0.586	-0.047	0.007	0.387	0.005	0.026
0.615	0.420	-0.040	0.006	0.549	-0.011	0.031
0.462	0.163	-0.033	0.002	0.775	-0.017	0.062
0.308	0.080	-0.036	-0.006	0.837	0.027	0.083
0.154	0.099	-0.039	-0.016	0.826	0.010	0.075
0.000	0.111	0.014	-0.036	0.818	-0.021	0.070
-0.154	0.172	-0.005	-0.050	0.763	-0.016	0.065
-0.308	0.234	-0.007	-0.058	0.714	0.008	0.052
-0.462	0.255	-0.039	-0.059	0.684	0.019	0.061
-0.615	0.315	0.002	-0.053	0.629	0.013	0.056
-0.769	0.352	0.003	-0.046	0.598	-0.008	0.051
-0.923	0.629	0.021	-0.060	0.333	0.010	0.037

Table E.44: Orientation measurement error for 50 wt% GF low viscosity PP molded at 5 bar at 0L 0W

Z/H	A11	A12	A13	A22	A23	A33
-0.923	0.019	0.003	0.007	0.003	0.004	0.000
-0.769	0.016	0.004	0.017	0.007	0.013	0.001
-0.615	0.015	0.005	0.017	0.010	0.017	0.001
-0.462	0.010	0.005	0.017	0.013	0.019	0.001
-0.308	0.008	0.005	0.017	0.014	0.021	0.001
-0.154	0.009	0.005	0.019	0.013	0.021	0.001
0.000	0.009	0.005	0.018	0.013	0.030	0.001
0.154	0.010	0.005	0.021	0.012	0.002	0.001
0.308	0.011	0.005	0.016	0.011	0.017	0.001
0.462	0.011	0.005	0.018	0.012	0.020	0.001
0.615	0.013	0.005	0.017	0.011	0.026	0.001
0.769	0.014	0.006	0.016	0.011	0.017	0.001
0.923	0.019	0.005	0.011	0.006	0.007	0.001

Table E.45: Orientation measurements for 50 wt% GF low viscosity PP molded at 5 bar at 10L 0W

Z/H	A11	A12	A13	A22	A23	A33
0.923	0.704	0.004	0.008	0.276	0.014	0.020
0.769	0.695	0.035	0.005	0.281	0.006	0.025
0.615	0.644	0.067	-0.003	0.331	0.003	0.024
0.462	0.311	-0.033	0.011	0.624	0.018	0.065
0.308	0.110	-0.038	0.004	0.800	0.019	0.090
0.154	0.103	-0.051	-0.006	0.806	0.046	0.091
0.000	0.151	-0.041	-0.025	0.762	-0.009	0.087
-0.154	0.183	0.005	-0.029	0.741	-0.028	0.076
-0.308	0.345	0.067	-0.029	0.604	-0.037	0.050
-0.462	0.449	0.004	-0.017	0.506	0.011	0.045
-0.615	0.627	0.010	-0.018	0.338	0.009	0.035
-0.769	0.706	-0.022	-0.036	0.260	-0.002	0.034
-0.923	0.571	0.063	-0.002	0.400	0.024	0.029

Table E.46: Orientation measurement error for 50 wt% GF low viscosity PP molded at 5 bar at 10L 0W

Z/H	A11	A12	A13	A22	A23	A33
-0.923	0.021	0.004	0.008	0.006	0.008	0.001
-0.769	0.018	0.004	0.010	0.006	0.010	0.001
-0.615	0.016	0.004	0.009	0.006	0.009	0.001
-0.462	0.014	0.006	0.017	0.013	0.015	0.002
-0.308	0.008	0.005	0.015	0.014	0.017	0.002
-0.154	0.008	0.005	0.020	0.014	0.030	0.002
0.000	0.009	0.005	0.015	0.014	0.016	0.002
0.154	0.011	0.005	0.018	0.014	0.018	0.001
0.308	0.013	0.005	0.012	0.011	0.013	0.001
0.462	0.015	0.005	0.013	0.010	0.011	0.001
0.615	0.016	0.004	0.009	0.007	0.009	0.001
0.769	0.018	0.004	0.007	0.006	0.008	0.001
0.923	0.018	0.005	0.013	0.007	0.011	0.001

Table E.47: Orientation measurements for 50 wt% GF low viscosity PP molded at 5 bar at 40L 0W

Z/H	A11	A12	A13	A22	A23	A33
0.923	0.727	-0.010	0.021	0.253	0.005	0.020
0.769	0.834	0.000	0.001	0.146	-0.003	0.020
0.615	0.846	0.003	0.006	0.139	0.003	0.015
0.462	0.763	-0.052	-0.002	0.216	0.004	0.021
0.308	0.358	0.009	0.012	0.609	-0.001	0.033
0.154	0.106	-0.016	0.001	0.836	-0.005	0.058
0.000	0.151	-0.016	-0.015	0.801	-0.008	0.048
-0.154	0.366	0.023	-0.016	0.595	0.003	0.040
-0.308	0.650	0.008	0.005	0.321	0.008	0.029
-0.462	0.765	-0.014	0.011	0.203	0.004	0.032
-0.615	0.826	-0.022	0.004	0.151	-0.002	0.023
-0.769	0.775	0.008	-0.020	0.203	0.004	0.022
-0.923	0.742	0.016	-0.016	0.245	0.004	0.014

Table E.48: Orientation measurement error for 50 wt% GF low viscosity PP molded at 5 bar at 40L 0W

Z/H	A11	A12	A13	A22	A23	A33
-0.923	0.021	0.004	0.012	0.005	0.011	0.001
-0.769	0.016	0.003	0.007	0.003	0.005	0.001
-0.615	0.015	0.003	0.008	0.003	0.009	0.000
-0.462	0.015	0.003	0.011	0.004	0.014	0.001
-0.308	0.012	0.004	0.023	0.010	0.019	0.001
-0.154	0.006	0.004	0.017	0.014	0.019	0.001
0.000	0.008	0.004	0.017	0.014	0.020	0.001
0.154	0.012	0.004	0.016	0.010	0.019	0.001
0.308	0.015	0.004	0.009	0.007	0.010	0.001
0.462	0.015	0.003	0.010	0.005	0.007	0.001
0.615	0.017	0.003	0.006	0.004	0.005	0.001
0.769	0.017	0.004	0.008	0.004	0.008	0.001
0.923	0.018	0.003	0.017	0.004	0.010	0.000

Table E.49: Orientation measurements for 50 wt% GF low viscosity PP molded at 5 bar at 90L 0W

Z/H	A11	A12	A13	A22	A23	A33
0.923	0.671	-0.078	0.021	0.303	0.002	0.026
0.769	0.362	-0.120	0.009	0.567	-0.009	0.071
0.615	0.175	-0.065	0.016	0.728	-0.026	0.097
0.462	0.131	-0.078	0.005	0.746	0.004	0.123
0.308	0.145	-0.078	0.011	0.727	0.039	0.128
0.154	0.143	-0.096	-0.004	0.725	0.033	0.132
0.000	0.141	-0.077	-0.011	0.722	0.007	0.137
-0.154	0.138	-0.087	-0.024	0.740	-0.011	0.121
-0.308	0.137	-0.098	-0.028	0.737	0.033	0.125
-0.462	0.220	-0.068	-0.074	0.650	0.041	0.131
-0.615	0.286	-0.060	-0.078	0.599	0.006	0.115
-0.769	0.580	-0.019	-0.073	0.348	-0.001	0.072
-0.923	0.719	-0.006	-0.006	0.247	0.011	0.034

Table E.50: Orientation measurement error for 50 wt% GF low viscosity PP molded at 5 bar at 90L 0W

Z/H	A11	A12	A13	A22	A23	A33
-0.923	0.022	0.006	0.009	0.007	0.011	0.001
-0.769	0.016	0.007	0.013	0.010	0.011	0.002
-0.615	0.011	0.006	0.014	0.011	0.013	0.002
-0.462	0.009	0.006	0.017	0.012	0.013	0.002
-0.308	0.009	0.005	0.012	0.011	0.012	0.002
-0.154	0.009	0.005	0.011	0.011	0.010	0.002
0.000	0.009	0.005	0.011	0.011	0.010	0.002
0.154	0.009	0.005	0.012	0.011	0.012	0.002
0.308	0.010	0.006	0.013	0.012	0.015	0.003
0.462	0.010	0.006	0.011	0.011	0.011	0.003
0.615	0.012	0.006	0.012	0.011	0.011	0.003
0.769	0.016	0.005	0.012	0.007	0.013	0.002
0.923	0.021	0.005	0.008	0.006	0.006	0.001

Table E.51: Orientation measurements for 50 wt% GF low viscosity PP molded at 5 bar at 40L 50W

Z/H	A11	A12	A13	A22	A23	A33
-0.923	0.829	-0.023	0.013	0.160	0.000	0.011
-0.769	0.859	0.032	0.003	0.122	0.002	0.019
-0.615	0.878	-0.004	0.001	0.102	0.016	0.020
-0.462	0.865	-0.049	0.000	0.111	0.005	0.024
-0.308	0.756	-0.004	0.025	0.211	-0.003	0.033
-0.154	0.648	0.143	0.007	0.317	0.002	0.035
0.000	0.676	0.168	-0.007	0.294	0.002	0.030
0.154	0.742	0.095	-0.026	0.227	0.005	0.031
0.308	0.822	-0.033	-0.025	0.152	0.007	0.026
0.462	0.873	-0.015	-0.004	0.103	0.006	0.024
0.615	0.881	-0.037	-0.012	0.097	0.007	0.022
0.769	0.855	-0.067	-0.015	0.124	0.012	0.021
0.923	0.702	-0.053	-0.039	0.269	0.013	0.029

Table E.52: Orientation measurement error for 50 wt% GF low viscosity PP molded at 5 bar at 40L 50W

Z/H	A11	A12	A13	A22	A23	A33
-0.923	0.021	0.003	0.005	0.003	0.006	0.000
-0.769	0.018	0.003	0.003	0.004	0.004	0.001
-0.615	0.017	0.003	0.003	0.003	0.003	0.001
-0.462	0.015	0.003	0.004	0.003	0.003	0.001
-0.308	0.015	0.004	0.006	0.005	0.007	0.001
-0.154	0.012	0.004	0.005	0.005	0.004	0.001
0.000	0.012	0.004	0.004	0.003	0.003	0.001
0.154	0.014	0.004	0.006	0.005	0.005	0.001
0.308	0.016	0.003	0.006	0.003	0.006	0.001
0.462	0.016	0.003	0.004	0.003	0.003	0.001
0.615	0.017	0.003	0.003	0.003	0.003	0.001
0.769	0.019	0.004	0.006	0.004	0.005	0.001
0.923	0.021	0.005	0.009	0.007	0.008	0.001

Table E.53: Orientation measurements for 50 wt% GF low viscosity PP molded at 5 bar at 40L 90W

Z/H	A11	A12	A13	A22	A23	A33
-0.923	0.831	-0.106	0.005	0.152	0.002	0.017
-0.769	0.816	-0.031	0.016	0.152	0.007	0.032
-0.615	0.847	-0.041	0.011	0.134	0.000	0.019
-0.462	0.870	-0.006	0.008	0.099	-0.002	0.031
-0.308	0.812	-0.021	-0.010	0.133	-0.004	0.055
-0.154	0.802	-0.021	-0.049	0.126	0.009	0.073
0.000	0.797	-0.009	-0.028	0.105	-0.006	0.098
0.154	0.807	-0.014	-0.010	0.114	0.006	0.079
0.308	0.811	-0.024	-0.024	0.137	0.011	0.052
0.462	0.851	-0.008	-0.051	0.117	0.006	0.032
0.615	0.836	-0.003	-0.029	0.133	-0.006	0.031
0.769	0.796	-0.041	-0.030	0.176	-0.004	0.027
0.923	0.755	-0.095	-0.027	0.226	-0.002	0.019

Table E.54: Orientation measurement error for 50 wt% GF low viscosity PP molded at 5 bar at 40L 90W

Z/H	A11	A12	A13	A22	A23	A33
-0.923	0.019	0.004	0.005	0.003	0.003	0.001
-0.769	0.016	0.004	0.004	0.004	0.004	0.001
-0.615	0.014	0.003	0.004	0.003	0.022	0.001
-0.462	0.015	0.003	0.002	0.003	0.003	0.001
-0.308	0.014	0.004	0.005	0.004	0.003	0.002
-0.154	0.014	0.004	0.002	0.004	0.002	0.002
0.000	0.013	0.004	0.002	0.004	0.002	0.002
0.154	0.014	0.004	0.003	0.004	0.003	0.002
0.308	0.015	0.004	0.005	0.005	0.004	0.002
0.462	0.015	0.003	0.003	0.003	0.003	0.001
0.615	0.015	0.003	0.003	0.003	0.002	0.001
0.769	0.017	0.004	0.006	0.005	0.005	0.001
0.923	0.019	0.004	0.007	0.005	0.007	0.001

Table E.55: Orientation measurements for 50 wt% GF low viscosity PP molded at 10 bar at 0L 0W

Z/H	A11	A12	A13	A22	A23	A33
-0.923	0.727	0.021	0.018	0.255	0.062	0.047
-0.769	0.520	0.009	0.035	0.446	0.060	0.089
-0.615	0.381	0.011	0.036	0.583	-0.001	0.109
-0.462	0.247	-0.006	0.039	0.714	-0.062	0.136
-0.308	0.147	0.001	0.049	0.803	-0.034	0.169
-0.154	0.130	0.001	0.058	0.813	-0.019	0.178
0.000	0.097	-0.015	0.052	0.851	-0.081	0.181
0.154	0.149	-0.020	0.045	0.806	-0.106	0.156
0.308	0.296	-0.031	0.038	0.667	-0.132	0.129
0.462	0.367	-0.027	0.047	0.585	-0.104	0.130
0.615	0.551	-0.021	0.032	0.417	-0.084	0.089
0.769	0.607	-0.019	0.029	0.363	-0.125	0.082
0.923	0.669	-0.021	0.020	0.310	-0.118	0.064

Table E.56: Orientation measurement error for 50 wt% GF low viscosity PP molded at 10 bar at 0L 0W

Z/H	A11	A12	A13	A22	A23	A33
-0.923	0.065	0.008	0.010	0.055	0.031	0.014
-0.769	0.132	0.026	0.014	0.124	0.059	0.027
-0.615	0.072	0.023	0.010	0.082	0.017	0.007
-0.462	0.030	0.021	0.010	0.020	0.072	0.019
-0.308	0.049	0.028	0.003	0.048	0.105	0.012
-0.154	0.051	0.026	0.006	0.053	0.082	0.009
0.000	0.034	0.015	0.005	0.033	0.050	0.019
0.154	0.034	0.017	0.008	0.033	0.065	0.020
0.308	0.133	0.012	0.006	0.127	0.058	0.026
0.462	0.130	0.022	0.011	0.120	0.046	0.028
0.615	0.181	0.046	0.017	0.165	0.113	0.041
0.769	0.260	0.039	0.011	0.249	0.129	0.051
0.923	0.096	0.024	0.011	0.087	0.074	0.030

Table E.57: Orientation measurements for 50 wt% GF low viscosity PP molded at 10 bar at 10L 0W

Z/H	A11	A12	A13	A22	A23	A33
-0.923	0.571	0.011	0.026	0.403	0.020	0.076
-0.769	0.699	0.009	0.027	0.275	-0.004	0.065
-0.615	0.597	0.002	0.030	0.373	-0.023	0.073
-0.462	0.499	0.003	0.040	0.461	-0.034	0.098
-0.308	0.389	0.018	0.037	0.574	0.046	0.111
-0.154	0.249	0.027	0.043	0.708	0.067	0.136
0.000	0.148	0.004	0.048	0.804	-0.003	0.166
0.154	0.084	-0.017	0.049	0.867	-0.078	0.179
0.308	0.150	-0.030	0.043	0.807	-0.107	0.158
0.462	0.404	-0.034	0.041	0.555	-0.093	0.121
0.615	0.638	-0.021	0.031	0.331	-0.079	0.069
0.769	0.708	-0.017	0.024	0.268	-0.058	0.061
0.923	0.715	-0.021	0.014	0.271	-0.055	0.045

Table E.58: Orientation measurement error for 50 wt% GF low viscosity PP molded at 10 bar at 10L 0W

Z/H	A11	A12	A13	A22	A23	A33
-0.923	0.101	0.012	0.004	0.101	0.063	0.012
-0.769	0.115	0.015	0.010	0.109	0.046	0.023
-0.615	0.087	0.009	0.012	0.085	0.050	0.019
-0.462	0.074	0.007	0.003	0.072	0.032	0.007
-0.308	0.032	0.019	0.013	0.021	0.122	0.022
-0.154	0.097	0.026	0.008	0.102	0.073	0.019
0.000	0.047	0.016	0.008	0.051	0.072	0.015
0.154	0.007	0.019	0.008	0.009	0.066	0.018
0.308	0.012	0.010	0.007	0.013	0.046	0.017
0.462	0.030	0.014	0.005	0.028	0.038	0.010
0.615	0.047	0.012	0.009	0.055	0.035	0.008
0.769	0.055	0.012	0.004	0.056	0.039	0.005
0.923	0.039	0.007	0.003	0.037	0.022	0.011

Table E.59: Orientation measurements for 50 wt% GF low viscosity PP molded at 10 bar at 40L 0W

Z/H	A11	A12	A13	A22	A23	A33
-0.923	0.650	0.010	0.016	0.334	0.001	0.056
-0.769	0.874	0.012	0.013	0.113	-0.013	0.027
-0.615	0.807	-0.008	0.022	0.171	-0.056	0.043
-0.462	0.780	-0.004	0.034	0.186	0.005	0.048
-0.308	0.705	0.015	0.020	0.275	0.019	0.053
-0.154	0.493	0.025	0.030	0.477	0.035	0.087
0.000	0.205	-0.010	0.046	0.749	-0.043	0.144
0.154	0.116	-0.030	0.050	0.835	-0.131	0.168
0.308	0.310	-0.033	0.042	0.647	-0.125	0.132
0.462	0.762	-0.018	0.023	0.215	-0.052	0.046
0.615	0.794	-0.024	0.024	0.182	-0.062	0.046
0.769	0.837	-0.023	0.031	0.132	-0.013	0.038
0.923	0.699	-0.034	0.026	0.274	-0.058	0.058

Table E.60: Orientation measurement error for 50 wt% GF low viscosity PP molded at 10 bar at 40L 0W

Z/H	A11	A12	A13	A22	A23	A33
-0.923	0.062	0.017	0.002	0.061	0.066	0.004
-0.769	0.050	0.019	0.005	0.044	0.043	0.012
-0.615	0.005	0.014	0.004	0.002	0.033	0.003
-0.462	0.063	0.007	0.021	0.045	0.021	0.016
-0.308	0.032	0.009	0.005	0.037	0.054	0.004
-0.154	0.225	0.023	0.010	0.216	0.044	0.041
0.000	0.014	0.011	0.010	0.024	0.048	0.008
0.154	0.034	0.011	0.008	0.029	0.045	0.019
0.308	0.122	0.014	0.007	0.117	0.039	0.023
0.462	0.030	0.006	0.006	0.027	0.038	0.009
0.615	0.040	0.030	0.005	0.045	0.081	0.002
0.769	0.024	0.008	0.009	0.026	0.033	0.008
0.923	0.066	0.016	0.021	0.056	0.010	0.017

Table E.61: Orientation measurements for 50 wt% GF low viscosity PP molded at 10 bar at 90L 0W

Z/H	A11	A12	A13	A22	A23	A33
-0.923	0.667	0.011	0.027	0.306	0.018	0.071
-0.769	0.720	-0.014	0.042	0.237	-0.027	0.070
-0.615	0.787	0.007	0.035	0.178	0.015	0.046
-0.462	0.716	-0.012	0.029	0.255	-0.044	0.058
-0.308	0.568	0.005	0.047	0.385	0.023	0.095
-0.154	0.204	-0.001	0.062	0.735	-0.017	0.169
0.000	0.143	-0.009	0.053	0.804	-0.061	0.168
0.154	0.170	-0.014	0.053	0.777	-0.060	0.165
0.308	0.354	-0.007	0.046	0.600	-0.029	0.131
0.462	0.486	0.004	0.042	0.471	0.009	0.101
0.615	0.544	0.037	0.047	0.409	0.043	0.095
0.769	0.704	0.000	0.040	0.255	-0.001	0.072
0.923	0.780	-0.024	0.019	0.201	-0.057	0.046

Table E.62: Orientation measurement error for 50 wt% GF low viscosity PP molded at 10 bar at 90L 0W

Z/H	A11	A12	A13	A22	A23	A33
-0.923	0.058	0.022	0.009	0.049	0.066	0.016
-0.769	0.030	0.016	0.005	0.029	0.011	0.004
-0.615	0.026	0.026	0.012	0.019	0.011	0.004
-0.462	0.021	0.031	0.013	0.023	0.072	0.011
-0.308	0.145	0.035	0.026	0.128	0.051	0.051
-0.154	0.041	0.021	0.025	0.045	0.063	0.020
0.000	0.025	0.027	0.007	0.033	0.108	0.006
0.154	0.050	0.030	0.005	0.055	0.090	0.009
0.308	0.144	0.031	0.018	0.127	0.095	0.038
0.462	0.300	0.021	0.008	0.293	0.054	0.055
0.615	0.189	0.015	0.005	0.184	0.039	0.035
0.769	0.071	0.010	0.010	0.063	0.065	0.021
0.923	0.027	0.005	0.004	0.029	0.048	0.004

Table E.63: Orientation measurements for 30 wt% CF PP at 0L 0W

z/h	A11	A12	A22	A33	A13	A23
-0.923	0.457	0.011	0.038	0.505	-0.008	0.087
-0.769	0.418	0.026	0.045	0.538	0.044	0.096
-0.615	0.347	0.019	0.048	0.605	0.001	0.119
-0.462	0.300	-0.008	0.052	0.649	-0.102	0.124
-0.308	0.263	0.001	0.049	0.688	-0.052	0.124
-0.154	0.236	0.003	0.057	0.707	-0.040	0.136
0.000	0.236	0.009	0.064	0.700	-0.017	0.141
0.154	0.243	-0.020	0.068	0.688	-0.106	0.153
0.308	0.265	-0.046	0.066	0.669	-0.191	0.135
0.462	0.364	-0.048	0.059	0.577	-0.181	0.116
0.615	0.444	-0.034	0.040	0.516	-0.139	0.090
0.769	0.692	-0.028	0.027	0.281	-0.084	0.059
0.923	0.532	-0.014	0.037	0.431	-0.054	0.084

Table E.64: Standard deviation for orientation measurements for 30 wt% CF PP at 0L 0W

z/h	A11	A12	A22	A33	A13	A23
-0.923	0.020	0.012	0.012	0.020	0.057	0.009
-0.769	0.039	0.009	0.016	0.039	0.036	0.016
-0.615	0.053	0.035	0.017	0.067	0.129	0.012
-0.462	0.041	0.011	0.026	0.064	0.044	0.018
-0.308	0.090	0.015	0.016	0.106	0.068	0.006
-0.154	0.099	0.026	0.020	0.119	0.083	0.015
0.000	0.124	0.031	0.028	0.152	0.084	0.018
0.154	0.104	0.051	0.030	0.134	0.153	0.010
0.308	0.100	0.023	0.037	0.132	0.082	0.013
0.462	0.030	0.007	0.026	0.010	0.027	0.012
0.615	0.039	0.007	0.013	0.048	0.016	0.002
0.769	0.043	0.002	0.001	0.044	0.007	0.003
0.923	0.129	0.012	0.011	0.118	0.077	0.033

Table E.65: Orientation measurements for 30 wt% CF PP at 10L 0W

z/h	A11	A12	A22	A33	A13	A23
-0.94118	0.498	-0.034	0.032	0.469	-0.150	0.092
-0.82353	0.521	-0.008	0.033	0.446	-0.064	0.081
-0.70588	0.702	0.005	0.024	0.274	-0.013	0.052
-0.58824	0.539	-0.011	0.027	0.434	-0.062	0.074
-0.47059	0.473	-0.017	0.034	0.493	-0.101	0.089
-0.35294	0.432	-0.010	0.035	0.534	-0.077	0.095
-0.23529	0.348	-0.004	0.048	0.604	-0.039	0.113
-0.11765	0.282	0.011	0.064	0.655	-0.038	0.133
0	0.243	-0.008	0.076	0.681	-0.069	0.149
0.117647	0.190	-0.031	0.097	0.713	-0.092	0.169
0.235294	0.264	-0.030	0.063	0.673	-0.099	0.148
0.352941	0.248	-0.034	0.055	0.696	-0.139	0.138
0.470588	0.459	-0.036	0.035	0.507	-0.154	0.089
0.588235	0.645	-0.026	0.029	0.326	-0.120	0.062
0.705882	0.819	-0.020	0.020	0.162	-0.046	0.037
0.823529	0.676	-0.022	0.027	0.298	-0.062	0.053
0.941176	0.606	-0.015	0.021	0.373	-0.092	0.061

Table E.66: Standard deviation for orientation measurements for 30 wt% CF PP at 10L 0W

z/h	A11	A12	A22	A33	A13	A23
-0.941	0.221	0.024	0.013	0.213	0.093	0.041
-0.824	0.032	0.010	0.011	0.025	0.051	0.010
-0.706	0.050	0.017	0.001	0.049	0.017	0.005
-0.588	0.043	0.019	0.004	0.046	0.069	0.005
-0.471	0.061	0.020	0.005	0.065	0.082	0.009
-0.353	0.061	0.025	0.010	0.063	0.105	0.005
-0.235	0.053	0.021	0.030	0.030	0.108	0.023
-0.118	0.056	0.029	0.043	0.066	0.097	0.031
0.000	0.043	0.020	0.044	0.017	0.075	0.028
0.118	0.045	0.038	0.059	0.089	0.097	0.026
0.235	0.179	0.067	0.011	0.187	0.206	0.032
0.353	0.119	0.020	0.016	0.114	0.093	0.024
0.471	0.125	0.006	0.007	0.122	0.044	0.020
0.588	0.034	0.001	0.008	0.026	0.023	0.010
0.706	0.021	0.013	0.003	0.018	0.026	0.002
0.824	0.033	0.022	0.002	0.031	0.058	0.003
0.941	0.066	0.015	0.007	0.069	0.075	0.009

Table E.67: Orientation measurements for 30 wt% CF PP at 40L 0W

z/h	A11	A12	A22	A33	A13	A23
-0.923	0.613	-0.014	0.028	0.359	-0.058	0.071
-0.769	0.789	0.021	0.020	0.192	0.018	0.038
-0.615	0.780	0.023	0.025	0.195	0.028	0.042
-0.462	0.550	0.003	0.034	0.415	-0.018	0.073
-0.308	0.503	0.037	0.042	0.454	0.097	0.091
-0.154	0.339	0.024	0.063	0.598	0.049	0.130
0.000	0.250	-0.009	0.073	0.677	-0.042	0.152
0.154	0.228	-0.024	0.082	0.690	-0.091	0.157
0.308	0.300	-0.053	0.073	0.628	-0.155	0.141
0.462	0.667	-0.031	0.034	0.299	-0.087	0.067
0.615	0.836	-0.009	0.020	0.144	-0.028	0.035
0.769	0.776	-0.012	0.022	0.202	-0.017	0.043
0.923	0.624	-0.002	0.027	0.349	0.017	0.066

Table E.68: Standard deviation for orientation measurements for 30 wt% CF PP at 40L 0W

z/h	A11	A12	A22	A33	A13	A23
-0.923	0.080	0.009	0.005	0.076	0.018	0.052
-0.769	0.095	0.008	0.010	0.085	0.021	0.018
-0.615	0.077	0.015	0.003	0.076	0.011	0.045
-0.462	0.121	0.015	0.008	0.114	0.022	0.069
-0.308	0.071	0.025	0.002	0.071	0.008	0.081
-0.154	0.051	0.021	0.017	0.048	0.027	0.060
0.000	0.071	0.022	0.016	0.068	0.021	0.120
0.154	0.055	0.011	0.013	0.044	0.023	0.061
0.308	0.082	0.006	0.003	0.079	0.011	0.023
0.462	0.077	0.007	0.007	0.073	0.014	0.025
0.615	0.028	0.016	0.003	0.028	0.006	0.031
0.769	0.096	0.028	0.010	0.093	0.023	0.067
0.923	0.078	0.012	0.009	0.071	0.015	0.037

Table E.69: Orientation measurements for 30 wt% CF PP at 90L 0W

z/h	A11	A12	A22	A33	A13	A23
-0.947	0.612	-0.031	0.038	0.351	-0.076	0.083
-0.842	0.746	-0.024	0.023	0.231	-0.064	0.049
-0.737	0.681	0.032	0.024	0.295	0.056	0.051
-0.632	0.543	0.044	0.045	0.413	0.066	0.097
-0.526	0.413	0.086	0.066	0.520	0.202	0.134
-0.421	0.315	0.110	0.099	0.586	0.224	0.177
-0.316	0.226	0.084	0.109	0.664	0.158	0.192
-0.211	0.135	0.048	0.137	0.728	0.078	0.221
-0.105	0.112	0.012	0.138	0.749	0.004	0.239
0.000	0.121	-0.030	0.149	0.730	-0.080	0.244
0.105	0.150	-0.069	0.156	0.694	-0.124	0.230
0.211	0.182	-0.091	0.137	0.682	-0.171	0.220
0.316	0.207	-0.090	0.113	0.681	-0.196	0.201
0.421	0.247	-0.070	0.082	0.671	-0.203	0.167
0.526	0.312	-0.076	0.071	0.617	-0.209	0.150
0.632	0.364	-0.074	0.056	0.580	-0.185	0.128
0.737	0.630	-0.033	0.027	0.343	-0.085	0.067
0.842	0.725	-0.031	0.020	0.255	-0.116	0.047
0.947	0.693	-0.006	0.016	0.291	-0.028	0.049

Table E.70: Standard deviation for orientation measurements for 30 wt% CF PP at 90L 0W

z/h	A11	A12	A22	A33	A13	A23
-0.947	0.087	0.040	0.017	0.071	0.156	0.027
-0.842	0.086	0.015	0.009	0.079	0.032	0.017
-0.737	0.087	0.024	0.002	0.086	0.074	0.008
-0.632	0.088	0.052	0.022	0.080	0.094	0.034
-0.526	0.047	0.030	0.033	0.015	0.060	0.046
-0.421	0.017	0.036	0.043	0.028	0.046	0.050
-0.316	0.052	0.032	0.058	0.044	0.049	0.064
-0.211	0.026	0.033	0.045	0.052	0.065	0.053
-0.105	0.025	0.032	0.060	0.049	0.090	0.049
0.000	0.015	0.031	0.055	0.041	0.082	0.045
0.105	0.026	0.018	0.049	0.046	0.081	0.033
0.211	0.022	0.006	0.052	0.072	0.046	0.027
0.316	0.032	0.010	0.047	0.072	0.048	0.036
0.421	0.005	0.021	0.046	0.046	0.052	0.034
0.526	0.093	0.028	0.046	0.053	0.106	0.061
0.632	0.072	0.043	0.033	0.070	0.081	0.036
0.737	0.072	0.028	0.002	0.071	0.071	0.011
0.842	0.049	0.034	0.003	0.052	0.097	0.008
0.947	0.086	0.020	0.006	0.080	0.078	0.016

Table E.71: Orientation measurements for 30 wt% CF PP at 40L 50W

z/h	A11	A12	A13	A22	A23	A33
-0.923	0.810	-0.014	-0.006	0.173	0.035	0.017
-0.769	0.858	-0.025	-0.010	0.119	0.029	0.023
-0.615	0.905	0.000	0.004	0.076	0.024	0.018
-0.462	0.881	0.038	0.011	0.099	0.021	0.020
-0.308	0.749	-0.068	-0.012	0.228	0.053	0.022
-0.154	0.751	-0.109	-0.028	0.219	0.064	0.030
0.000	0.636	-0.186	-0.048	0.329	0.089	0.035
0.154	0.586	-0.287	-0.065	0.391	0.076	0.023
0.308	0.820	-0.119	-0.032	0.165	0.033	0.016
0.462	0.860	-0.008	-0.007	0.122	0.031	0.018
0.615	0.885	0.007	0.005	0.095	0.029	0.020
0.769	0.869	0.008	0.003	0.119	0.023	0.012
0.923	0.924	-0.012	-0.005	0.067	0.017	0.009

Table E.72: Standard deviation for orientation measurements for 30 wt% CF PP at 40L 50W

z/h	A11	A12	A13	A22	A23	A33
-0.923	0.019	0.003	0.006	0.003	0.005	0.000
-0.769	0.018	0.003	0.005	0.003	0.004	0.001
-0.615	0.018	0.003	0.003	0.002	0.002	0.001
-0.462	0.017	0.003	0.005	0.003	0.003	0.001
-0.308	0.016	0.004	0.008	0.004	0.006	0.000
-0.154	0.014	0.004	0.011	0.005	0.007	0.001
0.000	0.013	0.005	0.014	0.007	0.010	0.001
0.154	0.012	0.005	0.011	0.006	0.008	0.001
0.308	0.016	0.004	0.008	0.004	0.006	0.001
0.462	0.019	0.003	0.005	0.003	0.004	0.001
0.615	0.019	0.003	0.003	0.002	0.003	0.001
0.769	0.018	0.003	0.007	0.003	0.005	0.001
0.923	0.020	0.003	0.006	0.003	0.004	0.000

Table E.73: Orientation measurements for 30 wt% CF PP at 40L 90W

z/h	A11	A12	A13	A22	A23	A33
-0.923	0.610	-0.029	0.004	0.371	0.055	0.019
-0.769	0.834	0.011	0.006	0.142	0.032	0.024
-0.615	0.846	0.046	0.006	0.125	0.028	0.029
-0.462	0.772	-0.039	-0.077	0.136	0.061	0.092
-0.308	0.798	-0.098	-0.119	0.090	0.055	0.112
-0.154	0.769	-0.092	-0.067	0.148	0.068	0.083
0.000	0.796	0.020	0.019	0.137	0.058	0.067
0.154	0.822	0.022	0.024	0.126	0.051	0.052
0.308	0.801	-0.110	-0.038	0.166	0.052	0.033
0.462	0.841	-0.089	-0.010	0.133	0.042	0.025
0.615	0.757	0.000	0.012	0.219	0.048	0.024
0.769	0.893	0.014	0.003	0.095	0.022	0.011
0.923	0.728	0.100	0.021	0.254	0.051	0.018

Table E.74: Standard deviation for orientation measurements for 30 wt% CF PP at 40L 90W

z/h	A11	A12	A22	A33	A13	A23
-0.923	0.145	0.015	0.006	0.140	0.026	0.064
-0.769	0.054	0.009	0.005	0.052	0.009	0.019
-0.615	0.053	0.007	0.004	0.054	0.007	0.021
-0.462	0.056	0.019	0.008	0.053	0.011	0.025
-0.308	0.071	0.018	0.007	0.066	0.015	0.037
-0.154	0.115	0.028	0.011	0.108	0.025	0.061
0.000	0.124	0.019	0.013	0.114	0.026	0.026
0.154	0.057	0.026	0.009	0.051	0.014	0.055
0.308	0.061	0.021	0.007	0.055	0.012	0.038
0.462	0.065	0.009	0.005	0.061	0.011	0.020
0.615	0.025	0.020	0.006	0.022	0.007	0.034
0.769	0.092	0.021	0.011	0.084	0.019	0.054
0.923	0.143	0.013	0.018	0.127	0.036	0.043